# STRUCTURAL DYNAMICS OF FUNGAL CELL WALLS ELUCIDATED BY SOLID-STATE NMR

By

Liyanage Devthilini Pasasum Fernando

A DISSERTATION

Submitted to
Michigan State University
in partial fulfillment of the requirements
for the degree of

Chemistry – Doctor of Philosophy

2023

## ABSTRACT

Fungi are the most ubiquitous eukaryotes widely distributed across various ecological niches and have a high significance in industrial, agricultural, and medicinal pathogenesis. These microbes are constantly exposed to environmental stress and host defenses during infection. The cell wall plays a vital role in protecting the fungus and maintaining the structural integrity of the cell; therefore, it is important to understand the structure, dynamics, and adaptation mechanisms of this organelle. First, we employed solid-state NMR techniques, functional genomics, and biochemical analysis to identify the functionality and diversity of cell wall carbohydrates in $^{13}C$-labeled *Aspergillus fumigatus* and four mutants depleted of major structural polysaccharides. We revealed a rigid inner core of the cell wall formed by tightly associated chitin and α-1,3-glucan, which are embedded in a soft matrix of β-glucans and capped by a mobile outer shell rich in galactosaminogalactan and galactomannan. The distribution of α-1,3-glucan in chemically and dynamically distinct domains supports its dual functionality in structure and pathogenicity. Second, we documented the structural fingerprints of chitin across six *Aspergillus*, *Candida,* and *Rhizopus* species. We discovered that the crystalline structure of chitin exhibits intrinsic heterogeneity that is resistant to antifungal treatment. Third, we discovered the highly conserved carbohydrate core in both conidia and mycelia using Dynamic Nuclear Polarization (DNP) methods. Finally, we characterized the structural responses of a model halophile *Aspergillus sydowii* continuously exposed to hypersaline conditions, which were found to enhance the biosynthesis of chitin and α-1,3-glucan to form a highly hydrophobic and stiff cell wall to resist external stress. Our findings provide essential structural information of cell wall carbohydrates and their adaptations at the atomic level, which can be used as the target of novel antifungal compounds with broad spectrums and improved efficacy.

This dissertation is dedicated in memory and honor of my grandparents.
Thank you for showing me the value of education.

## ACKNOWLEDGEMENTS

I would like to express my sincere gratitude to my research advisor Dr. Tuo Wang for his guidance and support throughout my doctoral studies. I am so grateful to be in the Wang group. Thank you for believing in me and giving me countless opportunities to develop my skills as a researcher. I could not have handled these challenges without his constant support. Dr. Wang gives us the chance to initiate and work on our own projects, allowing us to explore and learn along the way, but he is always there to provide insightful advice whenever needed. His deep knowledge of NMR spectroscopy, his critical mind and his high standards for data quality have helped me achieve great success.

A special thank you to my committee, Dr. Gary Blanchard, Dr. David Weliky, and Dr. Heedeok, for their continued guidance throughout the program at MSU. Also, I would like to thank my former committee members, Dr. Kermit Murray, Dr. Robert Cook, and Dr. Naohiro Kato at LSU.

Very special thank you to my colleagues, Dr. Qinghui Cheng, Dr. Jayasubba Yarava, Wancheng Zhoa, Isha Gautam, Kalpana Singh, Anand Jacob, Ankur, Debkumar Debnath, and Paninga Muiliya for all your support and for making the lab a fantastic place. Also, I would like to express my special gratitude to former members of the Wang group Dr. Xue Kang, Dr. Chandra Shekar, Dr. Fabien Deligey, Dr. Nader Ghassemi, Dr. Alex Kirui, Dr. Malitha Chathuranga, and Arnab Chakraborty, for all your support and training me during my Ph.D. journey.

I would like to thank all my scientific collaborators for their insightful projects and invaluable discussions, I am glad to work with all the exceptional people Dr. Jean-Paul Latgè at the Institute Pasteur, France and University of Crete, Greece, Ramon Alberto Batista-García at the Research Center for Cell Dynamics, Mexico, Dr. Ping Wang at LSU-HSC, New Orleans, Dr.

Andrew Lipton at Pacific Northwest National Laboratory. Many thanks also go to the National High Magnetic Field Laboratory for instrumental support. In addition, I would like to acknowledge Dr. Fred Mentink-Vigier, Dr. Zhenhong Gan, Dr. Ivan Hung, and Dr. Sungsool Wi, at National High Magnetic Field Laboratory for their assistance in experimental setup and guidance.

My love goes to my family, and I would like to give my deepest appreciation to my beloved husband Hashina Mamuhewa for his immense support during my Ph.D. journey and for encouraging me, without your unparalleled support I would not have achieved this. To my loving son Ashel, you are an inspiration, the light that keeps me going and you gave me a new meaning to life. My heartfelt gratitude goes to my parents, Prasad Fernando, and Deepika Fernando. You always gave me the best of everything in life. Thank you for the love, support, patience, sacrifices, and guidance to be who I am today. You paved the path for me to achieve great things, I owe a huge debt of gratitude to you. My sincere thanks go to my in-laws who always supported me and my family to the best they could, and I am lucky to have them in my life. Thank you to all my friends for helping me persevere through difficult times, the list is simply too long but knows that I truly appreciate you all. Also, I would like to thank my previous mentors, Dr. Rohini De Silva and Dr. Nalin De Silva for guiding me in my undergraduate studies and molding me to become a scientist. Finally, thank you God for letting me through all the difficulties. I will always trust in you!

## TABLE OF CONTENTS

# CHAPTER 1: INTRODUCTION

## 1.1 Fungal Kingdom and Cell Wall Polysaccharides

Fungi are eukaryotic organisms found in a wide range of habitats worldwide, with an estimated five million species[1]. Fungi are classified into phyla such as Chytridiomycota, Mucoromycota, Ascomycota, and Basidiomycota (mushrooms)[1]. This thesis (Chapters 3, 4, and 5) focuses on studying the model organisms in the Ascomycota (*Aspergillus fumigatus*, *Aspergillus sydowii*, *Candida albicans*, and *Candida aurius*) and Mucoromycota (*Rhizopus delemar*). Primarily most fungi are made of hyphae/mycelium (*Aspergillus, Rhizopus*) or multicellular fruiting bodies, and some fungi life forms are unicellular yeast (*Candida*)[2]. Fungi are important in terrestrial carbon and nitrogen cycling as decomposers and play a crucial role in maintaining the ecosystem[1]. Additionally, fungi secrete hydrolytic enzymes that are used in industrial food production and pharmaceuticals.[3] Despite these benefits, many pathogenic fungi, including many *Aspergillus* and *Candida* species, cause fatal infections in immunocompromised individuals.[4] *Aspergillus* species are among the most significant filamentous fungi that form the perspective of pathogenesis, industry, and mycotoxin production[5].

*Aspergillus fumigatus* is a saprophytic fungus and the most common airborne fungal pathogen found in soil and grows in organic debris; responsible for serious human diseases that kill estimated one million people each year[6]. It produces 2-3 μm sized airborne conidia through asexual reproduction[6]. Humans inhale at least several hundred conidia daily, which penetrate deep within the airway system and finally reach lung alveoli[7]. In immunocompromised hosts, *A. fumigatus* germinates and forms filamentous hyphae, causing allergies or severe fatal invasive aspergillosis (Figure 1.1)[6,7]. The first pivotal step in a pathogen's attempt to infect the host is to make contact with the host. The cell wall is comprised of complex and diverse polysaccharides

and has been implicated in multiple pathogenic processes and host-pathogen interactions. The fungal cell wall is a rigid structure with a core of β-1,3-glucan covalently linked to chitin and galactomannan. It is covered with an extracellular matrix consisting of α-1,3-glucan, galactomannan, and galactosaminogalactan[8,9] that helps adhesion and fungal virulence and conceals immunogenic β-1,3-glucan layer from the host immune system[10,11]. The fungal cell wall also contacts with cell proteins and actively uses cell wall enzymes and antigens against the lung phagocyte-killing mechanism[10,11]. The fungus cannot survive without a cell wall or even noticeably change from its native state[12]. Further, most cell wall polysaccharides are absent in mammalian cells. Therefore, fungal cell wall polysaccharide biosynthetic enzymes are an ideal target antifungal agent[13].

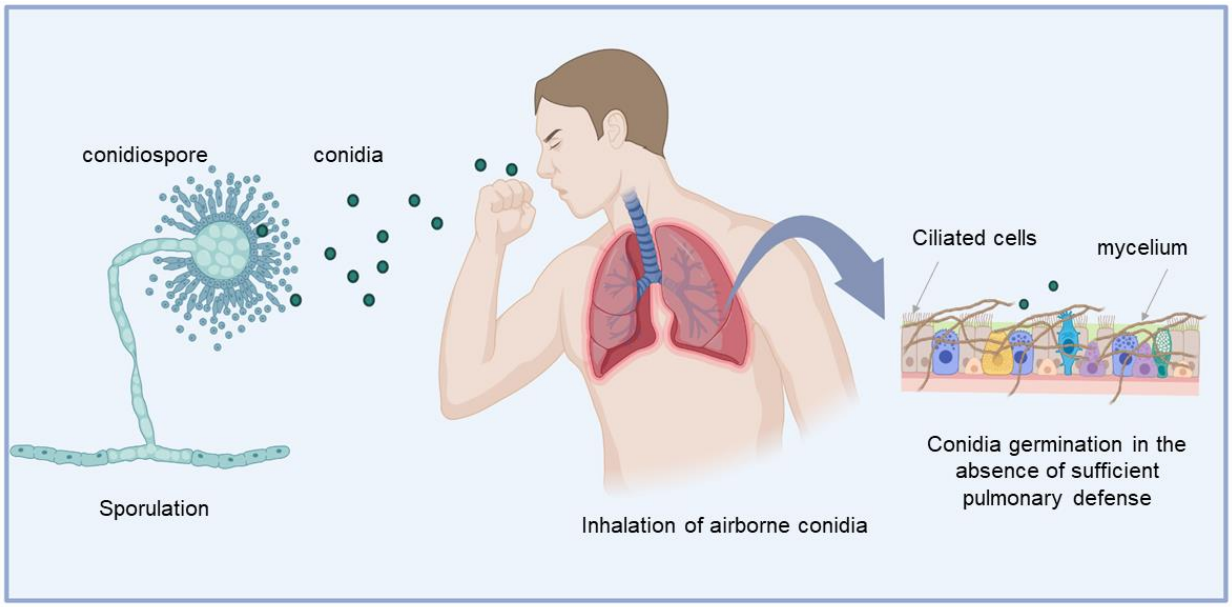


**Figure 1.1 Representative illustration of the infectious life cycle of *Aspergillus fumigatus* in immunocompromised hosts.** (Created with BioRender.com).

In Chapter 6, we will study halophilic fungi, which are a group of fungi that grow in high-salinity environments. These fungi are significant for identifying metabolites and understanding

cellular physiology and biochemistry that support survival, as this is important in various fields such as agriculture, pharmacological, environmental, and industrial applications[14-15]. Many halotolerant and halophilic fungi have been identified, such as *Wallemia, Cladosporium, Hortaea*[16] species, and some *Aspergillus* species like *Aspergillus niger*, *Aspergillus sydowii*[17], *Aspergillus flavus, Aspergillus tubingensis, Aspergillus atacamensis*[18], *Aspergillus destruens*[19], and *Aspergillus versicolor*[20]. *Aspergillus sydowii* is an ascomycetes filamentous fungus found in various habitats such as water of the salterns and dried foods, also in decaying plant matter. It has potential biotechnical aspects as a coral pathogen that cause tissue lesion and coral disease aspergillosis, which results in massive mortalities of coral colonies in the Caribbean Sea[21]. This fungus is a potential fungal model for analyzing molecular adaptation to saline conditions. Stress triggers the overexpression of hydrophobin genes[22], metal transporters in the cell membrane, forming pigmentations[23], and accumulation of compatible solutes[16] as survival mechanisms. However, the scientific community still lacks awareness regarding the cell wall adaptations and tremendous potential of these fungi.

### 1.1.1 Fungal Cell Wall Polysaccharides

The fungal cell walls are composed of highly cross-linked glycan polymers, chitin, galactomannan, galactosaminogalactan, and glycoproteins (Figure 1.2). The relative abundance and nature of these polysaccharides vary between fungal species, as well as during different morphological stages and under different growing conditions. These polysaccharides provide mechanical stability to the cell wall and contribute to the rigidity and morphology of the cell[24].

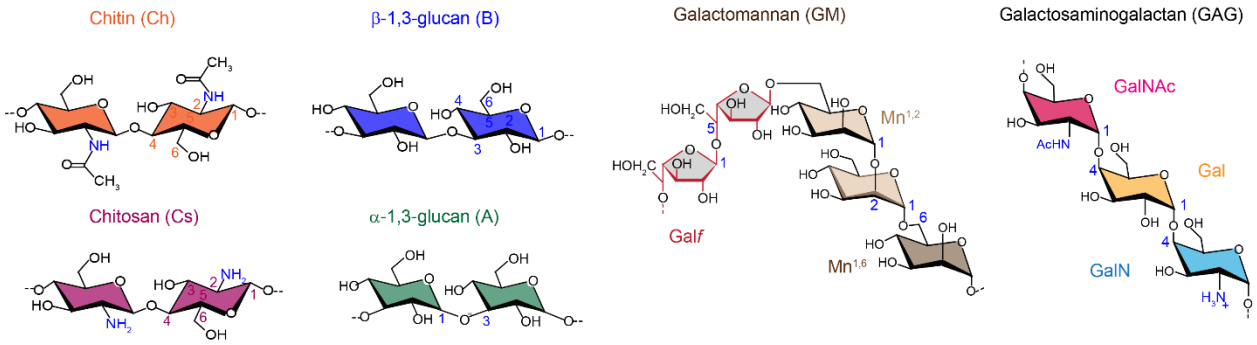


**Figure 1.2 Representative carbohydrate structures of the fungal cell wall.**

Chitin is a linear homopolymer of N-acetyl-glucosamine (GlcNAc) linked with β-1,4 linkages, and it is deposited in the inner core of the cell wall. Chitin is synthesized by multiple chitin synthase enzymes[25]. Chitin plays an important role in the cell wall structure and rigidity[26], but its influence on virulence is not fully understood. Chitin synthesis can be inhibited by nikkomycin and polyoxins, although these compounds are not currently licensed for commercial use. The deacetylated form of chitin, chitosan is also found in some fungal cell walls as a cationic polymer[27].

β-1,3-glucan is a major component in the cell wall, composed of D-glucose (Glc) linked with β-1,3 linkages. It makes up 30-80 % of cell wall mass and appears in microfibrils. The primary structure of β-glucan varies by the other linkages, including β-1,6-glucans, mixed β-1,3/β-1,4, and β-1,6 branching point of the β-1,3 chain[28-29]. β-1,6-glucans are a major component in *Candida albicans* and *Cryptococcus neoformans*, but it is absent in *Aspergillus fumigatus*. β-glucans in *Aspergillus fumigatus* presents as 1,3/β-1,4-glucan. β-1,3-glucan is synthesized by the β-1,3-glucan synthase complex in the plasma membrane, and there is a licensed class of antifungal drugs called echinocandins that block the synthesis of β-1,3-glucans[30]. β-1,3-glucan is a pathogen-associated molecular pattern (PAMP) that is recognized by the host pattern recognition receptors

(PRR) and there are many strategies in the fungal cell wall to minimize the exposure of β-1,3-glucan[31].

α-1,3-glucan is a homopolymer of glucose (Glc) linked by α-1,3 linkage. α-1,3-glucan presents in the cell wall distributed in the inner and the outer cell wall providing a role in structural rigidity, morphology, and virulence[32,33]. α-1,3-glucans are present in filamentous fungi (*Aspergillus*) but absent in some fungi like *Candida*. α-1,3 glucan is synthesized by α-1,3-glucan synthases cell membrane proteins (Ag1, Ag2, Ag3)[34]. Currently, there are no α-1,3-glucan inhibitors and further studies are needed to elucidate the role of α-1,3-glucan in the cell wall.

Galactomannan is a fungal cell wall component made of mannose and galactofuranose (Gal*f*) chains. Mannose provides the backbone of the chain linked with α-1,2 or α-1,6 linkages with side chains of β-1,5 linked Gal*f* residues[35]. Galactomannan plays an important role in the cell wall structure, although its role in virulence is unclear[35,36]. Galactosaminogalactan[8] is a highly variable heteropolymer composed of galactopyronose and N-acetyl-galactosamine (GalNAc) linked in α-1,4 linkage, and it is partially deacetylated. GAG is mostly found in the outer cell wall and contributes to virulence and also gives adhesion properties to the cell wall[37-38] .

Our limited understanding of the components, polymer network, function, and biogenesis of fungal cell walls has hindered the development of effective cell wall-targeted antifungal drugs, especially among filamentous fungi, due to the lack of high-resolution techniques to characterize the native state of the fungi cell wall. Recently, our group demonstrated the feasibility of using magic-angle spinning (MAS) solid-state NMR to elucidate the structure, spatial proximities, cell wall packing, and dynamics of intact fungal cell wall[39]. The fundamentals of the technical aspects of ssNMR will be introduced below.

## 1.2 Solid-state Nuclear Magnetic Resonance Spectroscopy

Solid-state nuclear magnetic resonance (ssNMR) spectroscopy has gained much attention over the past six decades due to new techniques developed to enhance both sensitivity and resolution. With the advancements in ssNMR techniques, such as high magnetic field spectrometers, ultra-fast magic-angle spinning probes, and isotopic labeling schemes ($^{13}C$, $^{15}N$, and $^{2}H$), along with robust pulse sequences, many versatile multi-dimensional correlation pulse sequences and dynamic nuclear polarization (DNP), it has become possible to obtain a wide variety of information such as structure, interaction, dynamics, polymorphism at atomic resolution. SsNMR has proven to be widely applicable across various fields, including biological macromolecules,[40] organic materials[41,42], inorganic solids[43], and material chemistry[44], where it provides valuable information that other techniques (solution NMR, X-ray crystallography) cannot obtain due to their complex, insoluble and amorphous nature. In recent years, ssNMR has become a promising technique to study cellular environments, intact, insoluble biopolymers, and whole cells such as plants[45, 46], bacteria[47], and algae[48] because it is a nondestructive and non-invasive technique and does not require covalent modification. Therefore, ssNMR accurately represents the native behavior of the system.

Although NMR was originally used to study both solids and liquids, the inherent lack of resolution in ssNMR has slowed the application of solid-state compared to the solution-state NMR. In solids, a number of NMR anisotropic interactions (such as shielding, dipolar and quadrupolar interactions) significantly cause line broadening and complicate the interpretation of the spectra. In contrast, molecular tumbling in the isotropic solutions averages orientation-dependent (anisotropic) interactions, resulting in narrow lines in the spectrum. However, ssNMR potentially provides more information than solution NMR because of the direct effect of the anisotropic interactions. For

instance, dipolar coupling can be used to measure internuclear distances, and chemical shift anisotropy can be used to extract molecular structure and dynamics information. Furthermore, solution NMR has molecular size limitations, whereas ssNMR can be applied to large molecules. SsNMR experiments enable a larger range of temperatures (physiological temperatures to cryogenic temperatures) than solution NMR[49]. SsNMR becomes a method of choice compared to XRD for non-crystalline samples. SsNMR does not require high-quality crystals, and it can be applied to any solid forms, such as amorphous, disordered solids. The complementarity of ssNMR and X-ray diffraction can be used to provide improved structural models. Recently, the combination of ssNMR with cryo-EM has shown great promise in the future, tackling the structure of larger bio-assemblies.

This chapter covers the basic principles of solid-state NMR, and it presents a collection of robust solid-state NMR strategies used to get high-resolution and sensitivity for structure determination of biopolymers in the native state.

### 1.2.1 Basics of Nuclear Magnetic Resonance

Nuclear magnetic resonance (NMR) spectroscopy is the oscillation response of the nuclei with non-zero spins (nuclear spin quantum number $I, I \neq 0$) in a magnetic ($B_0$) field to resonant excitation by radio frequency irradiation. When nuclear spins ($I \neq 0$) are placed in the large external magnetic field ($B_0$), the nuclear spin states are quantized into 2I+1 (which refers to the number of possible orientations of nuclear spin in the magnetic field). This phenomenon is known as Zeeman splitting. For spin $I = \frac{1}{2}$ nuclei, the degenerate energy levels split into two spin states (Figure 1.3). The energy difference $\Delta E$ between (I=1/2) two spin states is given by;

$$\Delta E = -\hbar\gamma B_O \qquad \textbf{Eq 1.1}$$

Where $\gamma$ is gyromagnetic ratio of the nucleus of interest, which indicates the strength of the nuclear magnet, $B_0$ is the strength of the external magnetic field, and $\hbar$ is the plank constant ($h$) divided by $2\pi$.

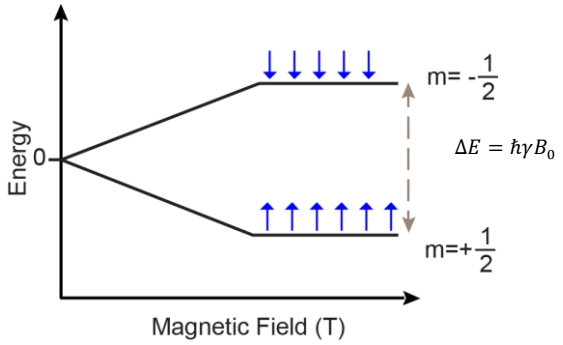


**Figure 1.3 Degenerate nuclear energy levels splitting (spin =1/2 nuclei) under applied magnetic field $B_0$.** For $\gamma > 0$, nuclear spins aligned with the magnetic field (low energy) or opposed to the magnetic field (higher).

The transitions between these nuclear spin states are induced by electromagnetic irradiation in the radio frequency (RF) regime. The nuclear spin system absorbs the energy (equal to $\Delta E$) and the spin system resonates. Following the RF pulse, the spin system relaxes to the thermal equilibrium, and a signal called free induction decay (FID) is detected as a result of the voltage induced by the absorption of energy[50-51]. FID is a time-domain signal that is Fourier-transformed into a frequency-domain spectrum. These NMR frequencies are sensitive to local electron distribution, which shields the nuclei, and any nuclei with a unique chemical environment will give a unique NMR frequency. The NMR frequency where the absorption lines occur depends on the magnetic field strength. Therefore, NMR frequencies are reported as chemical shifts (δ) relative to a standard reference compound such as tetramethylsilane (TMS; often used for organic molecules), sodiumtrimethylsilyl propane sulfonate (DSS; reference for protein NMR). The chemical shift

differences are in parts per million and can range from 10 ppm for $^{1}H$, 200 ppm for $^{13}C$, and 900 ppm for $^{15}N$ isotopes[52-53].

### 1.2.2 Nuclear-Spin Interactions

NMR signals depend on various NMR interactions, which could be external ($B_0$ or $B_{RF}$) or internal. Internal magnetic fields affect the spin system and cause extensive line broadening in the solid samples. All the internal interactions are anisotropic, meaning they depend on the sample's orientation relative to the magnetic field direction. The most important NMR interactions in solid-state NMR include chemical shielding (chemical shift), spin-spin coupling (scalar), dipolar-dipolar coupling, and quadrupolar coupling (Table 1.1)[53]. To achieve high-resolution NMR spectra, many techniques have been developed to minimize large anisotropic NMR interactions between nuclei. The most famous examples include magic-angle spinning and high-power dipolar heteronuclear decoupling.

**Table 1.1. Common internal NMR interactions in solids.**

| Interaction | Hamiltonian | Frequency (kHz) |
|---|---|---|
| Chemical shift | $\hat{H}_{cs} = -\gamma\hbar\hat{I}_z.\sigma_{zz}.B_o$<br>$\sigma_{zz}=\sigma_{iso} + \frac{1}{2}\delta_{ani}(3cos^2\theta - 1 - \eta sin^2\theta cos2\beta)$<br>$\delta_{ani}$ is anisotropic parameter and $\eta$ is asymmetry parameter. The external magnetic field creates an electron current around the nucleus (secondary field), which tends to shield the nucleus. | $0\text{-}10^2$ |
| Heteronuclear dipolar coupling | $\hat{H}_{dd}^{hetero} = -d(3cos^2\theta - 1)\hat{I}_z\hat{S}_z$ | $^{13}C$-$^{1}H$; ~20-25<br>$^{13}C$-$^{15}N$; ~1 |
| Homonuclear dipolar coupling | $\hat{H}_{dd}^{homo} = -d.\frac{1}{2}(3cos^2\theta - 1)\left[\hat{I}_z\hat{S}_z - \frac{1}{2}\left(\hat{I}_x\hat{S}_x + \hat{I}_y\hat{S}_y\right)\right]$<br>Here, $dipolar\ coupling\ constant = d$ | $^{13}C$-$^{13}C$ 2-3.2<br>$^{1}H$-$^{1}H$ ~120 |

Table 1.1 (cont'd)

| | | |
|---|---|---|
| | $d = \left(\frac{\mu_0}{4\pi}\right)\frac{\gamma_I \gamma_I \hbar}{r^3}$<br>Each nuclear spin with magnetic momentum interacts through space, known as dipolar coupling. The coupling strength falls off with the internuclear distance ($r^{-3}$). It can be used to measure the internuclear distances. | |
| Quadrupolar coupling | $\hat{H}_Q = \frac{eQ}{2I(2I-1)} h\hat{I}.V.\hat{I}$<br>Nuclides with a spin quantum number greater than ½ possess a nuclear electric quadrupole moment ($eQ$). | $^2$H; 0-$10^2$ |
| J-coupling | $\hat{H}_J = 2\pi J_{12} I_1 I_2$<br>Through chemical bond spin-spin coupling, it give information of molecular level connectivity and can be used to transfer magnetization between nuclear spins. Dominate interaction in solution NMR. | 0-10 |

### 1.2.3 Magic-Angle Spinning (MAS)

In liquid NMR, rapid tumbling averages out anisotropic NMR interactions to zero on the NMR timescale. This is because the rate of change of molecular orientation is fast relative to the chemical shift anisotropy and dipole-dipole coupling, resulting in well-resolved sharp peaks. In contrast, solid-state NMR relies on mechanically applied uniaxial rotation. The sample rotor is spun about an axis inclined at 54.74° ($\theta_r$) to the applied magnetic field $B_0$ to average all the anisotropic interactions, called magic-angle spinning (MAS). In this circumstance, the average ($3cos^2\theta$-1) orientation dependence of the chemical shift anisotropy and heteronuclear dipolar coupling can be shown as follows,

$$\langle\frac{1}{2}(3cos^2\theta - 1)\rangle = \frac{1}{2}(3cos^2\theta_r - 1)(3cos^2\beta - 1) \qquad \textbf{Eq:1.2}$$

Where $\theta_r, \theta$ and $\beta$ are defined in Figure 1.4. By setting $\theta_r$ to 54.74°, the anisotropic nuclear interactions average to zero. However, the spinning frequency must be higher than the anisotropic interaction (spinning speed $\omega_r$ >> static line width) to obtain fully narrowed peaks. At low spinning speeds, spinning sidebands appear with a center band at the isotropic chemical shift and sidebands spaced at spinning frequency. When the spinning rate is low, CSA is partially averaged out and becomes zero only after each rotor period. Although spinning sidebands complicate the appearance of the spectra, they are useful in determining the anisotropic interactions.

With the improvement of MAS rotor technology, the spinning frequencies can be increased from 10 kHz up to >100 kHz, which could lead to average out the strong anisotropic interactions such as H-H dipolar coupling, narrowing the $^{1}$H linewidth of ~20 Hz. Also, when the high MAS is combined with the sample deuteration, it further detects $^{1}$H with high resolution and sensitivity.

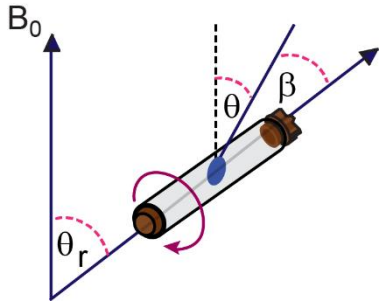


**Figure 1.4 Magic-angle spinning**. The sample is spun about an axis inclined at $\theta_r$. The angle θ is the angle between $B_0$ and the principal z-axis of the interaction and β is the angle between principal z-axis of the interaction and the rotor spinning axis.

### 1.2.4 Dipolar Decoupling

The heteronuclear dipolar coupling $^{13}$C-$^{1}$H ($^{15}$N-$^{1}$H) is not averaged to zero with moderate MAS frequencies (<20 kHz), which causes line broadening when observing the low abundant

$^{13}C/^{15}N$ spin with strongly coupled $^{1}H$ abundant spins nearby. However, MAS alone is not sufficient to achieve high-resolution in ssNMR. To address this, we combine MAS and high-power proton decoupling sequences to remove the effect of heteronuclear dipolar coupling[53]. The first decoupling was achieved by applying continuous irradiation on abundant spin ($^{1}H$) at the proton resonance frequency. Later, more efficient high-power decoupling sequences were developed, such as two-pulse phase modulated (TPPM) and SPINAL sequences.

On the other hand, homogenous interactions involve spatial dispersion of spins orientation (spin diffusion) via strongly coupled $^{1}H$, causing extensive line broadening. MAS can eliminate the impact of homonuclear dipolar coupling on NMR spectra as long as the sample spinning rate is sufficiently fast compared to homonuclear dipolar linewidth. In conventional ssNMR, it is not feasible; instead, this effect can be removed by special pulse sequences such as WAHUHA, MREV-8, and FSLG, etc.

### 1.2.5 Recoupling

Currently, the majority of ssNMR experiments are carried out using MAS and decoupling. However, use of MAS removes (averages) CSA, dipolar coupling, and J coupling, which contains valuable structural information. To selectively reintroduce these interactions while preserving the spectral resolution, a timed RF pulse can be utilized. This process is known as recoupling, and forms the foundation of many modern MAS NMR techniques, allowing to perform multi-phase and multi-dimensional experiments. For instance, recoupling can be used to mediate transitions between spins in muti-dimensional experiments such as radio frequency driven dipolar recoupling (RFDR)[54], which use direct homonuclear dipolar recoupling and PDSD[55]/DARR[56] or CORD[57] which reintroduce the $^{13}C$-$^{1}H$ heteronuclear dipolar coupling. The later recoupling sequences are used in this thesis.

### 1.2.6 One - and Multi-dimensional Correlation Spectroscopy

For the initial screening of a sample, one-dimensional $^{13}C$ spectra should be measured using different methods of initial magnetization. The most commonly used method is the 1D cross-polarization[58] experiments (Figure 1.5a)[58-59], CP is widely used technique in solid-state NMR for signal enhancement, where the polarization is transferred from abundant spins (such as $^{1}H$) to dilute spins (such as $^{13}C$) through dipolar coupling, enhancing the signal to noise (S/N) by a factor of $\frac{\gamma_I}{\gamma_S}$. The relaxation of the abundant $^{1}H$ spin is faster (due to strong homonuclear dipolar coupling and abundance) than that of the dilute $^{13}C$ spins. Thus, direct excitation of $^{13}C$ requires a longer recycle delay to establish equilibrium, especially for unlabeled samples where $^{13}C$ only accounts for 1.1% of the carbon pool. However, using CP enables indirect excitation of $^{13}C$ via $^{13}C$-$^{1}H$ dipolar coupling and allows the pulse sequence to be repeated more rapidly than direct excitation, significantly increasing the signal-to-noise ratio of the spectrum[53] .

This experiment involves a 90° excitation pulse on the proton channel, followed by simultaneous irradiation on the $^{13}C$ and $^{1}H$ channels, referred to as the contact time, during which the $^{1}H$ transfers the magnetization to the $^{13}C$ channel. Then, a long decoupling pulse is applied to $^{1}H$ channel during the acquisition on the $^{13}C$ channel to prevent the detected signals from being broadened by $^{1}H$-$^{13}C$ dipolar couplings.

Efficient cross polarization is obtained through the Hartmann-Hahn match, which matches the RF field (nutation rates) of the abundant spin ($\omega_1^H$) and dilute spin ($\omega_1^{13C}$) at the static condition[59].

$$\omega_1^{1H} = \omega_1^{13C} \qquad \textbf{Eq 1.3}$$

Under magic-angle spinning (MAS), the matching condition becomes the so-called sideband match condition.

$$\omega_1^{1H} = \omega_1^{13C} \pm n\omega_r \quad \textbf{Eq 1.4}$$

Where $\omega_r$ is the MAS rate and n is an integer number. When n is non-zero (1,2,3…), it represents different sideband match conditions, whereas n=0 corresponds to the center band match condition. The polarization transfer in CP is mediated by through-space dipolar coupling; therefore, it is most effective for rigid samples, where molecular motions do not average the dipolar coupling.

Second, the direct polarization experiment is also widely used to polarize the $^{13}$C spins with a 90° pulse directly (Figure 1.5b). The recycle delay ($d_1$) determines the type of molecules that are detected, depending on the spin-lattice relaxation time ($T_1$) of the molecule. A long recycle ($5*T_1^x$) delay ensures complete relaxation to the equilibrium between scans and detects all the molecules in the system, providing quantitative detection. On the other hand, a short recycle delay selectively detects mobile molecules.

The J-coupling-mediated $^1$H-$^{13}$C insensitive nuclei enhancement by polarization transfer (INEPT)[60] experiment is the third type of polarization method (Figure 1.5c). It is used to detect the most dynamic or even solvated molecules. The $^1$H magnetization of rigid segments is rapidly lost due to fast $T_2$ relaxation (due to strong $^1$H-$^1$H dipolar coupling) during the delays of the INEPT sequence.

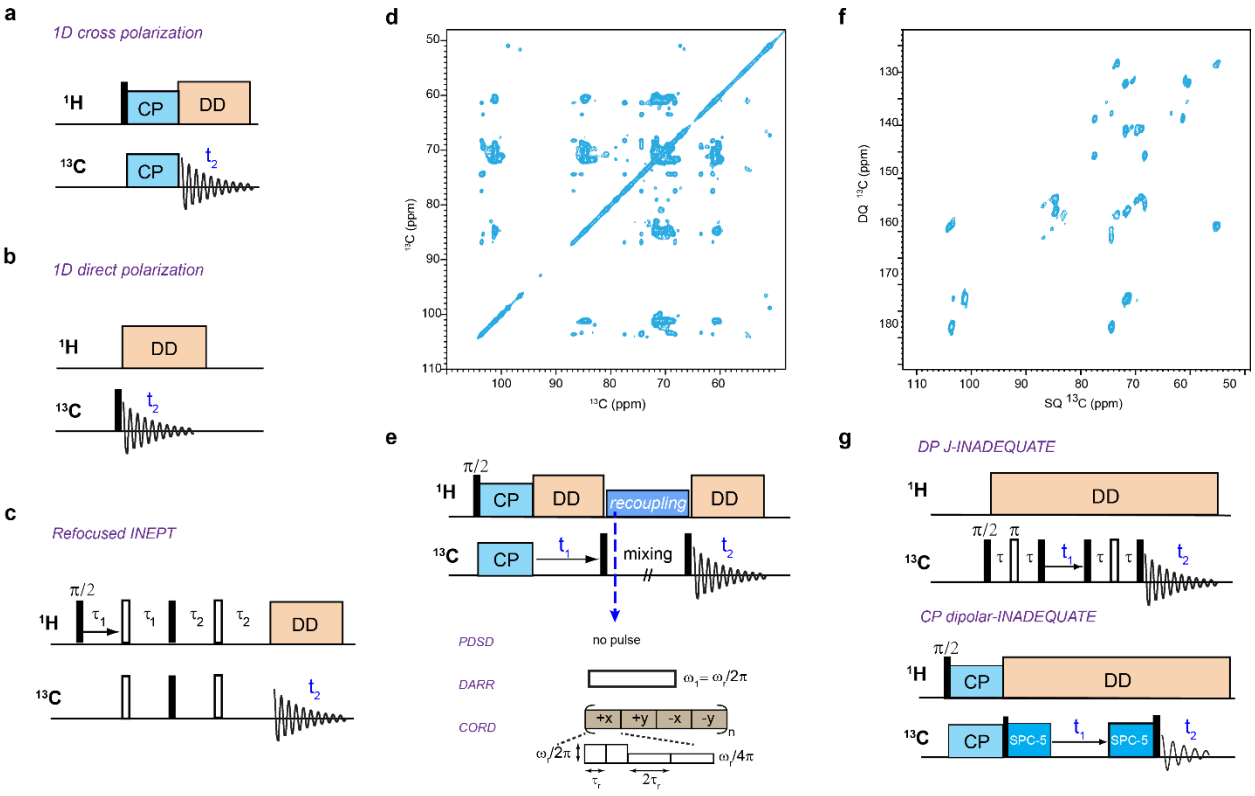


**Figure 1.5 Representative solid-state NMR pulse sequences. a,** 1D $^{13}C$ experiments of CP **b,** DP and **c,** refocused INEPT (bottom) **d,** Representative $^{13}C$-$^{13}C$ correlation spectra. **e,** Pulse sequence of $^{13}C$-$^{13}C$ spin diffusion assisted by reintroduction of $^{13}C$-$^{1}H$ dipolar coupling. **f,** Representative INADEQUATE (DQ-SQ) correlation spectra measured using **g,** Refocused INADEQAUTE experiment. Each horizontal line represents the time, it refers to a channel tuned to a particular nucleus resonance frequency. The pulses are represented in rectangles; 90° pulse in black, 180° is in white. The representative FID identifies the detection. Abbreviations are used in the pulse scheme; cross polarization[58], dipolar decoupling (DD), super cycled POST-C5 (SPC5) evolution time ($t_1$), acquisition time ($t_2$). The spectra are measured at 800 MHz spectrometer.

2D and 3D correlation ssNMR experiments are widely used in structural studies to provide additional spectral resolution. These experimental schemes can correlate the same type of nuclei, called homonuclear correlation, or different nuclei, called heteronuclear correlation. In these experiments, initial excitation is followed by an evolution time named $t_1$, during which magnetization evolves. These blocks are followed by a mixing period that allows magnetization to

exchange between different sites and, finally, direct detection of the NMR signal during the $t_2$ period that generates the direct dimension ($\omega_2$) of the spectra. The 2D data set is created by repeating this cycle with a regular increment of $t_1$ to sample the evolution in the indirect dimension ($\omega_1$).

During the mixing time, the polarization transfer is achieved via J coupling through-bond or dipolar coupling through-space. The flexibility in the basic schemes in the pulse sequence allows for the creation of a wide variety of experiments to serve different purposes and operational conditions. Here, we will briefly discuss two types of $^{13}C$ homonuclear correlation pulse sequences: $^{13}C$ spin diffusion assisted by reintroducing $^{13}C$-$^{1}H$ heteronuclear dipolar coupling (Figure 1.5d and e) and INADEQUATE-type experiments that correlate double-quantum (DQ) chemical shift with single-quantum chemical shift (Figure 1.5f and g).

The first 2D $^{13}C$-$^{13}C$ correlation scheme relies on dipolar recoupling, which reintroduces the dipolar coupling during the mixing period to facilitate polarization transfer. This could be achieved by directly recoupling $^{13}C$ dipolar coupling. However, the transfer of magnetization via $^{13}C$-$^{13}C$ dipolar coupling under moderate MAS is inefficient, as the residual $^{13}C$-$^{13}C$ dipolar couplings are very small. This problem has been circumvented by coupling the low $\gamma$ $^{13}C$ to the surrounding protons during the mixing time, where $^{13}C$ spin diffusion is assisted by reintroducing the $^{13}C$-$^{1}H$ heteronuclear dipolar coupling. Proton Driven Spin Diffusion (PDSD) is one of the experiments that use this scheme.[55] The pulse sequence is as follows: the CP creates the transverse magnetization, which evolves during the evolution time ($t_1$) time, giving the chemical shift information. During the mixing time ($t_m$), the dipolar coupling is recoupled and mediates coherence transfer between $^{13}C$ spins. If the mixing time is short, intra-residue correlations (close in the distance) that are useful for resonance assignment can be detected. Intermolecular cross peaks will be detected with long mixing times, which provides information on sub-nanometer molecular

packing. The PDSD is efficient at slow spinning frequencies (~10 kHz) and low magnetic fields (<14 T); however, it efficiently drops substantially with faster MAS frequencies and higher magnetic fields[61]. To circumvent these difficulties, a dipolar-assisted rotary resonance (DARR) sequence can be employed by applying RF irradiation on the $^{1}$H channel satisfying the rotary resonance recoupling ($R^3$) condition ($\omega_{RF} = \omega_r$)[56]. However, the hardware restrictions (sample and heating by the RF pulse) limit the length of the $t_m$ and also, DARR transfer is no longer efficient when the MAS frequency exceeds 30 kHz.

The Combined $R2_n^v$-Driven (CORD) sequence is developed for spin diffusion at fast MAS and exhibits broad-band homonuclear dipolar recoupling. During the mixing time, the RF field strengths are set at $\omega_{RF}^{1H} = \omega_r$ (1/3 of mixing period) and $\omega_{RF}^{1H} = \omega_r/2$ (2/3 of the mixing time)[57]. The CORD spectra display more uniform cross peak intensities across the spectrum, thus advantageous for homonuclear correlation in biological samples. The PDSD, DARR, and CORD applications on fungi cell walls are shown in the following Chapters in the thesis.

Another important experiment is the refocused Incredible Natural Abundance Double-Quantum (INADEQUATE) experiment. It correlates double-quantum (DQ) chemical shift with single-quantum chemical shift (Figure 1.5f)[62]. The J-based refocused INADEQUATE pulse scheme is illustrated in Figure 1.5g. The initial $^{13}$C magnetization is created by direct polarization using a $\frac{\pi}{2}$ pulse. Then the $\tau - \pi - \tau$ spin echo period allows $^{13}$C magnetization to evolve under J-coupling to create double-quantum coherences between coupled spins. Next, the DQ coherence evolves during the $t_1$ evolution (under the sum of chemical shift). Then, the DQ coherence is transferred to SQ coherence, and the second $\tau - \pi - \tau$ spin echo period establishes the in-phase SQ coherence prior to signal acquisition[63]. The dipolar-based CP INADEQUATE experiment uses the SPC-5 (Supercycled Post-C5) sequence[64]. This includes a rotor-synchronized RF field DQ excitation and

reconversion to SQ coherence for detection. The dipolar-based CP INADEQUATE selectively detects rigid signals, while DP J-INADEQUATE detects mobile signals.

In the INADEQUATE spectrum, the indirect dimension ($\omega_1$) displays the sum of chemical shifts of the spins that are still present after the double-quantum filter, and it is correlated with the isotropic chemical shifts of the individual spins in the direct dimension ($\omega_2$). The DQ/SQ spectra offer a significant advantage over single-quantum spectroscopy. Unlike single-quantum correlation spectra, which contain both diagonal and off-diagonal peaks, double-quantum spectra enable clear observation of coupled spins with small chemical shift differences without interference from diagonal peaks. The presence of those coupled cross peaks are interpreted in terms of chemical bonding (J-coupling-based) or spatial proximity (dipolar-based) of the spins involved[53].

2D $^{15}$N-$^{13}$C N(CA)CX heteronuclear correlation spectra are measured to detect amide and amine signals[65]. The N(CA)CX spectrum is recorded by transferring magnetization from $^{1}$H-$^{15}$N via cross-polarization, and then band-selective $^{15}$N–$^{13}$C polarization transfer is used to select $^{13}$Cα and record NCA spectra. PDSD or DARR step is then used to transfer the magnetization to other carbons nearby. This method has been applied to detect chitin, chitosan amide and amine signals in the fungi samples in Chapters 3 and 4.

### 1.2.7 Molecular Motions

In solid-state, the molecular motions are restricted to small amplitudes from the seconds to pico-seconds range (bond vibration, side chain rotation, local folding, global folding, domain motions) which also have an impact on the NMR spectrum. The molecular motions in the NMR have been studied using relaxation time measurements. Relaxation is the process by which the spins in the sample come to equilibrium with the surrounding environment (regaining the equilibrium state), where spin state population follows the Boltzmann distribution, and no

coherence is present in the system[66]. Relaxation is mediated by the fluctuation in the nuclear spin interactions and the fluctuation arising from molecular motion. In order of importance, spin ½ nuclei relaxation mechanisms are dipole-dipole>chemical shift anisotropy (CSA) > spin-rotation. CSA becomes effective as the dipole-dipole mechanism at the high magnetic field. In solid-state NMR, the relaxation process can be divided into three; spin-lattice relaxation ($T_1$), spin-spin relaxation ($T_2$), and spin-lattice relaxation in the rotating frame ($T_{1\rho}$).

Spin-lattice relaxation, also known as longitudinal relaxation, refers to the process by which the z component of the magnetization is regained (regaining equilibrium) following a perturbation to the system (RF pulse). The relaxation time constant $T_1$ ranges from seconds to hundreds of seconds and is sensitive to motion on the nanosecond-picoseconds (ns-ps) time scale. The spin-spin relaxation is described as transverse relaxation and relates to the xy component of the magnetization, which becomes nonzero when an RF pulse is applied. The relaxation time constant $T_2$ is in the microsecond range and reveals micro or millisecond motions. Furthermore, $T_2$ is related to the linewidth of the peak, the full width at half maximum (FWHM), which is inversely proportional to the apparent $T_2^*$.

$$\frac{1}{T_2^*} = \frac{1}{T_2} + \frac{1}{T_{2,inhomo}} \qquad \textbf{Eq 1.5}$$

$T_2$ refers to intrinsic $T_2$ measured using the Hahn Echo experiment, while $T_{2inhomo}$ results from field inhomogeneity.

The spin-lattice relaxation in the rotating frame ($T_{1\rho}$) is the return of equilibrium of the transverse magnetization in the RF magnetic field $B_1$, which is in the same direction. The relaxation time constant is $T_{1\rho}$, which is in the millisecond range and reveals micro-to-millisecond timescale motions.

The experimental techniques used to measure relaxation in my thesis are summarized below. The $T_1$ relaxation can be measured from inversion recovery and Torchia sequence. In inversion recovery, the initial magnetization ($M_0$) is flipped to -z direction by 180° pulses. After a time delay (t), the magnetization returns to equilibrium in the +z direction ($M_z$), and the final 90° pulse flips the magnetization to the xy plane for detection (Figure 1.6a). For spin 1/2, relaxation can be described mathematically as:

$$M_z = M_0\left[\left(1 - 2e^{-\frac{t}{T_1}}\right)\right] \qquad \textbf{Eq 1.6}$$

The $T_1$ Torchia sequence uses a cross polarization to create the $^{13}C$ initial magnetization, thus, it preferentially detects rigid molecules. Then the magnetization is flip to -z direction with a 90° pulse to monitor how fast it regains the equilibrium ($M_z$) (Figure 1.6b)[67].

The $T_{1\rho}$ spin-lattice relaxation in the rotating frame in the presence of an external RF pulse in the transverse plane is measured by applying a spin-lock field (Figure 1.6c).[68] Firstly, the $^1H$ magnetization is flipped to the y-axis by a 90°, and the 35.3° pulse is applied to rotate the $^1H$ magnetization to the magic-angle. Next, the spin-lock field is applied to the proton channel, resulting in no precision in the rotating frame. Lee-Goldburg CP (LG-CP) is then used to transfer the $^1H$ magnetization to $^{13}C$ through directly bonded $^{13}C$ for detection. These $^{13}C$-$T_1$ and $^1H$-$T_{1\rho}$ measurements are used to measure molecular motion in the fungal cell wall in Chapters 3, 5, and 6.

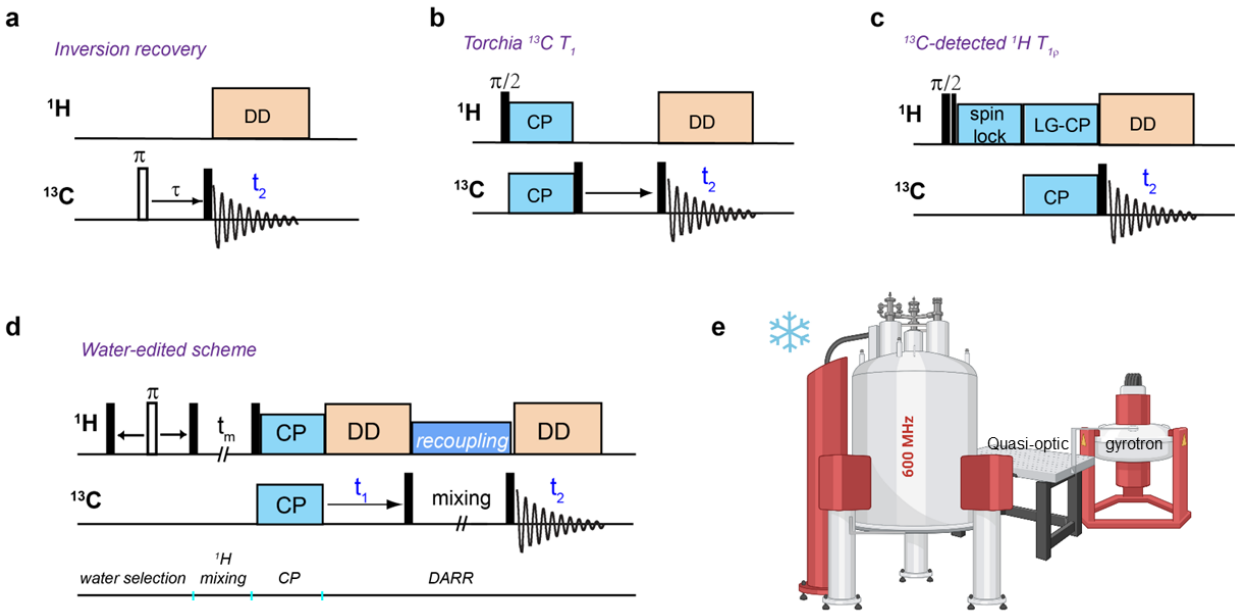


**Figure 1.6 Dynamics and water accessibility experiments. a,** 1D DP $^{13}C$ $T_1$ inversion recovery **b,** 1D CP Torchia $^{13}C$ $T_1$ **c,** $^{1}H$ $T_{1\rho}$ measured using $^{13}C$ detection. **d,** 2D $^{13}C$ -$^{13}C$ water-edited experiment to measure the water accessibility of the polysaccharides. **e,** Dynamic nuclear polarization: showing the polarization transfer pathways from electron to $^{13}C$ via DNP and representative illustration of 600 MHz DNP enhanced ssNMR spectrometer (Created with BioRender.com).

### 1.2.8 Site-Specific Hydration Level

Water plays an essential role in the structure and function of biological macromolecules. In this thesis, solid-state NMR was employed to investigate site-specific water-carbohydrate interactions or water contact. This is done by transferring the $^{1}H$ polarization from water to biomolecules (carbohydrates) using water-edited 2D $^{13}C$-$^{13}C$ correlation experiments. First, a $^{1}H$-$T_2$ relaxation filter is applied to eliminate all the original polysaccharide signals, followed by the transfer of water $^{1}H$ magnetization to carbohydrate $^{1}H$ and then detection through CP. As a result, only carbohydrates in close proximity to water can be detected (Figure 1.6d)[69]. During the $^{1}H$ mixing period, three mechanisms can transfer the water polarization to biomolecules: chemical exchange between proton, spin diffusion, and nuclear Overhauser effect (NOE). During $^{1}H$ spin

diffusion, the dipolar-mediated transfer is the most efficient and dominant mechanism within rigid solids with moderate MAS, and this effect increases with the decrease in temperature.

### 1.2.9 Sensitivity

NMR signals arise from a small excess number of nuclei in the lower energy state. In the presence of an external magnetic field, the distribution of the nuclei in two energy states unperturbed by the RF field is given by the Boltzmann equation:

$$\frac{N_{upper}}{N_{lower}} = e^{-\frac{\Delta E}{kT}} = e^{-\frac{\hbar v}{kT}} \qquad \textbf{Eq 1.7}$$

$N_{upper}$ and $N_{lower}$ are the populations of nuclei in the upper and lower energy states, respectively, $v$ is the Lamour frequency, $k$ is the Boltzmann constant, and T is the temperature in kelvin. The low sensitivity, which originates from small population differences, is the greatest limitation for application in biological systems. The NMR sensitivity is given by the signal-to-noise (S/N) ratio, and it will enhance as the number of nuclei in the lower energy state increases relative to the upper energy state. There are multiple ways to improve the NMR sensitivity, and factors are reflected in the S/N ratio:

$$\frac{S}{N} \propto nT^{-1}B_0^{\frac{3}{2}}\gamma_{ex}\gamma_{obs}^{\frac{3}{2}}T_2^*(NS)^{1/2} \qquad \textbf{Eq 1.8}$$

Where n is the total number of spins, T is temperature, $B_0$ is static magnetic field strength, $\gamma_{ex}$ and $\gamma_{obs}$ denotes the gyromagnetic ratios of excited and detected nucleus, respectively, $T_2^*$ is transverse relaxation, and NS is the number of scans. The most common ways of increasing sensitivity are by increasing the number of scans, isotopic labeling, and packing more materials into the rotors. Additionally, increasing $B_0$ or decreasing T can increase the Boltzmann factor, thereby increasing sensitivity. In recent years, improved polarization transfer techniques have been developed in ssNMR to enhance the signal of relatively low-$\gamma$ nuclei (i.e., that are low in abundance) by

transferring polarization from $^{1}$H. The signal of the low-$\gamma$ is generally enhanced by dipolar-based cross polarization or J-based INEPT by a factor of $\frac{\gamma_{1H}}{\gamma_{13C}}$, which is 4 or 10 for $^{13}$C and $^{15}$N, respectively.

### 1.2.10 Dynamic Nuclear Polarization

Similarly, a larger enhancement can be achieved when the polarization is transferred from electrons to $^{1}$H, with an enhancement factor of $\frac{\gamma_{1H}}{\gamma_{13C}} = 658$. This phenomenon is used in Dynamic Nuclear Polarization (DNP) MAS NMR, which is now used for natural abundance biological studies. Modern DNP-MAS NMR spectrometers combine high-power microwave sources, MAS and cryogenic cooling, polarizing radicals, and high magnetic fields (Figure 1.6e)[70]. The polarization from electron spins to nuclei occurs through microwave irradiation of the electron paramagnetic resonance (EPR) spectrum with the appropriate frequency. Currently, exogenous water-soluble biradicals such as AMUPol[71], TOTAPOL[72], AsymPolPOK[73] are the most efficient polarizing agents used in biomolecular DNP. These biradicals use the cross effect (CE) mechanism to mediate the polarization transfer, a three-spin process involving two dipolar-coupled electrons and a nuclear spin. First, the population difference in electrons is transferred to nuclear spin by matched CE condition $\omega_{e1} - \omega_{e2} = \omega_n$, where $\omega_{e1}$, $\omega_{e2}$ are EPR resonance frequencies and $\omega_n$ nuclear Lamour frequency. Then, nuclei polarization is transferred to the bulk nuclei via $^{1}$H-$^{1}$H spin diffusion (within tens of nanometers).[74] A successful implication of DNP-MAS NMR has been reported in Chapter 5.

### 1.2.11 Resolution

The resolution in NMR can be given by the absorption line shape, which has a full-width half maximum of $\frac{1}{T_2}$. As in Eq 1.5 the observed line shape has two contributions: the homogenous

contribution from the intrinsic line width (determined by $T_2$ relaxation) and an inhomogeneous contribution from the magnetic field's inhomogeneity. This variation in the magnetic field leads to an overall broadening of the line shape. The resolution can be improved by getting a slow FID decay by slowing the intrinsic $T_2$ relaxation. The field inhomogeneity can be reduced by the center packing and stable magnetic field shimming, hence increases the apparent $T_2$. SsNMR has other techniques, such as MAS, ultra-fast MAS, and high-power decoupling, to improve the resolution by reducing the residual anisotropic interaction that causes broadening. Also, complex biological systems like fungal cell walls suffer from spectral crowding, this is circumvented by introducing more dimensions to spectra, using high-power magnetic fields, and performing spectral editing experiments to simplify the spectra.

The signal resolution can be improved at post-measurement before processing the FID. The resolution in NMR is directly proportional to the duration for which the signal is acquired.

$$digital\ resolution = \frac{1}{aq} = \frac{sw}{td} \qquad \textbf{Eq 1.9}$$

Where $aq$ is the acquisition time, $sw$ is the spectral width, and td is the number of data points in the FID. For good resolution, FID can be acquired with a large number of sample points, or a set of zeroes equal to the number of data points can be added before processing (zero filling). A weighting function can be used to narrow the line in the spectra, which means that we need to multiply the FID by Gaussian, exponential sine, or sine squared to get a balance between S/N and resolution[66].

### 1.3 Sample Preparation for SsNMR Analysis

Depending on the objective of the project, samples with either isotopic enrichment (e.g., $^{13}C$ and $^{15}N$) or with natural isotopic abundance can be subjected to ssNMR measurement. Isotopic enrichment provides high sensitivity that enables the rapid measurement of 2D/3D ssNMR experiments to improve the spectral resolution[51] $^{13}C$ enriched precursors such as $^{13}C$-glucose, $^{13}C$-

moltose, and $^{15}$N-labeled amino acids or $^{15}$N-salts such as $Na^{15}NO_3$, $NH_4{}^{15}NO_3$, $(^{15}NH_4)_2SO_4$ can be used depending on the growth media required for culturing different fungal strains[75].

To prepare $^{13}$C,$^{15}$N-isotopic labeled fungi samples (Chapters 3, 4 and 6), 100 mL minimal media containing $^{13}$C-glucose,$^{15}$N salt and trace elements are used. The pH is adjusted to the range of 5.8-7, and the fungi are inoculated to autoclaved culture media. The culture media are then incubated in a shaking incubator at optimum temperature for 2-7 days, depending on the fungi species. Followed by the respective incubation period, fungal mycelium/conidia are harvested using deionized water twice and 10 mM phosphate buffer (pH 7.0) to remove excess molecules. The fungal materials are collected by centrifugation, for 5 min (5,000-10,000 × g), removing the supernatant. Samples are directly packed into Zirconium rotors with outer diameter of 3.2- and 4-mm, holding approximately 30-55 mg and 100 mg of materials, respectively. If needed, the excess water can be absorbed out with a Kim wipe[75].

Preparing samples for DNP experiments requires additional procedures, including the mixing of fungal material with appropriate DNP solvent (matrix) and polarizing agent. The polarizing agents are typically nitroxide-based bi-radicals, that are unreactive and soluble in a range of aqueous solvents. AMUPol, AsymPolPok are used in Chapter 5 and 5-20-mM concentration of radical is used for this study. The radical is dissolved in cryoprotective solvents, such as the mixture of $^{13}$C-depleted $d_8$-glycerol, $D_2O$ and $H_2O$ or the mixture of $d_6$-DMSO, $D_2O$, and $H_2O$. The resulting DNP juice is mixed with the fungal sample, by gently grinding the mixture with a pestle and mortar to ensure penetration of the radicals into the cell walls. The wet fungal paste is then packed into a 3.2 mm rotor (~30-50 mg) for DNP experiments. The enhancement ($\varepsilon_{onn/off}$) and the DNP buildup time are carefully optimized for each sample. Detailed protocols for sample preparations are provided in each chapter for each fungus in the thesis.

## 1.4 Thesis Organization

My thesis consists of papers published during my Ph.D. research and that are currently in the preprint version. My Ph.D. focused on studying the structure and dynamics of fungal cell wall biomacromolecules using solid-state NMR. Chapter 1 introduces fungi and the importance of studying the fungal cell wall. Later in the chapter, the basic principles of NMR and ssNMR strategies used in the following chapters in the thesis are briefly discussed.

Chapter 2 is a review article that summarizes the key findings and technical innovations of recent ssNMR studies on the cell wall biomaterials from model plants, fungal pathogens, bacteria, and microalgae. This review also emphasizes the new research opportunities enabled by ssNMR in cellular systems.

Chapter 3 presents the cell wall analysis of *A. fumigatus* using functional genomics, chemical, and ssNMR approach. This study used $^{13}C$, $^{15}N$ labeled four mutant strains: α-1,3-glucan deficient, chitin deficient, galactomannan deficient, and galactosaminogalactan deficient mutant. SsNMR revealed a cell wall model for *A. fumigatus*, consisting of rigid inner domain formed by chitin, β-1,3-glucan, and α-1,3-glucan, with galactomannan and galactosaminogalactan in the mobile pouter phase. This study confirmed the functional diversity of α-1,3-glucan through its distribution across the alkali-soluble and alkali-insoluble fractions of inner and outer cell walls. Additionally, the data demonstrated that *A. fumigatus* responds to biosynthesis deficiencies by significantly altering the polysaccharide composition to enhance the rigidity and hydrophobicity of the cell walls.

Chapter 4 investigates the structural polymorphism in chitin. This study used isotopically labeled six fungal strains: *A. fumigatus, A. nidulans, A. sydowii, Rhizopus delemar*, *C. albicans,* and *C. auris*. We employed root mean square deviation (RMSD), principal component

analysis (PCA), and linear discriminant analysis (LDA) to compare 62 chitin forms from literature-reported and observed chitin chemical shifts. The chitin in fungi are highly heterogenous and showed similarities with α-allomorph. It also demonstrated the structural resistance of chitin to external stresses. Additionally, this study showed chitosan structure is closely related to the two-fold conformation structure.

In Chapter 5**,** we utilized the dynamic nuclear polarization technique to compare the cell walls of *A. fumigatus* and *C. albicans* prepared using liquid and solid culture media. We have identified conserved carbohydrate structures in the cell walls of liquid and solid cultures and confirmed the structural function of α-1,3-glucan in *A. fumigatus*. This study demonstrated the feasibility of DNP in the unlabeled fungal cell walls and the potential to extend this technique to other challenging label cellular systems.

Finally, in Chapter 6, we conducted a study on *Aspergillus sydowii*, a halophilic fungus, and revealed its cell wall adaptation strategies when growing in high-salt environments. The high-resolution ssNMR experimental approach showed that fungi produced thicker, more hydrophobic, adhesive cell walls compared to optimal condition (0.5 M) to survive the harsh habitats.

## 1.5 Copyright Permissions

Chapter 3, 4, and 5 are reprints of published papers. The papers published in *Nature Communication* and *Frontiers in Molecular Biosciences* are in open access and authors have copyright of the paper to reuse. The paper published in *Journal of Structural Biology: X* authors retain the copyright of the paper. The copyright permissions are obtained from following publishing groups.

Chapter 2: *John Wiley and Sons:* licensed number 5523101085230

Chapter 3: *Nature Communication*

Chapter 4: *Frontiers*

Chapter 5: *Elsevier*

Chapter 6: Submitted to *Nature Communication*: Preprint in *bioRxiv* 2023.04.15.537024

## REFERENCES


1 Blackwell, M. The fungi: 1, 2, 3 ... 5.1 million species? *Am J Bot* 98, 426-438, doi:10.3732/ajb.1000298 (2011).

2 McGinnis, M. R. & Tyring, S. K. Introduction to mycology. *Medical Microbiology; Baron, S., Ed.; University of Texas Medical Branch at Galveston: Galveston, TX, USA* (1996).

3 Kitagaki, H. Medical application of substances derived from non-pathogenic fungi Aspergillus oryzae and A. luchuensis-containing Koji. *Journal of Fungi* 7, 243 (2021).

4 Denning, D. W. Invasive aspergillosis. *Clin. Infect. Dis.* 26, 781-803 (1998).

5 Yoshimi, A., Miyazawa, K. & Abe, K. Cell wall structure and biogenesis in Aspergillus species. *Bioscience, biotechnology, and biochemistry* 80, 1700-1711 (2016).

6 Paterson, R. R. M. & Lima, N. Filamentous fungal human pathogens from food emphasising Aspergillus, Fusarium and Mucor. *Microorganisms* 5, 44 (2017).

7 Latgé, J. P. Aspergillus fumigatus and aspergillosis. *Clin. Microbiol. Rev.* 12, 310-350 (1999).

8 Furukawa, T. *et al.* The negative cofactor 2 complex is a key regulator of drug resistance in Aspergillus fumigatus. *Nat. Commun.* 11, 427 (2020).

9 Chakraborty, A. *et al.* A molecular vision of fungal cell wall organization by functional genomics and solid-state NMR. *Nature communications* 12, 1-12 (2021).

10 Beauvais, A. & Latgé, J.-P. Membrane and cell wall targets in Aspergillus fumigatus. *Drug Resistance Updates* 4, 38-49 (2001).

11 Lee, M. J. & Sheppard, D. C. Recent advances in the understanding of the Aspergillus fumigatus cell wall. *Journal of microbiology* 54, 232-242 (2016).

12 Latgé, J.-P. The cell wall: a carbohydrate armour for the fungal cell. *Mol. Microbiol.* 66, 279-290, doi:https://doi.org/10.1111/j.1365-2958.2007.05872.x (2007).

13 Latgé, J. P. The cell wall: a carbohydrate armour for the fungal cell. *Mol. Microbiol.* 66, 279-290, doi:10.1111/j.1365-2958.2007.05872.x (2007).

14 Ali, I., Khaliq, S., Sajid, S. & Akbar, A. Biotechnological applications of halophilic fungi: past, present, and future. *Fungi in extreme environments: ecological role and biotechnological significance*, 291-306 (2019).

15 Jiménez-Gómez, I. *et al.* Haloadaptative responses of Aspergillus sydowii to extreme water deprivation: Morphology, compatible solutes, and oxidative stress at NaCl saturation. *Journal of Fungi* 6, 316 (2020).

16 Gunde-Cimerman, N. & Plemenitaš, A. Ecology and molecular adaptations of the halophilic black yeast Hortaea werneckii. *Reviews in Environmental Science and Bio/Technology* 5, 323-331, doi:10.1007/s11157-006-9105-0 (2006).

17 Pérez-Llano, Y. *et al.* Stress reshapes the physiological response of halophile fungi to salinity. *Cells* 9, 525 (2020).

18 Martinelli, L. *et al.* Aspergillus atacamensis and A. salisburgensis: two new halophilic species from hypersaline/arid habitats with a phialosimplex-like morphology. *Extremophiles* 21, 755-773 (2017).

19 González-Abradelo, D. *et al.* First demonstration that ascomycetous halophilic fungi (Aspergillus sydowii and Aspergillus destruens) are useful in xenobiotic mycoremediation under high salinity conditions. *Bioresource technology* 279, 287-296 (2019).

20 Oren, A. & Gunde-Cimerman, N. Fungal life in the Dead Sea. *Biology of marine fungi*, 115-132 (2012).

21 Alker, A. P., Smith, G. W. & Kim, K. Characterization of Aspergillus sydowii (Thom et Church), a fungal pathogen of Caribbean sea fan corals. *Hydrobiologia* 460, 105-111 (2001).

22 Tafer, H., Poyntner, C., Lopandic, K., Sterflinger, K. & Piñar, G. Back to the salt mines: Genome and transcriptome comparisons of the halophilic fungus Aspergillus salisburgensis and its halotolerant relative Aspergillus sclerotialis. *Genes* 10, 381 (2019).

23 Plemenitaš, A. *et al.* Adaptation to high salt concentrations in halotolerant/halophilic fungi: a molecular perspective. *Frontiers in Microbiology* 5, doi:10.3389/fmicb.2014.00199 (2014).

24 Bowman, S. M. & Free, S. J. The structure and synthesis of the fungal cell wall. *Bioessays* 28, 799-808 (2006).

25 Hochstenbac, F. *et al.* Identification of a putative alpha-glucan synthase essential for cell wall construction and morphogenesis in fission yeast. . *Proc. Natl. Acad. Sci. USA* 95, 9161-9166 (1998).

26 Jimenez-Ortigosa, C. *et al.* Chitin synthases with a myosin motor-like domain control the resistance of Aspergillus fumigatus to echinocandins. *Antimicrob. Agents Chemother.* 56, 6121-6131 (2012).

27 Rinaudo, M. Chitin and chitosan: Properties and applications. *Progress in polymer science* 31, 603-632 (2006).

28 Manabe, N. & Yamaguchi, Y. 3D structural insights into β-glucans and their binding proteins. *International Journal of Molecular Sciences* 22, 1578 (2021).

29 Kollar, R., Petrakova, E., Ashwell, G., Robbins, P. W. & Cabib, E. Architecture of the Yeast-Cell Wall - the Linkage between Chitin and Beta(1-3)-Glucan. *J. Biol. Chem.* 270, 1170-1178, doi:DOI 10.1074/jbc.270.3.1170 (1995).

30 Denning, D. W. Echinocandin antifungal drugs. *The Lancet* 362, 1142-1151 (2003).

31 Van De Veerdonk, F. L., Gresnigt, M. S., Romani, L., Netea, M. G. & Latge, J.-P. Aspergillus fumigatus morphology and dynamic host interactions. *Nature Reviews Microbiology* 15, 661-674 (2017).

32 Henry, C., Latgé, J. P. & Beauvais, A. alpha1,3 glucans are dispensable in Aspergillus fumigatus. *Eukaryot. Cell* 11, 26-29 (2012).

33 Rappleye, C. A., Eissenberg, L. G. & Goldman, W. E. Histoplasma capsulatum alpha-(1,3)-glucan blocks innate immune recognition by the beta-glucan receptor. *Proc. Natl. Acad. Sci. USA* 104, 1366-1370, doi:10.1073/pnas.0609848104 (2007).

34 Maubon, D. *et al.* AGS3, an alpha(1-3)glucan synthase gene family member of Aspergillus fumigatus, modulates mycelium growth in the lung of experimentally infected mice. *Fungal Genet. Biol.* 43, 366-375 (2006).

35 Fontaine, T. & Latgé, J. P. Galactomannan Produced by Aspergillus fumigatus: An Update on the Structure, Biosynthesis and Biological Functions of an Emblematic Fungal Biomarker *J. Fungi* 6, 283 (2020).

36 Latgé, J. P. *et al.* Chemical and Immunological Characterization of the Extracellular Galactomannan of Asperillus fumigatus. *Infect. Immun.* 62, 5424-5433 (1994).

37 Speth, C., Rambach, G., Lass-Flörl, C., Howell, P. L. & Sheppard, D. C. Galactosaminogalactan (GAG) and its multiple roles in Aspergillus pathogenesis. *Virulence* 10, 976-983, doi:10.1080/21505594.2019.1568174 (2019).

38 Briard, B. *et al.* Galactosaminogalactan activates the inflammasome to provide host protection. *Nature* 588, 688-692 (2020).

39 Kang, X. *et al.* Molecular architecture of fungal cell walls revealed by solid-state NMR. *Nat. Commun.* 9, 2747, doi:Artn 2747 10.1038/S41467-018-05199-0 (2018).

40 Mandala, V. S. & Hong, M. High-sensitivity protein solid-state NMR spectroscopy. *Current opinion in structural biology* 58, 183-190 (2019).

41 Mao, J. D. & Schmidt-Rohr, K. Accurate quantification of aromaticity and nonprotonated aromatic carbon fraction in natural organic matter by C-13 solid-state nuclear magnetic resonance. *Environ. Sci. Technol.* 38, 2680-2684, doi:Doi 10.1021/Es034770x (2004).

42 Mao, J., Cao, X., Olk, D. C., Chu, W. & Schmidt-Rohr, K. Advanced solid-state NMR spectroscopy of natural organic matter. *Progress in nuclear magnetic resonance spectroscopy* 100, 17-51 (2017).

43 Hanna, J. V. & Smith, M. E. Recent technique developments and applications of solid state NMR in characterising inorganic materials. *Solid State Nuclear Magnetic Resonance* 38, 1-18 (2010).

44 Massiot, D. *et al.* Topological, geometric, and chemical order in materials: insights from solid-state NMR. *Accounts of Chemical Research* 46, 1975-1984 (2013).

45 Wang, T., Yang, H., Kubicki, J. D. & Hong, M. Cellulose Structural Polymorphism in Plant Primary Cell Walls Investigated by High-Field 2D Solid-State NMR Spectroscopy and Density Functional Theory Calculations. *Biomacromolecules* 17, 2210-2222, doi:10.1021/acs.biomac.6b00441 (2016).

46 Kang, X. *et al.* Lignin-polysaccharide interactions in plant secondary cell walls revealed by solid-state NMR. *Nat. Commun.* 10, 347, doi:10.1038/s41467-018-08252-0 (2019).

47 Takahashi, H., Hediger, S. & De Paepe, G. Matrix-free dynamic nuclear polarization enables solid-state NMR $^{13}C$-$^{13}C$ correlation spectroscopy of proteins at natural isotopic abundance. *Chem. Commun.* 49, 9479-9481, doi:10.1039/c3cc45195j (2013).

48 Ghassemi, N. *et al.* Solid-state NMR investigations of extracellular matrixes and cell walls of algae, bacteria, fungi, and plants. *Chemical reviews* 122, 10036-10086 (2021).

49 Tycko, R. NMR at low and ultralow temperatures. *Accounts of chemical research* 46, 1923-1932 (2013).

50 Levitt, Malcolm H. *Spin dynamics: basics of nuclear magnetic resonance.* (John Wiley & Sons, 2013).

51 Reif, B., Ashbrook, S. E., Emsley, L. & Hong, M. Solid-state NMR spectroscopy. *Nature Reviews Methods Primers* 1, 2 (2021).

52 Duer, M. J. *Solid state NMR spectroscopy: principles and applications*. (John Wiley & Sons, 2008).

53 Apperley, D. C., Harris, R. K. & Hodgkinson, P. *Solid-state NMR: Basic principles and practice*. (Momentum Press, 2012).

54 Bayro, M. J., Ramachandran, R., Caporini, M. A., Eddy, M. T. & Griffin, R. G. Radio frequency-driven recoupling at high magic-angle spinning frequencies: Homonuclear recoupling sans heteronuclear decoupling. *The Journal of chemical physics* 128, 052321 (2008).

55 Szeverenyi, N. M., Sullivan, M. J. & Maciel, G. E. Observation of spin exchange by two-dimensional fourier transform 13C cross polarization-magic-angle spinning. *Journal of Magnetic Resonance (1969)* 47, 462-475 (1982).

56 Oas, T., Griffin, R. & Levitt, M. Rotary resonance recoupling of dipolar interactions in solid-state nuclear magnetic resonance spectroscopy. *The Journal of chemical physics* 89, 692-695 (1988).

57 Hou, G., Yan, S., Trebosc, J., Amoureux, J. P. & Polenova, T. Broadband homonuclear correlation spectroscopy driven by combined R2(n)(v) sequences under fast magic angle spinning for NMR structural analysis of organic and biological solids. *J. Magn. Reson.* 232, 18-30, doi:10.1016/j.jmr.2013.04.009 (2013).

58 Hohwy, M., Jaroniec, C., Reif, B., Rienstra, C. & Griffin, R. Local structure and relaxation in solid-state NMR: accurate measurement of amide N− H bond lengths and H− N− H bond angles. *Journal of the American Chemical Society* 122, 3218-3219 (2000).

59 Hartmann, S. & Hahn, E. Nuclear double resonance in the rotating frame. *Physical Review* 128, 2042 (1962).

60 Elena, B., Lesage, A., Steuernagel, S., Bockmann, A. & Emsley, L. Proton to carbon-13 INEPT in solid-state NMR spectroscopy. *J. Am. Chem. Soc.* 127, 17296-17302, doi:10.1021/ja054411x (2005).

61 De Paepe, G. Dipolar recoupling in magic angle spinning solid-state nuclear magnetic resonance. *Annu. Rev. Phys. Chem.* 63, 661-684, doi:10.1146/annurev-physchem-032511-143726 (2012).

62 Nierman, W. C. *et al.* Genomic sequence of the pathogenic and allergenic filamentous fungus Aspergillus fumigatus. *Nature* 438, 1151-1156, doi:10.1038/nature04332 (2005).

63 Lesage, A., Bardet, M. & Emsley, L. Through-bond carbon− carbon connectivities in disordered solids by NMR. *Journal of the American Chemical Society* 121, 10987-10993 (1999).

64 Hohwy, M., Jaroniec, C. P., Reif, B., Rienstra, C. M. & Griffin, R. G. Local Structure and Relaxation in Solid-State NMR: Accurate Measurement of Amide N−H Bond Lengths and H−N−H Bond Angles. *J. Am. Chem. Soc.* 122, 3218-3219, doi:10.1021/ja9913737 (2000).

65 Pauli, J., Baldus, M., van Rossum, B.-J., de Groot, H. & Oschkinat, H. Backbone and Side-Chain $^{13}C$ and $^{15}N$ Signal Assignments of the α-Spectrin SH3 Domain by Magic Angle Spinning Solid-State NMR at 17.6 Tesla *Chem. Biochem.* 2, 272-281 (2001).

66 Keeler, J. *Understanding nmr spectroscopy.* (John Wiley & Sons, 2010).

67 Torchia, D. A. Measurement of Proton-Enhanced $^{13}C$-$T_1$ Values by a Method Which Suppresses Artifacts. *J. Magn. Reson.* 30, 613-616, doi:Doi 10.1016/0022-2364(78)90288-3 (1978).

68 Fu, R., Tian, C. & Cross, T. A. Vol. 154 130-135 (Elsevier, 2002).

69 Williams, J. K. & Hong, M. Probing membrane protein structure using water polarization transfer solid-state NMR. *Journal of Magnetic Resonance* 247, 118-127 (2014).

70 Su, Y., Andreas, L. & Griffin, R. G. Magic angle spinning NMR of proteins: high-frequency dynamic nuclear polarization and $^{1}$H detection. *Annu. Rev. Biochem.* 84, 465-497, doi:10.1146/annurev-biochem-060614-034206 (2015).

71 Sauvée, C. *et al.* Highly efficient, water-soluble polarizing agents for dynamic nuclear polarization at high frequency. *Angewandte Chemie International Edition* 52, 10858-10861 (2013).

72 McCoy, K. M., Rogawski, R., Stovicek, O. & McDermott, A. E. Stability of nitroxide biradical TOTAPOL in biological samples. *J. Magn. Reson.* 303, 115-120, doi:10.1016/j.jmr.2019.04.013 (2019).

73 Mentink-Vigier, F. *et al.* Computationally Assisted Design of Polarizing Agents for Dynamic Nuclear Polarization Enhanced NMR: The AsymPol Family. *J. Am. Chem. Soc.* 140, 11013-11019, doi:10.1021/jacs.8b04911 (2018).

74 Equbal, A., Tagami, K. & Han, S. Balancing dipolar and exchange coupling in biradicals to maximize cross effect dynamic nuclear polarization. *Physical Chemistry Chemical Physics* 22, 13569-13579 (2020).

75 Kirui, A. *et al.* Preparation of Fungal and Plant Materials for Structural Elucidation Using Dynamic Nuclear Polarization Solid-State NMR. *J. Vis. Exp.* 144, e59152 (2019).

# CHAPTER 2: SOLID-STATE NMR AND DNP INVESTIGATIONS OF CARBOHYDRATES AND CELL WALL BIOMATERIALS

Review paper reprinted with permission from Liyanage D. Fernando, Wancheng Zhao, Malitha C. Dickwella Widanage, Frederic Mentink-Vigier, and Tuo Wang eMagRes 9, 251-259 (2020). 

## 2.1 Abstract

The cell walls in plants and microbes serve as a central source for bio-renewable energy and biomaterials, as well as the target for novel antibiotics and antifungals. They are biocomposites abundant in complex carbohydrates, a class of biologically important but under-investigated molecules. Solid-state NMR (ssNMR) of carbohydrate materials and cell walls has made significant progress over the last ten years. This article summarizes the recent ssNMR studies that have elucidated the polymorphic structure and heterogeneous dynamics of polysaccharides and other biomolecules, such as proteins, lignin, and pigment, in the intact cell walls or biofilms of eleven species across plants, fungi, bacteria, and algae. We also highlight the assistance of Magic Angle Spinning Dynamic Nuclear Polarization (MAS-DNP) in the enhanced detection of the interaction interface involving lowly populated biopolymers and summarize the recent applications of natural-abundance MAS-DNP in cell wall research, which could substantially broaden the scope of biomolecular NMR by skipping isotope-labeling.

## 2.2 Introduction

Complex carbohydrates are a class of fundamental biomolecules that are spectroscopically difficult to handle. This is because the basic structures of the constituent monosaccharide units are similar, but the polymerized macromolecules are highly polymorphic due to the significant variations in the covalent linkage, torsional conformation, chemical substitution, and hydrogen bonding network. The structural complexity is further enhanced when these polysaccharides are

placed in the cell wall and assembled with other biopolymers. Since carbohydrates are crucial to cellular signaling and recognition, energy storage, and structural building, and the cell walls are the central sources for biofuel and biomaterial production, there is a strong need for establishing a non-destructive and high-resolution method to elucidate the structure and dynamics of polysaccharides and the architecture of their supramolecular composites.

For decades, magic-angle-spinning (MAS) ssNMR has been widely employed to elucidate the structural polymorphism of native and engineered carbohydrates. At the early stages, 1D $^{13}C$ ssNMR is the primary technique for distinguishing the magnetically non-equivalent glucose units in the Iα, Iβ, and other allomorphs of the highly crystalline cellulose[1]. Molecular insights have also been obtained to estimate the relative crystallinity and the number of glucan chains in cellulose microfibril by quantifying the intensity ratio between the peaks of surface and interior glucan chains, as well as to probe the polymer distribution in mobile or rigid domains of plant cell walls by measuring relaxation-filtered spectra[2,3]. Most of these studies are focused on isolated and purified carbohydrate components or specialized cell walls that are rich in certain carbohydrate components, and the limitations in resolution and sensitivity have made it difficult to investigate the more complicated whole-cell systems.

Recently, by combining multidimensional correlation techniques, high magnetic fields, and isotope-labeling, it becomes possible for us to resolve the sophisticated structure and packing of carbohydrates in their cellular environment and explore their functional relevance to material properties. The spectroscopic methods mainly include a series of through-space (CORD, DARR, RFDR, PAR, CHHC, etc.) and through-bond (J-INADEQUATE, INEPT, etc.) correlation methods that allow for resonance assignment and determination of covalent linkages or spatial proximities[4-7], measurements of relaxation and dipolar couplings for understanding polymer dynamics, water-

editing experiments for probing water accessibility[8,9], dipolar- or paramagnetic-based distance measurements for determining ligand-binding (REDOR, PRE, etc.)[10,11], sensitivity-enhancing DNP methods for magnifying the signals of minor species [12-14], and spectral editing techniques for lightening the spectral crowding issue in whole-cell studies[15,16].

These ssNMR measurements are often coupled with supplementary biochemical techniques. For example, the *de novo* assignment of polysaccharide signals is usually validated by involving the genetic mutants or chemically treated samples that specifically knock out certain carbohydrate components[17-20]. The polymer structure and molecular composition derived using NMR chemical shifts and peak intensities are typically compared with the results from the biochemical analyses of glycosyl composition and linkage patterns[21,22].

This established spectroscopic and biochemical toolbox has substantially promoted high-resolution carbohydrate ssNMR studies over the last decade: among the 450 compounds indexed by Complex Carbohydrate Magnetic Resonance Database (CCMRD)[23], 312 entries are from publications after 2010. This review will selectively discuss the key findings and technical innovations of recent ssNMR studies on the cell wall biomaterials from model plants (*Arabidopsis thaliana, Brachypodium distachyon, Zea mays*, poplar, and spruce), fungal pathogens (*Aspergillus fumigatus* and *Cryptococcus neoformans*), bacteria (*Escherichia coli and Bacillus subtilis*), and microalgae (*Chlamydomonas reinhardtii*). We will also discuss how cell wall research has been benefited from the development of MAS-DNP methods and emphasize the new research opportunities enabled by natural-abundance DNP.

## 2.3 Solid-State NMR Investigations of Cell Walls in Plants, Fungi, Bacteria and Algae

### 2.3.1 Polysaccharide Networks and Protein-mediated Loosening of Primary Plant Cell Walls

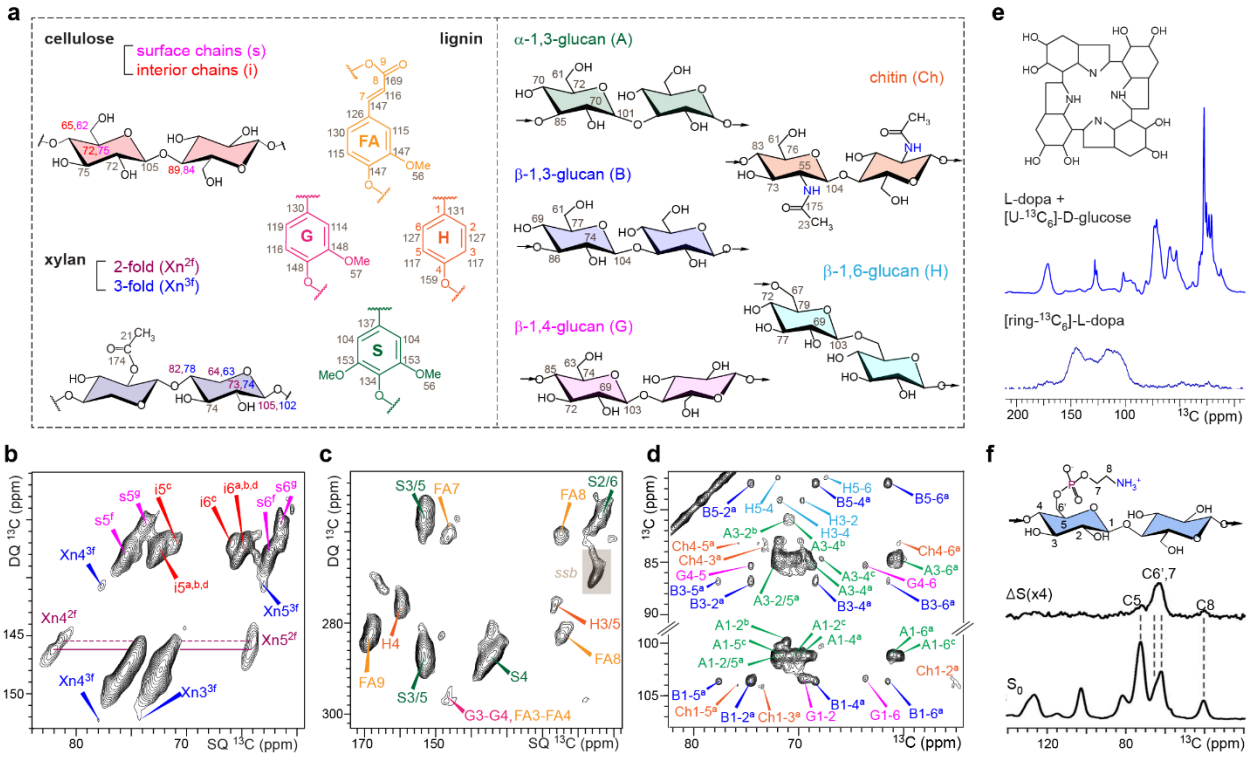


**Figure 2.1 Representative $^{13}C$ spectra and structures of cell wall molecules. a,** Typical biomolecules in secondary plant cell walls (left) and fungi (right). The NMR abbreviations are in parenthesis or annotated on the structure, with representative chemical shift values labeled. The 2D $^{13}C$ INADEQUATE spectra of **b,** carbohydrates and **c**, lignin are shown for maize stem. **d,** 2D $^{13}C$-$^{13}C$ CORD spectrum of A. Fumigatus fungus. Superscripts annotate different conformers. **e,** Proposed molecular structures of melanin and 1D $^{13}C$ CP spectra for C. Neoformans prepared with natural abundance L-dopa and [U-$^{13}C_6$]-D-glucose (top), and [ring-$^{13}C_6$]-L-dopa (bottom). **f,** Phosphoethanolamine cellulose produced in E. Coli as revealed by $^{13}C$ {$^{31}P$}REDOR. $S_0$: full-echo spectrum; ΔS: difference spectrum. Figures are adapted from references [22], [41], [44] and [51] with copyright permission.

Since 2011, Hong and coworkers have been employing a series of 2D/3D ssNMR techniques to elucidate the packing of polysaccharides in uniformly $^{13}C$-labeled primary plant cell walls (grown using $^{13}CO_2$ or $^{13}C$-glucose) and the mechanism through which a class of functional protein (expansin) unlocks the polysaccharide networks for cell expansion[24]. The primary cell wall

being studied is a component synthesized during plant growth; it is mainly a composite of three types of polysaccharides: the partially crystalline cellulose microfibrils that are formed by 18 or more glucan chains (3-4 nm across), the hemicellulose that interacts with cellulose microfibrils, and the acidic pectin that regulates cell wall hydration and porosity. Multiple model plants have been investigated, including the intact cell walls as well as the chemically/enzymatically digested residuals of *Arabidopsis*, *Brachypodium*, and maize. A more detailed discussion of these studies can be found in Reference [[24]], and here we only briefly highlight three major contributions. First, the spectral resolution on high-field magnets (0.7 ppm on 800 MHz) is sufficient for unambiguously resolving the seven types of glucose units that coexist in a cellulose microfibril, determining their hydroxymethyl torsional conformation through $^{1}$H-$^{1}$H distance measurements, and mapping out their relative location within a microfibril[25,26]. Second, a systematic investigation of polymer packing, mobility, and hydration using intact, extracted, wild-type, and mutant samples has demonstrated that at least 25-50% of cellulose surface is in sub-nanometer contact with pectin, which has revised the long-standing concept where these two polymers are phase-separated[27-32]. Third, two novel techniques that rely on MAS-DNP and paramagnetic methods have been developed to determine protein-carbohydrate binding in cell walls[33,34]. The protein expansin is found to perturb the cellulose-xyloglucan junctions in *Arabidopsis* (a dicot) but disrupts the connections of highly and lowly substituted glucuronoarabinoxylan in maize (a commelinid monocot); therefore, expansins bind different carbohydrates in compositionally distinct cell walls for function. These molecular insights have been integrated with many biochemical, modeling, and spectroscopic studies[35-38] to substantially advance our understanding of primary cell walls and the structural aspects underlying plant growth.

### 2.3.2 Lignin-carbohydrate Interactions in Secondary Plant Cell Walls

Inspired by the impactful studies of primary cell walls, recent efforts have been devoted to characterizing the secondary plant cell wall, which is a component synthesized once the cell ceases expansion and forms the majority of the lignocellulosic biomass. The secondary cell wall contains an aromatic polymer named lignin and multiple classes of polysaccharides such as cellulose and the hemicellulose xylan in either 2-fold (2 residues per helical turn; flat-ribbon) or 3-fold (3 residues for a 360° fold; non-flat) helical screw symmetry (Figure 2.1a, left). Benefited from the distinct chemical structures and torsional conformations, the $^{13}C$ signals of these biomolecules are well-resolved in 2D correlation spectra (Figure 2.1b, c**)**. Dupree and colleagues have conducted a series of 2D and 3D CCC experiments on *Arabidopsis* secondary cell walls, which have revealed that only the flat xylan with a regular pattern of acetate or glucuronate substitutions can bind cellulose[18,39,40]. We have further elucidated how carbohydrates interact with lignin, which is a key interaction that determines the biomass recalcitrance to enzymatic treatment and limits the efficiency of biofuel production. Using multiple model plants, such as *Arabidopsis* and maize, we have identified 234 intermolecular cross peaks that pinpoint sub-nanometer packing, 325 relaxation curves that probe polymer mobilities, and 62 site-specific data that identify site-specific water-interactions of biomolecules, which resolved a unique cell wall architecture: xylan is bridging the lignin nanodomains (through its non-flat conformers) to cellulose (through its flat-ribbon form) in a conformation-dependent manner[41]. Considering the large chemical shift anisotropy of aromatics, a 600 MHz NMR, instead of higher magnetic fields, is chosen to simultaneously guarantee sufficient resolution and sensitivity.

This structural frame does not apply to all plant species. In 2019, Dupree and colleagues have found that in the softwood spruce, both xylan and galactoglucomannan (GGM, a uniquely

abundant hemicellulose in softwood) experience a two-domain distribution, with one domain in contact with cellulose and the other one filling the interfibrillar space[19]. It is thus proposed that some GGM and xylan bind to the same cellulose microfibrils, with lignin in association with these cellulose-bound polysaccharides. Apparently, plant species with distinct biopolymer composition expect different cell wall architectures; there are multiple ongoing projects attempting to reveal the assorted schemes of polysaccharides-lignin assembly in a variety of plant species.

Due to the highly complex nature of these whole-cell systems, ssNMR could not provide a high-resolution structure as for the studies of purified proteins or nucleic acids. However, the conceptual schemes of cell wall structures derived from the substantive, molecular evidence have already presented a major improvement from the prevailing models purely based on biochemical assays that either substantially perturb the cellular environment or lack the sub-nanometer resolution to probe the intermolecular contacts between biomolecules.

### 2.3.3 The Carbohydrate Armor and Pigment Deposition of Fungal Pathogens

In 2018, we have initiated a project to investigate the cell walls of fungal pathogens. These microbes cause invasive infections to more than two million patients annually, with high mortality. The fungal cell wall is of high biomedical significance as it is a major target for antifungal agents (for example, caspofungin), and this carbohydrate-rich armor confers the fungi with mechanical strength and structural flexibility to survive through external stress. The fungal cell wall contains 50–60% glucans, 20–30% glycoproteins, and a small portion of chitin (Figure 2.1a, right), and these molecules exhibit beautiful resolution in native, never-dried, and living *A. fumigatus*: on an 800 MHz NMR, the $^{13}$C linewidths are 0.5-0.7 ppm for rigid components (Figure 2.1d) and 0.3-0.5 ppm for mobile molecules[22]. This allows us to resolve the signals of 23 conformers from 7 major types of polysaccharides. Notably, on the world-record 1.5 GHz (35 Tesla) NMR[42], the $^{13}$C

resolution has been further improved to 0.3-0.5 ppm even for the rigid molecules, providing a magnified view of structural polysaccharides (unpublished results).

Because α-1,3-glucans are partially extractable using alkali, they have long been assumed an insignificant role in cell wall mechanics[43], but they exhibit tens of intermolecular cross peaks with chitin microfibrils in long-range $^{13}C$-$^{13}C$ Proton-Assisted Recoupling (PAR) spectra[22]. This unexpected observation echoes the limited water accessibility and low mobility consistently observed in both molecules, and for the first time reveals that the mechanical scaffold of *A. fumigatus* cell wall is formed by tightly packed α-1,3-glucan and chitin. These highly hydrophobic and rigid cores are enclosed within a well-hydrated and dynamic matrix of β-glucans and further capped by an outermost layer that is rich in glycoproteins. With this structural frame, we are currently identifying the structural features that contribute to fungal virulence and drug resistance.

Besides polysaccharides and glycoproteins, fungi also contain a natural pigment named melanin. Stark and coworkers have been tracking down the biosynthesis pathway and molecular structure of melanin, as well as its interactions with carbohydrate components in *Cryptococcus neoformans* cell walls[44-47]. The incorporation of a $^{13}C$-labeled, aromatic precursor L-Dopa during melanization selectively labels aromatic polymers, while feeding exogenous $^{13}C$-sugars highlights the alkyl, alkoxy, alkene, carboxylate, and amide groups (Figure 2.1e). These labeling schemes, used individually or in combination, allow the identification of an indole-based oligomeric structure for the melanin with putative associations with chitin as elucidated via many 2D $^{13}C$-$^{13}C$ DARR and COSY spectra[44]. Melanin is also found to undergo a progressive aromatization process in the cell wall. The versatile techniques of labeling and ssNMR have paved the way for investigating these supramolecular complexes of biopolymers that directly determine fungal pathogenicity.

### 2.3.4 Carbohydrates of Bacterial Biofilm and Microalgae

In bacteria, ssNMR has been employed to investigate the composition and structure of cell walls and their structural responses to antibiotics[48-50], as well as the biofilm, an extracellular nanocomposite of cellulose and amyloid curli fibers[51]. Recently, Cegelski, Hengge, and coworkers have identified a chemically modified form of cellulose in *E. coli*, which is required for the assembly of the biofilm. This polymer has evaded high-resolution detection but is now picked up by the $^{13}C\{^{31}P\}$ REDOR technique, with the major dephasing of intensities happening ($\Delta S$) to the carbon sites that are spatially proximal to the phosphate group (Figure 2.1f)[51]. The genetic basis and molecular signaling involved in introducing this novel structure have also been elucidated.

Like plants, algae are another important photosynthesis biosystem with a high content of polysaccharides. Marcotte and coworkers have measured a model microalgae *C. reinhardtii*. With the dynamical filtering by multiple polarization methods, such as INEPT, heteronuclear NOE, CP, and single pulse, the signals from membrane galactolipids, structural carbohydrates in cell walls, and the storage polysaccharide starch are unambiguously selected and assigned in 1D/2D $^{13}C$ spectra[52,53]. They also identified the major crystalline form of amylose in the starch of microalgae and compared it with other crystalline forms obtained from various organisms[54].

## 2.4 What Could MAS-DNP Contribute to Cell Wall NMR?

### 2.4.1 Selective Detection of The Porous and Outermost Cell Walls

The cell wall is a suitable system for MAS-DNP studies as this outer shell is easily selected over the intracellular components, and uniform polarization throughout the cell wall can be achieved after sample optimization. Hediger and coworkers have first revealed that the biradical TOTAPOL mainly accumulates in the bacterial cell walls of *Bacillus subtilis*, which allows them to preferentially detect the cell wall component and identify the optimal concentration of radicals

for obtaining satisfactory resolution and sensitivity[50]. Bardet, Luterbacher, and coworkers have further shown that maximally 40–200 nm from the surface of poplar wood cell walls can be hyperpolarized via relayed DNP, which allows the selection of secondary cell walls over the inner middle lamellae[55]. Consistently, we have demonstrated that the microscopically porous plant materials (interfibrillar space of ~20-40 nm for primary cell walls) can easily accommodate the small biradicals (e.g. 1.3 nm across for AMUPol) to achieve a homogeneous polarization across the material, which has been confirmed by the identical spectral patterns measured with and without microwave irradiation[33]. A video protocol and the optimized procedures have been published to guide the preparation of samples that ensure a homogeneous distribution of radicals in the cell wall region of whole-cell samples and efficient polarization of the cell wall molecules[56].

### 2.4.2 Detection of The Polymer Interaction Interface Involving Lowly Populated Molecules

The weak intensities of intermolecular cross peaks, due to the small dipolar couplings for long-range correlations and the relaxations occurring during the mixing period, have placed an obstacle to structural determination. The naturally low sensitivity is further worsened by multiple structural factors: 1) the dominance of water (50-80 wt%) in whole cells substantially reduces the effective volume of biomolecules, 2) the coexistence of many polymers decreases the relative concentration of the molecules of interest, and 3) certain molecules involved in the intermolecular interface has low abundance in cell, for example, chitin in *A. fumigatus* (accounting for ~10-15 wt% of the dry mass of cell walls) and lignin in the secondary cell walls of maize[22,41]. Despite the low concentration, these molecules are often of high significance to the mechanical and physical properties of cell walls, for example, chitin is the only partially crystalline polysaccharide in fungi and lignin-carbohydrate interactions waterproof and strengthen the plant biomass. Therefore, a feasible technique for elucidating their intermolecular packing has become a necessity.

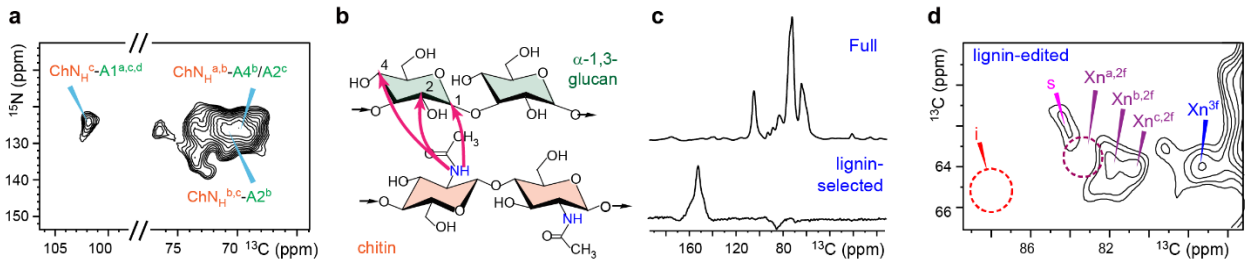


**Figure 2.2 Polymer interface viewed by MAS-DNP. a,** A difference spectrum between two $^{15}$N-$^{13}$C 2D spectra that were measured with a long (3 s) and short (0.1 s) $^{13}$C-$^{13}$C PDSD mixing. Only intermolecular cross peaks are present in the difference spectrum. **b,** Illustration of chitin-glucan packing discovered by the spectrum in panel a. **c,** Selection of lignin aromatics against carbohydrates. **d,** Lignin-edited 2D spectra reveal the composition of lignin-bound carbohydrates. Dashline circles show the carbohydrate components that lack interactions with lignin. Adapted from references [22] and [41] with copyright permission.

These technical barriers can be overcome by integrating the sensitivity enhancement of MAS-DNP with the resolution improvement from spectral editing techniques, which enables efficient detection of intermolecular contacts. We have recently demonstrated this strategy using the following examples. First, in *A. fumigatus*, long-range $^{15}$N-$^{15}$N PAR spectrum has revealed extensive cross peaks between the amide signals from different chitin conformers, confirming the coexistence of these conformers in the same microfibril[22]. This is impressive considering that the nucleus being manipulated has worse sensitivity than $^{13}$C, the experimental scheme is sensitivity-challenging, and the inter-residue correlations occur only between the chitin conformers that account for <10 wt% of the hydrated material. Second, the spectral subtraction of two parent $^{15}$N-$^{13}$C correlation spectra measured with long and short $^{13}$C-$^{13}$C mixing times has unambiguously resolved multiple cross peaks between the nitrogen of chitin amide and the carbons of α-1,3-glucans (Figure 2.2a, b). Notably, in order to subtract two spectra measured with different mixing times, a constant-time experimental scheme is often required at ambient temperature in order to compensate for the heterogeneous relaxations of rigid and mobile molecules during the mixing period[32], but it is not needed at the cryogenic temperature of DNP at which longitudinal relaxation

becomes uniformly long for most structural molecules. Third, with dipolar and frequency filters, as well as the microwave gating achieved through a mechanical shutter[57], the weak signals of lignin are efficiently selected against the polysaccharide peaks that are 260-fold stronger (Figure 2c). This allows us to measure lignin-edited spectra to detect the carbohydrate components in close spatial proximity to these aromatics, which discovers that the 3-fold twisted xylan ($Xn^{3f}$) associates with lignin while the extended flat-ribbon form ($Xn^{a,2f}$) lacks such binding (Figure 2.2d).

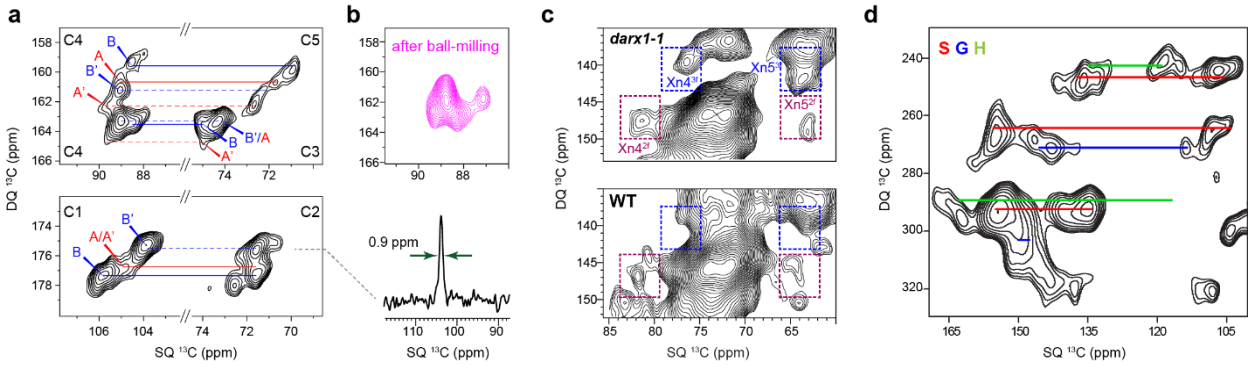


**Figure 2.3 Natural-Abundance DNP of cellulose, matrix polysaccharides, and lignin in plant biomass. a,** Natural-abundance 2D $^{13}C$-$^{13}C$ INADEQUATE spectrum of cellulose in unlabeled cotton. A and A' indicate the glucose units in Iα cellulose allomorph while B and B' are glucose units in Iβ allomorph. 1D $^{13}C$ cross section extracted at $\omega_1$=175 ppm shows the $^{13}C$ linewidth of 0.9 ppm. **b,** C4 region of the crystalline cellulose in cotton after 2 hours of ball-milling. **c,** Resolved signals for 2-fold (purple) and 3-fold (blue) xylan in the stems of wild-type rice and its mutant. **d,** Lignin regions of refocused INADEQUATE of wild-type poplar. S, H, G indicate three fundamental units of lignin. Panel **a-c** were measured on a 600 MHz/395 GHz DNP and panel **d** was collected on a 400 MHz/263 GHz DNP. Figures are adapted from references [58-60] with copyright permission.

### 2.4.3 Skip the Labeling: Natural-Abundance Investigations of Unlabeled Biomaterials

In addition to the assistance in structural analysis, MAS-DNP has also presented an exciting opportunity that could substantially expand the territory of carbohydrate NMR. This is achieved by enabling high-resolution characterization of unlabeled biomaterials utilizing the sensitivity boost from DNP. The typical sensitivity enhancement ($\varepsilon_{on/off}$) factors for cell wall biomaterials is ~30 fold on the 600 MHz/395 GHz MAS-DNP spectrometers[22,41], and ~70 fold on

the lower field (e.g. 400 MHz/263 GHz DNP)[58]. The tremendous timesaving makes it feasible to measure 2D correlation spectra using the very low natural abundance of NMR-active isotopes, 1.1% for $^{13}C$ and 0.4% for $^{15}N$, in unlabeled biomaterials.

Recently, we have optimized a protocol for preparing ssNMR/DNP samples using labeled or unlabeled materials[56]. Starting from this protocol, we have investigated the structure of both microcrystalline carbohydrates (cellulose) and disordered matrix polysaccharides (xylan) in intact plant stems or biomaterials, without isotope-labeling[59,60]. A matrix-free protocol[61,62] are used to maximize the efficient volume of biomolecules, and 2D $^{13}C$-$^{13}C$ INADEQUATE spectra are collected within 5-9.5 hours for each cotton sample and 17-37 hours for each of the more complicated, rice stems. The $^{13}C$ resolution of the partially crystalline cellulose in cotton is largely retained at 100 K, with narrow $^{13}C$ linewidths of 0.9 ppm on a 600 MHz/395 GHz DNP system (Figure 2.3a)[59]. As a result, the carbon connectivities of four magnetically non-equivalent glucose units in cellulose can be fully resolved, and we have further revealed that the ball-milling process, a standard procedure widely used in solution-NMR studies, has totally destroyed the native structure of cellulose microfibrils as evidenced by the distinct spectra (Figure 2.3b). In contrast, the $^{13}C$ linewidth for the mobile matrix polysaccharides has been broadened at low temperature due to the restriction of molecular motions that are important for averaging out the conformational distribution of these disordered molecules. Fortunately, we are still capable of resolving at least the flat-ribbon conformer and the twisted form of xylan in rice stems[60]. We have shown that, compared to the wild-type rice, a *darx1* mutant has dramatically increased the content of non-flat 3-fold xylan but reduced the relative amount of the flat-ribbon 2-fold xylan that associates with cellulose surface, revealing how this mutation perturbs xylan-cellulose interactions on the molecular level (Figure 2.3c).

In addition, Pruski, Abu-Omar, and coworkers have elucidated the lignin composition of poplar biomass: natural-abundance DNP enables the identification of various lignin subunits (Figure 2.3d), p-hydroxyphenyl, H; guaiacyl, G; syringyl, S) and their complex linkages in catalytically processed and genetically engineered poplar species (with high- or low-content of S-units)[58].

Notably, Dr. De Paëpe and coworkers have demonstrated that long-range intermolecular correlations, with distances up to ~7 Å, can be detected using natural-abundance DNP, and this method is employed to probe π-stacking of the nanoassemblies formed by a cyclic diphenylalanine peptide[63]. They have also demonstrated the feasibility of measuring natural-abundance 2D $^{13}C$-$^{15}N$ correlation spectra on small organic molecules[64,65]. As dipolar truncation is no longer an issue at natural isotopic abundance, pulse sequences that efficiently recouple homonuclear (for example, S3) or heteronuclear (for example, TEDOR) dipolar couplings start to play a critical role in the structural determination of unlabeled molecules[66-68]. These technical advances have presented a unique opportunity for further exploring the structure of nitrogenated carbohydrates and intermolecular packing in unlabeled cells, which will be facilitated by the development of better radicals, for example, the AsymPolPOK that shortens DNP buildup time[69,70] and more efficient polarizing mechanisms for high-field DNP at 800 MHz/527 GHz or above[71-73].

## 2.5 Conclusions

High-resolution ssNMR of complex carbohydrates and cell wall biomaterials is exactly at a turning point where high-resolution, large-scale investigations just became possible. The combination of various isotope-labeling schemes, a complete set of $^{13}C/^{15}N$-based techniques, and sensitivity enhancement from DNP has completed the toolbox and enabled many studies of cell walls and biomaterials in plants, fungi, bacteria, and algae. Since polysaccharides are significantly under-investigated, there are many unresolved questions in this field. In addition, the development

of natural-abundance DNP methods has eliminated the difficulty and expenses associated with isotope-labeling, allowing us to investigate a large variety of biomaterials. Besides these highlights, there are many other advances in the field that could substantially facilitate carbohydrate ssNMR research such as database and software development[23], proton detection under ultrafast MAS[74,75], and the materialization of ultrahigh-field magnets. We hope this article could encourage more NMR colleagues to join the ongoing efforts in unveiling the function-structure relationship of polysaccharides and cell wall architecture, which will, on the molecular level, guide the rationale development of advanced technologies to produce better biorenewable energy, biomaterials, antibiotics and antifungal agents, as well as other high-value products based on carbohydrates or their complex with other biomolecules.

## 2.6 Acknowledgments

This work was supported by *National Science Foundation* through NSF MCB-1942665. T.W. is supported as part of the Center for Lignocellulose Structure and Formation, an Energy Frontier Research Center funded by the US Department of Energy, Office of Science, Basic Energy Sciences under award number DE-SC0001090.

## REFERENCES


1 Atalla, R. H. & Vanderhart, D. L. Native cellulose: a composite of two distinct crystalline forms. *Science* 223, 283-285, doi:DOI 10.1126/science.223.4633.283 (1984).

2 Jarvis, M. C. & Apperley, D. C. Direct Observation of Cell-Wall Structure in Living Plant-Tissues by Solid-State C-13 Nmr-Spectroscopy. *Plant Physiol.* 92, 61-65, doi:Doi 10.1104/Pp.92.1.61 (1990).

3 Fernandes, A. N. *et al.* Nanostructure of cellulose microfibrils in spruce wood. *Proc. Natl. Acad. Sci. USA* 108, E1195-E1203, doi:DOI 10.1073/pnas.1108942108 (2011).

4 Hou, G., Yan, S., Trebosc, J., Amoureux, J. P. & Polenova, T. Broadband homonuclear correlation spectroscopy driven by combined R2(n)(v) sequences under fast magic angle spinning for NMR structural analysis of organic and biological solids. *J. Magn. Reson.* 232, 18-30, doi:10.1016/j.jmr.2013.04.009 (2013).

5 De Paepe, G., Lewandowski, J. R., Loquet, A., Bockmann, A. & Griffin, R. G. Proton assisted recoupling and protein structure determination. *J. Chem. Phys.* 129, doi:Artn 245101 Doi 10.1063/1.3036928 (2008).

6 Lesage, A., Auger, C., Caldarelli, S. & Emsley, L. Determination of through-bond carbon-carbon connectivities in solid-state NMR using the INADEQUATE experiment. *J. Am. Chem. Soc.* 119, 7867-7868, doi:Doi 10.1021/Ja971089k (1997).

7 Aluas, M. *et al.* CHHC and $^{1}$H-$^{1}$H magnetization exchange: Analysis by experimental solid-state NMR and 11-spin density-matrix simulations. *J. Magn. Reson.* 199, 173-187, doi:10.1016/j.jmr.2009.04.013 (2009).

8 Ader, C. *et al.* Structural Rearrangements of Membrane Proteins Probed by Water-Edited Solid-State NMR Spectroscopy. *J. Am. Chem. Soc.* 131, 170-176, doi:10.1021/ja806306e (2009).

9 Gelenter, M. D., Wang, T., Liao, S. Y., O'Neill, H. & Hong, M. $^{2}$H-$^{13}$C correlation solid-state NMR for investigating dynamics and water accessibilities of proteins and carbohydrates. *J. Biol. NMR* 68, 257-270, doi:10.1007/s10858-017-0124-7 (2017).

10 Gullion, T. & Schaefer, J. Rotational-Echo Double-Resonance NMR. *J. Magn. Reson.* 81, 196-200, doi:Doi 10.1016/0022-2364(89)90280-1 (1989).

11 Bertini, I., Luchinat, C., Parigi, G. & Pierattelli, R. NMR spectroscopy of paramagnetic metalloproteins. *ChemBioChem* 6, 1536-1549, doi:10.1002/cbic.200500124 (2005).

12 Ni, Q. Z. *et al.* High Frequency Dynamic Nuclear Polarization. *Acc. Chem. Res.* 46, 1933-1941 (2013).

13 Rossini, A. J. *et al.* Dynamic Nuclear Polarization Surface Enhanced NMR Spectroscopy. *Acc. Chem. Res.* 46, 1942-1951, doi:10.1021/ar300322x (2013).

14 Mentink-Vigier, F., Akbey, U., Oschkinat, H., Vega, S. & Feintuch, A. Theoretical aspects of Magic Angle Spinning - Dynamic Nuclear Polarization. *J. Magn. Reson.* 258, 102-120, doi:10.1016/j.jmr.2015.07.001 (2015).

15 Schmidt-Rohr, K., Fritzsching, K. J., Liao, S. Y. & Hong, M. Spectral editing of two-dimensional magic-angle-spinning solid-state NMR spectra for protein resonance assignment and structure determination. *J. Biomol. NMR* 54, 343-353, doi:10.1007/s10858-012-9676-8 (2012).

16 Williams, J. K., Schmidt-Rohr, K. & Hong, M. Aromatic spectral editing techniques for magic-angle-spinning solid-state NMR spectroscopy of uniformly (13)C-labeled proteins. *Solid State Nucl. Magn. Reson.* 72, 118-126, doi:10.1016/j.ssnmr.2015.09.006 (2015).

17 Dick-Perez, M. *et al.* Structure and interactions of plant cell wall polysaccharides by two- and three-dimensional magic-angle-spinning solid-state NMR. *Biochemistry* 50, 989-1000, doi:Doi 10.1021/Bi101795q (2011).

18 Simmons, T. J. *et al.* Folding of xylan onto cellulose fibrils in plant cell walls revealed by solid-state NMR. *Nat. Commun.* 7, 13902, doi:10.1038/ncomms13902 (2016).

19 Terrett, O. M. *et al.* Molecular architecture of softwood revealed by solid-state NMR. *Nat. Commun.* 10, 4978, doi:10.1038/s41467-019-12979-9 (2019).

20 Dick-Perez, M., Wang, T., Salazar, A., Zabotina, O. A. & Hong, M. Multidimensional solid-state NMR studies of the structure and dynamics of pectic polysaccharides in uniformly $^{13}$C-labeled Arabidopsis primary cell walls. *Magn. Reson. Chem.* 50, 539-550, doi:Doi 10.1002/Mrc.3836 (2012).

21 Wang, T., Salazar, A., Zabotina, O. A. & Hong, M. Structure and dynamics of *Brachypodium* primary cell wall polysaccharides from two-dimensional $^{13}$C solid-state nuclear magnetic resonance spectroscopy. *Biochemistry* 53, 2840-2854, doi:Doi 10.1021/Bi500231b (2014).

22 Kang, X. *et al.* Molecular architecture of fungal cell walls revealed by solid-state NMR. *Nat. Commun.* 9, 2747, doi:Artn 2747 10.1038/S41467-018-05199-0 (2018).

23 Kang, X. *et al.* CCMRD: A Solid-State NMR Database for Complex Carbohydrates. *J. Biomol. NMR* accepted (2019).

24 Wang, T., Phyo, P. & Hong, M. Multidimensional solid-state NMR spectroscopy of plant cell walls. *Solid State Nucl. Magn. Reson.* 78, 56-63, doi:10.1016/j.ssnmr.2016.08.001 (2016).

25 Phyo, P., Wang, T., Yang, Y., O'Neill, H. & Hong, M. Direct Determination of Hydroxymethyl Conformations of Plant Cell Wall Cellulose Using $^{1}$H Polarization Transfer Solid-State NMR. *Biomacromolecules* 19, 1485-1497, doi:10.1021/acs.biomac.8b00039 (2018).

26 Wang, T., Yang, H., Kubicki, J. D. & Hong, M. Cellulose Structural Polymorphism in Plant Primary Cell Walls Investigated by High-Field 2D Solid-State NMR Spectroscopy and Density Functional Theory Calculations. *Biomacromolecules* 17, 2210-2222, doi:10.1021/acs.biomac.6b00441 (2016).

27 Wang, T., Zabotina, O. & Hong, M. Pectin-cellulose interactions in the *Arabidopsis* primary cell wall from two-dimensional magic-angle-spinning solid-state nuclear magnetic resonance. *Biochemistry* 51, 9846-9856, doi:Doi 10.1021/Bi3015532 (2012).

28 White, P. B., Wang, T., Park, Y. B., Cosgrove, D. J. & Hong, M. Water-polysaccharide interactions in the primary cell wall of *Arabidopsis thaliana* from polarization transfer solid-state NMR. *J. Am. Chem. Soc.* 136, 10399-10409, doi:Doi 10.1021/Ja504108h (2014).

29 Wang, T., Park, Y. B., Cosgrove, D. J. & Hong, M. Cellulose-Pectin Spatial Contacts Are Inherent to Never-Dried Arabidopsis thaliana Primary Cell Walls: Evidence from Solid-State NMR. *Plant Physiol.* 168, 871-884 (2015).

30 Phyo, P. *et al.* Gradients in Wall Mechanics and Polysaccharides along Growing Inflorescence Stems. *Plant Physiol.* 175, 1593-1607, doi:10.1104/pp.17.01270 (2017).

31 Phyo, P., Wang, T., Xiao, C. W., Anderson, C. T. & Hong, M. Effects of Pectin Molecular Weight Changes on the Structure, Dynamics, and Polysaccharide Interactions of Primary Cell Walls of Arabidopsis thaliana: Insights from Solid-State NMR. *Biomacromolecules* 18, 2937-2950, doi:10.1021/acs.biomac.7b00888 (2017).

32 Wang, T., Williams, J. K., Schmidt-Rohr, K. & Hong, M. Relaxation-compensated difference spin diffusion NMR for detecting 13C-13C long-range correlations in proteins and polysaccharides. *J. Biomol. NMR* 61, 97-107, doi:10.1007/s10858-014-9889-0 (2015).

33 Wang, T. *et al.* Sensitivity-enhanced solid-state NMR detection of expansin's target in plant cell walls. *Proc. Natl. Acad. Sci. USA* 110, 16444-16449, doi:DOI 10.1073/pnas.1316290110 (2013).

34 Wang, T., Chen, Y. N., Tabuchi, A., Cosgrove, D. J. & Hong, M. The Target of beta-Expansin EXPB1 in Maize Cell Walls from Binding and Solid-State NMR Studies. *Plant Physiol.* 172, 2107-2119, doi:10.1104/pp.16.01311 (2016).

35 Zhang, T., Zheng, Y. Z. & Cosgrove, D. J. Spatial organization of cellulose microfibrils and matrix polysaccharides in primary plant cell walls as imaged by multichannel atomic force microscopy. *Plant J.* 85, 179-192, doi:10.1111/tpj.13102 (2016).

36 Zhang, T., Vavylonis, D., Durachko, D. M. & Cosgrove, D. J. Nanoscale movements of cellulose microfibrils in primary cell walls. *Nat. Plants* 3, doi:Artn 17056 10.1038/Nplants.2017.56 (2017).

37 Lee, C. M., Chen, X., Weiss, P. A., Jensen, L. & Kim, S. H. Quantum Mechanical Calculations of Vibrational Sum-Frequency-Generation (SFG) Spectra of Cellulose:

Dependence of the CH and OH Peak Intensity on the Polarity of Cellulose Chains within the SFG Coherence Domain. *J. Phys. Chem. Lett.* 8, 55-60, doi:10.1021/acs.jpclett.6b02624 (2017).

38 Zheng, Y. Z., Wang, X., Chen, Y. N., Wagner, E. & Cosgrove, D. J. Xyloglucan in the primary cell wall: assessment by FESEM, selective enzyme digestions and nanogold affinity tags. *Plant J.* 93, 211-226, doi:10.1111/tpj.13778 (2018).

39 Dupree, R. *et al.* Probing the Molecular Architecture of Arabidopsis thaliana Secondary Cell Walls Using Two- and Three-Dimensional $^{13}C$ Solid State Nuclear Magnetic Resonance Spectroscopy. *Biochemistry* 54, 2335-2345, doi:10.1021/bi501552k (2015).

40 Grantham, N. J. *et al.* An even pattern of xylan substitution is critical for interaction with cellulose in plant cell walls. *Nat. Plants* 3, 859-865, doi:10.1038/s41477-017-0030-8 (2017).

41 Kang, X. *et al.* Lignin-polysaccharide interactions in plant secondary cell walls revealed by solid-state NMR. *Nat. Commun.* 10, 347, doi:10.1038/s41467-018-08252-0 (2019).

42 Gan, Z. H. *et al.* NMR spectroscopy up to 35.2 T using a series-connected hybrid magnet. *J. Magn. Reson.* 284, 125-136, doi:10.1016/j.jmr.2017.08.007 (2017).

43 Latgé, J. P. The cell wall: a carbohydrate armour for the fungal cell. *Mol. Microbiol.* 66, 279-290, doi:10.1111/j.1365-2958.2007.05872.x (2007).

44 Chatterjee, S., Prados-Rosales, R., Itin, B., Casadevall, A. & Stark, R. E. Solid-state NMR Reveals the Carbon-based Molecular Architecture of Cryptococcus neoformans Fungal Eumelanins in the Cell Wall. *J. Biol. Chem.* 290, 13779-13790, doi:10.1074/jbc.M114.618389 (2015).

45 Chatterjee, S. *et al.* Using Solid-State NMR To Monitor the Molecular Consequences of Cryptococcus neoformans Melanization with Different Catecholamine Precursors. *Biochemistry* 51, 6080-6088, doi:10.1021/bi300325m (2012).

46 Zhong, J. Y., Frases, S., Wang, H., Casadevall, A. & Stark, R. E. Following fungal melanin biosynthesis with solid-state NMR: Biopolyrner molecular structures and possible connections to cell-wall polysaccharides. *Biochemistry* 47, 4701-4710, doi:10.1021/bi702093r (2008).

47 Chatterjee, S. *et al.* The melanization road more traveled by: Precursor substrate effects on melanin synthesis in cell-free and fungal cell systems. *J. Biol. Chem.* 293, 20157-20168, doi:10.1074/jbc.RA118.005791 (2018).

48 Romaniuk, J. A. & Cegelski, L. Bacterial cell wall composition and the influence of antibiotics by cell-wall and whole-cell NMR. *Phil. Trans. R. Soc. B* 370, doi:10.1098/rstb.2015.0024 (2015).

49 Nygaard, R., Romaniuk, J. A. H., Rice, D. M. & Cegelski, L. Spectral snapshots of bacterial cell-wall composition and the influence of antibiotics by whole-cell NMR. *Biophys. J.* 108, 1380-1389, doi:10.1016/j.bpj.2015.01.037 (2015).

50 Takahashi, H. *et al.* Solid-state NMR on bacterial cells: selective cell wall signal enhancement and resolution improvement using dynamic nuclear polarization. *J. Am. Chem. Soc.* 135, 5105-5110, doi:10.1021/ja312501d (2013).

51 Thongsomboon, W. *et al.* Phosphoethanolamine cellulose: A naturally produced chemically modified cellulose. *Science* 359, 334-338, doi:10.1126/science.aao4096 (2018).

52 Arnold, A. A. *et al.* Identification of lipid and saccharide constituents of whole microalgal cells by $^{13}C$ solid-state NMR. *Biochim. Biophys. Acta* 1848, 369-377, doi:10.1016/j.bbamem.2014.07.017 (2015).

53 Arnold, A. A. *et al.* Whole cell solid-state NMR study of Chlamydomonas reinhardtii microalgae. *J. Biomol. NMR* 70, 123-131, doi:10.1007/s10858-018-0164-7 (2018).

54 Poulhazan, A., Arnold, A. A., Warschawski, D. E. & Marcotte, I. Unambiguous Ex Situ and in Cell 2D (13)C Solid-State NMR Characterization of Starch and Its Constituents. *Int. J. Mol. Sci.* 19, doi:10.3390/ijms19123817 (2018).

55 Viger-Gravel, J. *et al.* Topology of Pretreated Wood Fibers Using Dynamic Nuclear Polarization. *J. Phys. Chem. C.* 123, 30407-30415, doi:10.1021/acs.jpcc.9b09272 (2019).

56 Kirui, A. *et al.* Preparation of Fungal and Plant Materials for Structural Elucidation Using Dynamic Nuclear Polarization Solid-State NMR. *J. Vis. Exp.* 144, e59152 (2019).

57 Dubroca, T. *et al.* A quasi-optical and corrugated waveguide microwave transmission system for simultaneous dynamic nuclear polarization NMR on two separate 14.1 T spectrometers. *J. Magn. Reson.* 289, 35-44, doi:10.1016/j.jmr.2018.01.015 (2018).

58 Perras, F. A. *et al.* Atomic-Level Structure Characterization of Biomass Pre- and Post-Lignin Treatment by Dynamic Nuclear Polarization-Enhanced Solid-State NMR. *J. Phys. Chem. A* 121, 623-630, doi:10.1021/acs.jpca.6b11121 (2017).

59 Kirui, A. *et al.* Atomic Resolution of Cotton Cellulose Structure Enabled by Dynamic Nuclear Polarization Solid-State NMR. *Cellulose* 26, 329-339 (2019).

60 Zhang, L. *et al.* Arabinosyl Deacetylase Modulates the Arabinoxylan Acetylation Profile and Secondary Wall Formation. *Plant Cell*, doi:10.1105/tpc.18.00894 (2019).

61 Takahashi, H., Hediger, S. & De Paepe, G. Matrix-free dynamic nuclear polarization enables solid-state NMR $^{13}C$-$^{13}C$ correlation spectroscopy of proteins at natural isotopic abundance. *Chem. Commun.* 49, 9479-9481, doi:10.1039/c3cc45195j (2013).

62 Takahashi, H. *et al.* Rapid Natural-Abundance 2D 13C-13C Correlation Spectroscopy Using Dynamic Nuclear Polarization Enhanced Solid-State NMR and Matrix-Free Sample Preparation. *Angew. Chem. Int. Edit.* 51, 11766-11769, doi:10.1002/anie.201206102 (2012).

63 Marker, K. *et al.* Welcoming natural isotopic abundance in solid-state NMR: probing pi-stacking and supramolecular structure of organic nanoassemblies using DNP. *Chem. Sci.* 8, 974-987, doi:10.1039/c6sc02709a (2017).

64 Marker, K. *et al.* A New Tool for NMR Crystallography: Complete $^{13}C/^{15}N$ Assignment of Organic Molecules at Natural Isotopic Abundance Using DNP-Enhanced Solid-State NMR. .*J Am. Chem. Soc.* 137, 13796-13799, doi:10.1021/jacs.5b09964 (2015).

65 Smith, A. N., Marker, K., Hediger, S. & De Paepe, G. Natural Isotopic Abundance $^{13}C$ and $^{15}N$ Multidimensional Solid-State NMR Enabled by Dynamic Nuclear Polarization. *J. Phys. Chem. Lett.* 10, 4652-4662, doi:10.1021/acs.jpclett.8b03874 (2019).

66 Kristiansen, P. E., Carravetta, M., Lai, W. C. & Levitt, M. H. A robust pulse sequence for the determination of small homonuclear dipolar couplings in magic-angle spinning NMR. *Chem. Phys. Lett.* 390, 1-7, doi:10.1016/j.cplett.2004.03.075 (2004).

67 Teymoori, G., Pahari, B., Stevensson, B. & Eden, M. Low-power broadband homonuclear dipolar recoupling without decoupling: Double-quantum C-13 NMR correlations at very fast magic-angle spinning. *Chem. Phys. Lett.* 547, 103-109, doi:10.1016/j.cplett.2012.07.053 (2012).

68 Jaroniec, C. P., Filip, C. & Griffin, R. G. 3D TEDOR NMR experiments for the simultaneous measurement of multiple carbon-nitrogen distances in uniformly (13)C,(15)N-labeled solids. *J. Am. Chem. Soc.* 124, 10728-10742 (2002).

69 Mentink-Vigier, F. *et al.* Computationally Assisted Design of Polarizing Agents for Dynamic Nuclear Polarization Enhanced NMR: The AsymPol Family. *J. Am. Chem. Soc.* 140, 11013-11019, doi:10.1021/jacs.8b04911 (2018).

70 Mentink-Vigier, F. Optimizing nitroxide biradicals for cross-effect MAS-DNP: the role of g-tensors' distance. *Phys. Chem. Chem. Phys.* 22, 3643-3652, doi:10.1039/c9cp06201g (2020).

71 Mathies, G. *et al.* Efficient Dynamic Nuclear Polarization at 800 MHz/527 GHz with Trityl-Nitroxide Biradicals. *Angew. Chem. Int. Edit.* 54, 11770-11774, doi:10.1002/anie.201504292 (2015).

72 Jaudzems, K. *et al.* Dynamic Nuclear Polarization-Enhanced Biomolecular NMR Spectroscopy at High Magnetic Field with Fast Magic-Angle Spinning. *Angew. Chem. Int. Edit.* 57, 7458-7462, doi:10.1002/anie.201801016 (2018).

73 Mentink-Vigier, F. *et al.* Efficient cross-effect dynamic nuclear polarization without depolarization in high-resolution MAS NMR. *Chemical science* 8, 8150-8163 (2017).

74 Phyo, P. & Hong, M. Fast MAS $^{1}H$-$^{13}C$ correlation NMR for structural investigations of plant cell walls. *J. Biomol. NMR* 73, 661-674, doi:10.1007/s10858-019-00277-x (2019).

75 Bougault, C., Ayala, I., Vollmer, W., Simorre, J. P. & Schanda, P. Studying intact bacterial peptidoglycan by proton-detected NMR spectroscopy at 100 kHz MAS frequency. *J. Struct. Biol.* 206, 66-72, doi:10.1016/j.jsb.2018.07.009 (2019).

# CHAPTER 3: A MOLECULAR VISION OF FUNGAL CELL WALL ORGANIZATION BY FUNCTIONAL GENOMICS AND SOLID-STATE NMR

Reprinted with permission from A Chakraborty*, Liyanage D. Fernando*, W Fang* MC Dickwella Widanage*, P Wei, C Jin, T Fontaine, J-P Latge, and T Wang. *Nature Communication* (2021)**,** 12, 6346. 

*Denotes equal contribution

## 3.1 Abstract

Vast efforts have been devoted to the development of antifungal drugs targeting the cell wall, but the supramolecular architecture of this carbohydrate-rich composite remains insufficiently understood. Here we compared the cell wall structure of a fungal pathogen *Aspergillus fumigatus* and four mutants depleted of major structural polysaccharides. High-resolution solid-state NMR spectroscopy of intact cells reveals a rigid core formed by chitin, β-1,3-glucan, and α-1,3-glucan, with galactosaminogalactan and galactomannan present in the mobile phase. Gene deletion reshuffles the composition and spatial organization of polysaccharides, with significant changes in their dynamics and water accessibility. The distribution of α-1,3-glucan in chemically isolated and dynamically distinct domains supports its functional diversity. Identification of valines in the alkali-insoluble carbohydrate core suggests a putative function in stabilizing macromolecular complexes. The substantially revised model of cell wall architecture will improve our understanding of the structural response of fungal pathogens to stresses.

## 3.2 Introduction

Life-threatening fungal infections are found in more than two million people worldwide every year[1-3]. The insufficient efficacy of commercially available drugs, the substantial rise of azole-resistant strains, and the extensive application of immunosuppressive agents call for the

development of novel antifungal compounds[4-6]. Polysaccharides in fungal cell walls are absent in humans, making them uniquely suitable as the target of antifungal treatments. A family of drugs (echinocandins) inhibiting the synthesis of *β*-1,3-glucan, one of the major cell wall components, have been developed and are clinically used[6,7]. The loss of β-1,3-glucan, however, is partially compensated by the increased content of chitin and the paradoxical effect of this drug (reduced activity at high concentration), both of which have restricted the performance of echinocandins[8-10]. To date, among the many cell wall components, only the inhibition of β-1,3 glucan has been successfully involved in the development of antifungals. To enable the identification of new drug targets, it is of high significance to understand the structural dynamics of fungal polysaccharides and their compensatory responses to cell wall stress or injury.

The current study is focused on the cell wall of *Aspergillus fumigatus*, one of the most threatening human opportunistic pathogens and one of the best understood genetically and biochemically[5,11]. The major carbohydrate components of *A. fumigatus* cell walls include chitin, *β*-1,3-glucan (primarily linear or with β-1,6-branching and β-1,3/1,4-sequences), galactomannan, α-1,3-glucan, and galactosaminogalactan (Figure 3.1a)[2,12]. Until recently the organization of cell walls was only characterized using protocols that require chemical extraction of this polymer network by alkali and other chemicals[13,14]. The chemical method for analyzing the composition of the cell wall sequentially involves enzymatic or chemical degradation, purification of the produced soluble oligomers, and identification of covalent linkages between monosaccharide residues[13]. In addition, these chemical treatments can also separate the polysaccharides in amorphous alkali-soluble material and fibrillar alkali-insoluble material[12].

Recently, solid-state NMR spectroscopy has been employed to characterize the molecular architecture of cell walls and melanin deposition in multiple fungal species including *A. fumigatus*,

*Cryptococcus neoformans*, and *Schizophyllum commune*[15-20]. This non-destructive method allows for the direct use of untreated intact cells and gives atomic-level indications of polymer rigidity and physical packing as defined by the native properties in cell walls[21,22]. The solid-state NMR analysis of *A. fumigatus* cell wall has suggested that α-1,3-glucans are spatially packed with chitin and are likely distributed in a soft and hydrated matrix formed by diversely linked β-glucans[15], whereas the chemical data suggested that α-1,3-glucan and chitin were separated based on their differential alkali-solubility. Therefore, it is essential to reconcile the NMR-restrained structure and the model based on biochemical analysis[12,15].

For this purpose, we coupled NMR studies with a functional genomics approach using *A. fumigatus* cell wall mutants that have been characterized previously using chemical methods. The parental strain is $\Delta akuB^{KU80}$, which is a widely used model strain resulting from the deletion of the KU80 gene to enhance homologous recombination[23]. Based on this parental strain, four mutants, each of which selectively eliminates a major cell wall polysaccharide, were generated. The first mutant is the quadruple Δ*csmA/csmB/chsF/chsG* mutant with the deletion of four chitin synthase genes, resulting in cell walls almost devoid of chitin[24]. The second mutant used is exempt from α-1,3-glucan consecutively to the deletion of genes encoding three synthases (AGS1, AGS2, and AGS3)[25,26]. The third one is a GAG-deficient mutant ensued from the deletion of the *GT4C* gene encoding a glycosyltransferase, which is devoid of GAG[27]. The fourth mutant has the deletion of *KTR4* and *KTR7* genes encoding two mannosyltransferases, and this double mutant no longer contains any GM linked to the inner β-1,3-glucan-chitin core, without affecting the N-glycan moiety of proteins[28].

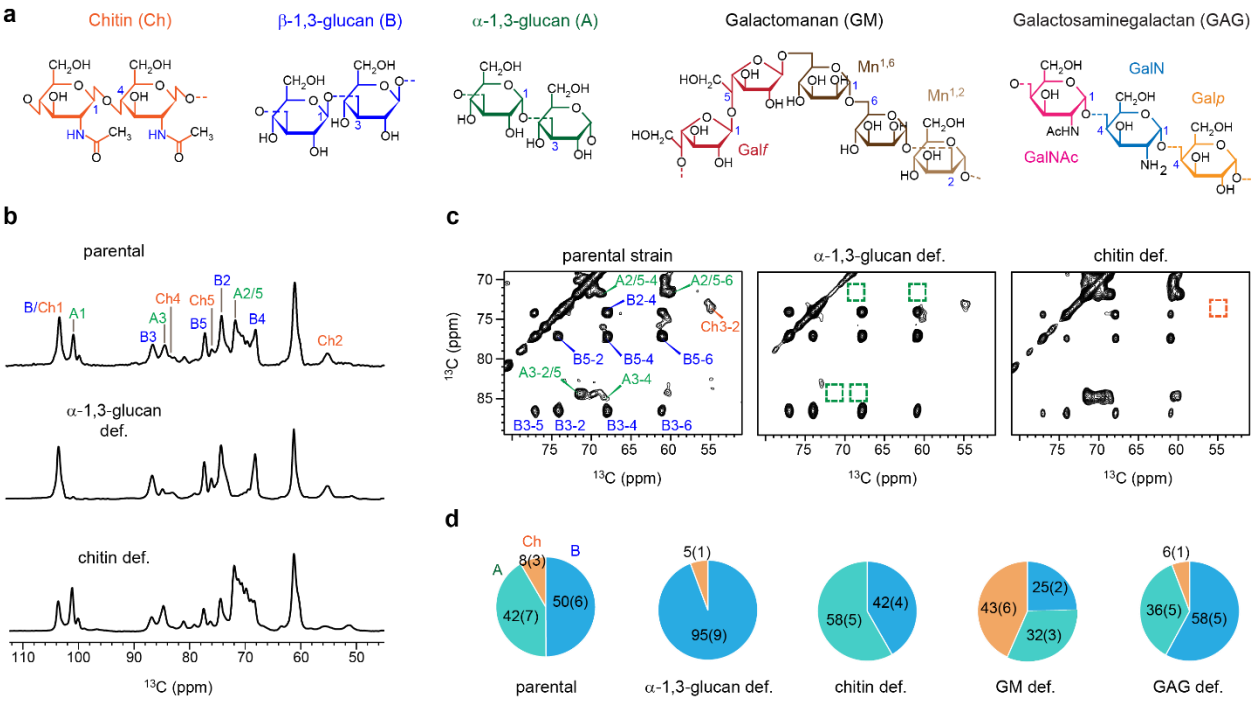


**Figure 3.1 Structural changes in the rigid core of *A. fumigatus* mutant cell walls. a,** Representative structures of fungal carbohydrates. Abbreviations are shown for different polysaccharides and sugar units. **b,** 1D $^{13}$C-CP spectrum showing different intensities for rigid polysaccharides. Abbreviations are used for resonance assignments. For example, A1 denotes α-1,3-glucan carbon 1. Ch and B represent chitin and β-1,3-glucan, respectively. **c,** 2D $^{13}$C-$^{13}$C correlation spectrum with 53 ms CORD mixing detecting intramolecular cross-peaks. For example, B3-5 is the cross peak between β-1,3-glucan carbon 3 and carbon 5. The missing peaks of α-1,3-glucan and chitin in two mutants are highlighted using dash line boxes. **d,** Estimation of polysaccharide composition in the rigid portion of cell walls. Chitin, α-1,3-glucan, and β-glucans are shown in orange, green, and blue, respectively. The percentage values represent the molar fraction of rigid polysaccharides as estimated using the integrals of cross peaks in 2D CORD spectra, which is detailed in Supplementary Table 3. Standard errors included in the parentheses are based on data presented in Figure 3.8 and computed as described in the Appendix Methods. Source data of Figure 3.1d are provided as a Source Data file.

In this work, we employ a series of 2D $^{13}$C/$^{15}$N/$^{1}$H-$^{13}$C correlation solid-state NMR methods to analyze the uniformly $^{13}$C,$^{15}$N-labeled hyphal cell walls of the parental *A. fumigatus* strain and the four mutants described above (Table 3.1). Polysaccharide composition of the rigid and mobile cell wall domains is interrogated in parental and mutant strains. We confirm the functional diversity of α-glucans through its distribution heterogeneity, in the alkali-soluble and

alkali-insoluble fractions of the inner and outer cell walls. Our data also show that *A. fumigatus* substantially reshuffles polysaccharide composition to increase the rigidity and hydrophobicity of cell walls, in response to biosynthesis deficiencies. This study shows the power of a joint genomic, chemical, and biophysical approach to characterize the supramolecular assembly of biopolymers in cell walls and provides a readily applicable method for evaluating the structural responses of fungal cell walls to genetic mutations and external stresses.

## 3.3 Results

### 3.3.1 Polysaccharide Structure and a Vision of Their Role in Cell Wall Organization

For atomic-level characterization using solid-state NMR, we produced uniformly $^{13}C$, $^{15}N$-labeled samples by growing the five strains for 1.5 days in a fully defined medium containing $^{13}C$-glucose and $^{15}N$-$NaNO_3$. Intact cells were directly packed into a solid-state NMR rotor, without any chemical perturbation; therefore, the physical and structural status of the cell wall was kept native. Tailoring the solid-state NMR methods allowed us to selectively detect the rigid and mobile molecules as defined by their native dynamics in cell wall materials, with no relevance to covalent linkage patterns or their susceptibility to chemical extraction (for example, alkali treatment). It is quite common that a single type of polysaccharides could possibly have mobile domains that are present in the soft matrix and rigid phases that are physically packed with stiff molecules such as the cellulose microfibrils in plants and the chitin molecules in fungi[15,29].

The mobile phase represents those molecules with rapid $^{13}C$-$T_1$ relaxation, which can survive through the short recycle delay used in $^{13}C$ direct polarization (DP). The rigid components described here refer to those polysaccharides that efficiently retain their dipolar couplings and thus can be detected using the dipolar-based $^{1}H$-$^{13}C$ cross polarization method. These methods have been applied in solid-state NMR studies of carbohydrate-rich materials such as the cell walls of

plants and algae as well as the biofilms and cell walls of fungi[18,30-34]. In *A. fumigatus*, combining these two methods enables efficient detection of both mobile and rigid molecules at ambient temperature (Figure 3.7). This physical vision differs from the classification accepted after chemical extraction and solubilization of the cell wall, where the alkali-soluble and water-insoluble molecules are recognized as amorphous polysaccharides as observed by electron microscopy (EM) whereas the alkali-insoluble fraction contains fibrillar molecules also seen by EM[35]. The compositional and dynamical characteristics of all strains were extremely reproducible between different batches (Figure 3.8).

Only three polysaccharides were found to constitute the rigid core of *A. fumigatus* cell walls, including chitin, α-1,3-glucan, and β-1,3-glucan (Figure 3.1b). The absence of signature peaks confirmed the exclusion of α-1,3-glucan and chitin in the cell walls of their corresponding mutants. The key peaks of α-1,3-glucans, for example, carbon 1 at 101 ppm (A1) and carbon 2/5 at 72 ppm (A2/5), were substantially suppressed in the α-1,3-glucan deficient mutant. Similarly, the resolved peak of chitin carbon 2 (Ch2) at 55.5 ppm, with partial overlap with lipid and protein carbons, was weaker in the chitin-deficient mutant.

Two-dimensional (2D) $^{13}C$-$^{13}C$ correlation spectra substantially improved the spectral resolution, allowing us to resolve a large number of carbon sites in the rigid macromolecules (Figure 3.9). The $^{13}C$ full width at half maximum (FWHM) linewidths are mostly in the range of 0.45-0.75 ppm for the rigid molecules (Figure 3.10). The chemical shifts are summarized in Table 3.2. Alteration in the polysaccharide amount can be closely examined by tracking the intensities of corresponding cross peaks (Figure 3.1c), for instance, α-1,3-glucan carbon 3 to carbon 4 (A3-4) cross peak at (84.5, 69.5) ppm and chitin carbon 3 to carbon 2 (Ch3-2) at (72.9, 55.5 ppm). Analysis of cross peak integrals led to an estimate of the molar fractions of rigid polysaccharides

(Figure 3.1d). In parental cell walls, the percentages of β-1,3-glucan, α-1,3-glucan, and chitin were estimated to be 50%, 42%, and 8%, respectively (Table 3.3). Defects in α-1,3-glucan biosynthesis were compensated by an upsurge of the β-1,3-glucan amount to 95% whereas the removal of chitin was accompanied by a higher content of α-1,3-glucan (58%).

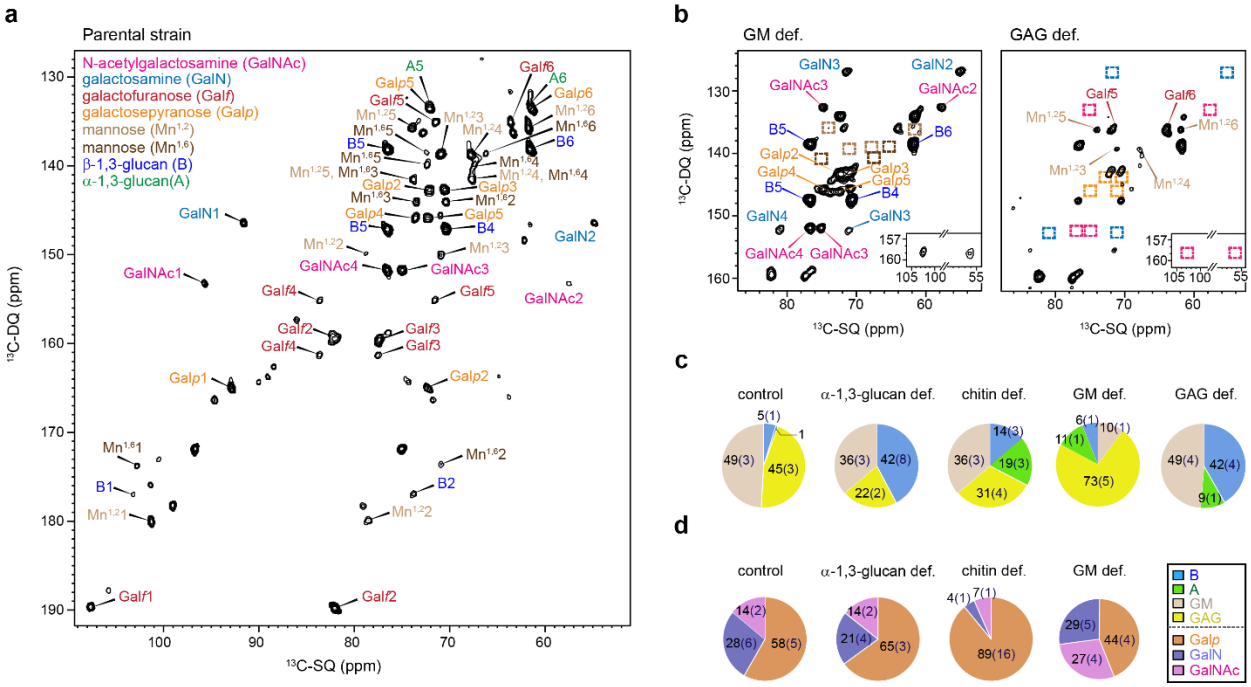


**Figure 3.2 The mobile domain of *A. fumigatus* cell wall is rich in GM and GAG. a**, $^{13}C$ DP J-INADEQUATE spectrum resolving the carbon connectivity for each polysaccharide. Abbreviations are used for resonance assignments and different polysaccharides are color-coded. **b,** Comparison of mobile polysaccharides in GM- and GAG-deficient mutants. Missing peaks of GM and GAG are highlighted using dash line boxes (typically, brown for mannose, orange for galactopyranose, cyan for galactosamine, and magenta for N-acetylgalactosamine). Insets show the signals of GalN'/GalNAc' residue in the GM-deficient mutant. **c**, Molar fractions of mobile polysaccharides in each cell wall sample estimated from peak volume. **d,** Monosaccharide compositional changes of GAG observed in the four samples. Standard errors are included in parentheses. The numbers in the pie charts shown by panels **c** and **d** are molar percentages as detailed in Table 3.4. Source data of Figures 3.2c and 3.2d are provided as a Source Data file.

Although both GAG and GM only exist in the mobile phase (discussed later), the rigid cell wall polysaccharides were still modified in their corresponding mutants (Figure 3.9). There was no change in the rigid portion of the GAG-deficient cell walls in comparison to the parental strain,

however, the mannan deficiency resulted in an increase in the chitin amount (43%), indicative of a concerted change of both rigid and mobile polymers. This increase in the rigid chitin polymer might be associated with the growth defect seen in the *Δktr4/Δktr7* double mutant[28]. Two other molecules, α- and β-glucans, exhibited lower amounts in the GM-deficient mutant; therefore, the observed increase of chitin content is not a direct consequence of the reduced amount of GM.

The signals of mobile molecules absent in the above CP-based experiments were preferentially detected using 2D $^{13}$C DP J-INADEQUATE spectra, which showed numerous carbon peaks from GM, GAG, α-1,3-glucan, and β-1,3-glucan (Figure 3.2a). The observed mobile phase has rapid $^{13}$C-$T_1$ relaxation to survive through the short recycle delay (for example, 2 s) used in $^{13}$C-DP excitation. As this study is using uniformly $^{13}$C-labeled samples and slow magic-angle spinning (MAS) frequencies, $^{13}$C-$^{13}$C spin-exchange induces multiexponential relaxation feature, with fast and slow relaxation components for each carbon site[36]. In cell wall NMR, this physical principle has been used to distinguish different domains of mobile molecules present in the soft matrix or in contact and efficient spin exchange with rigid scaffolds, with the former being better detected in the DP J-INADEQUATE experiment[29,31]. The linewidth is typically 0.30-0.75 ppm for dynamic molecules (Figure 3.10). The variation of linewidths is partially attributable to the highly heterogeneous dynamics of molecules in cellular samples, with the most mobile components showing narrow lines and the partially mobile molecules showing slightly broader peaks where the conformational distribution of a large number of monosaccharide units could not be competently averaged out by motion. Covalent and physical interactions between molecules may also contribute to the observed distribution of NMR linewidth.

Galactomannan can be tracked using the signals of α-1,2-mannose ($Mn^{1,2}$) and α-1,6-mannose ($Mn^{1,6}$), which showed reduced intensity in the GM-deficient mutant (Figure 3.2b and

Figure 3.11). Galactosaminogalactan is an exopolysaccharide featured by a complex structure comprised of α-linked galactopyranose (Gal*p*), galactosamine (GalN), and N-acetylgalactosamine (GalNAc) units with no particular order (Figure 3.1a)[37-39]. Covalently bonded to a nitrogen, the carbon 2 of GalN and GalNAc exhibited characteristic chemical shifts below 60 ppm, like the carbon 2 signals in chitin. Weak signals have been observed for the GalNAc and GalN carbon 2 at 54-56 ppm. Most of their carbon 1 signals were observed in the range of 92-97 ppm, likely due to the α-linkages and a solvated environment, but weaker signals were also observed at 102 ppm (Figure 3.2b, inset). The key signals of GalNAc, GalN, and Gal*p* residues were eliminated in the GAG-deficient mutant.

Differences exist between the two types of galactose units in the mobile polysaccharides. Structurally, both Gal*f* and Gal*p* have 6 carbons, however, the former has a 5-membered ring and a unique large C1 chemical shift at 108 ppm (Figure 3.1a). Functionally, Gal*f* is present in the GM of the inner cell wall and in the glycolipids and N- and O- glycans of glycoproteins whereas Gal*p* is present in GAG[39-43].

GM and GAG turned out to be the most populated molecules in the mobile phase of fungal cell walls, each accounting for 46-49 mol% (Figure 3.2c). In GM, Gal*f* was the major component, with a moderately different repartition of 1,2- and 1,6-linked mannose residues in all these mutants (Table 3.4). The NMR signals used for screening the polysaccharide composition were provided in Supplementary Table 5. In GM-deficient cell walls, the amount of GM was reduced to 9% but it evaded complete removal (Figure 3.2c). The low amount of mannan in this *Δktr* mutant could originate from membrane-bound mannan[44] or from the *N*- or/and *O*-glycan moieties of the glycoproteins, which, in contrast to the cell wall GM, are untouched in the *Δktr* mutants[28]. Moreover, the mannan composition was different: the ratio of $Mn^{1,2}$: $Mn^{1,6}$ of 5:1 and 1:1 in the

parental strain and Δ*ktr4/7* mutant, respectively (Table 3.4), which is in agreement with biochemical data[44,45]. GAG was completely depleted in the Δ*gt4C* mutant, followed by a significant increase in β-1,3-glucan in the mobile region. Mutations regarding the biosynthesis of α-1,3-glucan and chitin, two molecules that are largely rigid, also substantially perturbed the mobile polymers. Therefore, the compositional changes of mobile and rigid molecules happened in a concerted manner. Although NMR showed that Gal*p* was consistently the dominant component (~60-90 mol%) of GAG in most samples, we have observed an almost even distribution of Gal*p*, GalN and GalNAc in the GM-deficient mutant (Figure 3.2d). Biochemical data of degraded and isolated oligomers have shown that Gal*p* is a minor component (around 10%) and GalNAc is the major unit[46]. This controversy suggests that Gal*p* plays a key role in the flexibility behavior of GAG observed by ssNMR as has been described for the solubility of GAG in urea in biochemical analyses[39].Compared to the parental strain, the chitin-deficient mutant also altered the ratio of the three major monosaccharide residues in GAG (Figure 3.2d). When lacking one major polysaccharide, the cell wall does not scale up the remaining polysaccharides proportionally.

Compensatory reactions in response to the lack of a cell wall component due to gene deletion were previously observed with data obtained by chemical and enzymatic analysis[12]. The absence of each of the two rigid polymers, α-1,3-glucan and chitin, led to an increase in the amount of AI-insoluble fraction containing the fibrillar polysaccharides[24,35]. The lack of chitin was compensated by an increase in GAG and the absence of α-1,3-glucan was replaced by β-1,3-glucan. In contrast, the deletion of genes coding for GAG and GM did not modify the ratio of fibrillar and amorphous polysaccharides as distinguished using alkali-treatment[27,28]. Although data obtained by ssNMR or by chemical approaches in the analysis of the cell wall mutants were from different experimental strategies, both methodologies agreed in the fact that the composition of

polysaccharides is fully reshuffled to better compensate for structural defects introduced by biosynthesis deficiencies and that no structural rules can be established yet based on these modifications.

### 3.3.2 Molecular Partitioning After Alkali Treatment

For decades, the molecular organization of fungal cell walls and especially of *A. fumigatus* cell walls has been analyzed chemically after solubilization of this water-insoluble matrix by alkali and glycosyl hydrolases[13,47]. We have treated the $^{13}C/^{15}N$-labeled parental *A. fumigatus* mycelium with 1 M sodium hydroxide at 65°C, which discriminates polymers by their alkali-solubility and removes the (glyco-)proteins and (glyco-)lipids bound to the cell wall[13,24]. Previous chemical analysis showed that α-1,3-glucans were only found in the alkali-soluble (AS) fraction, with minor β-1,3-glucan contamination[26]. However, the 1D $^{13}C$ CP spectra that selectively detect rigid molecules showed a mixture of chitin, β-1,3-glucan, and α-1,3-glucan in the alkali-insoluble (AI) part (Figure 3.3a). The two-phase distribution of α-1,3-glucans was confirmed by their overlapped signals in the 2D $^{13}C$-$^{13}C$ correlation spectra collected on both AI and AS fractions (Figure 3.3b). Furthermore, α-1,3 glucan was still present in the AI fraction even after a second treatment by NaOH (Figure 3.12). Intensity analysis showed that α-1,3-glucan accounted for 16 mol% of all rigid polysaccharides in the AI portion of the sample analyzed here, with 57% of β-1,3-glucan and 27% of chitin (Table 3.6). This finding shifts from the prevailing paradigm based on chemical analysis and support the recently reported concept obtained by NMR in which α-1,3-glucan is a structural polysaccharide that tightly packs with chitin to form a hydrophobic and stiff skeleton providing mechanical strengths to the cell walls[15].

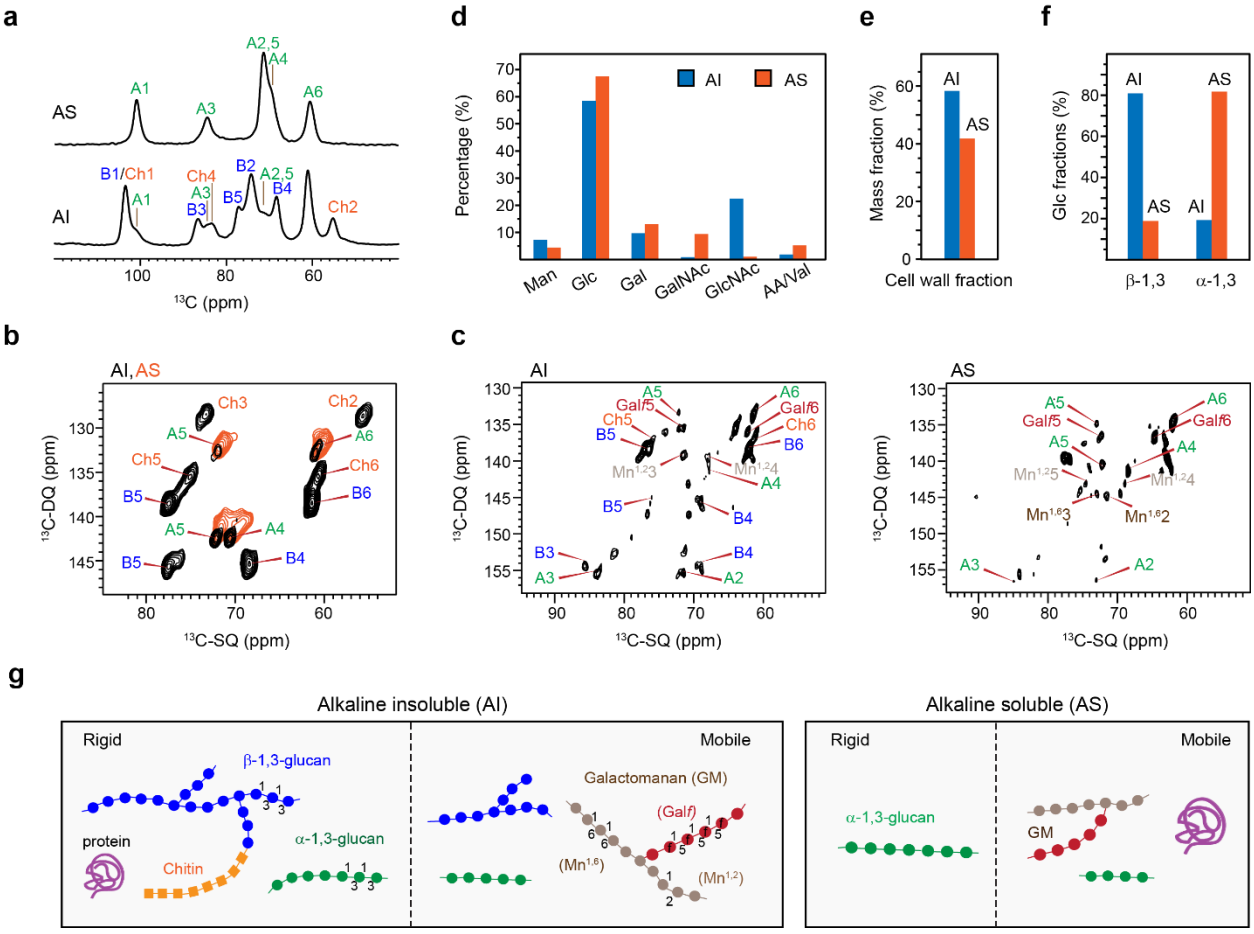


**Figure 3.3 α-1,3-glucan is present in both alkali-soluble and insoluble fractions of the parental sample. a,** 1D $^{13}C$ CP spectra detecting the rigid molecules in the alkali-soluble (AS) and alkali-insoluble (AI) fractions of the parental sample. **b,** Overlay of 2D $^{13}C$ CP dipolar-INADEQUATE spectra showing the rigid molecules in the alkaline-soluble (AS, orange) and alkaline-insoluble (AI, black) portions of *A. fumigatus* cell walls. Signals of α-1,3-glucans, such as A4, A5, and A6, are present in both portions. **c,** $^{13}C$ DP J-INADEQUATE spectrum showing the mobile polysaccharides in the alkali insoluble (top) and soluble (bottom) parts. **d,** Compositional analysis of both AI (blue) and AS (orange) fractions obtained by GC-HPLC and enzymatic degradation. The x-axis reports different monosaccharide units as well as the amino acids (AA) or valine (Val). **e,** Relative mass percentages of the AI and AS fractions. **f,** Relative fractions of β-1,3-glucan and α-1,3-glucan. **g,** Summary of polysaccharides and proteins identified in both rigid and mobile portions within the alkali insoluble and soluble fractions. Source data of Figure 3.3d-f are provided as a Source Data file.

When the mobile carbohydrates were specifically analyzed, AI showed peaks from β-1,3-glucan, mannan, chitin, and α-1,3-glucan, while AS exhibited unique signals of α-1,3-glucan and

mannan (Figure 3.3c). Although the high structural polymorphism of chitin has been recently demonstrated by the statistical analysis of their chemical shifts[16], the presence of chitin in the mobile phase of the AI fraction was still unexpected. These chitin molecules should represent a poorly populated and structurally disordered domain that is associated with matrix polymers, for example, β-1,3-glucans[24]. Both AI and AS samples showed signals from the mannose and Gal*f* residues of GM. Protein signals were mainly observed in the mobile phase of AS molecules (Figure 3.13), together with a small portion in the rigid phase of AI components as shown later.

After NMR measurements, the same batch of AI and AS samples were subjected to chemical analysis. There was a general agreement between the data computed with the two different methodological approaches: β-1,3-glucans and chitin were the major components of AI and α-1,3-glucan was the dominant component of the AS fraction (Figure 3.3d and Tables 3.6 and 3.7). Mannan was distributed in both fractions. The amount of amino acid was low in the AI fraction (2%), where valine is the major amino acid, and increased to 5% in the AS sample. The AI fraction accounted for three-fifth of the total mass of the cell wall and was better populated than the AS part (Figure 3.3e). The ratio between β-1,3-glucan and α-1,3-glucan was around 4:1 in the AI fraction but swapped to 1:4 in the AS sample (Figure 3.3f), which confirmed the presence of α-1,3-glucan in both AI and AS fractions. Indeed, an earlier study of a mutant lacking the only β-1,3-glucan synthase Fks1 still reported Glc residues in the AI fraction, which may originate from α-1,3-glucans[48].

The only discrepancy happened to GAG, which was detected as a minor molecule (9%) of the AS fraction in chemical analysis (Figure 3.3d), but we did not identify its signature peaks (Figure 3.14) in the temperature range of 280-298 K. This might be resulted from the very limited amount of AS sample due to the low yield in chemical extraction, the potentially unfavorable

dynamical scheme, and the low content of GAG in the AS portion. Sensitivity-enhancement techniques, such as Dynamic Nuclear Polarization (DNP), might provide a solution to the detection of this polysaccharide and other lowly populated molecules[49-51].

These findings allow us to summarize the partitioning of polysaccharides in four fractions corresponding to the rigid and mobile domains of AI and AS portions (Figure 3.3g). β-1,3-glucans span across the rigid and mobile phases of AI fractions while chitin mainly exists in the rigid phase of AI materials. GM remains highly dynamic. The rigid domain of AS portion is dominated by α-1,3-glucan but this molecule also exists in all the other three phases: the distribution heterogeneity is an indicator of its functional complexity.

### 3.3.3 Valine, an Amino Acid Associated with The Rigid Cell Wall Matrix

The $^{13}C$ DP J-INADEQUATE spectra also showed signals from mobile proteins and only the amino acids showing strong intensities were assigned (Figure 3.4a). Some signals of the mobile proteins were retained after alkali extraction, primarily present in the alkali-soluble portion (Figure 3.13), suggesting that they are polysaccharide-associated proteins instead of the intracellular proteins in transit to be secreted, which are normally removed by the treatment. Protein backbone chemical shifts are sensitive to φ and ψ torsion angles, which is useful for probing the secondary structure[52]. Analysis of the Cα and CO chemical shifts revealed α-helicity of most residues except for tyrosine (Figure 3.4b). Protein signals were decreased in the GM-deficient mutant (Figure 3.4c and Figure 3.15). In spite of the variable intensity, the observation of protein signals in the parental and mutant samples suggests that these proteins might be a constitutive component of the cell wall.

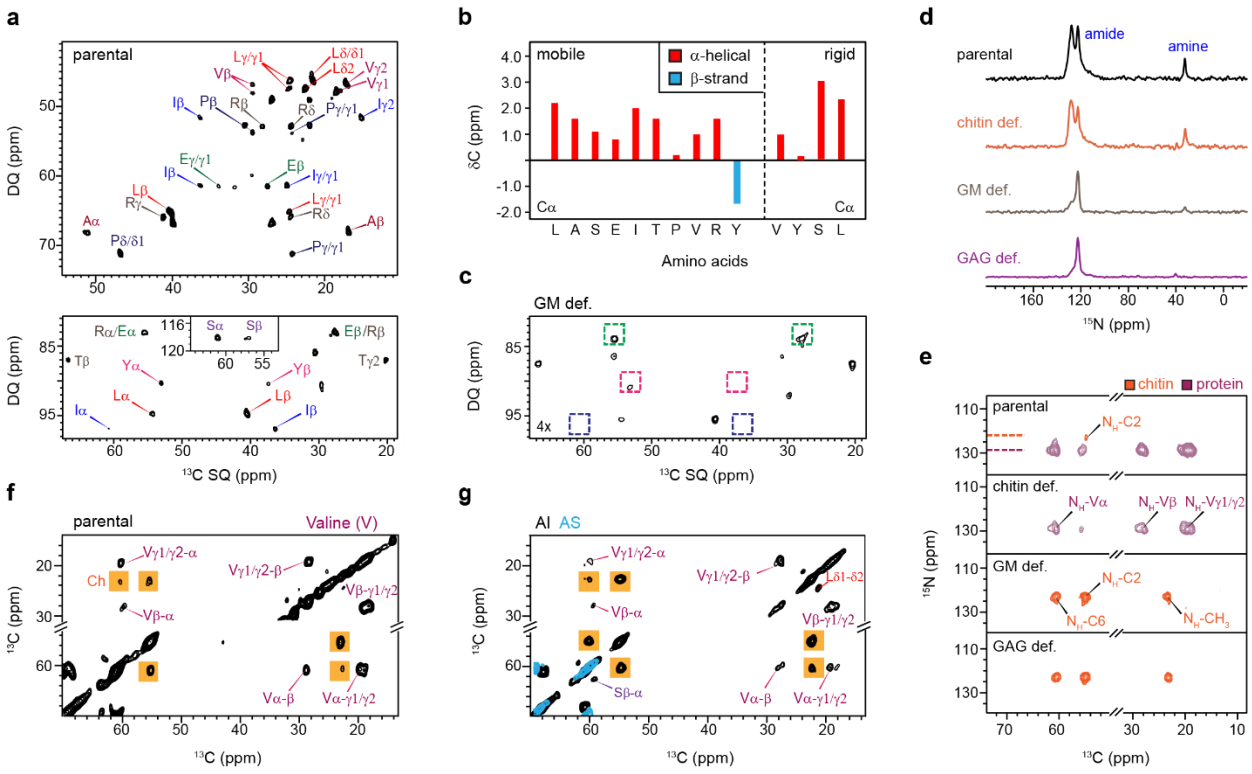


**Figure 3.4 Structural assembly of glycoproteins in fungal cell walls. a,** 2D $^{13}C$ DP J-INADEQUATE spectrum detecting the amino acids of mobile proteins. The assignments represent the amino acid types and carbon sites. For example, $A_\beta$ represents the carbon-β of alanine. The inset shows the signals of Serine. **b,** Backbone $^{13}C$ chemical shifts suggest the dominance of α-helix secondary structure in both mobile and rigid phases of proteins. **c,** Removal of galactomannan results in protein depletion indicated by the decline in amino acid signals as highlighted using dash line boxes. **d**, 1D $^{15}N$ CP spectra showing multiple amide and amine signals from cell wall polysaccharides and proteins. The $^{15}N$ signals vary in the parental sample and mutants. **e,** 2D $^{15}N$-$^{13}C$ correlation spectra showing chitin (orange) and protein (purple) signals. Chitin signals are missing in the chitin-deficient mutant. Rigid proteins are absent in the GM-deficient and GAG-deficient samples. **f,** Valine is the major rigid amino acid in the whole cell of the parental sample as shown by the 2D $^{13}C$-$^{13}C$ CORD spectrum. Chitin signals are shown in yellow boxes. **g**, Valine is preserved in the rigid portion of the alkali-insoluble (AI) part but becomes absent in the alkali-soluble (AS) fraction. Source data of Figure 3.4d are provided as a Source Data file.

We collected 1D $^{15}N$ CP spectra to examine the structure of proteins and nitrogenated polysaccharides, primarily chitin (Figure 3.4d). GAG was not detected in the CP-based $^{15}N$ experiment due to the high mobility of this molecule and the selective detection of rigid components by this technique. Two amide peaks at 124 ppm and 129 ppm, together with an amine

peak at 38 ppm, have been resolved. The peak intensity is sample-dependent, revealing major changes in the identities and amount of nitrogenated molecules. Compared to the parental sample, the chitin-deficient mutant showed a decline in the height of the amine signal and the 124-ppm amide peak, which can be attributed to the reduced amount of chitin. In GM- and GAG-deficient samples, the 129 ppm peaks were missing, likely caused by the mobilization or removal of proteins. 2D $^{15}$N-$^{13}$C correlation spectra revealed that the 124-ppm signal mainly originated from chitin and 129-ppm peak was from protein backbones (Figure 3.4e). The lack of rigid proteins in GAG- and GM-deficient mutants suggested direct associations between structural proteins and these two polysaccharides.

Strikingly, the protein region of 2D $^{15}$N-$^{13}$C spectra mainly has valine (V) signals (Figure 3.4e), with only minor contributions from other hydrophobic amino acids such as leucine and serine. This unexpected finding was verified by the strong valine cross peaks observed in the aliphatic region of the 2D $^{13}$C-$^{13}$C correlation spectrum (Figure 3.4f). The same signals were fully retained in the alkali-insoluble carbohydrate core of the cell wall, which mainly contains the covalently linked mannan-β-1,3-glucan-chitin complex, but disappeared in the alkali-soluble fraction (Figure 3.4g). Further confirmation is provided by the chemical analysis after acid hydrolysis, where the 2% of amino acid content in AI is predominantly valine (Figure 3.3d). The presence of rigid valine may suggest a structural function in polysaccharide complex that has never been investigated.

### 3.3.4 Polymer Dynamics and Hydration in The Mutants

The dynamical and hydration characteristics of biopolymers reflect the extent of molecular aggregation and water permeability, which helps to rationalize the structural organization of cell walls. Enhanced rigidity and hydrophobicity are typical indicators of large or ordered aggregates,

for example, the chitin and cellulose microfibrils in fungi and plants, respectively[21]. In contrast, molecules spatially separated from these mechanical cores are typically mobile and hydrated. The motional dynamics of polysaccharides on the nanosecond timescale were probed using $^{13}C$ spin-lattice ($T_1$) relaxation, which was measured as an array of 2D $^{13}C$-$^{13}C$ correlation spectra with a variable z-filter (Figure 3.16 and Table 3.8). The use of CP selected the rigid components that are structurally meaningful. Due to the perturbation of the spin-exchange effect[36], the experiments and the use of uniformly labeled materials do not allow the accurate determination of the $^{13}C$-$T_1$ relaxation. Therefore, we only use it as a qualitative indicator of polymer dynamics. After 1 s of relaxation, the signals of β-1,3-glucans decayed rapidly, but the α-1,3-glucan cross peaks still retained high intensities (Figure 3.5a). Therefore, polymer dynamics are heterogeneous. The data were fit using single exponential equations to obtain $^{13}C$-$T_1$ relaxation time constants for different carbon sites (Figure 3.5b). In the parental sample, the average $^{13}C$-$T_1$ relaxation times for β-1,3-glucan, α-1,3-glucan, and chitin were 1.2 s, 3.3 s, and 2.1 s, respectively. Therefore, the rapid local reorientation is most pronounced in β-1,3-glucan, and becomes subsequently less in chitin and even less in α-1,3-glucan. When α-1,3-glucan was removed, chitin became further rigidified as evidenced by its 3.5 s average $^{13}C$-$T_1$ but β-1,3-glucan became even more mobile. This is an indicator of polymer separation in the α-1,3-glucan-deficient cell walls, as the spin-exchange, an effect averaging the $^{13}C$-$T_1$ of closely packed molecules, failed to equilibrate between the two polysaccharides. However, in chitin-deficient cell walls, both α-1,3- and β-1,3-glucans became less dynamic, with their time constants increased to 4.1 s and 2.1 s, respectively.

We further conducted a water-to-polysaccharide $^{1}H$ polarization transfer experiment to examine the changes brought about by genetic mutation to the water accessibility of

polysaccharides[53,54]. This experiment depends on a $^{1}H$-$T_2$ relaxation filter to eliminate all polysaccharide magnetization and then transfers the water $^{1}H$ polarization to carbohydrates so that

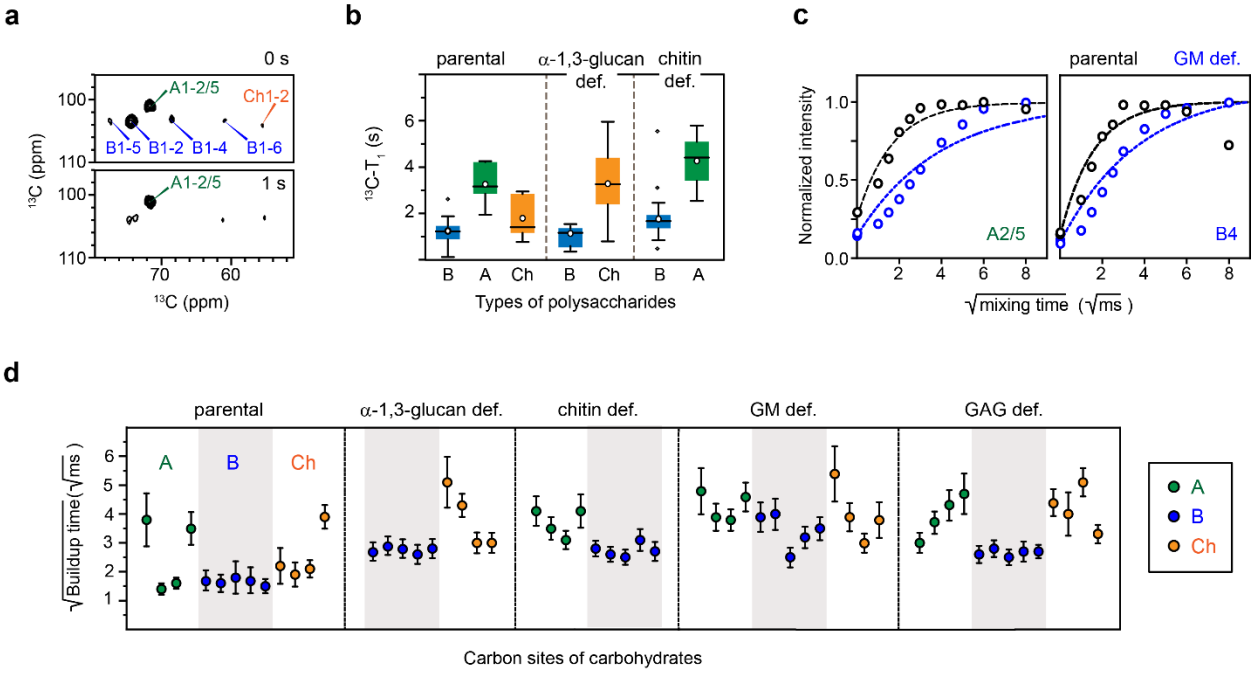


**Figure 3.5 Modulated dynamics and water contact of polysaccharides in *A. fumigatus* mutants.** The NMR data of β-1,3-glucan (B), α-1,3-glucan (A), and chitin (Ch) are plotted in blue, green, and orange, respectively. **a,** Representative 2D $^{13}$C-$^{13}$C spectra with 0 s (top) and 1 s (bottom) z-filter time for measuring $^{13}$C-$T_1$ relaxation. Signals of α-1,3-glucans are effectively retained after 1 s, indicating the slow $^{13}$C-$T_1$ relaxation of this polysaccharide. **b,** Box and whisker diagram plotting the $^{13}$C $T_1$ relaxation time constants of β-1,3-glucan (B; n=19), α-1,3-glucan (A; n=6), and chitin (Ch; n=13) for parental and mutant samples. The box starts from lower quartile to upper quartile, with the horizontal bar and the open circle presenting the median and mean, respectively. The length of the whiskers is determined by the product of 1.5 and interquartile range, with outliers shown as separate dots. **c,** Representative buildup curves for the water-edited spectrum of parental (black) and GM-deficient (blue) samples. **d,** Data representing the buildup time constants that reflect the degree of water retention at various carbon sites of different polysaccharides. Time constants for β-1,3-glucan (n = 5), α-1,3-glucan (n = 4) and chitin (n = 4) are generated from the fit to exponential function. Each point reflects the best-fit value for buildup time constant ± s.e. Shaded area represents the data of β-1,3-glucan. The data plotted in panels b and d are summarized in Tables 3.8 and 3.9, respectively.

only carbohydrates with bound water can be detected. The time taken for the signal to reach equilibrium can be used as an indicator of water retention around each carbon site (Figure 3.11

and Table 3.15). The polysaccharides with a slower intensity buildup have a reduction in water accessibility (Figure 3.5c).

In the parental strain, chitin and α-1,3-glucan require long buildup times due to the formation of a rigid and hydrophobic complex by these two polysaccharides (Figure 3.5d). In contrast, the mobile β-1,3-glucan has short buildup time constants, thus forming a soft and hydrated matrix. Compared to the parental sample, all mutant cell walls are more hydrophobic. Polysaccharides have a compromised capability of retaining water molecules in these mutants. This effect is probably caused by the formation of denser cell walls in these mutants, and consequently, enhanced molecular aggregation, which might serve as a mechanism of fungal cell wall remodeling in response to structural defects or external stresses.

## 3.4 Discussion

High-resolution solid-state NMR data and chemical analysis of the intact cells and alkali-treated materials of *A. fumigatus* have substantiated our understanding of fungal cell wall architecture. To the best of our knowledge, the physical vision of polymer mobility and the chemical perspective of alkali-solubility have never been combined before. A structural scheme is constructed to represent the conceptual setup of the parental cell wall, which is composed of an outer shell and an internal domain (Figure 3.6a). A mobile layer containing GM, protein, a small amount of α-1,3-glucan, and GAG should be mainly at the outside of the cell wall. The occurrence of these molecules in the external position has been shown by immunolabelling with specific antibodies[47,55,56], and NMR data revealed their dynamic nature. Part of the GM molecule is dissolvable in alkali while the part covalently bound to the chitin-glucan complex remains insoluble despite its high mobility. Our results also confirmed a recently proposed structural scheme[15], where the inner domain is comprised of a stiff and hydrophobic complex of α-1,3-glucan

and chitin, which is distributed in a soft and hydrated matrix of β-glucans. Chitin and β-glucans are joined together by covalent linkages, forming the rigid mechanical hotspots that are resistant to hot alkali treatment[26,35], whereas α-1,3-glucan is physically associated with the chitin-β-glucan-GM core as shown by NMR data. The unequilibrated dynamics suggests that some β-glucans and α-1,3-glucans remain distant from chitin; the former are mobile and alkali-insoluble while the latter are rigid but extractable. Therefore, there is no direct correlation between the chemical digestibility and the rigidity of a molecule.

These studies have shown the synergism of both chemical and biophysical methods. SsNMR has identified a prominent role of α-1,3 glucans in the cell wall structuration whereas chemical analysis has often missed the presence of this polysaccharide in the alkali-insoluble fraction. Similarly, the presence of β-1,3-glucans in the alkali-soluble fraction was underestimated. Chemical analysis may be more accurate to identify the presence of a polysaccharide in a very low concentration: this could be one of the reasons for not seeing the GAG signals in the AS fraction or chitin signals in the chitin-deficient mutants.

Earlier chemical analyses have shown that the composition varies between mycelium and conidium cell wall and the culture medium used[12,57], which could be at the origin of the discrepancies seen between our earlier ssNMR study[15] and the present one. Previously, 1,6- and 1,4-linkages were identified in the β-glucans[15], with the former likely attributable to the branching points of β-1,3/1,6-glucan and the latter belonging to β-1,3/1,4-glucans. However, such signals were not detected in the current samples. The wild-type strain (RL 578) used in the previous study[15] differs from the one for the current study. In addition, the fungal material used previously was obtained after 14 days of growth in unshaken conditions in a sucrose-based medium. Under these experimental conditions, the material recovered was somehow heterogenous with conidium

and mycelium and autolyzed mycelium due to the long growth time. In the current study we use short culture times to recover actively growing mycelium and in a shaken condition to recover a homogenous mycelial pellet, which is a well-controlled system for analyzing the cell wall.

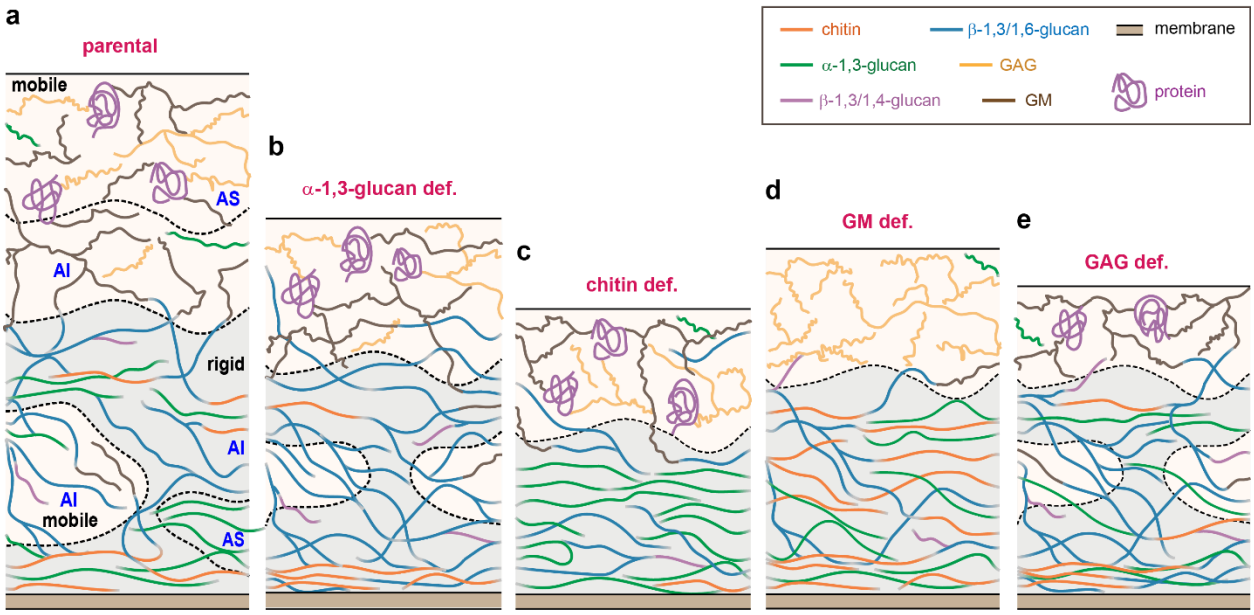


**Figure 3.6 Structural scheme of fungal cell walls substantiated by NMR data and mutant strains.** For each sample, the mobile and rigid phases are highlighted in pale yellow and pale blue, respectively. **a,** Cell walls of the parental sample, with the alkali-soluble (AS) and alkali-insoluble (AI) portions labeled. The rigid and mobile portions of AI and AS are also shown. The molar fractions of the rigid and mobile domains from solid-state NMR have been considered, but the scheme may not be strictly to scale. The molecule types are labeled and color-coded. Templated from the parental cell wall, schematic illustrations are also shown for the four mutants devoid of **b,** α-1,3-glucan, **c,** chitin, **d,** GM, and **e,** GAG, with the major changes shown. The cell wall thickness is proportional to the average value of each strain observed by TEM, but a broad distribution of thicknesses was observed in Figure 3.18.

Comparing the parental and mutant cell walls has made it possible to evaluate the structural role of each polysaccharide. Removal of either α-1,3-glucan, GM, or GAG will result in a moderate decline in the average thickness of cell walls (Figure 3.18), suggesting that the overall biosynthesis of cell wall component has been quantitatively reduced. In the α-1,3-glucan-deficient cell walls, *A. fumigatus* tunes up the synthesis of β-1,3-glucan in the inner core (Figure 3.1d). Without α-1,3-

glucan as spacers, chitin polymers now become tightly packed as depicted in Figure 3.6b, which explains the enhanced rigidity and reduced water accessibility of chitin in this mutant (Figure 3.5b, d). The structural roles of chitin and α-1,3-glucan are not interchangeable: the removal of most α-1,3-glucan is not associated to growth defects since the α-1,3-glucan-less mutant is growing like wild-type strains. There is still a missing link between the molecular rigidity and assembly with the mechanics and growth as shown in plants[58,59]. Chitin bears a variety of hydrogen bonds using its amide and carbonyl groups[16], which increases the entropy of the system and thermodynamically stabilizes the rigid phase. Hence it is not surprising that the chitin-deficient mutant showed morphological defects, likely due to the failure of cell walls to withstand high turgor pressure during cell growth. On the molecular level, the inner domain should be predominantly a binary mixture of α- and β-1,3-glucans (Figure 3.6c). It is likely that these two molecules are extensively associated, which, together with the increase of α-1,3-glucan content, could explain the increased rigidity and hydrophobicity of both molecules (Figure 3.5). The chitin-β-glucan-GM core is no longer present in the chitin-deficient mutant. It also becomes questionable whether the inner domain still contains mobile mannan and glucans. GM deficiency depletes proteins but increases the content of GAG. This agrees with the similar roles played by these two mobile molecules present in the outer cell wall layer. Simultaneously, we have observed a five-fold upsurge in the chitin content, and consequently, the production of an extremely hydrophobic and rigid cell wall (Figure 3.6d), which is speculated to be a compensatory effect to the loss of cell wall mannan. Supporting this hypothesis, the GAG-deficient cell wall cannot retain water molecules, although its inner domain only shows minor compositional changes when compared with the parental strain (Figure 3.6e).

Fungi are adapting two structural principles to respond to cell wall defects. First, the impaired biosynthesis of any polysaccharide will be compensated by compositional changes in both the internal and external domains[23-28]. However, the high level of complexity in these compensatory mechanisms in response to cell wall stress suggested a multitude of coordinated and interacting biosynthetic pathways more complicated than early thought. Second, the re-structuring cell wall tends to increase the polymer rigidity but decrease the water retention in the mesh of the inner domain (Figure 3.5d). The balance of plasticity and rigidity maintained in parental strain has been changed in the mutants, thus perturbing the dual functions of cell walls in maintaining cellular integrity and accommodating cell growth. We suspect that these rules allow fungi to resist not only mechanical deficiencies but also environmental stimuli.

We have observed the coexistence of a significant amount of valine residues with polysaccharides in the parental cell walls (Figure 3.4f, g), which becomes undetectable in GM- and GAG-deficient mutants. The origin of the valine is unknown. If present as peptides, they could come from the GPI signal domains that are rich in valine and are removed from the GPI-anchored proteins present in high amount in the cell wall. However, no data showed to date the involvement of this signal peptide after its release from the linkage of the protein moiety to the GPI anchor[60,61]. The unexpected results have however suggested a role of valine residues in the association between cell wall proteins and glycans in *A. fumigatus* and suggested the function of GM and GAG in stabilizing proteins on the cell wall surface. The occurrence or modification of the protein outer layer has not been investigated by SDS-PAGE in these different cell wall mutants. The coexistence of the polysaccharide-protein complexes on the cell wall surface may have impacts on the immune recognition of the fungus by C-type lectins. Such findings certainly deserve further investigation and the isolation and characterization of valine-rich fractions from cell walls.

This joint comparative study of the cell wall structure using two complementary biophysical and chemical approaches has paved the way for future exciting research avenues[20,62,63]. Our results have better revealed the great plasticity of the fungal cell wall and the capacity of the fungus to implement different strategies to survive in the case of the absence or significant modification of an essential cell wall component. This research strategy may reveal new compensatory pathways which could explain why the absence of α-1,3-glucans did not modify fungal growth, and at the opposite, the absence of β-1,3-glucan or chitin or mannan had a strong morphological impact. These are major reasons for the difficulty to set up an antifungal strategy that targets the cell wall[64,65]. A substantiated molecular understanding of how cell walls structurally respond to antifungal treatments or mutants may guide the design of new antifungal compounds to combat invasive infections.

## 3.5 Methods

### 3.5.1 Preparation of Isotopically Labeled Samples

To obtain isotopically labeled fungal cells, minimum media containing $^{13}$C-glucose as the sole carbon source and $^{15}$N-$NaNO_3$ as the sole nitrogen source were prepared, with the detailed composition listed in the Supplementary Methods. The parental strain used in this study was Δ*akuB*$^{KU80}$, a widely used model strain[23]. The α-1,3-glucan deficient strain was the triple mutant with Ags1p, Ags2p, and Ags3p encoding genes deleted[26]. The chitin-deficient strain was the quadruple Δ*csmA/csmB/chsF/chsG* mutant in which the genes encoding both chitin synthase family 1 (*csmA, csmB, and chsF*) and family 2 (*chsG*) were deleted[24]. The GM-deficient strain was the double knockout mutant of *KTR4* and *KTR7,* encoding two KTR mannosyltransferases[28]. The GAG-deficient strain was the knockout mutant of *gt4c* that encoding GAG synthase[27]. Conidia of $5\times10^8$ from the parental and the four deficient mutants were inoculated into 100 mL $^{13}$C,$^{15}$N-

labeled media at 37°C under 200 rpm for 36 h growth. The mycelia were harvested by filtering through two layers of miracloth, and then washed extensively using $ddH_2O$. Around 100 mg of the never-dried and intact mycelia of the parental and mutant strains were used for solid-state NMR structural characterization. Three batches of replicates were prepared for each strain under identical conditions. The NMR fingerprints of all strains were highly reproducible between batches (Figure 3.8).

### 3.5.2 Alkali Treatment and Sugar Analysis

Alkali treatment was conducted on the parental sample. After flash frozen in liquid nitrogen, the mycelia were stored at -80°C for further manipulations. Cell wall extraction and alkali fractionation were proceeded[66]. Briefly, mycelia were ground and added into 50 mL tubes. To get rid of cell wall-bound proteins mixtures of 50 mM Tris, 50 mM EDTA, 2% SDS and 1 mM TCEP were added and boiled for 20 min twice. After removing the supernatant, cell wall pellets were washed 6 times and lyophilized. Alkali fractionation was carried out with 1 M NaOH in 0.5 M $NaBH_4$ for incubation at 68°C for 1 h. After centrifugation, the supernatant was the alkali-soluble fraction, which was dialyzed in $ddH_2O$ for 2 days. The alkali-insoluble pellet was thoroughly washed by $ddH_2O$ until the pH reaches 6. The AS and AI fractions were lyophilized and rehydrated for solid-state NMR studies. The amount of sample recovered was around 15 mg of the AI sample and 10 mg of AS fraction was obtained for the batch analyzed. Hexosamines were identified and quantified by high-performance anion exchange chromatography (HPAEC) on a CarboPAC-PA1 column (Dionex) after acid hydrolysis (8 N HCl, 4 h at 100 °C) using glucosamine and galactosamine as standards. Monosaccharides were analyzed by gas liquid chromatography as their alditol acetates obtained after hydrolysis (4 N trifluoroacetic acid, 100 °C, 6 h) followed by reduction with sodium borohydride and peracetylation[67]. Degradation of α- and β-1,3-glucans of

the cell wall fractions was undertaken with recombinant α-1,3-glucanase from *Trichoderma harzianum* and recombinant β-1,3-glucananses from *Thermotoga neapolitan*a. Digestions were undertaken by treating the cell wall fraction with enzyme solution in 50 mm sodium acetate buffer for up to 96 h at 37°C. Degradation products were analyzed by HPAEC[68,69]. Amino acids were classically identified after 24 h 6M HCl hydrolysis and ninhydrin derivatization before quantification[70].

### 3.5.3 Solid-State NMR Experiments

Most of the solid-state NMR experiments were conducted on a Bruker Avance 800 MHz (18.8 Tesla) spectrometer except for the measurements of $^{13}$C-$T_1$ relaxation and $^{13}$C-$^{13}$C RFDR experiments, which were performed on a Bruker 400 MHz (9.4 Tesla) NMR. The radiofrequency field strengths were 62.5-83.3 kHz for $^{1}$H hard pulses and CP, 50-62.5 kHz for $^{13}$C, and 41.5 kHz for $^{15}$N in all experiments unless specifically mentioned. The $^{13}$C chemical shifts were reported on the tetramethylsilane (TMS) scale and externally referenced to the Met Cδ of a model peptide N-formyl-Met-Leu-Phe-OH (f-MLF) at 14.0 ppm[71]. The analysis and plotting of NMR data were achieved using TopSpin, Microsoft Excel, OriginPro, and Adobe Illustrator.

Resonance assignments of cell wall biomolecules were made using 1) 2D $^{13}$C-$^{13}$C correlation spectra with $^{13}$C-CP and a 53ms CORD mixing for rigid components[72,73], 2) 2D refocused J-INADEQUATE spectrum with $^{13}$C-DP and recycle delay of 2 s for the mobile components[74,75], 3) 2D SPC5 dipolar-INADEQUATE spectrum with $^{13}$C CP for the rigid components[76], 4) 2D $^{13}$C-$^{15}$N NCA(CX) heteronuclear correlation spectrum with a 5 ms $^{15}$N-$^{13}$C CP and a 15 ms or 100 ms PDSD mixing time for nitrogenated molecules[77], and 5) 2D $^{13}$C-$^{13}$C radio frequency-driven recoupling (RFDR) experiment for the selective detection of one bond cross-peaks with a recoupling time of 1.5 ms[78]. Most data were collected at 298 K under 10 kHz

MAS; only the SPC-5 dipolar-INADEQUATE experiment was conducted at a slow MAS of 7.5 kHz. Experiments 1, 2, 4 were collected using the intact cells of parental *A. fumigatus* and mutants. Experiments 3 and 5 were conducted on the alkali-soluble and insoluble samples. Chemical shifts previously obtained on model polysaccharides or cell wall materials were used as references for assigning the signals[79] The experimental parameters of all NMR experiments were provided in Table 3.1.

Compositional analysis of the polysaccharides by solid-state NMR in the rigid and mobile portions of cell walls was achieved by taking the integrals of well-resolved cross-peaks in 2D $^{13}$C-$^{13}$C correlation spectra: the 53 ms CORD spectra for rigid components and 2D refocused $^{13}$C DP J-INADEQUATE spectra with 2 s recycle delays for the mobile components. For the rigid molecules, the results of well-resolved C1-C3, C1-C2, and C1-C4 cross peaks were averaged. For the mobile polymers, the average of the resolved C1-C2 spin connections gave their relative amount. A more detailed description of the compositional analysis and error propagation is included in the Supplementary Methods. The best-fit relaxation time constants are plotted as a box and whisker diagram.

A series of 1D water-buildup curves were measured using a $^{1}$H-$T_2$ relaxation filter of 0.6 ms × 2, which abolished 90% of carbohydrate magnetization but retained 80% of water magnetization. A $^{1}$H mixing period varied from 0.1 μs to 64 ms is then used to allow water-to-polysaccharide polarization transfer, followed by a $^{1}$H-$^{13}$C CP to enable high-resolution $^{13}$C detection[54,80]. The buildup curves of intensities were plotted for each resolvable carbon site.

The dynamics of polysaccharides in the parental and mutant samples were probed using NMR relaxation. $^{13}$C-$T_1$ relaxation was measured at 298 K under 10 kHz MAS on a 400-MHz spectrometer to provide information about the mobility of components in the rigid portion of cell

walls. The experiments were measured in a CP-based pseudo-3D format by measuring a series of 2D $^{13}C$-$^{13}C$ correlation spectra with a variable z-filter time[81] of 0 s, 0.2 s, 1 s, 3 s, and 8 s. The relaxation data were fit using a single exponential decay function.

## 3.6 Acknowledgments

This work was supported by the National Institutes of Health (NIH) grant AI149289 to T.W. Preparation of isotopically labeled samples was supported by the Bagui Scholar Program Fund of Guangxi Zhuang Autonomous Region 2016A24 to C.J. A portion of this work was performed at the National High Magnetic Field Laboratory, which is supported by the National Science Foundation Cooperative Agreement No. DMR-1644779 and the State of Florida. The authors thank Françoise Baleux and Christelle Ganneau (Unité de Chimie des biomolecules, Institut Pasteur) for their help in the quantification of amino acids.

## REFERENCES


1 Brown, G. D. *et al.* Hidden Killers: Human Fungal Infections. *Sci. Transl. Med.* 4, doi:ARTN 165rv13 10.1126/scitranslmed.3004404 (2012).

2 Erwig, L. P. & Gow, N. A. R. Interactions of fungal pathogens with phagocytes. *Nat. Rev. Microbiol.* 14, 163-176 (2016).

3 Casadevall, A. Fungal diseases in the 21st century: the near and far horizons. *Pathog. Immun.* 3, 183-196 (2018).

4 Beardsley, J., Halliday, C. L., Chen, S. C.-A. & Sorrell, T. C. Responding to the emergence of antifungal drug resistance: perspectives from the bench and the bedside. *Furture Microbiol.* 13, 1175-1191 (2018).

5 Latgé, J. P. & Chamilos, G. Aspergillus fumigatus and Aspergillosis in 2019. *Clin. Microbiol. Rev.* 33, e00140-00118 (2020).

6 Perlin, D. S. Mechanisms of echinocandin antifungal drug resistance. *Ann. N. Y. Acad. Sci.* 1354, 1-11 (2015).

7 Denning, D. W. Echinocandin antifungal drugs. *The Lancet* 362, 1142-1151 (2003).

8 Stevens, D. A., Espiritu, M. & Parmar, R. Paradoxical effect of caspofungin: reduced activity against Candida albicans at high drug concentrations. *Antimicrob. Agents Chemother*. 48 (2004).

9 Loiko, V. & Wagener, J. The Paradoxical Effect of Echinocandins in Aspergillus fumigatus Relies on Recovery of the β-1,3-Glucan Synthase Fks1. *Antimicrob. Agents Chemother.* 61, e01690-01616 (2017).

10 Wagener, J. & Loiko, V. Recent Insights into the Paradoxical Effect of Echinocandins. *J. Fungi* 4, 5 (2017).

11 Nierman, W. C. *et al.* Genomic sequence of the pathogenic and allergenic filamentous fungus Aspergillus fumigatus. *Nature* 438, 1151-1156, doi:10.1038/nature04332 (2005).

12 Latgé, J. P., Beauvais, A. & Chamilos, G. The Cell Wall of the Human Fungal Pathogen Aspergillus fumigatus: Biosynthesis, Organization, Immune Response, and Virulence. *Annu. Rev. Microbiol.* 71, 99-116 (2017).

13 Fontaine, T. *et al.* Molecular organization of the alkali-insoluble fraction of Aspergillus fumigatus cell wall. *J. Biol. Chem.* 275, 41528-41529 (2000).

14 Francois, J. M. A simple method for quantitative determination of polysaccharides in fungal cell walls. *Nat. Protoc.* 1, 2995-3000, doi:10.1038/nprot.2006.457 (2006).

15 Kang, X. *et al.* Molecular architecture of fungal cell walls revealed by solid-state NMR. *Nat. Commun.* 9, 2747, doi:Artn 2747 10.1038/S41467-018-05199-0 (2018).

16 Fernando, L. D. *et al.* Structural Polymorphism of Chitin and Chitosan in Fungal Cell Walls from Solid-State NMR and Principal Component Analysis. *Front. Mol. Biosci.* , 727053 (2021).

17 Kirui, A. *et al.* Preparation of Fungal and Plant Materials for Structural Elucidation Using Dynamic Nuclear Polarization Solid-State NMR. *J. Vis. Exp.* 144, e59152 (2019).

18 Chrissian, C. *et al.* Solid-state NMR spectroscopy identifies three classes of lipids in Cryptococcus neoformans melanized cell walls and whole fungal cells. *J. Biol. Chem.* 295, 15083-15096 (2020).

19 Chatterjee, S., Prados-Rosales, R., Itin, B., Casadevall, A. & Stark, R. E. Solid-state NMR Reveals the Carbon-based Molecular Architecture of Cryptococcus neoformans Fungal Eumelanins in the Cell Wall. *J. Biol. Chem.* 290, 13779-13790, doi:10.1074/jbc.M114.618389 (2015).

20 Ehren, H. L. *et al.* Characterization of the cell wall of a mushroom forming fungus at atomic resolution using solid-state NMR spectroscopy. *Cell Surface* 6, 2020 (2020).

21 Zhao, W., Fernando, L. D., Kirui, A., Deligey, F. & Wang, T. Solid-state NMR of plant and fungal cell walls: A critical review. *Solid State Nucl. Magn. Reson.* 107, 101660, doi:10.1016/j.ssnmr.2020.101660 (2020).

22 Reif, B., Ashbrook, S. E., Emsley, L. & Hong, M. Solid-state NMR spectroscopy. *Nat. Rev. Methods Primers* 1, 2 (2021).

23 da Silva Ferreira, M. E. *et al.* The akuBKU80 mutant deficient for nonhomologous end joining is a powerful tool for analyzing pathogenicity in Aspergillus fumigatus. *Eukaryot. Cell* 5, 207-211 (2006).

24 Muszkieta, L. *et al.* Deciphering the role of the chitin synthase families 1 and 2 in the in vivo and in vitro growth of Aspergillus fumigatus by multiple gene targeting deletion. *Cell Microbiol.* 16, 1784-1805 (2014).

25 Maubon, D. *et al.* AGS3, an alpha(1-3)glucan synthase gene family member of Aspergillus fumigatus, modulates mycelium growth in the lung of experimentally infected mice. *Fungal Genet. Biol.* 43, 366-375 (2006).

26 Henry, C., Latgé, J. P. & Beauvais, A. alpha1,3 glucans are dispensable in Aspergillus fumigatus. *Eukaryot. Cell* 11, 26-29 (2012).

27 Briard, B. *et al.* Galactosaminogalactan activates the inflammasome to provide host protection. *Nature* 588, 688-692 (2020).

28 Henry, C. *et al.* Two KTR Mannosyltransferases Are Responsible for the Biosynthesis of Cell Wall Mannans and Control Polarized Growth in Aspergillus fumigatus. *mBio* 10 (2019).

29 Wang, T., Park, Y. B., Cosgrove, D. J. & Hong, M. Cellulose-Pectin Spatial Contacts Are Inherent to Never-Dried Arabidopsis thaliana Primary Cell Walls: Evidence from Solid-State NMR. *Plant Physiol.* 168, 871-884 (2015).

30 Kang, X. *et al.* Lignin-polysaccharide interactions in plant secondary cell walls revealed by solid-state NMR. *Nat. Commun.* 10, 347, doi:10.1038/s41467-018-08252-0 (2019).

31 Wang, T., Salazar, A., Zabotina, O. A. & Hong, M. Structure and dynamics of *Brachypodium* primary cell wall polysaccharides from two-dimensional $^{13}C$ solid-state nuclear magnetic resonance spectroscopy. *Biochemistry* 53, 2840-2854, doi:Doi 10.1021/Bi500231b (2014).

32 Arnold, A. A. *et al.* Whole cell solid-state NMR study of Chlamydomonas reinhardtii microalgae. *J. Biomol. NMR* 70, 123-131, doi:10.1007/s10858-018-0164-7 (2018).

33 Reichhardt, C., Joubert, L. M., Clemons, K. V., Stevens, D. A. & Cegelski, L. Integration of electron microscopy and solid-state NMR analysis for new views and compositional parameters of Aspergillus fumigatus biofilms. *Med Mycol.* 57, S239-244 (2019).

34 El Nokab, M. E. H. & van der Wel, P. C. A. Use of Solid-state NMR spectroscopy for Investigating Polysaccharide-based Hydrogels: A Review. *Carbohydr. Polym.* 240, 116276 (2020).

35 Latgé, J. P. The cell wall: a carbohydrate armour for the fungal cell. *Mol. Microbiol.* 66, 279-290, doi:10.1111/j.1365-2958.2007.05872.x (2007).

36 Asami, S., Porter, J. R., Lange, O. F. & Reif, B. Access to Ca Backbone Dynamics of Biological Solids by $^{13}C$ $T_1$ Relaxation and Molecular Dynamics Simulation. *J. Am. Chem. Soc.* 137, 1094-1100, doi:10.1021/ja509367q (2015).

37 Speth, C., Rambach, G., Lass-Flörl, C., Howell, P. L. & Sheppard, D. C. Galactosaminogalactan (GAG) and its multiple roles in Aspergillus pathogenesis. *Virulence* 10, 976-983, doi:10.1080/21505594.2019.1568174 (2019).

38 Briard, B., Muszkieta, L., Latgé, J. P. & Fontaine, T. Galactosaminogalactan of Aspergillus fumigatus, a bioactive fungal polymer. *Mycologia* 108 (2016).

39 Fontaine, T. *et al.* Galactosaminogalactan, a New Immunosuppressive Polysaccharide of Aspergillus fumigatus. *PloS Pathog.* 7 (2011).

40 Leitao, E. A. *et al.* Beta-galactofuranose-containing O-linked oligosaccharides present in the cell wall peptidogalactomannan of Aspergillus fumigatus contain immunodominant epitopes. *Glycobiology* 13, 681-692 (2003).

41 Simenel, C., Coddeville, B., Delepierre, M., Latgé, J. P. & Fontaine, T. Glycosylinositolphosphoceramides in Aspergillus fumigatus. *Glycobiology* 18, 84-96 (2008).

42 Haido, R. M. *et al.* Analysis of peptidogalactomannans from the mycelial surface of Aspergillus fumigatus. *Med. Mycol.* 36, 313-321 (1998).

43 Morelle, W. *et al.* Galactomannoproteins of Aspergillus fumigatus. *Eukaryot. Cell* 4, 1308-1316 (2005).

44 Fontaine, T. & Latgé, J. P. Galactomannan Produced by Aspergillus fumigatus: An Update on the Structure, Biosynthesis and Biological Functions of an Emblematic Fungal Biomarker *J. Fungi* 6, 283 (2020).

45 Onoue, T. *et al.* Identification of Two Mannosyltransferases Contributing to Biosynthesis of the Fungal-type Galactomannan α-Core-Mannan Structure in Aspergillus fumigatus *Sci. Rep.* 8, 16918 (2018).

46 Gressler, M. *et al.* Definition of the Anti-inflammatory Oligosaccharides Derived From the Galactosaminogalactan (GAG) From Aspergillus fumigatus. *Front. Cell. Infect. Microbiol.* 9, 365 (2019).

47 Valsecchi, I. *et al.* The puzzling construction of the conidial outer layer of Aspergillus fumigatus. *Cell Microbiol.* 21, e12994 (2019).

48 Dichtl, K. *et al.* Aspergillus fumigatus devoid of cell wall beta-1,3-glucan is viable, massively sheds galactomannan and is killed by septum formation inhibitors. *Mol. Microbiol.* 95, 458-471, doi:10.1111/mmi.12877 (2015).

49 Chakraborty, A. *et al.* Biomolecular complex viewed by dynamic nuclear polarization solid-state NMR spectroscopy. *Biochem. Soc. Trans.* 48, 1089-1099 (2020).

50 Su, Y., Andreas, L. & Griffin, R. G. Magic angle spinning NMR of proteins: high-frequency dynamic nuclear polarization and $^{1}$H detection. *Annu. Rev. Biochem.* 84, 465-497, doi:10.1146/annurev-biochem-060614-034206 (2015).

51 Kaplan, M. *et al.* Probing a cell-embedded megadalton protein complex by DNP-supported solid-state NMR. *Nat. Methods* 12, 649-+, doi:10.1038/Nmeth.3406 (2015).

52 de Dios, A. C., Pearson, J. G. & Oldfield, E. Secondary and tertiary structural effects on protein NMR chemical shifts: an ab initio approach. *Science* 260, 1491-1496 (1993).

53 Wang, T., Jo, H., DeGrado, W. F. & Hong, M. Water Distribution, Dynamics, and Interactions with Alzheimer's beta-Amyloid Fibrils Investigated by Solid-State NMR. *J. Am. Chem. Soc.* 139, 6242-6252, doi:10.1021/jacs.7b02089 (2017).

54 White, P. B., Wang, T., Park, Y. B., Cosgrove, D. J. & Hong, M. Water-polysaccharide interactions in the primary cell wall of *Arabidopsis thaliana* from polarization transfer

solid-state NMR. *J. Am. Chem. Soc.* 136, 10399-10409, doi:Doi 10.1021/Ja504108h (2014).

55 Latgé, J. P. *et al.* Chemical and Immunological Characterization of the Extracellular Galactomannan of Asperillus fumigatus. *Infect. Immun.* 62, 5424-5433 (1994).

56 Loussert, C. *et al.* In vivo biofilm composition of Aspergillus fumigatus. *Cell Microbiol.* 12, 405-410 (2010).

57 Beauvais, A., Fontaine, T., Aimanianda, V. & Latgé, J. P. Aspergillus cell wall and biofilm. *Mycopathologia.* 178, 371-377 (2014).

58 Phyo, P. *et al.* Gradients in Wall Mechanics and Polysaccharides along Growing Inflorescence Stems. *Plant Physiol.* 175, 1593-1607, doi:10.1104/pp.17.01270 (2017).

59 Kirui, A. *et al.* A Pectin Methyltransferase Modulates Polysaccharide Dynamics and Interactions in Arabidopsis Primary Cell Walls: Evidence from Solid-State NMR. *Carbohydr. Polym.* 270, 118370 (2021).

60 Ouyang, H. *et al.* One single basic amino acid at ω-1 or ω-2 site is a signal that retains glycosylphosphatidylinositol (GPI) anchored protein in plasma membrane of Aspergillus fumigatus. *Eukaryot. Cell* 12, 889-899 (2013).

61 Vogt, M. S., Schmitz, G. F., Silva, V. D., Mosch, H.-U. & Essen, L.-O. Structural base for the transfer of GPI-anchoredglycoproteins into fungal cell walls. *Proc. Natl. Acad. Sci. USA* 117, 22061-22067 (2020).

62 Gow, N. A. R., Latgé, J. P. & Munro, C. A. The Fungal Cell Wall: Structure, Biosynthesis, and Function. *Microbiol. Spectr.* 5 (2017).

63 Anderson, T. M. *et al.* Amphotericin forms an extramembranous and fungicidal sterol sponge. *Nat. Chem. Biol.* 10, 400-406 (2014).

64 Furukawa, T. *et al.* The negative cofactor 2 complex is a key regulator of drug resistance in Aspergillus fumigatus. *Nat. Commun.* 11, 427 (2020).

65 Latgé, J. P. 30 years of battling the cell wall. *Med Mycol.* 55, 4-9 (2017).

66 Jimenez-Ortigosa, C. *et al.* Chitin synthases with a myosin motor-like domain control the resistance of Aspergillus fumigatus to echinocandins. *Antimicrob. Agents Chemother.* 56, 6121-6131 (2012).

67 Liu, Z. *et al.* Functional Genomic and Biochemical Analysis Reveals Pleiotropic Effect of Congo Red on Aspergillus fumigatus. *mBio* 18, e00863-00821 (2021).

68 Fontaine, T. *et al.* Cell wall alpha1-3glucans induce the aggregation of germinating conidia of Aspergillus fumigatus. *Fungal Genet. Biol.* 47, 707-712 (2010).

69 Stalhberger, T. *et al.* Chemical Organization of the Cell Wall Polysaccharide Core of Malassezia restricta. *J. Biol. Chem.* 289, 12647-12656 (2014).

70 Moore, S. & Stein, W. H. Chromatographic determination of amino acids by the use of automatic recording equipment. *Methods Enzymol.* 6, 819-831 (1958).

71 Rienstra, C. M. *et al.* De novo determination of peptide structure with solid-state magic-angle spinning NMR spectroscopy. *Proc. Natl. Acad. Sci. USA* 99, 10260-10265, doi:10.1073/pnas.152346599 (2002).

72 Hou, G., Yan, S., Trebosc, J., Amoureux, J. P. & Polenova, T. Broadband homonuclear correlation spectroscopy driven by combined R2(n)(v) sequences under fast magic angle spinning for NMR structural analysis of organic and biological solids. *J. Magn. Reson.* 232, 18-30, doi:10.1016/j.jmr.2013.04.009 (2013).

73 Lu, X., Guo, C., Hou, G. & Polenova, T. Combined zero-quantum and spin-diffusion mixing for efficient homonuclear correlation spectroscopy under fast MAS: broadband recoupling and detection of long-range correlations. *J. Biomol. NMR* 61, 7-20, doi:10.1007/s10858-014-9875-6 (2015).

74 Lesage, A., Auger, C., Caldarelli, S. & Emsley, L. Determination of through-bond carbon-carbon connectivities in solid-state NMR using the INADEQUATE experiment. *J. Am. Chem. Soc.* 119, 7867-7868, doi:Doi 10.1021/Ja971089k (1997).

75 Cadars, S. *et al.* The refocused INADEQUATE MAS NMR experiment in multiple spin-systems: Interpreting observed correlation peaks and optimising lineshapes. *J. Magn. Reson.* 188, 24-34, doi:10.1016/j.jmr.2007.05.016 (2007).

76 Hohwy, M., Rienstra, C. M., Jaroniec, C. P. & Griffin, R. G. Fivefold symmetric homonuclear dipolar recoupling in rotating solids: Application to double quantum spectroscopy. *J. Chem. Phys.* 110, 7983-7992, doi:Doi 10.1063/1.478702 (1999).

77 Baldus, M., Petkova, A. T., Herzfeld, J. & Griffin, R. G. Cross polarization in the tilted frame: assignment and spectral simplification in heteronuclear spin systems. *Mol. Phys.* 95, 1197-1207, doi:10.1080/00268979809483251 (1998).

78 Bennett, A. E. *et al.* Homonuclear radio frequency-driven recoupling in rotating solids. *J. Chem. Phys.* 108, 9463-9479, doi:Doi 10.1063/1.476420 (1998).

79 Kang, X. *et al.* CCMRD: A Solid-State NMR Database for Complex Carbohydrates. *J. Biomol. NMR* 74, 239-250 (2020).

80 Etzkorn, M. *et al.* Secondary structure, dynamics, and topology of a seven-helix receptor in native membranes, studied by solid-state NMR spectroscopy. *Angew. Chem. Int. Ed. Engl.* 46, 459-462, doi:10.1002/anie.200602139 (2007).

81 Wang, T., Williams, J. K., Schmidt-Rohr, K. & Hong, M. Relaxation-compensated difference spin diffusion NMR for detecting 13C-13C long-range correlations in proteins and polysaccharides. *J. Biomol. NMR* 61, 97-107, doi:10.1007/s10858-014-9889-0 (2015).

82 Shim, J. H. *et al.* Antitumor effect of soluble beta-1,3-glucan from Agrobacterium sp. R259 KCTC 1019. *J. Microbiol. Biotechnol.* 17, 1513-1520 (2007).

83 Fairweather, J. K., Him, J. L., Heux, L., Driguez, H. & Bulone, V. Structural characterization by (13)C-NMR spectroscopy of products synthesized in vitro by polysaccharide synthases using (13)C-enriched glycosyl donors: application to a UDP-glucose:(1-->3)-beta-D-glucan synthase from blackberry (Rubus fruticosus). *Glycobiology* 14, 775-781, doi:10.1093/glycob/cwh097 (2004).

84 Saitô, H., Ohki, T. & Sasaki, T. A 13C-nuclear magnetic resonance study of polysaccharide gels. Molecular architecture in the gels consisting of fungal, branched (1 → 3)-β-d-glucans (lentinan and schizophyllan) as manifested by conformational changes induced by sodium hydroxide. *Carbohydr. Res.* 74, 227-240 (1979).

85 Bhanja, S. K. *et al.* Water-insoluble glucans from the edible fungus Ramaria botrytis. *Bioactive Carbohydrates and Dietary Fibre* 3, 52-58 (2014).

86 Puanglek, S. *et al.* In vitro synthesis of linear alpha-1,3-glucan and chemical modification to ester derivatives exhibiting outstanding thermal properties. *Sci. Rep.* 6, doi:Artn 3047910.1038/Srep30479 (2016).

87 Kono, H., Numata, Y., Erata, T. & Takai, M. $^{13}C$ and $^{1}H$ resonance assignment of mercerized cellulose II by two-dimensional MAS NMR spectroscopies. *Macromolecules* 37, 5310-5316, doi:Doi 10.1021/Ma030465k (2004).

88 Heux, L., Brugnerotto, J., Desbrieres, J., Versali, M. F. & Rinaudo, M. Solid state NMR for determination of degree of acetylation of chitin and chitosan. *Biomacromolecules* 1, 746-751, doi:Doi 10.1021/Bm000070y (2000).

89 Kameda, T., Miyazawa, M., Ono, H. & Yoshida, M. Hydrogen bonding structure and stability of alpha-chitin studied by C-13 solid-state NMR. *Macromol. Biosci.* 5, 103-106, doi:10.1002/mabi.200400142 (2004).

90 King, C., Stein, R. S., Shamshina, J. L. & Rogers, R. D. Measuring the Purity of Chitin with a Clean, Quantitative Solid-State NMR Method. *ACS Sustain. Chem. Eng.* 5, 8011-8016, doi:10.1021/acssuschemeng.7b01589 (2017).

91 Tanner, S. F., Chanzy, H., Vincendon, M., Roux, J. C. & Gaill, F. High-Resolution Solid-State C-13 Nuclear-Magnetic-Resonance Study of Chitin. *Macromolecules* 23, 3576-3583, doi:Doi 10.1021/Ma00217a008 (1990).

92 K J Fritzsching, Y Yang, K Schmidt-Rohr & Mei Hong. Practical use of chemical shift databases for protein solid-state NMR: 2D chemical shift maps and amino-acid assignment with secondary-structure information. *J Biomol NMR.* 56 (2013).

# APPENDIX

## 3.7 Methods

### 3.7.1 Composition of Minimum Media for Isotopically Labeling Fungal Cells

To obtain isotopically labeled fungal cells, minimum media were prepared with the following components: 1% $^{13}$C-glucose, 0.6% $^{15}$N-$NaNO_3$, 1 mL/L of 1000X trace elements, 20 mL/L 50X salt solution, 50 mM Mops to adjust the final pH to 7. 1000X trace elements solution was composed of 0.04 % $Na_2B_4O_7 \cdot 10H_2O$, 0.4 % $CuSO_4 \cdot 5H_2O$, 0.8 % $MnSO_4 \cdot 4H_2O$, 0.8 % $Na_2MoO_4 \cdot 10H_2O$, 8 % $ZnSO_4 \cdot 7H_2O$, 5 mM $FeCl_3$, and 0.2 M HCl to prevent oxidation. 50X salt solution is composed of 26% KCl, 26 % $MgSO_4 \cdot 7H_2O$, and 76% $KH_2PO_4$.

### 3.7.2 Transmission Electron Microscope Measurement

In total, 3 μL of each sample was placed onto a glow discharged TEM grid for several minutes and stained using a mixture of 2% uranyl acetate and lead citrate solution. A thin film was spanned on the grid by removing the excess solution with the paper filter. The TEM images were collected using a JEOL JEM-1400 electron microscope. Cell wall thickness was measured using ImageJ software after setting the scale in accordance with known bar scales on the cell images. Statistical analysis was done using unpaired student's t-test for all the mutant samples on the cell wall thickness measurements performed.

### 3.7.3 Estimation of Carbohydrate Composition Using Resolved NMR Signals

To estimate the amount of different polysaccharides, we used 2D 53-ms CORD and DP J-INADEQUATE spectra for rigid and mobile phases, respectively. The peak volumes in the 2D spectra are obtained using the integration function of the Bruker Topspin software. The assignment of the cross peaks and the peak volumes are provided in the Source Data as well as the descriptions associated with Tables 3.3 and 3.4. To minimize the effect from spectral overlapping in the CORD

spectrum (which has diagonal), we typically avoid considering the cross peaks involving any of the heavily overlapped carbon sites such as the C6 position of β-1,3-glucan, the chitin C1, unless a resolved cross peak is present. For the closely placed signals of the C2 (71.9 ppm) and C4 (71.7 ppm) of the α-1,3-glucan, we divided the sum of their peak integral equally. For the diagonal-free INADEQUATE spectrum: we mostly rely on the resolved C1-C2 and C4-C5 spin connections. The NMR peaks used for quantification are provided in Table 3.5 and Source Data file.

The relative abundance of a specific polysaccharide ($\mathrm{RA}^{\mathrm{poly}.x}$) was calculated by normalizing the sum of integrals by the number of peaks using the following equation:

$$\mathrm{RA}^{\mathrm{poly}.x}(\%) = \frac{\sum_{n=1}^{n_{\mathrm{peaks}}^{\mathrm{poly}.x}} \mathrm{I}_n^{\mathrm{poly}.x} / n_{\mathrm{peaks}}^{\mathrm{poly}.x}}{\sum_{m=1}^{m^{\mathrm{poly}.}} (\sum_{n=1}^{n_{\mathrm{peaks}}^{\mathrm{poly}.x}} \mathrm{I}_n^{\mathrm{poly}.x} / n_{\mathrm{peaks}}^{\mathrm{poly}.x})} \times 100 \qquad \textbf{Eq 3.1}$$

where $n_{\mathrm{peaks}}^{\mathrm{poly}.x}$ is the number of cross-peaks, $\mathrm{I}_n^{\mathrm{poly}.x}$ is the integral (peak volume), and $m^{\mathrm{poly}.}$ is the total number of cell wall polysaccharides.

The Error was determined by calculating the standard error of a specific polysaccharide ($\mathrm{std.ERR}^{\mathrm{poly}.x}$) using the standard deviation of integrated peak volume dividing by square summation of the number of cross-peaks. The total standard error ($\sum \mathrm{std.ERR}$) calculated by the square sum of the standard error of each polysaccharide. Finally, percentage error of specific polysaccharide ($\mathrm{ERR}^{\mathrm{poly}.x}$) calculated by the fraction of standard error ($\mathrm{std.ERR}^{\mathrm{poly}.x}$) in average integrated peak volume of specific polysaccharide ($\overline{x}^{V^{\mathrm{poly}.x}}$) and the fraction of total standard error ($\sum \mathrm{std.ERR}$) in total integrated peak volume ($\sum V^{\mathrm{poly}.}$) followed by multiplication with the relative abundance of the specific polysaccharide($\mathrm{RA}^{\mathrm{poly}.x}$). The process can be presented using the following equation:

$$\mathrm{ERR}^{\mathrm{poly}.x} = \frac{\mathrm{std.\,ERR}^{\mathrm{poly}.x}}{\overline{x}^{V^{\mathrm{poly}.x}}} \times \frac{\sum \mathrm{std.\,ERR}}{\sum V^{\mathrm{poly.}}} \times \mathrm{RA}^{\mathrm{poly}.x} \qquad \textbf{Eq 3.2}$$

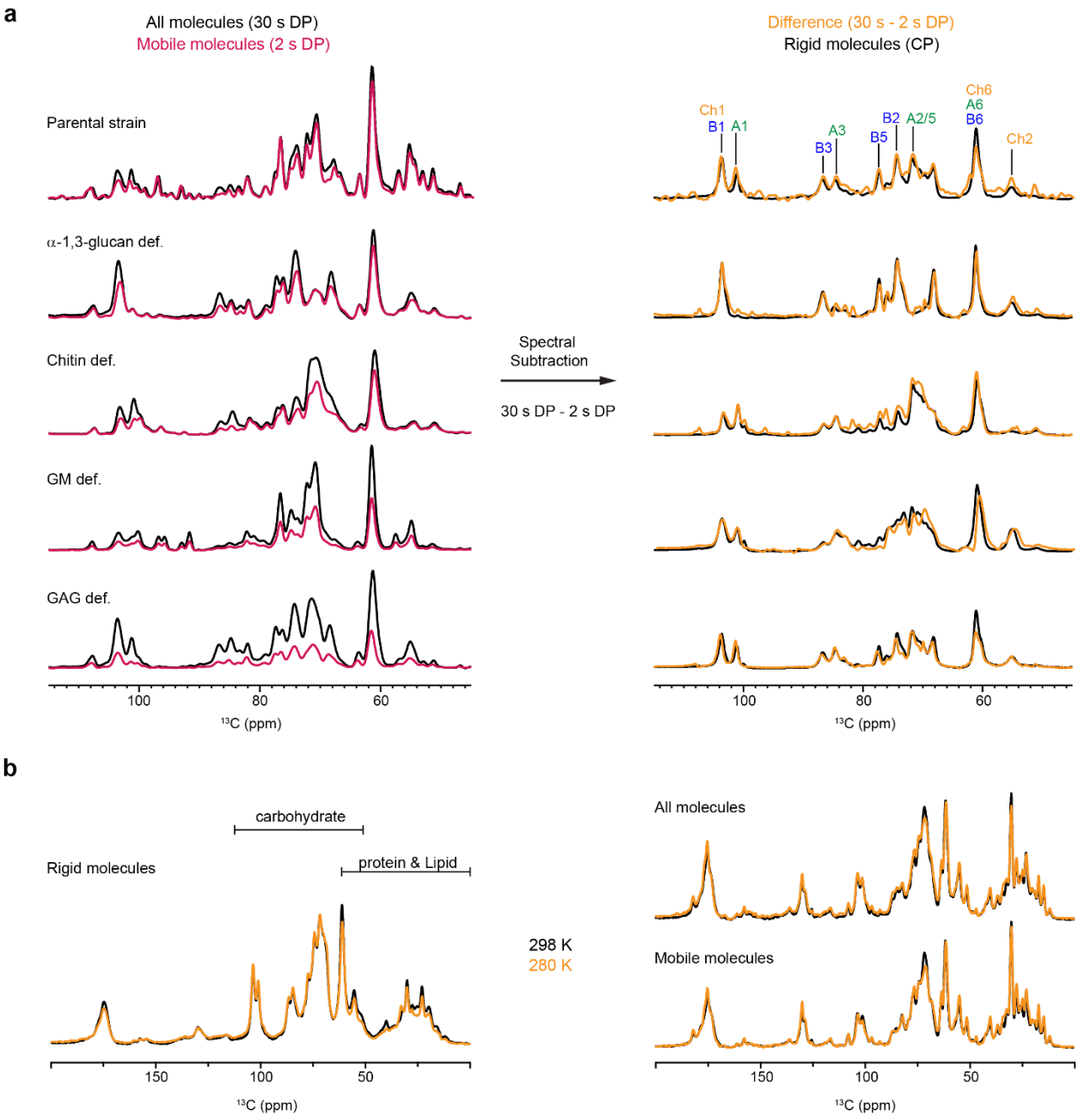


**Figure 3.7 Differentiation of the rigid and mobile molecules in *A. fumigatus*. a,** Overlay of 1D $^{13}C$ DP spectra measured using recycle delays of 30 s (black spectrum; quantitatively detecting all molecules) and 2 s (magenta spectrum, selectively detecting the mobile molecules). For each sample, subtraction of the two DP spectra generates a difference spectrum (yellow) reporting the rigid molecules. The patterns of the difference spectra are similar to those of the CP spectra. Therefore, the use of CP and DP with short recycle delays and CP in 2D spectra will efficiently probe most molecules in the sample. **b,** 1D $^{13}C$ CP and DP spectra of the parental strain measured at 298 K and 280 K. The difference in the pattern of carbohydrate signals at these two temperatures is negligible.

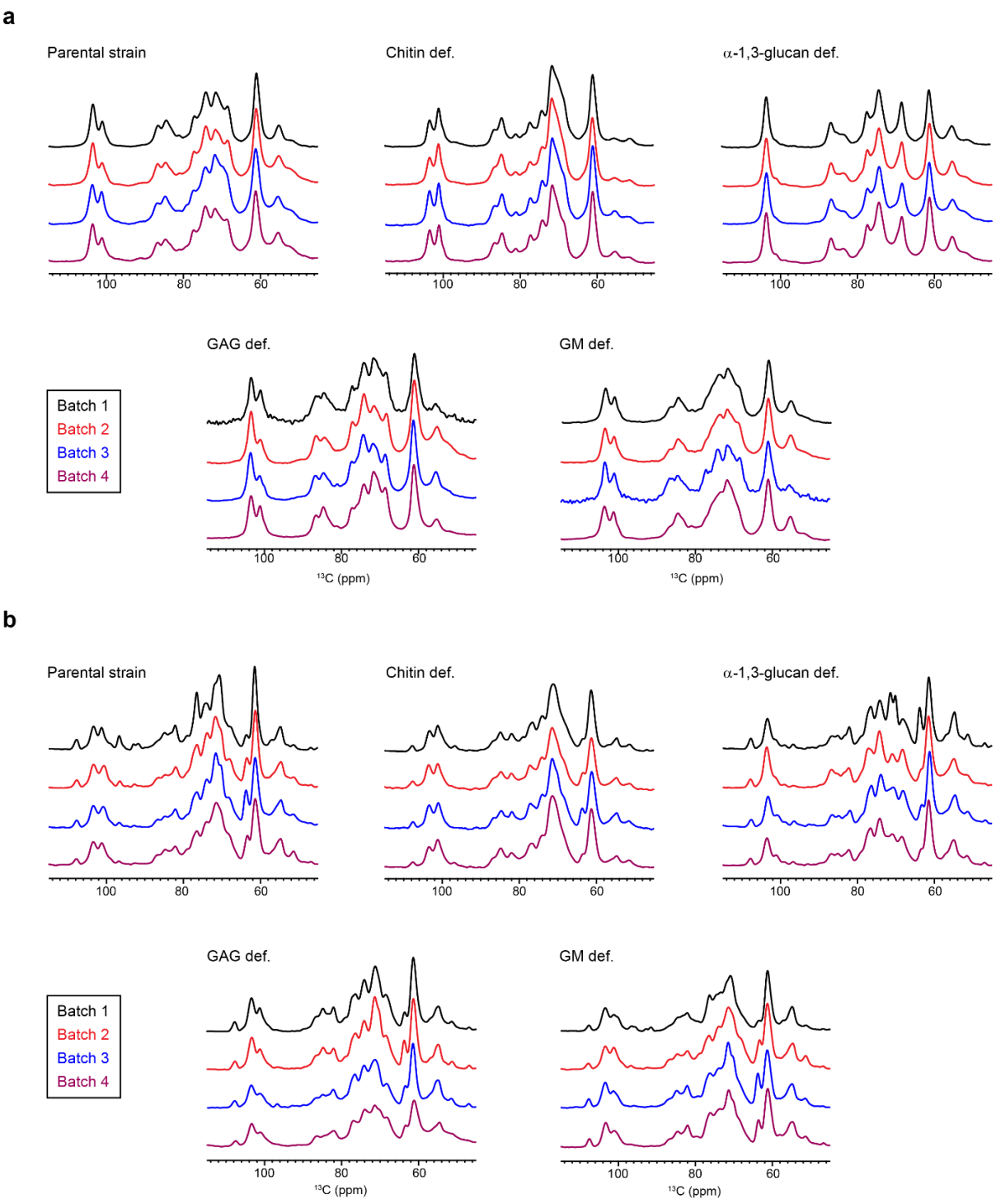


**Figure 3.8 Reproducibility evidenced by 1D $^{13}C$ spectra of four batches of *A. fumigatus* samples.** Four $^{13}C$,$^{15}N$-labeled samples were prepared for each of the five strains. Batch 1 was the original sample used for the majority of the research described in this study, and batch 2-4 were prepared freshly for reproducibility test. **a,** 1D $^{13}C$ CP detecting the rigid molecules. **b,** 1D quantitative DP spectra collected using a long recycle delay of 30 s for the unbiased detection of all molecules.

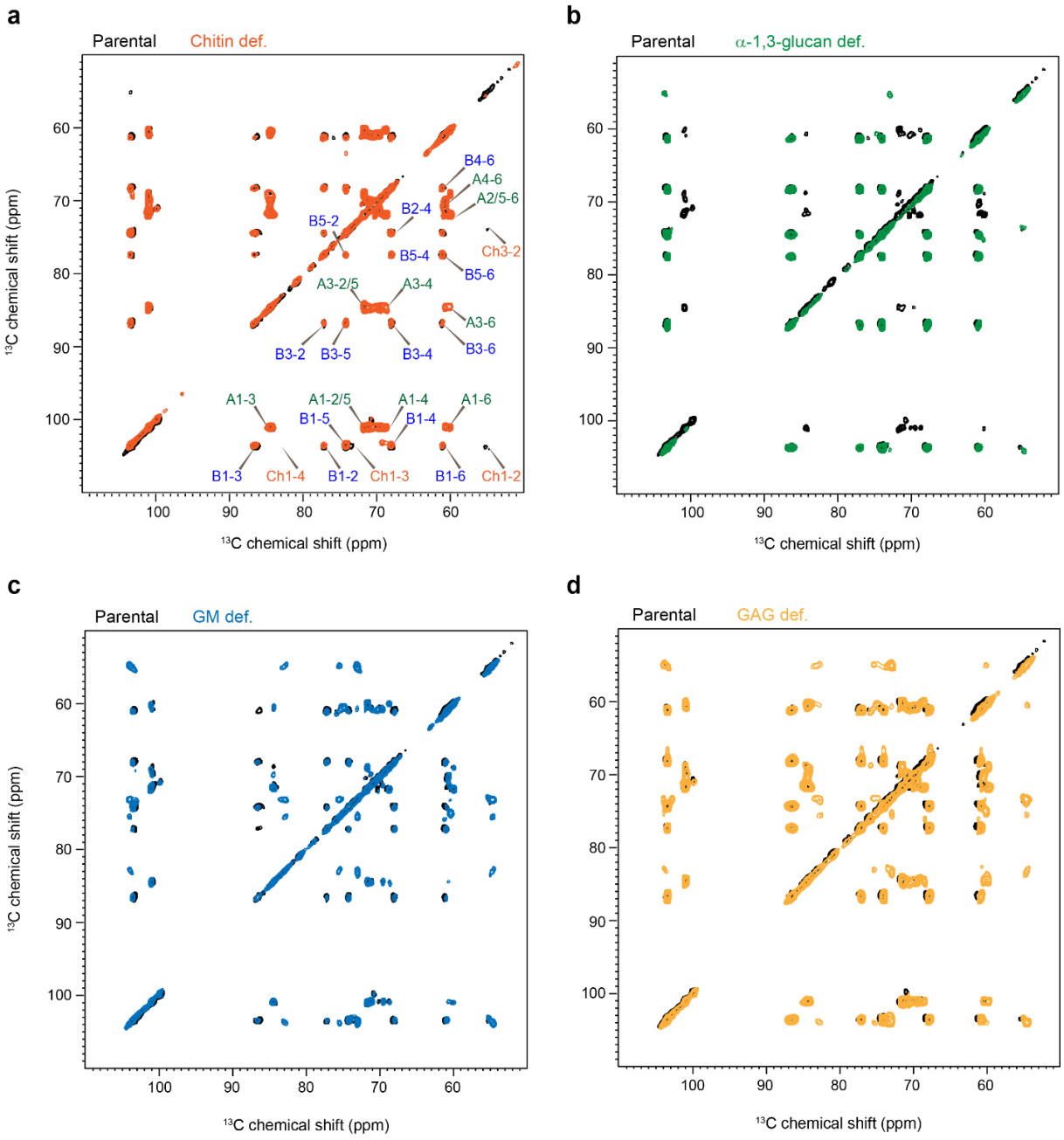


**Figure 3.9 Comparison of cell walls of different mutants of *A. fumigatus.*** The overlay of 2D $^{13}C$-$^{13}C$ CORD spectra of wild-type sample (black) with **a,** chitin-deficient mutant (orange), **b,** α-1,3-glucan-deficient strain (green), **c,** galactomannan-deficient mutant (cyan), and **d,** galactosaminogalactan-deficient mutant (yellow). These spectra selectively detect rigid molecules including chitin, α-1,3-glucan, and β-glucan. Signals of either chitin or α-1,3-glucan are missing in the corresponding mutants. The galactomannan-deficient and galactosaminogalactan-deficient mutants do not miss any signals. The galactomannan-deficient sample has a higher amount of chitin. All the spectra were measured on an 800 MHz spectrometer under 13 kHz MAS.

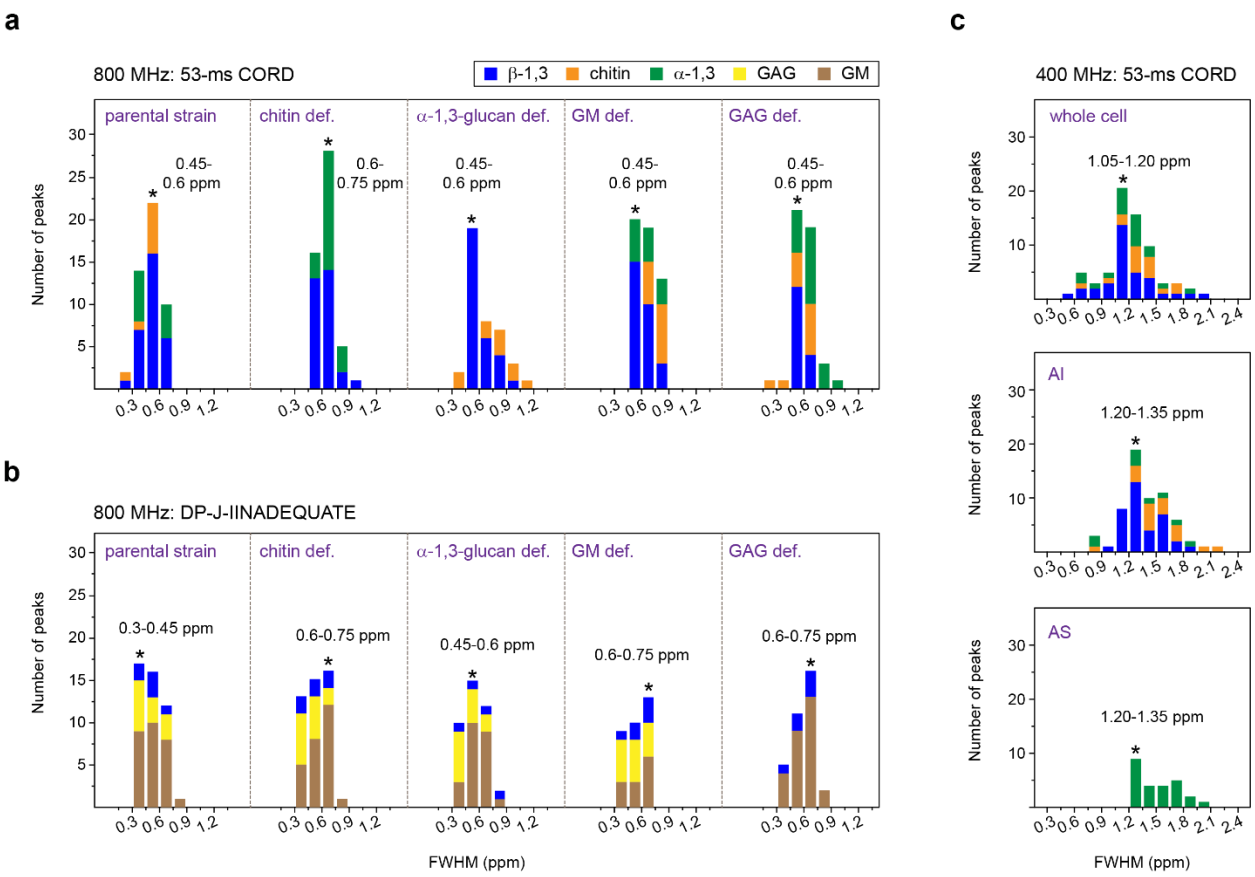


**Figure 3.10 Distribution of FWHM linewidth. a,** Spectral linewidth of $^{13}C$ whole cell sample centered at 0.45-0.75 ppm region for the 53 ms CORD spectra collected on an 800 MHz NMR. **b,** FWHM linewidth of DP J-INADEQUATE spectra clustered in the 0.3-0.75 ppm region. The data shown are whole-cell samples measured on an 800 MHz spectrometer. Source data are provided as a Source Data file.

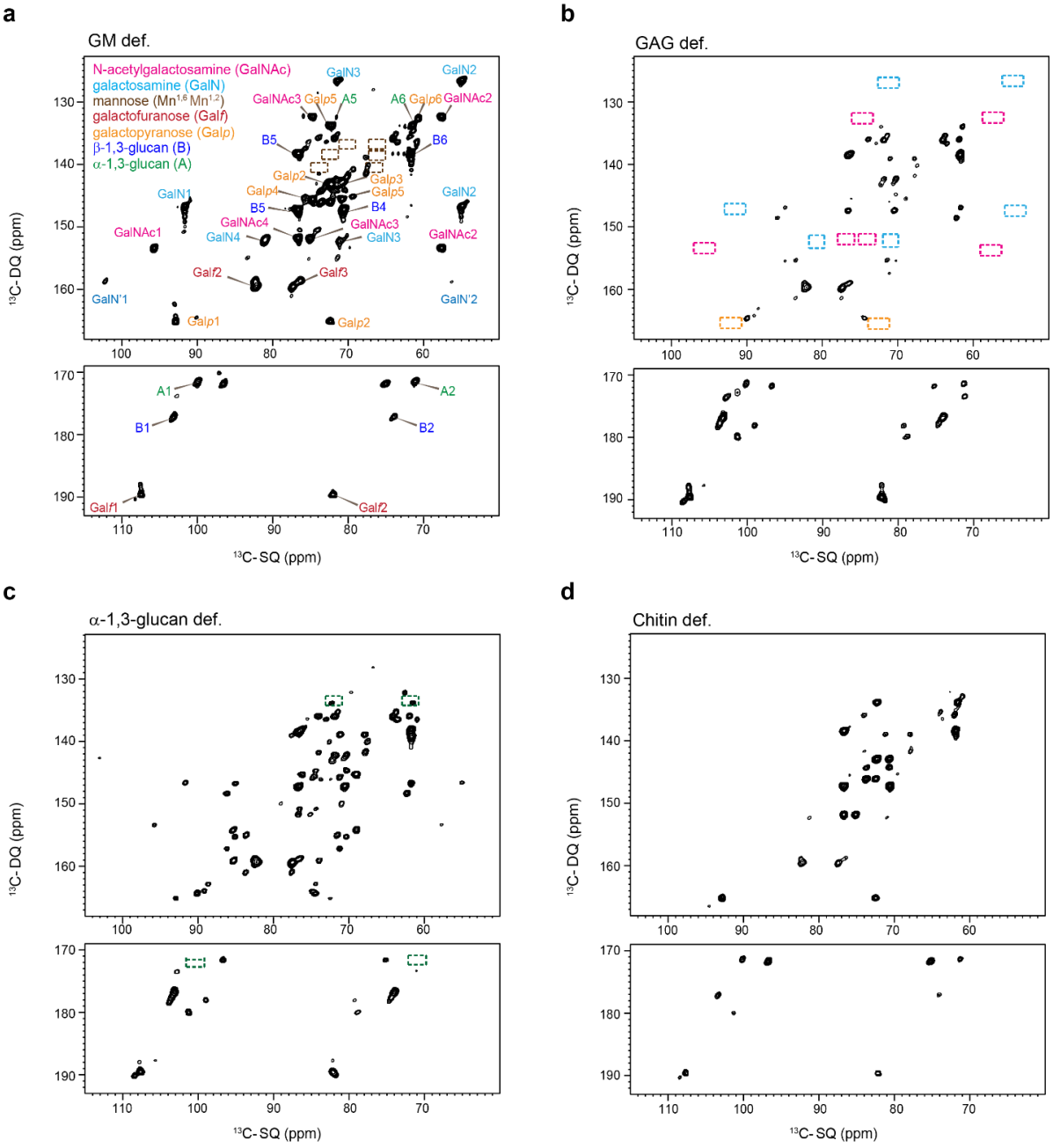


**Figure 3.11 Mobile Polysaccharides of fungal cell walls.** 2D $^{13}C$ DP J-INADEQUATE spectra are compared among **a,** GM-deficient mutant, **b,** GAG-deficient sample, **c,** α-1,3-glucan-deficient strain, and d, chitin-deficient sample. The use of $^{13}C$-DP and short recycle delays selectively probes the rigid domains of polysaccharides. Dashline boxes are used to indicate the absence of mannose signals in the GM-deficient mutant, the absence of GalNAc and $GalNH_2$ peaks in the GAG-deficient sample, as well as the missing α-1,3-glucan regions in the α-1,3-glucan-deficient mutant. Chitin is not present in the mobile region hence no missing peaks were observed in the chitin-deficient sample.

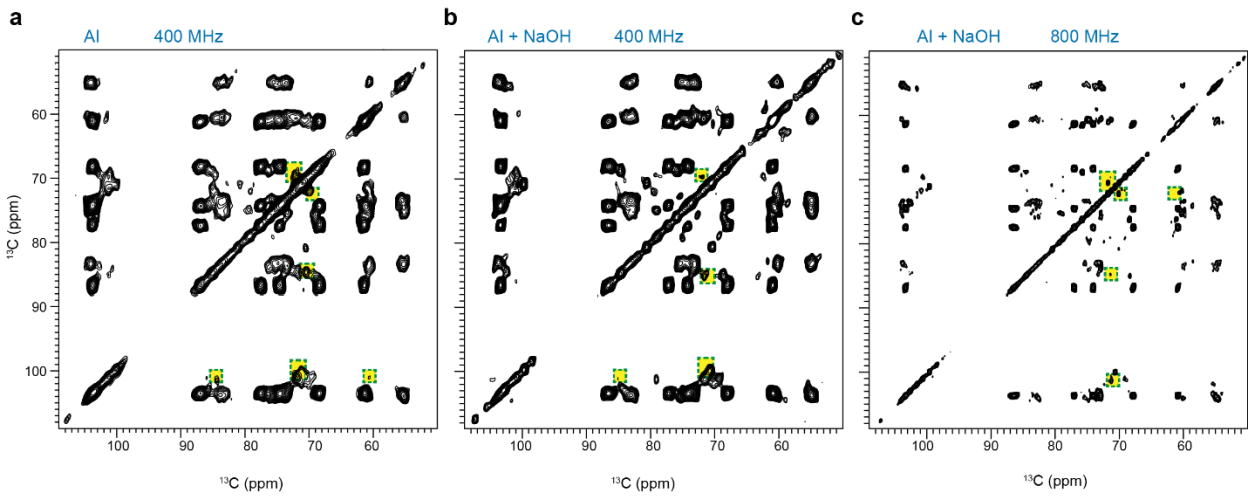


**Figure 3.12 NaOH treated alkali-insoluble fraction.** $^{13}C$-$^{13}C$ 2D CORD spectra of the alkali-insoluble (AI) fraction **a**, before a second NaOH treatment, and **b,** after a second NaOH at a 400 MHz spectrometer. **c,** AI portion treated again with NaOH and measured on an 800 MHz spectrometer, which shows much narrower peaks as benefited from the resolution improvement. Highlighted regions show the α-1,3-glucan signals, which were retained after multiple times of NaOH treatments.

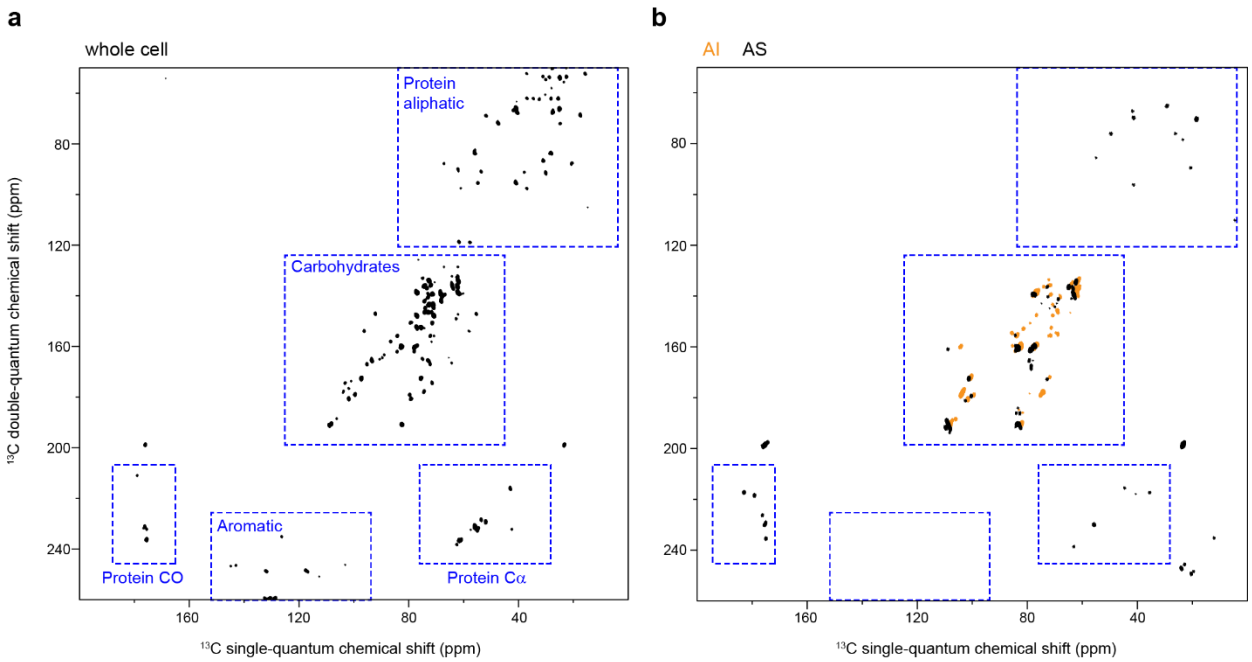


**Figure 3.13 Presence of proteins in alkali-soluble fraction. a,** Full DP J-INADEQUATE spectra of parental *A. fumigatus* cells detecting mobile molecules. **b,** Overlay of DP J-INADEQUATE spectra collected on the alkali-insoluble (AI; yellow) and alkali-soluble (AS) fractions of *A. fumigatus* cell walls. Protein signals are mainly identified in the mobile part of the AS fraction.

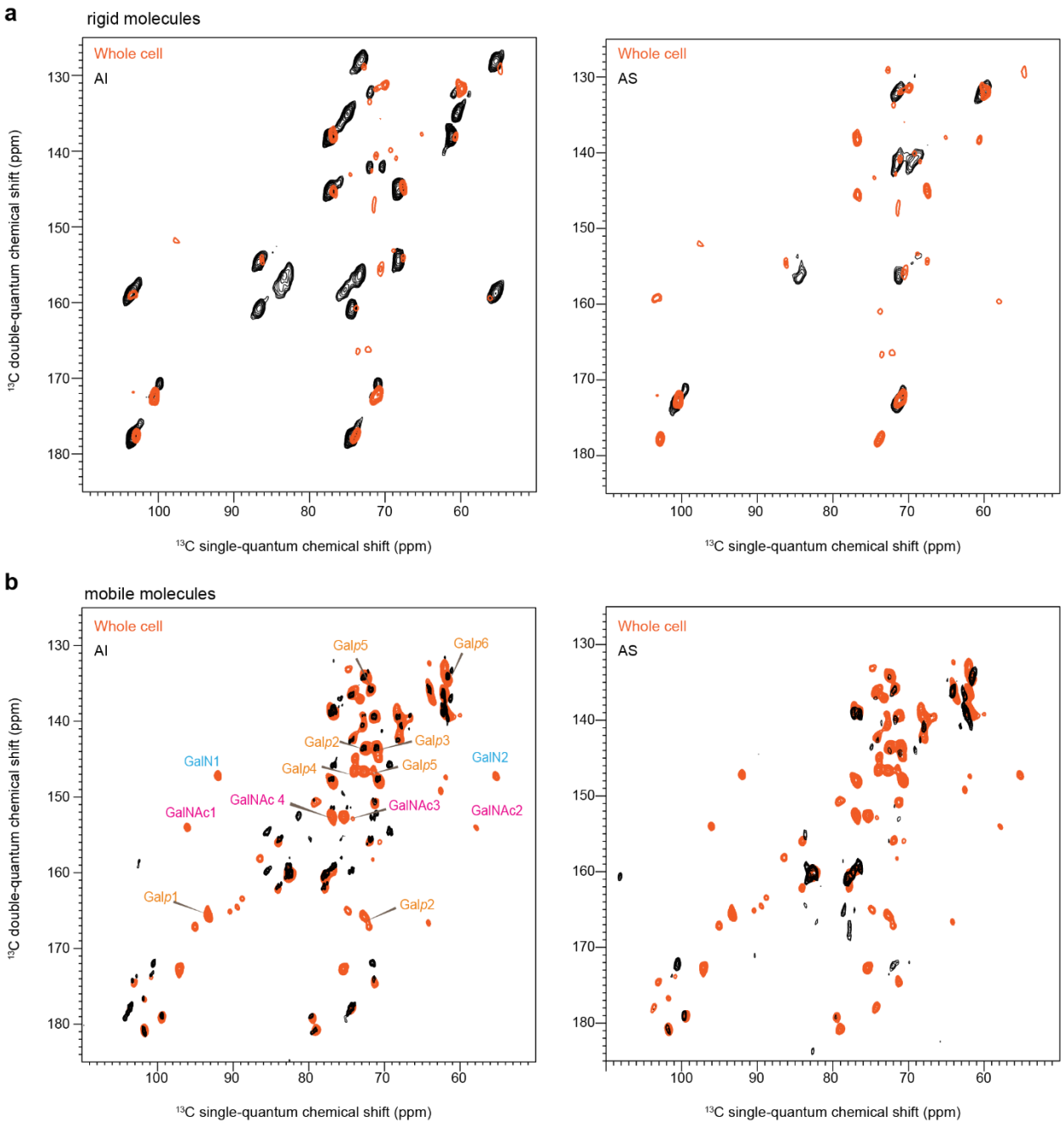


**Figure 3.14 Overlay of 2D $^{13}$C spectra of whole cells and alkali extracts. a,** $^{13}$C CP INADEQUATE spectra of wild-type intact cells and the alkali-insoluble (AI) and alkali-soluble (AS) samples, showing signals of rigid molecules These spectra preferentially detect rigid molecules. **b,** DP J-INADEQUATE spectra of the whole cell of the parental strain, as well as the AI and AS samples, detecting only the mobile molecules.

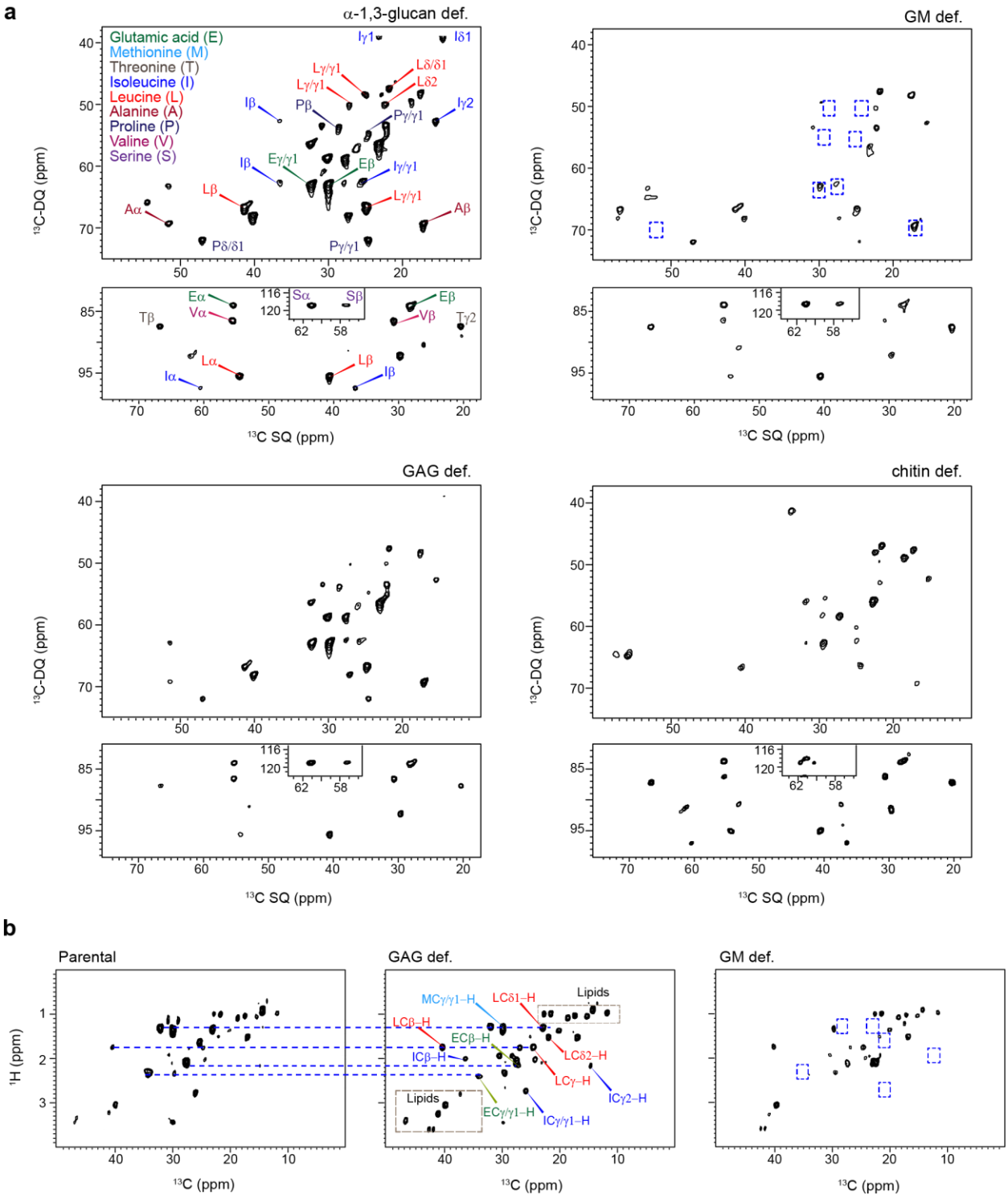


**Figure 3.15 Mobile proteins in *A. fumigatus*. a,** Protein regions of $^{13}$C DP J-INADEQUATE spectra that probe mobile molecules. GM-deficient sample is missing most amino acid signals (blue boxes). **b,** 2D $^{1}$H-$^{13}$C INEPT spectra reinforcing that the GM-deficient mutant lacks many protein signals.

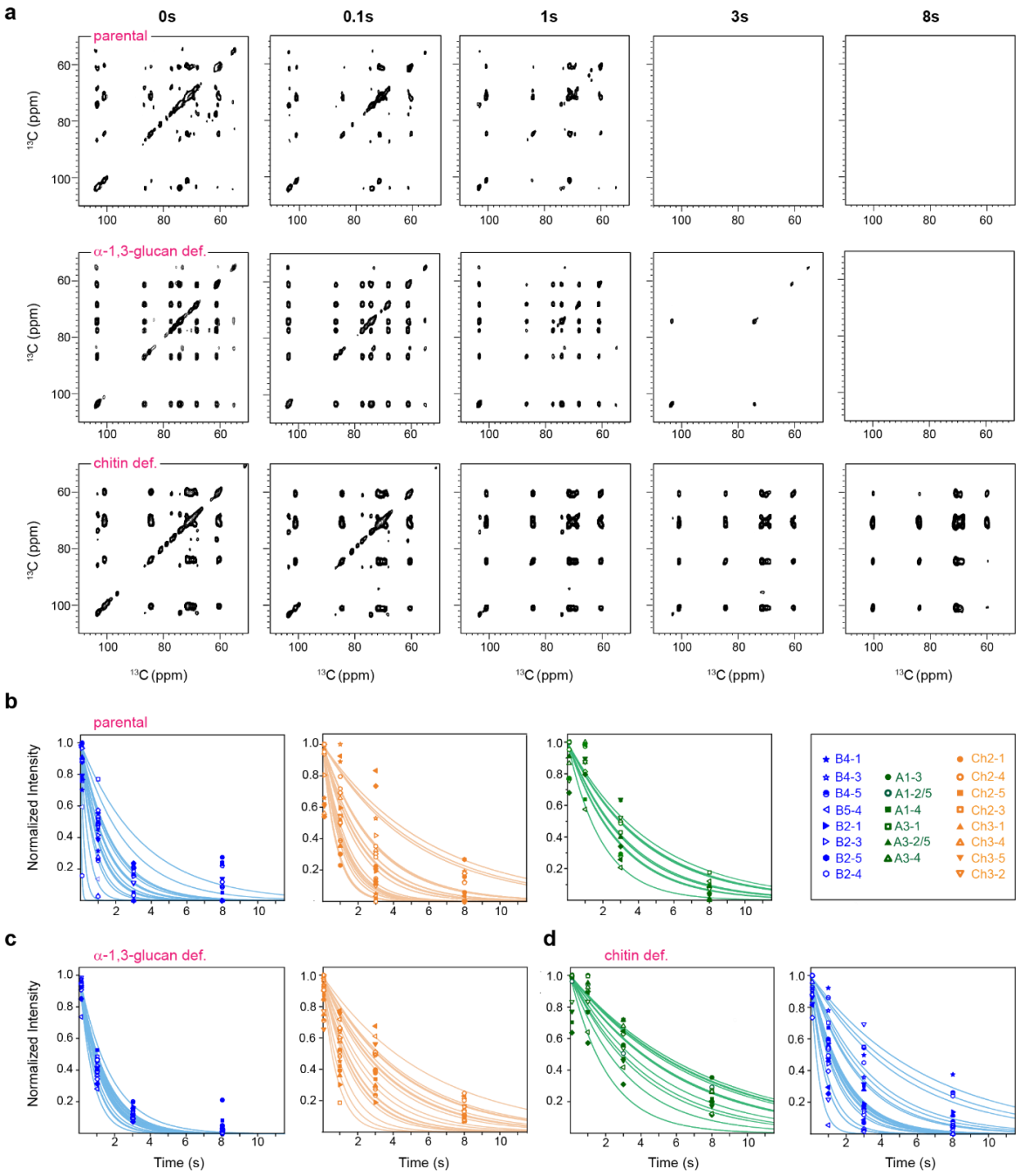


**Figure 3.16 $^{13}$C-$T_1$ relaxation measurements of *A. fumigatus*. a,** 2D $^{13}$C-$^{13}$C spectra with a variable z-filter collected on the parental strain (top), α-1,3-glucan-deficient, and chitin-deficient samples (bottom). Within each sample, 5 representative spectra are shown with different z-filter times of 0s, 0.1s, 1 s, 3s, and 8s. $^{13}$C-$T_1$ relaxation curves of polysaccharides of **b,** parental strain, **c,** a-1,3-glucan deficient strain and **d,** chitin-deficient sample were obtained by plotting the normalized intensities as a function of time. Data were collected on a 400 MHz spectrometer and best-fits were obtained using a single exponential equation. Source data are provided as a Source Data file.

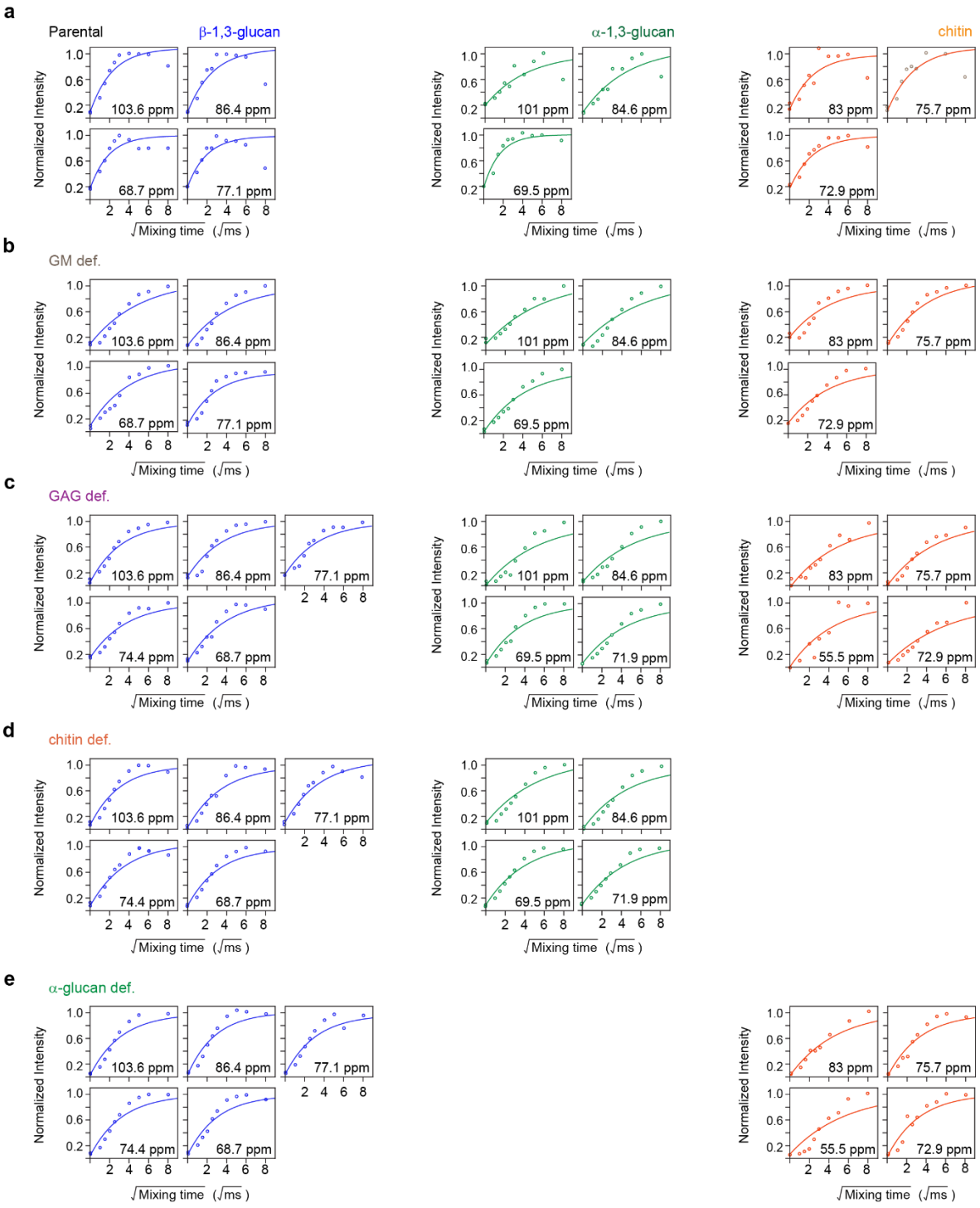


**Figure 3.17 Water-to-polysaccharide buildup curves.** The data are plotted separately for **a,** wild-type sample, **b,** GM-deficient mutant, **c,** GAG-deficient strain, **d,** chitin-deficient sample, and **e,** α-1,3-glucan deficient mutant. Source data are provided as a Source Data file.

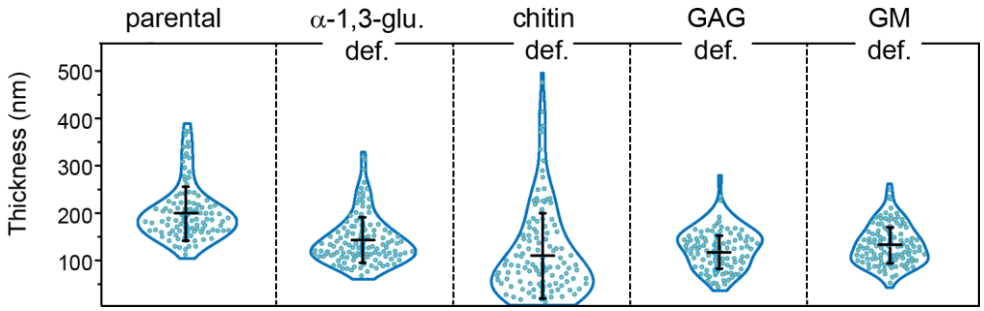


**Figure 3.18 Distribution of cell wall thickness.** Violin plots showing the distribution of cell wall thickness measured using TEM of parental, chitin-deficient, α-1,3-glucan-deficient, GM-deficient, and GAG-deficient cell walls (n=143). Source data are provided as a Source Data file.

**Table 3.1 Parameters of ssNMR experiments measured on each *A. fumigatus* strain.** All the experiments were conducted on each of the five fungal strains, mostly on an 800 MHz NMR spectrometer. In addition, the alkaline soluble and insoluble samples were measured on a 400 MHz spectrometer. The key experimental parameters listed here include recycle delay (d1), number of scans (NS), number of points for the direct (td2) and indirect (td1) dimensions, the acquisition time of the direct dimension (aq2) and the evolution time of indirect dimension (aq1), $^{13}C$-$^{13}C$ or $^{1}H$-$^{1}H$ mixing time ($t_m$), z-filter time ($t_z$), and $^{1}H$ Larmor frequency.

| | Experiment | d1 (s) | NS | td2 | td1 | aq2 (ms) | aq1 (ms) | $t_m$ (ms) | $t_z$(s) | $\upsilon_0$, $^{1}H$ (MHz) |
|---|---|---|---|---|---|---|---|---|---|---|
| 1D | CP | 2 | 128 | 2400 | 1 | 16.8 | | | | 800 |
| | DP | 2<br>30 | 128<br>64 | 4096<br>4096 | 1<br>1 | 28.7<br>28.7 | | | | |
| | Water-edited | 1.8 | 2048 | 1400 | 1 | 14.0 | | 0, 1, 2.25, 4, 6.25, 9, 16, 25, 36, 64 | | 400 |
| 2D | CORD | 2<br>2 | 32<br>128 | 2400<br>1600 | 200<br>280 | 16.8<br>16.0 | 5.6<br>7.0 | 53<br>53 | | 800<br>400 |
| | N(CA)CX | 1.7 | 256 | 2200 | 84 | 16.4 | 4.4 | 100 | | 800 |
| | DP-J-INDQUATE | 2 | 8 | 2600 | 1024 | 19.4 | 10.2 | | | |
| | CP-SPC-5-INDQUATE | 2 | 16 | 2400 | 200 | 17.9 | 7.0 | | | |
| | Pseudo 3D $^{13}C$-$T_1$ | 1.6 | 64 | 1600 | 98 | 16 | 5.39 | | 0, 0.1, 1, 3, 8 | 400 |
| | INEPT | 3 | 8 | 2048 | 160 | 20.5 | 11.0 | | | |

**Table 3.2 $^{13}$C and $^{13}$N chemical shifts of polysaccharides and proteins in *A. fumigatus* cell walls.** Superscripts are used to denote different allomorphs. Underline denotes the $^{13}$C connectivity with ambiguity. Weak signals or minor species are indicated using "w." Not applicable ( /). Unidentified (-). Unk: unknown.

| Biomolecule | C1 | C2 | C3 | C4 | C5 | C6 | CO | $CH_3$ | N | Experiment | Cell wall portion | References |
|---|---|---|---|---|---|---|---|---|---|---|---|---|
| B | 103.6 | 74.4 | 86.4 | 68.7 | 77.1 | 61.3 | / | / | / | $^{13}$C -$^{13}$C PDSD, $^{13}$C CP J-INADEQUATE | Rigid | Shim et al. 2007[82] Fairweather et al. 2004[83] Hazime Saitô et al. 1979[84] |
| B | 103.3 | 74.2 | 88.3 | 70.1 | 77.0 | 61.2 | / | / | / | $^{13}$C DP J-INADEQUATE | Mobile | Shim et al. 2007[82] Fairweather et al. 2004[83] Hazime Saitô et al. 1979[84] |
| A | 101.0 | 71.9 | 84.6 | 69.5 | 71.7 | 60.5 | / | / | / | $^{13}$C -$^{13}$C PDSD, $^{13}$C CP J-INADEQUATE | Rigid | Bhanja et al. 2014[85] Puanglek et al. 2016[86] |
| Ch | 103.6 | 55.5 | 72.9 | 83.0 | 75.7 | 60.9 | 174.8 | 22.6 | 123.6 | $^{13}$C -$^{13}$C PDSD, $^{13}$C CP J-INADEQUATE, $^{15}$N -$^{13}$C N(CA)CX-DARR | Rigid | Kono et al. 2004[87] Heux et al. 2000[88] Kameda et al. 2004[89] King et al. 2017[90] Tanner 1990[91] |
| Mn[1,2] | 101.3 | 78.7 | 71.2 | 67.7 | 73.9 | 61.7 | | / | | $^{13}$C DP J-INADEQUATE | Mobile | Latge et al.1994[55] |

Table 3.2 (cont'd)

| | | | | | | | | | | | | |
|---|---|---|---|---|---|---|---|---|---|---|---|---|
| Mn[1,6] | 102.7 | 70.6 | 73.2 | 67.9 | 73.7 | 66.1 | | / | | $^{13}$C DP J-INADEQUATE | Mobile | |
| Galf | 107.5 | 81.6 | 77.7 | 83.5 | 71.5 | 63.5 | | / | | $^{13}$C DP J-INADEQUATE | Mobile | |
| Galp | 93.2 | 72.2 | 70.7 | 73.5 | 72.5 | 60.9 | | / | | $^{13}$C DP J-INADEQUATE | Mobile | Fontaine et al. 2011[39] |
| GalN | 91.7 | 54.8 | 71.1 | 81.1 | / | / | | / | / | $^{13}$C DP J-INADEQUATE | Mobile | |
| GalN'/ GalNAc' | 102.5 | 55.8 | 71.1 | 83.6 | / | / | | / | / | $^{13}$C DP J-INADEQUATE | Mobile | |
| GalNAc | 95.7 | 57.5 | 75.2 | 76.9 | / | / | 175.2 | 22.7 | / | $^{13}$C DP J-INADEQUATE | Mobile | |
| Leucine | 54.9 | 40.6 | 24.4 | 22.7 | | | 175.5 | 21.6 | - | $^{13}$C DP J-INADEQUATE | Mobile | Fritzsching et al. 2013[92] |
| Leucine | 55.1 | / | / | 22.7 | | | 175.6 | 21.7 | | $^{13}$C -$^{13}$C CORD | Rigid | |
| Isoleucine | 60.7 | 36.4 | 25.2 | 11.9 | | | 175.2 | 15.8 | - | $^{13}$C DP J-INADEQUATE | Mobile | |
| Alanine | 52.1 | 16.7 | | | | | 176.5 | | | $^{13}$C DP J-INADEQUATE | Mobile | |
| Serine | 57.3 | 60.9 | | | | | 174.4 | | | $^{13}$C DP J-INADEQUATE | Mobile | |
| Serine | 59.2 | 62.7 | | | | | 174.8 | | | $^{13}$C -$^{13}$C CORD | Rigid | |
| Glutamic acid | 55.5 | 27.7 | 34.4 | / | / | / | 175.8 | / | - | $^{13}$C DP J-INADEQUATE | Mobile | |
| Methionine | 53.7 | 29.4 | 29.8 | / | / | / | 176.4 | 14.2 | - | $^{13}$C DP J-INADEQUATE | Mobile | |
| Threonine | 61.1 | 66.6 | 19.9 | / | / | / | 175.3 | / | - | $^{13}$C DP J-INADEQUATE | Mobile | Fritzsching et al. 2013[92] |
| Proline | 61.3 | 27.1 | 24.2 | 46.8 | / | / | 174.7 | / | - | $^{13}$C DP J-INADEQUATE | Mobile | |

Table 3.2 (cont'd)

| | | | | | | | | | | | | |
|---|---|---|---|---|---|---|---|---|---|---|---|---|
| Argenine | 55.2 | 27.9 | 24.7 | 25.9 | 40.9 | / | 175.8 | | | $^{13}$C DP J-INADEQUATE | Mobile | Fritzsching et al. 2013[92] |
| Tyrosine | 53.9 | 34.3 | 129.3 | / | / | 115.7 | 172.9 | | 128.7 | $^{13}$C DP J-INADEQUATE | Mobile | |
| Tyrosine | 55.7 | 36.4 | / | / | / | / | 173.2 | | 129.6 | $^{13}$C -$^{13}$C CORD | Rigid | |
| Valine | 60.8 | 29.5 | 17.3 | 19.5 | / | / | 173.8 | 18.6 | 128.7 | $^{13}$C DP J-INADEQUATE | Mobile | Fritzsching et al. 2013[92] |
| Valine | 60.8 | 28.6 | 18.9 | 19.5 | | | 174 | / | 129 | $^{13}$C -$^{13}$C CORD | Rigid | |

**Table 3.3 Compositional change of rigid polysaccharides in different samples.** UD: undetected. Error bars are standard errors of cross peak intensities.

| Wild type | | | |
|---|---|---|---|
| | β-1,3-glucan | Chitin | α-1,3-glucan |
| Percentage (mol%) | 50±6 | 8±3 | 42±7 |
| α−1,3-glucan def. | | | |
| | β-1,3-glucan | Chitin | α-1,3-glucan |
| Percentage (mol%) | 95±9 | 5.3±0.6 | UD |
| Chitin def. | | | |
| | β-1,3-glucan | Chitin | α-1,3-glucan |
| Percentage (mol%) | 42±4 | UD | 58±5 |
| GM def. | | | |
| | β-1,3-glucan | Chitin | α-1,3-glucan |
| Percentage (mol%) | 25±2 | 43±6 | 32±3 |
| GAG def. | | | |
| | β-1,3-glucan | Chitin | α-1,3-glucan |
| Percentage (mol%) | 58±5 | 5.9±0.8 | 36±5 |

The areas of the following resolved cross peaks of 53ms CORD spectra are used for the calculation:
β-1,3-glucan: the average of C1- C3/C4/C5, C3-C2/C4/C5, C2-C4, C5-C4
α-1,3-glucan: the average of C1-C4/C2/C5, C3-C2/C4/C5
Chitin: the average of C1-C2/ C3/ C4/ C5, C4- C2/C3/C5, C5-C3, C3-C2, C5-C2

**Table 3.4 Compositional changes in the mobile polysaccharides of *A. fumigatus*.** UD: undetected. Error bars are standard errors of cross peak intensities.

| Parental | | | | | | | | |
|---|---|---|---|---|---|---|---|---|
| | GM | | | GAG | | | β-1,3-glucan | α-1,3-glucan |
| Percentage (mol%) | Gal*f* | $Mn^{1,2}$ | $Mn^{1,6}$ | Gal*p* | GalN | GalNAc | 4±1 | 0.83±0.09 |
| | 20±2 | 24±1 | 5.1±0.3 | 27±2 | 13±3 | 6±1 | | |
| α–1,3-glucan def. | | | | | | | | |
| | GM | | | GAG | | | β-1,3-glucan | α-1,3-glucan |
| Percentage (mol%) | Gal*f* | $Mn^{1,2}$ | $Mn^{1,6}$ | Gal*p* | GalN | GalNAc | 42±8 | UD |
| | 27±2 | 5±1 | 4±1 | 14±1 | 4.5±0.8 | 3.0±0.5 | | |
| Chitin def. | | | | | | | | |
| | GM | | | GAG | | | β-1,3-glucan | α-1,3-glucan |
| Percentage (mol%) | Gal*f* | $Mn^{1,2}$ | $Mn^{1,6}$ | Gal*p* | GalN | GalNAc | 14±3 | 19±3 |
| | 20±3 | 9±1 | 7±1 | 28±4 | 1.3±0.4 | 2.0±0.4 | | |
| GM def. | | | | | | | | |
| | GM | | | GAG | | | β-1,3-glucan | α-1,3-glucan |
| Percentage (mol%) | Gal*f* | $Mn^{1,2}$ | $Mn^{1,6}$ | Gal*p* | GalN | GalNAc | 5.8±0.9 | 10±1 |
| | 7.8±0.9 | 0.62±0.05 | 0.97±0.07 | 33±3 | 22±4 | 19±3 | | |
| GAG def. | | | | | | | | |
| | GM | | | GAG | | | β-1,3-glucan | α-1,3-glucan |
| Percentage (mol%) | Gal*f* | $Mn^{1,2}$ | $Mn^{1,6}$ | Gal*p* | GalN | GalNAc | 42±4 | 10±1 |
| | 33±3 | 7.0±0.8 | 8±2 | UD | UD | UD | | |

The areas of the well-resolved peaks derived from 2D $^{13}C$-$^{13}C$ DP INADEQUATE spectra.
mannose ($Mn^{1,6}$): the average of C1,C2,C3,C4
mannose ($Mn^{1,2}$): the average of C1,C2,C3,C4
β-1,5-galactofuranose (Gal*f*): the average of C1,C2,C3,C4
galactopyranose (Gal*p*): the average of C1,C2,C3,C4
galactosamine (GalN): the average of C1,C2,C3,C4
N-acetylgalactosamine (GalNAc): the average of C1,C2,C3,C4
α-1,3-glucan: the average of C1,C2,C5 and C6
β-1,3-glucan: the average of C1,C2,C3,C4

**Table 3.5 NMR peaks used for compositional analysis.** Composition analysis were carried out using 2D 53-ms CORD and 2D J-INADEQUATE for rigid and mobile potions, respectively. Listed cross peaks (for CORD) or peak pairs (for INADEQUATE) were used for composition analysis.

| Rigid Phase | | | | Mobile Phase | | |
|---|---|---|---|---|---|---|
| Molecule | Cross peak | | | Molecule/unit | Spin connection | |
| | F1 | F2 | Assignment | | Chemical shifts | Assignment |
| α-1,3-glucan | 101.0 | 69.5 | C1-C4 | α-1,6-mannose | 102.7, 70.6 | C1,C2 |
| | 101.0 | 71.9 | C1-C2 | | 73.2, 67.9 | C3,C4 |
| | 101.0 | 71.7 | C1-C5 | α-1,2-mannose | 101.3, 78.7 | C1,C2 |
| | 84.6 | 71.9 | C3-C2 | | 67.7, 73.9 | C4,C5 |
| | 84.6 | 71.7 | C3-C5 | Galactofuranose | 107.5, 81.6 | C1,C2 |
| | 84.6 | 69.5 | C3-C4 | | 77.7, 83.5 | C3,C4 |
| β-1,3-glucan | 103.6 | 86.4 | C1-C3 | Galactopyranose | 72.2, 70.7 | C2,C3 |
| | 103.6 | 77.1 | C1-C5 | | 73.5, 72.5 | C4,C5 |
| | 103.6 | 68.7 | C1-C4 | Galactosamine | 91.7, 54.8 | C1,C2 |
| | 86.4 | 68.7 | C3-C4 | | 71.1, 81.1 | C3,C4 |
| | 86.4 | 77.1 | C3-C5 | N-acetylgalactosamine | 95.7, 57.5 | C1,C2 |
| | 86.4 | 74.4 | C3-C2 | | 75.2, 76.9 | C3,C4 |
| | 77.1 | 68.7 | C5-C4 | α-1,3-glucan | 101.0, 71.9 | C1,C2 |
| | 74.4 | 68.7 | C2-C4 | | 69.5, 71.7 | C4,C5 |
| Chitin | 103.6 | 83.0 | C1-C4 | β-1,3-glucan | 103.6, 74.4 | C1,C2 |
| | 103.6 | 75.7 | C1-C5 | | 68.7, 77.1 | C4,C5 |
| | 103.6 | 55.5 | C1-C2 | | | |
| | 103.6 | 72.9 | C1-C3 | | | |
| | 83.0 | 55.5 | C4-C2 | | | |
| | 83.0 | 72.9 | C4-C3 | | | |
| | 83.0 | 75.7 | C4-C5 | | | |
| | 75.7 | 72.9 | C5-C3 | | | |
| | 72.9 | 55.5 | C3-C2 | | | |
| | 75.7 | 55.5 | C5-C2 | | | |

**Table 3.6 Polysaccharide composition from ssNMR data.** The results are presented for the mobile and rigid phases of the alkali-soluble and alkali-insoluble fractions of parental *A. fumigatus*. UD: undetected. GAG is not detected using the AI and AS samples.

| Component | AI (mole%) | | AS (mole%) | |
|---|---|---|---|---|
| | Rigid | mobile | Rigid | mobile |
| β-1,3-glucan | 49 ± 9 | 41 ± 15 | UD | UD |
| α-1,3-glucan | 14 ± 3 | 16 ± 4 | 100 ± 30 | 14 ± 4 |
| chitin | 23 ± 4 | 13 ± 3 | UD | UD |
| GM | UD | 30 ± 10 | UD | 78 ± 26 |
| Amino acid (valine) | 14 ± 3 | UD | UD | 8 ± 2 |

**Table 3.7 Chemical analysis of *A. fumigatus* polysaccharides.** The alkali-soluble and alkali-insoluble fractions of the parental samples are analyzed using GC-MS methods coupled with Enzymatic degradation and HPLC purification. The samples prepared using the minimal medium were the ones characterized by NMR in this study.

| Component | Minimal medium | |
|---|---|---|
| | AI | AS |
| β-1,3 glucan | 47 | 13 |
| α-1,3 glucan | 11 | 55 |
| chitin | 22 | 1 |
| GM | 7 | 4 |
| GAG | 1 | 9 |

The chemical data of the sample prepared using minimal medium is in general agreement with the NMR results presented in Table 3.6.

**Table 3.8 $^{13}$C-$T_1$ relaxation times of major polysaccharides in wild-type *A. fumigatus*.** A single exponential equation is used to fit the data: $I(t)=e^{-t/T1}$. Error bars are standard deviations of the fit parameters.

| Component | Cross-peaks | $T_1$ (s) | | |
|---|---|---|---|---|
| | | Parental | α-1,3-glucan def. | Chitin def. |
| β-1,3-glucan | B1-3 | 1.8±0.6 | 1.4±0.4 | 1.7±0.4 |
| | B1-5 | 1.4±0.5 | 1.4±0.1 | 1.5±0.4 |
| | B1-2 | 1.2±0.2 | 1.8±0.2 | 2.7±0.5 |
| | B1-4 | 2.6±0.6 | 1.47±0.06 | 5.0±0.7 |
| | B3-1 | 0.5±0.1 | 1.18±0.08 | 1.8±0.4 |
| | B3-5 | 1.0±0.4 | 1.1±0.1 | 1.65±0.04 |
| | B3-2 | 1.1±0.2 | 1.22±0.07 | 1.9±0.4 |
| | B5-1 | 1.3±0.2 | 0.88±0.06 | 0.8±0.2 |
| | B5-3 | 4±2 | 1.00±0.07 | 1.0±0.2 |
| | B5.2 | 1.2±0.2 | 0.9±0.1 | 0.8±0.1 |
| | B5-4 | 0.2±0.1 | 0.7±0.2 | 0.46±0.07 |
| | B2-1 | 1.4±0.3 | 1.5±0.1 | 1.9±0.7 |
| | B2-3 | 1.4±0.2 | 1.23±0.04 | 1.4±0.4 |
| | B2-5 | 1.1±0.3 | 1.14±0.09 | 1.6±0.3 |
| | B2-4 | 0.05±0.02 | 1.37±0.09 | 3.4±0.9 |
| | B4-1 | 0.7±0.2 | 1.3±0.2 | 5.5±0.4 |
| | B4-3 | 1.6±0.2 | 1.2±0.1 | 1.4±0.4 |
| | B4-5 | 0.8±0.3 | 1.15±0.07 | 1.6±0.3 |
| | B4-2 | 1.7±0.2 | 1.4±0.2 | 3.4±0.9 |
| | Average | 1.3 | 1.2 | 2.1 |
| α-1,3-glucan | A1-2/5 | 4.2±0.9 | - | 5.2±0.7 |
| | A2/5-1 | 2.9±0.6 | - | 3.9±0.9 |
| | A2/5-4 | 1.9±0.7 | - | 5.1±0.2 |
| | A3-1 | 4.3±0.8 | - | 4.0±0.9 |
| | A3-2/5 | 3.4±0.6 | - | 2.6±0.6 |
| | A4-2/5 | 2.9±0.9 | - | 3.9±0.8 |
| | Average | 3.3 | - | 4.1 |
| Chitin | Ch1-4 | 5±1 | 3.5±0.9 | - |
| | Ch1-5 | 2.2±0.4 | 1.8±0.5 | - |
| | Ch1-3 | 1.2±0.2 | 0.8±0.4 | - |
| | Ch3-5 | 1.4±0.6 | 4±1 | - |
| | Ch3-1 | 1.9±0.1 | 5±2 | - |
| | Ch5-4 | 2.9±0.8 | 3.6±0.7 | - |
| | Ch5-3 | 0.8±0.4 | 2.4±0.5 | - |
| | Ch5-2 | 2.9±0.2 | 3.3±0.8 | - |
| | Ch4-5 | 2.8±0.4 | 4.4±0.8 | - |
| | Ch2-1 | 1.1±0.4 | 5.9±0.8 | - |

Table 3.8 (cont'd)

| | | | | |
|---|---|---|---|---|
| Chitin | Ch2-4 | 2.9±0.4 | 4.6±0.6 | - |
| | Ch2-5 | 1.2±0.4 | 3.2±0.8 | - |
| | Ch2-3 | 1.3±0.3 | 2.7±0.7 | - |
| | Average | 2.1 | 3.5 | - |

**Table 3.9 Water-edited buildup curves of major polysaccharides.** The data are fit using exponential growth equation: $I(t) = 1\text{-}Ae^{-t/T}$, where the prefactor accounts for the initial residual intensity. Error bars are standard deviations of the fit parameters.

| Sample type | Assignment | ppm ($^{13}C$) | Prefactor | $\sqrt{Buildup\ time}$ ($\sqrt{ms}$) |
|---|---|---|---|---|
| Parental | A1 | 101.0 | 0.78 | 3.8 ± 0.9 |
| | A3 | 84.6 | 0.92 | 3.5 ± 0.6 |
| | A4 | 69.5 | 0.80 | 1.4 ± 0.2 |
| | A2/5 | 71.9 | 0.71 | 1.6 ± 0.2 |
| | B1 | 103.6 | 0.88 | 1.6 ± 0.3 |
| | B2 | 74.4 | 0.83 | 1.6 ± 0.3 |
| | B3 | 86.4 | 0.91 | 1.7 ± 0.5 |
| | B4 | 68.7 | 0.81 | 1.7 ± 0.4 |
| | B5 | 77.1 | 0.80 | 1.8 ± 0.6 |
| | Ch2 | 55.5 | 0.84 | 3.9 ± 0.4 |
| | Ch3 | 72.9 | 0.79 | 2.1 ± 0.3 |
| | Ch4 | 83.0 | 0.86 | 2.2 ± 0.6 |
| | Ch5 | 75.7 | 0.88 | 1.9 ± 0.4 |
| GM def. | A1 | 101.0 | 0.88 | 4.6 ± 0.5 |
| | A3 | 84.6 | 0.91 | 4.8 ± 0.8 |
| | A4 | 69.5 | 0.93 | 3.8 ± 0.4 |
| | A2/5 | 71.9 | 0.85 | 3.9 ± 0.5 |
| | B1 | 103.6 | 0.87 | 4.0 ± 0.5 |
| | B2 | 74.4 | 0.88 | 3.2 ± 0.4 |
| | B3 | 86.4 | 0.92 | 4.0 ± 0.5 |
| | B4 | 68.7 | 0.93 | 3.5 ± 0.4 |
| | B5 | 77.1 | 0.83 | 2.5 ± 0.3 |
| | Ch2 | 55.5 | 0.80 | 5.4 ± 0.9 |
| | Ch3 | 72.9 | 0.87 | 3.9 ± 0.5 |
| | Ch4 | 83.0 | 0.75 | 3.8 ± 0.6 |
| | Ch5 | 75.7 | 0.90 | 3.1 ± 0.3 |
| GAG def. | A1 | 101.0 | 0.92 | 4.8 ± 0.8 |
| | A3 | 84.6 | 0.92 | 4.6 ± 0.7 |
| | A4 | 69.5 | 0.89 | 3.3 ± 0.4 |
| | A2/5 | 71.9 | 0.89 | 4.1 ± 0.5 |
| | B1 | 103.6 | 0.94 | 2.8 ± 0.3 |
| | B2 | 74.4 | 0.83 | 3.4 ± 0.4 |
| | B3 | 86.4 | 0.83 | 3.2 ± 0.5 |
| | B4 | 68.7 | 0.85 | 3.0 ± 0.4 |
| | B5 | 77.1 | 0.83 | 3.1 ± 0.3 |
| | Ch2 | 55.5 | 0.90 | 4.0 ± 0.8 |

Table 3.9 (cont'd)

| | | | | |
|---|---|---|---|---|
| | Ch3 | 72.9 | 0.93 | 5.5 ± 0.6 |
| GAG def. | Ch4 | 83.0 | 0.98 | 4.5 ± 0.5 |
| | Ch5 | 75.7 | 0.85 | 3.9 ± 0.4 |
| Chitin def. | A1 | 101.0 | 0.91 | 4.1 ± 0.6 |
| | A3 | 84.6 | 0.94 | 4.1 ± 0.5 |
| | A4 | 69.5 | 0.91 | 3.1± 0.3 |
| | A2/5 | 71.9 | 0.88 | 3.5 ± 0.4 |
| | B1 | 103.6 | 0.88 | 2.7 ± 0.3 |
| | B2 | 74.4 | 0.86 | 2.6 ± 0.3 |
| | B3 | 86.4 | 0.93 | 3.1 ± 0.4 |
| | B4 | 68.7 | 0.92 | 2.8 ± 0.3 |
| | B5 | 77.1 | 0.86 | 2.5 ± 0.3 |
| α-1,3- glucan def. | B1 | 103.6 | 0.93 | 2.8 ± 0.3 |
| | B2 | 74.4 | 0.91 | 2.9 ± 0.3 |
| | B3 | 86.4 | 0.96 | 2.6 ± 0.3 |
| | B4 | 68.7 | 0.90 | 2.7 ± 0.3 |
| | B5 | 77.1 | 0.90 | 2.8 ± 0.3 |
| | Ch2 | 55.5 | 0.96 | 5.1 ± 0.9 |
| | Ch3 | 72.9 | 0.95 | 3.0 ± 0.4 |
| | Ch4 | 83.0 | 0.98 | 4.3 ± 0.4 |
| | Ch5 | 75.7 | 0.93 | 3.0 ± 0.4 |

# CHAPTER 4: STRUCTURAL POLYMORPHISM OF CHITIN AND CHITOSAN IN FUNGAL CELL WALLS FROM SOLID-STATE NMR AND PRINCIPAL COMPONENT ANALYSIS

Reprinted with permission from Liyanage D. Fernando, Malitha C. Dickwella Widanage, Jackson Penfield, Andrew S. Lipton, Nancy Washton, Jean-Paul Latgé, Ping Wang, Liqun Zhang, and Tuo Wang, *Frontiers in Molecular Biosciences*, 8,727053 (2021). 

## 4.1 Abstract

Chitin is a major carbohydrate component of the fungal cell wall and a promising target for novel antifungal agents. However, it is technically challenging to characterize the structure of this polymer in native cell walls. Here, we recorded and compared $^{13}C$ chemical shifts of chitin using isotopically enriched cells of six *Aspergillus*, *Rhizopus*, and *Candida* strains, with data interpretation assisted by principal component analysis (PCA) and linear discriminant analysis (LDA) methods. The structure of chitin is found to be intrinsically heterogeneous, with peak multiplicity detected in each sample and distinct fingerprints observed across fungal species. Fungal chitin exhibits partial similarity to the model structures of α- and γ-allomorphs; therefore, chitin structure is not significantly affected by interactions with other cell wall components. Addition of antifungal drugs and salts did not significantly perturb the chemical shifts, revealing the structural resistance of chitin to external stress. In addition, the structure of the deacetylated form, chitosan, was found to resemble a relaxed two-fold helix conformation. This study provides high-resolution information on the structure of chitin and chitosan in their cellular contexts. The method is applicable to the analysis of other complex carbohydrates and polymer composites.

## 4.2 Introduction

Chitin is the second-most abundant biopolymer in nature, only behind cellulose. Widely distributed in different organisms, chitin is often found as a supportive and protective component of the body armor (namely the exoskeleton) in arthropods and the cell walls of fungi and some algal species [1,2]. The structures of chitin and its largely deacetylated form called chitosan have similarity to the organization of cellulose [1,3-6]. All these three polysaccharides are linear polymers of β-1,4-linked glucoses or their amide derivatives. Structurally, the hydroxyl group at position C-2 of a glucopyranose unit is replaced by an acetamido or an amino group, changing to the N-acetylglucosamine (GlcNAc) unit in chitin and the glucosamine (GlcN) residue in chitosan (Figure 4.1a). Chitin and chitosan, especially the latter, have also drawn tremendous attention due to their promising applications as polymer scaffolds for tissue engineering, wound dressing, drug delivery, and pharmaceuticals [7].

The amide and carbonyl groups in chitins drive the formation of hydrogen bonds and crystalline fibrils. X-ray crystallography has reported three chitin allomorphs, with substantial variation in the chain orientation and the hydrogen-bonding pattern [8,9]. Adjacent chains are packed in an antiparallel or parallel way in the α- and β-forms, respectively (Figure 4.1b). The third type of structure, γ-chitin, can be considered as a mixture of parallel and antiparallel packings, but sometimes it is treated simply as a variant of the α-allomorph [1]. The structure of α-chitin is stabilized simultaneously by intra-chain O-H…O and inter-chain N-H…O hydrogen bonding (Figure 4.1c) [10,11]. The former is a hydrogen bond consistently observed in all three allomorphs. The latter is relatively rare in the γ-form and is absent in the β-chitin [12-14]. The coexistence of inter- and intra-chain hydrogen bonds has made α-chitin the most stable, ordered, and tightly packed structure, widely found in arthropods, Porifera, Bryozoa, and fungi [15,16]. β- and γ-allomorphs are

less common: the former can be found in diatoms and cephalopods, while the latter was reported in beetles and loligo species [17,18]. The currently available information on chitin structure was obtained using highly crystalline materials isolated and purified mainly from marine sources. Although chitin is also a major fungal polysaccharide [19,20], our understanding of its structural characteristics in the fungal cell wall remains inadequate.

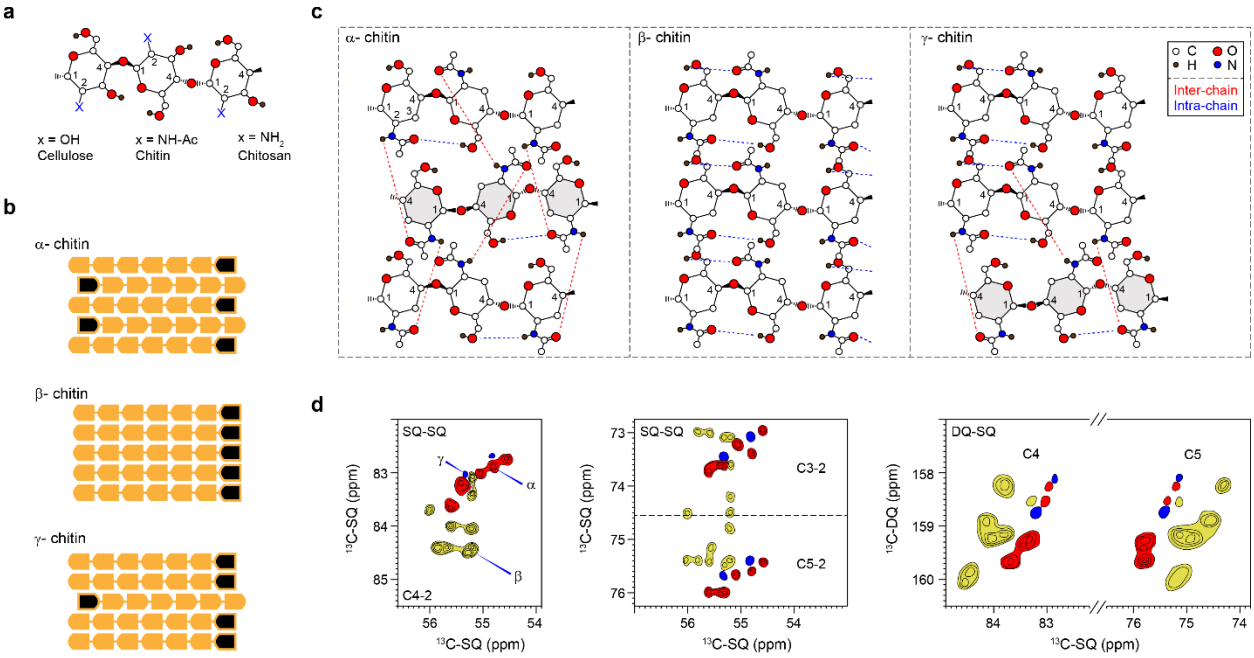


**Figure 4.1 Representative structures and NMR signals of chitin. a,** Substitutions at the C2 position for chitin and chitosan. **b,** Polymorphic types (α, β, and γ) of chitin showing different chain orientations. Black marks denote the non-reducing ends of chains. **c,** Hydrogen-bonding patterns of different chitin allomorphs. Blue and red dash lines indicate intra-chain and inter-chain hydrogen bonds, respectively. The antiparallel chains in α and γ chitins are in grey. The hydroxyl at C3 is not shown to make the structure less complex. The structural schemes are adapted from [11,13,21]. **d,** 2D $^{13}$C-$^{13}$C correlation spectra simulated using literature-reported chemical shifts on model samples (Table 4.2). Representative C4-2 and C3/5-2 regions were shown for single-quantum [22]-SQ correlation spectra. The C4 and C5 region is also shown for a double-quantum (DQ)-SQ correlation spectrum. α, β, and γ are represented in red, yellow, and blue respectively. Contour lines represent the number of data sets used (and the number of overlapped peaks).

Biochemical assays have revealed that chitin, β-glucan, and mannan are held together by covalent linkages in the human pathogen *Aspergillus fumigatus*, forming the core of the cell wall

[23,24]. This structural module is resistant to alkali treatment and therefore has been proposed as the central scaffold of fungal cell walls [25]. Recently, we have employed high-resolution solid-state NMR methods to investigate the structure of biomolecules in the intact cells of *A. fumigatus* [26,27]. Unexpectedly, we identified three major types (and in total eleven subtypes) of GlcNAc units, as resolved from their distinct $^{13}C$ and $^{15}N$ chemical shifts, which are indicators of structural variations [26]. These chitin forms were found to be extensively associated with each other inside chitin microfibrils as shown by their strong inter-residue interactions. These findings have unveiled the surprisingly high structural polymorphism of chitin in its cellular environment and raised three unresolved questions related to the chitin structure. First, is the structure of chitin in the fungal cell wall similar to the crystallographic structures determined using standard samples? Second, is there any dependence between the chitin structure and the fungal type? Third, is chitin structure modulated by external stresses such as antifungal drugs and hypersaline environments?

To answer these questions, we compared the $^{13}C$ chemical shifts of chitins identified in the cells prepared from three *Aspergillus* species (*Aspergillus fumigatus, A. nidulans,* and *A. sydowii*), *Rhizopus delemar*, and two *Candida* pathogens (*C. albicans* and *C. auris*), following exposure to various antifungal drugs and salt concentrations. All these fungal species investigated here are significant human pathogens causing life-threatening infections in immunodeficient individuals and known to display different chitin composition in their cell walls [28,29]. Root mean square deviation (RMSD) heatmap, principal component analysis (PCA), and linear discriminant analysis (LDA) of chemical shifts were performed for the comparison of 62 chitin forms. Most fungal chitins align well with literature-reported α- and γ- allomorphs but deviate substantially from the β-form. The structure of chitin proved robust, remaining unaffected even under high salinity or in the presence of antifungal drugs, caspofungin and amphotericin B (AmB). In addition, chitosan

was also identified in *R. delemar* and *A. sydowii*. Comparison of the literature-reported and our observed chemical shifts showed that most chitosan molecules are closely related to the Type-II salt model compound that has a relaxed two-fold conformational structure. This study presents a widely applicable research strategy for evaluating the structure of cellular carbohydrates and provides the structural basis for developing chitin-targeting antifungal agents.

## 4.3 Materials and methods

### 4.3.1 Preparation of $^{13}C$, $^{15}N$-Labeled Fungal Cells

In total, nine $^{13}C$,$^{15}N$-labeled samples were prepared for six fungal species including *A. fumigatus*, *A. nidulans*, *A. sydowii*, *C. albicans*, *C. auris*, and *R. delemar* following a recently established protocol [30]. To examine the potential effect of antifungal drugs on chitin structure, three parallel batches were prepared for *A. fumigatus:* without drug, with caspofungin (2.5 μg/mL: above the minimum inhibitory concentration), and with AmB (2.5 μg/mL). To examine if salt concentration and osmotic pressure affect chitin structure, two batches of materials were prepared for the seawater inhabitant *A. sydowii*, with 0.5 M and 2.0 M NaCl to represent optimal and high salinity conditions, respectively [31]. Briefly, uniformly $^{13}C$,$^{15}N$-labeled materials were obtained by culturing the fungi in modified minimum liquid media containing $^{13}C$-glucose as the sole carbon source. The nitrogen sources are different for various fungal species, with $^{15}N$-sodium nitrate for *A. fumigatus* and *A. nidulans*, $^{15}N$-ammonium nitrate for *A. sydowii*, and $^{15}N$-ammonium sulfate for *C. albicans*, *C. auris*, and *R. delemar*. All these species are able to grow on inorganic nitrogen source and were cultivated alternatively on ammonium or nitrate salts. The cultures were incubated at the optimum temperatures of 25-31 °C for respective fungal species. The culture duration was 3 days for *A. fumigatus*, *A. nidulans*, *R. delemar*, *C. albicans*, and *C. auris*, and 7 days for *A. sydowii*. Fungal materials were then collected by centrifugation at 7000 × g for 20 min. The

harvested fungal pellets were washed thoroughly using phosphate buffer (pH 7.4) to remove small molecules and reduce the ion concentration. For each sample, approximately 30 mg of the hydrated whole-cell material was packed into a 3.2 mm magic-angle spinning (MAS) rotor for solid-state NMR characterization.

### 4.3.2 Solid-State NMR Experiments

All the high-resolution solid-state NMR data were collected on a Bruker 800 MHz (18.8 Tesla) Bruker Avance III HD spectrometer at the National High Magnetic Field Laboratory (Tallahassee, FL) and a Varian VNMRS 850 MHz (19.9 Tesla) spectrometer at the Environmental Molecular Sciences Laboratory (EMSL; Richland, WA). The experiments were conducted in 3.2 mm MAS HCN probes under 12-13.5 kHz MAS at 290-293 K. The $^{13}C$ chemical shifts were externally referenced to the adamantane $CH_2$ signal at 38.48 ppm on the tetramethylsilane scale. The $^{15}N$ chemical shifts were referred externally through the methionine nitrogen peak (127.88 ppm) in the model peptide formyl-Met-Leu-Phe (MLF). Typical $^{1}H$ radiofrequency field strengths 50-83 kHz and 50-62.5 kHz for $^{13}C$. The $^{13}C$ chemical shifts were recorded using the 2D Dipolar-Assisted Rotational Resonance (DARR) experiment with a 100-ms mixing time and the 2D $^{13}C$-$^{13}C$ COmbined $R2_n^v$ -Driven (CORD) sequence with a 53-ms mixing time [32]. 2D $^{15}N$-$^{13}C$ N(CA)CX heteronuclear correlation spectra were measured to detect chitin amide signals [33]. The N(CA)CX spectrum was recorded using a 0.6-ms $^{1}H$-$^{15}N$ cross polarization [34], a 5-ms $^{15}N$-$^{13}C$ CP contact, and a 100-ms DARR mixing time. The experimental and processing parameters used for 2D $^{13}C$-$^{13}C$ and $^{13}C$-$^{15}N$ spectra are summarized in Table 4.1. Resonance assignment was facilitated by comparison with previously reported chemical shifts indexed in a carbohydrate database [35], which distinguish chitin from glucans and other nitrogenated polysaccharides. To compare the chemical shift differences in different chitin forms observed in fungi and from

different model samples, a heat map was constructed from the root-mean-square deviation (RMSD) values calculated using the comparison of the literature-reported and observed chemical shifts with normalization by the total number of carbon atoms in a monomer (*i.e.* 8 for chitin carbons of C1-C6, CO, and $CH_3$). Similar approaches are also used for comparing different forms of fungal chitin. Good correlations give low RMSD values.

### 4.3.3 Principal Component Analysis and Linear Discriminant Analysis

We conducted PCA to facilitate the analysis of the species- and condition-dependent data of chitin chemical shifts. PCA is a form of multivariate analysis employed to reduce the many correlated variables to just a few new variables (the principal components) that describe most of the variation in a dataset. Recently, PCA has been successfully employed to provide valuable insights on chemical shift data for small molecules and proteins [36] and proteins [37,38]. The PCA was first conducted using MATLAB for the entire dataset from both the available literature and freshly measured spectra (Tables 4.2 and 4.3). A 62 × 8 matrix was composed, with each row representing a different chitin form identified in the NMR spectra, and each column corresponding to the chemical shifts observed for a $^{13}C$ atom at a particular location in the chitin structure. Similarly, PCA was also run separately for three subsets of chitin chemical shift data to compare 1) only the data from fungal chitin, 2) drug-free and drug-treated samples, and 3) optimal and high salinity conditions. For each PCA, a singular value decomposition (SVD) analysis was performed on the data matrix to generate orthogonal eigenvectors with values known as “loadings” or “PCA coefficients” arranged in a matrix by column. Loadings are normalized and used to describe the contribution made by each chemical shift, while the magnitude of the eigenvector shows how much of the variance in the data is explained by each eigenvector. The largest eigenvector defines the axis principal component 1 (PC1), and the next largest one defines PC2, etc. Each NMR dataset

can be given a score based on the loadings and is projected onto the principal axes to show how the chemical conditions in that sample affect the observed chemical shifts. Samples of molecules within similar chemical environments are expected to cluster together in the "PC-space" if the dimension-reduction is successful. Because loadings describe a linear combination of the original variables, the relationship between the mean-centered data, score, and loadings is the matrix product: [PC score] = [data] × [PC loadings].

In addition, we performed linear discriminant analysis (LDA) to identify the factor that distinguishes the chitins produced in *Candida* species and other fungi. LDA was performed on the PCA scores, which provide linear discriminant (LD) loadings and LD scores. The scores of observations in separate classes fall approximately into a normal distribution with as little overlap with other classes as possible. The addition of more classes requires additional linear discriminants. Similar to PCA, the relationship between LD scores and LD loadings is: [LD score] = [data] × [LD loadings].

## 4.4 Results and Discussion

### 4.4.1 Solid-State NMR Fingerprints of Chitin in Fungal Cell Walls

Solid-state NMR has been widely applied to differentiate the hydrogen-bonding patterns, identify the type of chitin, and determine the degree of acetylation of chitin and chitosan (by tracking the intensities of CO and $CH_3$ peaks) in model samples [4,12,39-42]. The spectroscopic signatures of model chitin allomorphs are summarized in 2D $^{13}C$-$^{13}C$ correlation spectra simulated and plotted using literature-reported chemical shifts (Table 4.2) (Jang et al., 2004, Kono et al., 2004, Tanner et al. 1990, Brunner et al., 2009, Kaya et al., 2017, Kolbe et al., 2021) (Figure 4.1d). α-chitin has its C3 and C5 peaks distributed as two separated regions (72-73.7 and 75.4-76 ppm like a doublet) while most β-chitins have characteristic C3 and C5 signals sharply clustered in the

74-76 ppm region. The signals of γ-chitin are mixed with those of α- and β-allomorphs, with better alignment to the α-form. The same trend is retained in the double-quantum (DQ)-SQ correlation spectrum. The INADEQUATE spectrum, with an example shown in Figure 4.7, was not explicitly used in this study but have been frequently measured for characterizing cellular samples.

Different from the model compounds, analysis of cellular systems using solid-state NMR spectroscopy has remained challenging due to the coexistence of a large variety of biomolecules, whose signals often exhibit significant overlap [27,43-46]. Fortunately, the presence of nitrogen in the amide group has made chitin chemically unique among the structural polysaccharides in the cell wall. At the same time, the nitrogenated sugars in the intracellular content have already been filtered out using CP-based methods, which remove the signals of mobile sugars but selectively highlight the stiff molecules in the cell wall. The $^{15}$N chemical shifts (~128 ppm) and the unique $^{13}$C chemical shift of the nitrogen-linked carbon 2 (54-56 ppm) are the characteristic signals of chitin for initiating the resonance assignment. High-resolution 2D $^{13}$C-$^{13}$C and $^{15}$N-$^{13}$C correlation spectra collected on freshly prepared *A. fumigatus* mycelia resolved the signals of 6 major types of chitins (type a-f), together with 2 forms with some carbon sites being ambiguously assigned (types g and h) (Figure 4.2a and Figure 4.8). The $^{13}$C full width at half maximum (FWHM) linewidth is in the range of 0.5-0.7 ppm for the chitin in native cell walls.

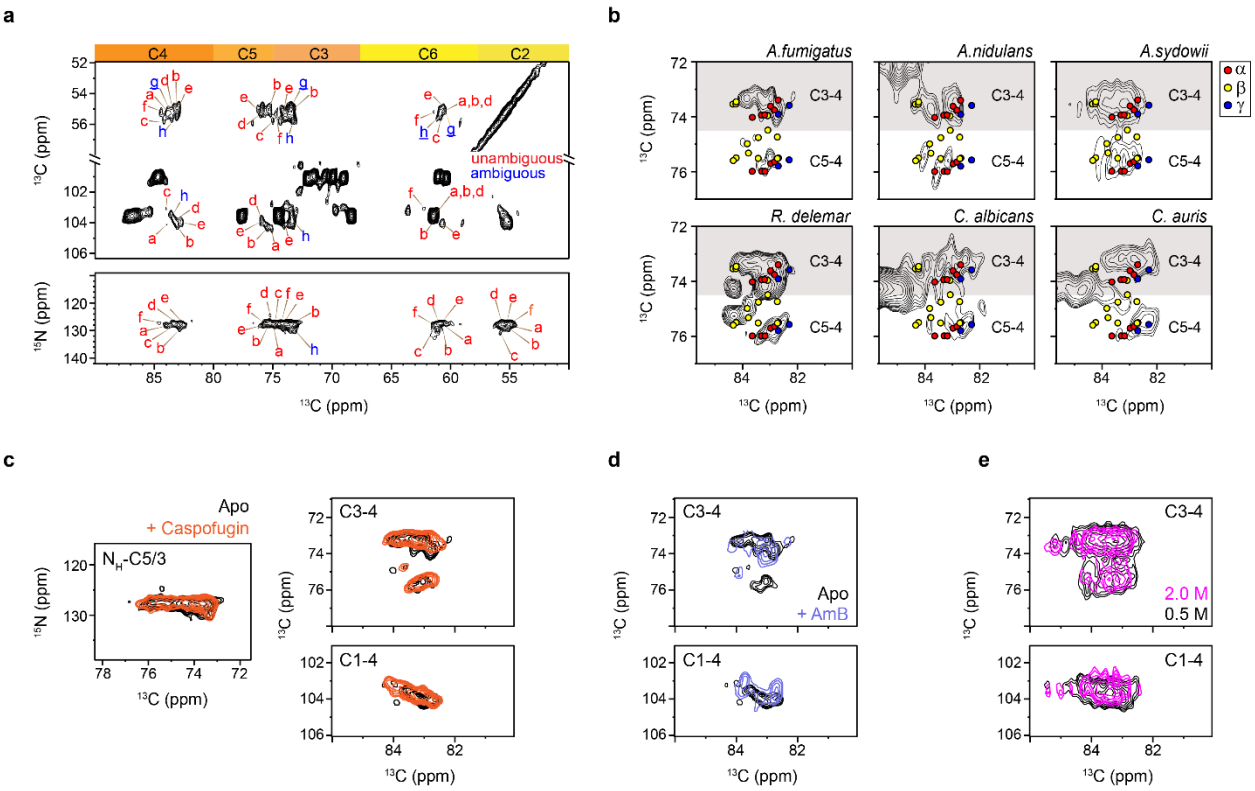


**Figure 4.2 Peak multiplicity of chitin in different fungi. a**, Representative signals of different chitin types in *A. fumigatus*. $^{13}$C-$^{13}$C (top) and $^{15}$N-$^{13}$C (bottom) correlation spectra resolved different forms of chitin molecules. Chitin forms with all carbon sites unambiguously resolved are labeled in red (types a-f), while the ambiguous forms are in blue (types g and h), with the ambiguous (partially resolved) carbon sites underlined. **b,** Comparison of chitin signals in different fungi. The C5-C4 and C3-C4 regions are shown. Colored dots denote the data from three crystalline forms of chitin: α-chitin (red), β-chitin (yellow), and γ-chitin (blue). **c,** 2D $^{15}$N-$^{13}$C and $^{13}$C-$^{13}$C correlation spectra of *A. fumigatus* without drug (apo; black) and with caspofungin treatment (orange). **d,** 2D $^{13}$C-$^{13}$C spectra of *A. fumigatus* without drug (apo; black) and with amphotericin B (AmB; blue). **e,** Overlay of 2D $^{13}$C-$^{13}$C correlation spectra collected on two *A. sydowii* samples cultured with 0.5 M NaCl (black) and 2 M NaCl (magenta).

The C5-C4 and C3-C4 cross-peaks showed comparable spectral patterns among the three *Aspergillus* samples, indicative of structural similarity (Figure 4.2b). *R. delemar*, however, had more extensive signals in this spectral region due to its uniquely high content of chitin and chitosan molecules [47-49]. The spectra of *C. albicans* and *C. auris* looked alike, but their spectral patterns differ from the other filamentous fungi studied. Comparing to α and γ chitin, the characteristic signals of β-chitin were less overlapped with the spectra of all the fungal samples. Chains in β-

chitin are arranged in a parallel way, with only intramolecular H-bonds. This results in a unique and less tightly packed structure for β-chitin, which is swollen in water and exhibiting high reactivity. Most of the literature-reported chemical shifts (Table 4.2) from the α-allomorph are enclosed in the spectral envelope of the fungal samples studied here. Still, the expected signals of β-chitin mostly fell out of the spectral region.

Caspofungin inhibits the β-1,3-glucan synthesis, but when above the minimal inhibitory concentration, it causes a paradoxical effect enhancing the production of chitin to compensate for the loss of β-1,3-glucan [50]. Consistently, the intensities of chitin peaks were enhanced relative to other cell wall components (Figure 4.9), but no major changes were observed in the chemical shifts (Figure 4.2c). Therefore, the increased amount of chitin has insignificant effects on the structure of this molecule. Similarly, the addition of AmB that targets ergosterol in fungal membranes [51] only redistributed the intensities among chitin subtypes without inducing new signals (Figure 4.2d) The robustness of the chitin structure is further confirmed by the comparable signals observed in the saprophytic A. sydowii samples cultured with either optimal or high salinities (Figure 4.2e) [31]. Although chitin structure altered moderately among different fungi, it remained resistant to these external stresses (Tables 4.4 and 4.5). These observations are not surprising because AmB and caspofungin do not directly target chitin. Nikkomycin is the most notable chitin synthesis inhibitor and is thus of significant interest for further investigations [52-54]. Recently combinatorial biosynthetic approaches have been used integrating echinocandin and chitin inhibitors which shows potent antifungal activity [54].

### 4.4.2 Comparison of chitin structures using chemical shift analysis

We compared the $^{13}C$ chemical shifts obtained on the 45 chitin forms in 9 fungal samples (Table 4.3) with the 17 datasets reported in the literature (Table 4.2) (Jang et al., 2004, Kono et al., 2004, Tanner et al., 1990, Brunner et al., 2009, Kaya et al., 2017, Kolbe et al., 2021), generating a chemical shift RMSD heatmap (Figure 4.3). The 45 subforms identified and assigned in the intact fungal cell wall include 8 chitin forms (a-h) in drug-free *A. fumigatus*, 6 forms (a-f) in each of the two *A. fumigatus* samples treated with either caspofungin or amphotericin B, 4 chitin forms (a′-d′) in *A. nidulans*, 5 forms (A-E) in each of the two *A.sydowii* samples cultured with 0.5 M or 2 M NaCl, 3 chitin forms (i-k) in *R. delemar*, and 4 chitin forms (l-o) in each of the two *Candida* samples. Each of the 765 comparisons was represented by an RMSD value based on 16 $^{13}C$ chemical shifts of C1-C6, CO, and $CH_3$ from two different chitin forms. Similar methods have been used to compare the NMR data collected on other fibrillar biomolecules including cellulose and amyloid fibrils [55-57]. We found that fungal chitin correlated relatively well with α-chitin. Small RMSD values below the spectroscopic resolution (0.5 ppm) were observed for some datasets of *A. fumigatus* and *C. albicans*. Reasonable correlations between the cell wall chitin and the γ-chitin model structure were also noted, which can be understood by treating γ-chitin as a derivative of α-chitin due to their structural similarities. In contrast, β-chitins failed to correlate with our observations, with large RMSD typically in the range of 0.7-1.6 ppm. Exceptions were observed for *R. delemar* (Figure 4.3), suggesting the formation of structurally unique chitin domains in this fungus.

The NMR chemical shift data were subjected to PCA. As a dimension-reduction analysis tool, a useful PCA result necessitates that the importance of each consecutive PC declines rapidly. PCs are constructed by the SVD algorithm in an unsupervised manner, beginning with a new axis

that maximizes the variance of all data points when projected onto it, then constructing orthogonal axes according to the same criteria. The eigenvectors returned from the SVD calculation are shown in Figure 4.4a, with the sum normalized to 100, showing the percent of variance in the data explained by each PC. With the first three PCs explaining 70% of the variance in the data, a safe majority of the variance is now explained in those three variables, and the first three PCs should be able to account for the major factors contributed to the chemical shift.

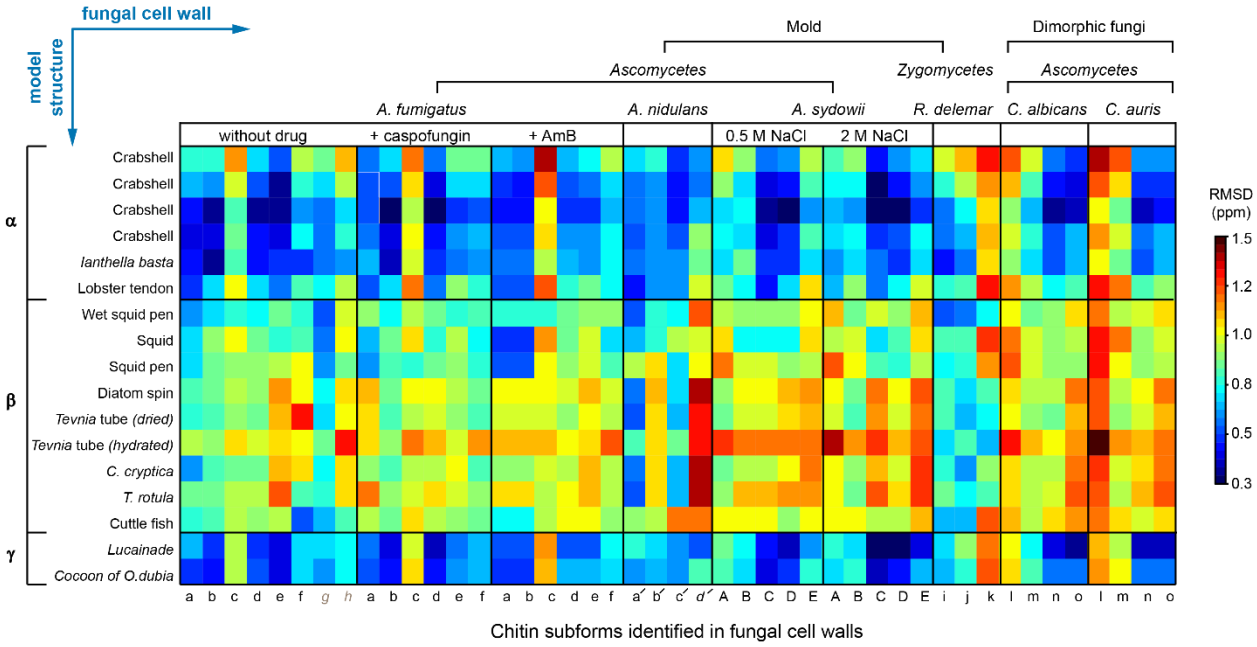


**Figure 4.3 $^{13}$C chemical shift RMSD map comparing chitin structure.** Data were compared between the observed 45 chitin forms in nine fungal cell walls (x-axis) and the three crystalline forms reported by literature (y-axis). Data from six fungal species were shown, including three species of *Ascomycetes* (*A. fumigatus*, *A nidulans* and *A. sydowii*), a sample from Zygomycetes (*R. delemar*), and two Ascomycetes yeast species (*C. albicans* and *C. auris*). Most chitin types showed similarity to α-chitin form. The color scale is shown, with units of ppm. Good correlation with RMSD less than 0.5 ppm (within NMR linewidth) are in dark blue. The forms with certain ambiguous carbon sites are labeled in italics and grey. The chemical shift values used for the analysis are provided in Tables 4.2 and 4.3.

The 3D PCA score plot composed using the first three PCs (Figure 4.4b) illustrates the relationship between each chitin sample in the PC space. Consistent with the heatmap representation, principal component 1 (PC1) primarily differentiated the α and β chitin standards,

with the γ-chitin standards more closely associated with the former. This is more clearly recognizable in the 2D presentation of PC1 vs. PC2 (Figure 4.4c), that the spreading of α and β chitins are on the negative side and positive sides of PC1, respectively. We only observed a relatively small amount of stretching of β-chitins to the negative side. In addition, γ-chitin are distributed mostly to the α-chitin side. Therefore, it is likely that PC1 can sense the difference in hydrogen bonding and chain-packing. This is confirmed by the loadings where the first principal component experiences the most significant change at the carbonyl group (Figure 4.4d). Together, PC1 and PC2 can clearly resolve most forms of β-chitins as a self-isolated group. *Candida* chitins and β-chitins show up on the two extreme positions of PC2, with scores distributed somewhat evenly between -1 and 1 of PC2 and PC3.

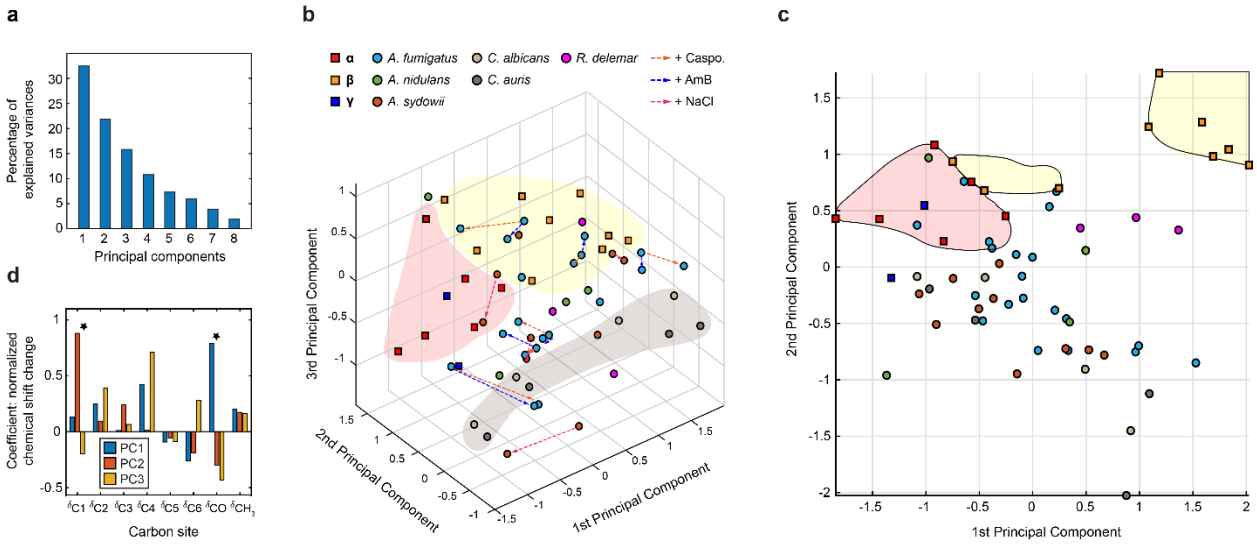


**Figure 4.4 Principal component analysis of chitin chemical shifts. a,** Variance explained by each principal component (PC). **b,** PCA scores for chitin NMR chemical shifts projected onto principal component 1 (PC1) vs. PC2 vs. PC3. Model chitin allomorphs (α, β, and γ-types) are shown using squares while chitin forms identified in fungal cell walls are presented using circles. Shaded regions in red and yellow are used to enclose α- and β-type chitins, respectively. The shaded region in grey mainly contains data from *Candida* species. Data from different model samples and fungal species are color-coded. Arrows in orange, blue, and magenta represents the changes induced by caspofungin (Caspo.), the amphotericin B (AmB), and NaCl (from 0.5 M to 2.0 M), respectively. **c,** PCA scores of chitin chemical shifts projected onto PC1 and PC2 proving

Figure 4.4 (cont'd)
a better visualization of most chitin forms. **d,** Loadings for each PC. Asterisks indicate the most pronounced differences for PC1 and PC2.

The PCA loadings shown in Figure 4.4d are the weight given to each original variable (chemical shifts) in the linear combination that defines each PC, from which one can gather the relative magnitude and direction (as indicated by the sign) of change in those variables expected to occur over positive displacement in the respective PC score. The loadings show that while PC1 is mostly concerned with the carbonyl, PC2 focuses on the C1 atom, while PC3 and PC1 focus on C4 atom that also (together with C1) participates in the glycosidic linkages of chitin molecule.

To only focus on fungal chitin, we conducted a separate PCA by excluding the data from α, β, and γ model allomorphs (Figure 4.10). PCA scores for all fungi chitins indicate that similarities between chitins within a single fungal species are sparse, as many allomorphs of the same species can be found at opposite extremes of both PC1 and PC2, accounting together for almost 60% of variation. Two other PCAs were conducted to respectively focus on the effect of drug and salt conditions (Figure 4.11 and 4.12). It should be noted that the changes caused by antifungal drugs and increased salinity are trivial when compared with the large structural dispersion of native chitin molecules.

In addition, partial structural similarities were noted for some chitin subtypes residing in different fungal strains (Figure 4.5a). For *A. fumigatus*, a few reasonably good correlations can be found with *A. nidulans* and *A. sydowii*, *Candida* species, and *R. delemar*. These observations revealed the partial alignment of chitin structure in different species. The best correlation was found between the type-d chitin of A. fumigatus and the type-D form of *A. sydowii*, with a small RMSD (0.19 ppm) well below the NMR linewidth. Just like the *Aspergillus* samples, *R. delemar*

is also a filamentous fungus, but it exhibited only a single modest correlation with *Aspergillus* species, indicating the structural uniqueness of the chitin produced in *R. delemar*.

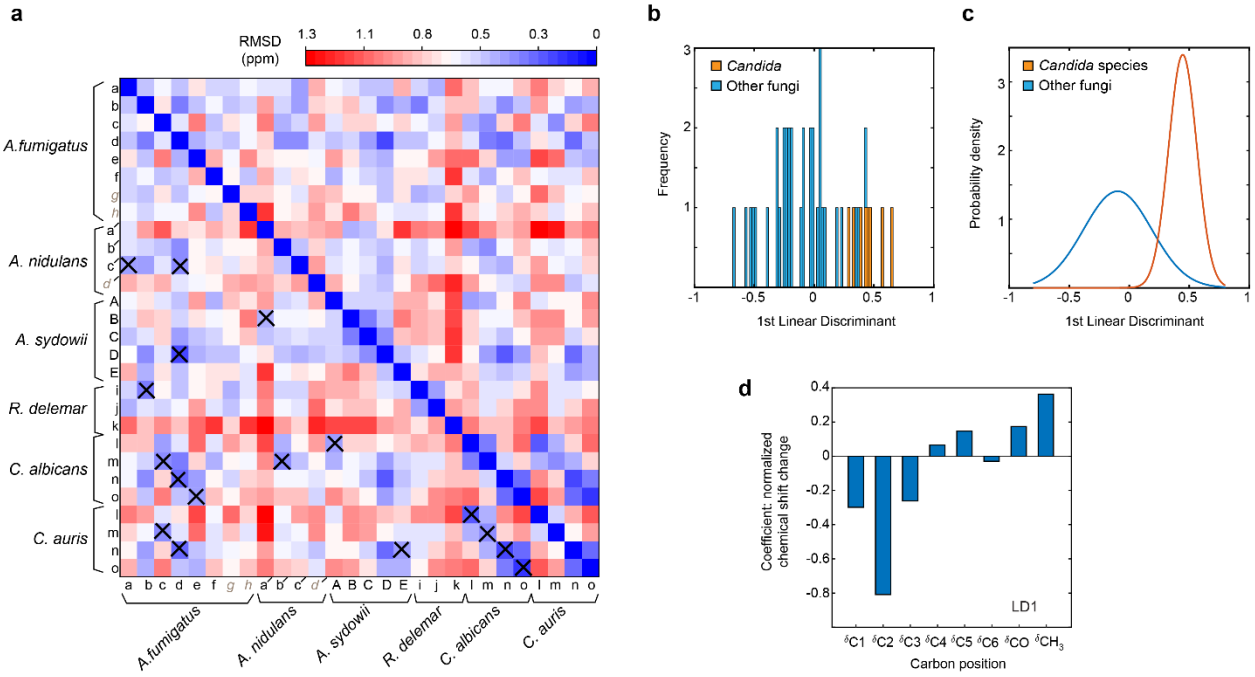


**Figure 4.5 Comparison of chitin forms identified in different fungal species. a,** Chemical shift RMSD heatmap comparing the chitin forms observed in different fungi. Good correlations with RMSD of less than 0.5 ppm are highlighted using crosses. **b,** Linear discriminant analysis with candida fungi (*C. albicans* and *C. auris*) classified differently from other fungal species, with linear discriminant 1 (LD1) scores shown in a histogram. This panel mainly shows the frequency in which LD1 scores fall into a particular range (the width of each bar). **c,** Gaussian probability distributions of LD1 scores. The *Candida* data falls into a smaller range than the other fungi, therefore, there is a much higher probability that a *Candida* species will fall near their statistical mean. **d,** LD1 loadings corresponding to the chemical shifts of each carbon site.

The *Candida* samples prepared in this study were grown only as a yeast form. The two *Candida* species are highly similar to each other, with small RMSD values (0.16-0.32 ppm) when comparing each type of chitin between two *Candida* species. For example, the RMSD is 0.16 for the comparison of type-m chitins in *C. albicans* and *C. auris*. The RMSD is similarly good for the comparisons of type-n (0.21 ppm) and type-l (0.26 ppm) chitins, and only slightly larger for the type-m form (0.32 ppm). In contrast, the filamentous fungi (*Aspergillus* and *Rhizopus* species)

studied here only exhibited partial similarities to the *Candida* species. It is possible that filamentous fungi require for their hypha a specific form of chitin because the strength to hold the tube-shaped mycelium should be different and stronger than holding a balloon shape like a yeast.

The results also aligned with the number and families of chitin synthase [58] genes seen in these species. In yeasts (*Candida* and *Saccharomyces* for example), 3 to 4 CHS genes have been encountered belonging to the families I, II and IV. In *Aspergillus* and *Rhizopus*, however, 9 to 23 genes have been found and they not only belong to the 3 classes (I, II and IV) that were also identified in yeasts, but also have contributions from additional classes (III, V, VII, VI or VIII) [59-61].

To directly identify the structural factor that differentiates the chitin types in yeasts and filamentous fungi, we conducted linear discriminant analysis (LDA). Different from the PCA method described above, LDA is a supervised learning method. LDA can pinpoint the variables that distinguish between the observations that have already been arranged into classes by their properties of interest. Here, we categorized the data into two separate classes to distinguish *Candida* strains (grown as yeasts) from other fungal species (grown as mycelium), which produced a linear discriminant (Figure 4.5b). Their probability distributions (Figure 4.5c) only overlapped slightly, and the loadings (Figure 4.5d) indicated that Candida chitin and the chitins of other fungal species could be best distinguished by the chemical shifts of C2 and $CH_3$, thus revealing the key sites for tracking fungal chitin structure.

The results provided three structural implications. First, the structure of chitin is highly polymorphic in fungal cell walls. At this moment, it is unclear whether the observed polymorphism is related to the diverse groups of chitin synthases involved in the biosynthesis of this polymer, which should be further investigated using functional genomics and spectroscopic approaches. It

also raised a major question on the individual function of all the CHS genes (>20 genes in the Zygomycetes). This study raises unanswered questions about the function of the different classes of chitin synthases in the cell wall structuration. Based on the ssNMR data presented here it does suggest that all CHS synthesized a chitin with very similar structure. The actual biological role of each CHS should be totally dependent on the cellular localization of each synthase in the cell wall as recently suggested [62].

Second, the model structures of α-chitins, as characterized using the highly crystalline material isolated and purified from marine sources, are remarkably preserved among different fungi. This is intriguing as the interactions with other polysaccharides, often by covalent linkages in fungal cell walls [20], did not substantially perturb the structure of chitin. This result agrees with the low number of linkages identified biochemically in the β-1,3-glucan-chitin core of A. fumigatus cell wall and the poor growth phenotype resulting from the deletion of the CRH genes coding for the glycosyltransferases that are responsible for forming glucan-chitin linkages [25]. It is a supplementary argument to suggest that these chitin-glucan covalent connections might not be structurally important for the building of the cell wall.

Third, the structure of chitin is resistant to environmental stimuli, such as non-chitin-focused drug treatment as well as hypersaline environment and osmotic pressure. The structural robustness of chitin and its central role in mechanically supporting the cell wall confirmed the suitability of chitin as a potential target for the development of novel antifungal compounds. It also indicated that the increase in chitin concentration in the cell wall is a survival response, which is not depending on the stress proposed. At this moment, it remains unknown how to reconcile the microscopic structure of the different chitin microfibrils seen in electron microscopy [60,61,63] with the atomic level ssNMR data.

### 4.4.3 Spectroscopic and Structural Features of Fungal Chitosan

Deacetylation of chitin leads to chitosan. Chitosan exists in a semicrystalline form in solids but can be solubilized by acidic solutions. In the fungal cell wall, chitosan has been proposed to serve as a backbone to bind other biomolecules, such as dityrosines or melanin [64,65]. The NMR signals of chitosan are resolved from those of chitin by the absence of $CH_3$ and CO peaks at 22 and 174 ppm (Figure 4.13). The substantial modification in the chemical structure and the hydrogen-bonding patterns induce unique chemical shifts at most carbon sites as shown by Figure 4.6a. The structures of two major chitosan forms, Types I and II salts with inorganic acids, have been reported (Figure 4.6b), which exhibited different helical conformations [5,66,67]. Type-I chitosan has a fully extended two-fold helical structure. The repeating unit of type-II chitosan is four times longer than that of type-I, with a relaxed two-fold helix and a tetrasaccharide repeat in a helical asymmetric unit. Overlay of the spectra predicted using the chemical shifts available in the literature and our dataset revealed that *R. delemar* chitosan could not structurally align with those extracted from various sources such as crab tendon, crab shell, and shrimp shell (Figure 4.6c). The same discrepancy was also present for the Type-I compound, but a better correlation was observed with the Type-II structure.

No chitosan signal was observed in these fresh *A. fumigatus* samples. This is in agreement with a recent genomic study which indicates that the deletion of all deacetylase genes in *A. fumigatus* does not lead to any significant growth phenotype [68]. Interestingly, the occurrence of a significant amount of chitosan in xerophilic *Aspergillus* species may indicate that the fungus synthesizes chitosan to make the cell wall more flexible to fight against the increase in osmotic pressure.

The type-c chitosan in *R. delema*r exhibited bad correlations with the chitosan prepared using extracted chitin (RMSD ~5 ppm) and Type-I chitosan in inorganic salt. RMSD values as large as that should be originated from totally different structures. In contrast, the type-c chitosan correlated reasonably with Type-II chitosan (RMSD < 1.5 ppm) (Figure 4.6d). Similar trends were observed for the other two types (a and b) of chitosan molecules. For example, comparison of chitosan-a in *R. delemar* with Type-II model structures gave very small RMSDs of 0.6-0.8 ppm. The results indicate that chitin chitosan differs from the extracted forms or the Type I structure, but closely resembles the Type-II structure. This trend was projected in the RMSD heatmap of $^{13}C$ chemical shifts for both *R. delemar* and A. sydowii (Figure 4.6d). In the PCA plot, chitosan signals were separated remarkably well by the first two principal components, which account for 89% of the variation in the data (Figure 4.6e and Figure 4.14). *R. delemar* and A. sydowii samples shared more in common with the Type-II chitosan standards but lacked structural similarity to the Type-I standard and extracted chitosan. Therefore, chitosan in the fungal cell wall only has moderate correlations to the Type-II standard structure.

It should be noted that the RMSD values between different chitosan forms are substantially larger than those calculated for chitin. The NMR data actually suggest a new type of chitosan structure that is different from those previously characterized. It is also intriguing that chitosan molecules in extracted materials and intact fungal cell walls are structurally distinct. A possible reason is the solubilization and extraction procedures used in previous studies might have restructured this molecule before subjection to structural characterization. For example, alkali treatment was known to induce chitin deacetylation. The distinct organization of molecules in arthropods and fungi, as well as the potential difference in the degree of deacetylation [69], might also contribute to the observed discrepancy. This differs from the case of chitin, which is an

insoluble polymer and often found in the crosslinked core of fungal cell walls, thus being more resistant to isolation and processing procedures. More in-depth investigations are needed to identify the biochemical reason driving the structural complexity of chitosan and to fully understand its function-related structures in fungal cell walls.

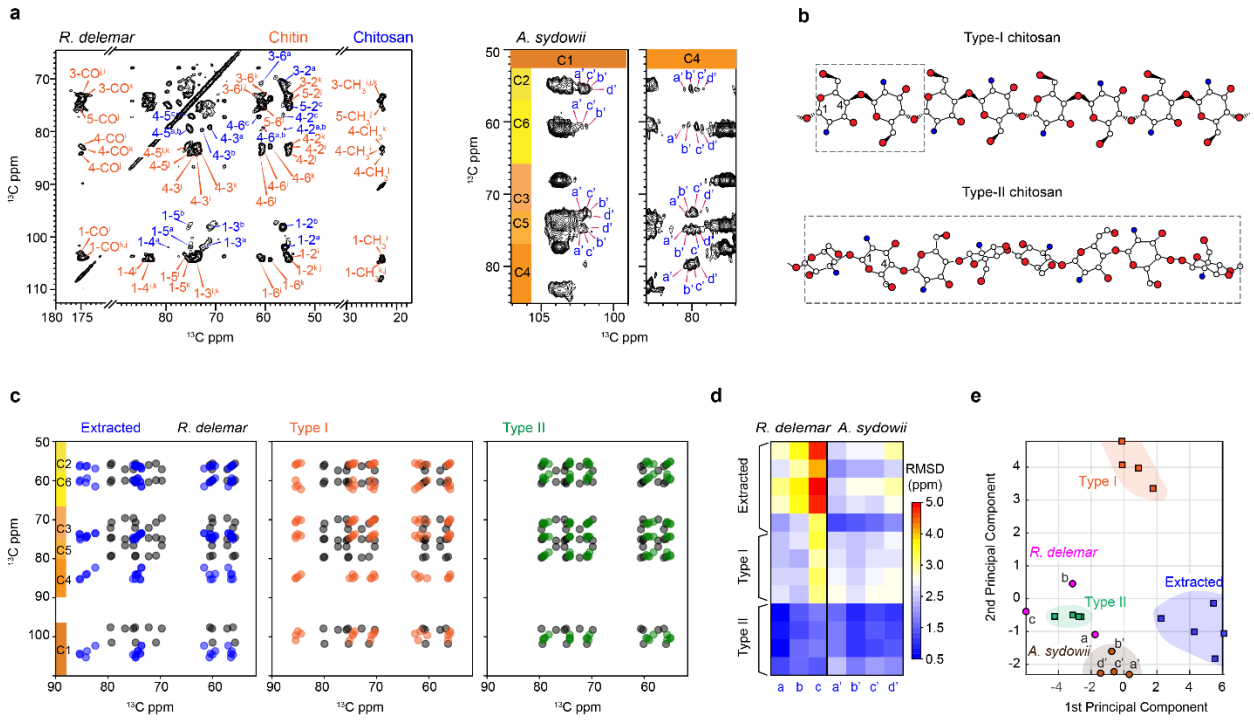


**Figure 4.6 *R. delemar* and *A. sydowii* cell walls are rich in chitosan. a,** Representative 2D $^{13}$C-$^{13}$C CORD spectrum of *R. delemar* and *A. sydowii* cells showing many sets of chitosan signals (blue). **b,** Representative structures of Type-I and Type-II chitosan molecules. Nitrogen (blue), oxygen (red), and carbon (white) atoms are shown but hydrogen atoms are not included for simplicity. The repeating units are shown in dash line boxes. Structure schemes are adapted from [6]. **c,** Simulated spectra of *R. delemar* chitosan (black) overlaid with the literature-reported chitosan forms including extracted chitosan (blue; left panel), Type-I salts with inorganic acids (orange; middle panel), and Type-II salts with inorganic acids (green; right panel). **d,** $^{13}$C chemical shift RMSD map for the comparison between fungal cell wall chitosan (X-axis) and model samples (Y-axis). The color scale unit is ppm. **e,** PCA scores of chitosan. The data analyzed include Type-I (orange squares) and Type-II (green squares) salts with inorganic acids, extracted chitosan (blue square), as well as the chitosan forms identified in *R. delemar* (magenta circles) and *A. sydowii* (brown circles).

## 4.5 Conclusions

The high-resolution dataset enabled by solid-state NMR spectroscopy has made it possible to analyze and compare the structural features of cell wall polysaccharides using statistical approaches. Such protocols will accommodate the rapidly expanding ssNMR dataset and open new research avenues related to the structural investigations of cellular and extracellular biomolecules as well as natural and artificial biomaterials [44,70-73]. The polymorphic structure of chitin and its resistance to external stress was determined in fungal species of biomedical and environmental significance. This information has the potential to facilitate the development of antifungal strategies targeting the unique structures of chitin or its biosynthesis.

## 4.6 Acknowledgments

This work was supported by the National Institute of Health (NIH) grant AI149289. A portion of this work was performed at the National High Magnetic Field Laboratory, which is supported by the National Science Foundation Cooperative Agreement No. DMR-1644779 and the State of Florida. A portion of the NMR dataset was collected at the Environmental Molecular Sciences Laboratory (grid.436923.9), a DOE Office of Science scientific user facility sponsored by the Department.

## REFERENCES


1 Rinaudo, M. Chitin and chitosan: Properties and applications. *Prog. Polym. Sci.* 31, 603-632 (2006).

2 Pillai, C. K. S., Paul, W. & Sharma, C. P. Chitin and chitosan polymers: Chemistry, solubility and fiber formation. *Prog. Polym. Sci.* 34, 641-678 (2009).

3 Jarvis, M. Chemistry: cellulose stacks up. *Nature* 426, 611-612, doi:Doi 10.1038/426611a (2003).

4 Heux, L., Brugnerotto, J., Desbrieres, J., Versali, M. F. & Rinaudo, M. Solid state NMR for determination of degree of acetylation of chitin and chitosan. *Biomacromolecules* 1, 746-751, doi:Doi 10.1021/Bm000070y (2000).

5 Saito, H., Tabeta, R. & Ogawa, K. High-resolution solid-state $^{13}C$ NMR study of chitosan and its salts with acids: conformational characterization of polymorphs and helical structures as viewed from the conformation-dependent $^{13}C$ chemical shifts. *Macromolecules* 20, 2424-2430, doi:10.1021/ma00176a017 (1987).

6 Okuyama, K. *et al.* Structural diversity of chitosan and its complexes. *Carbohydr. Polym.* 41, 237-247 (2000).

7 Jayakumar, R., Menon, D., Manzoor, K., Nair, S. V. & Tamura, H. Biomedical applications of chitin and chitosan based nanomaterials—A short review. *Carbohydr. Polym.* 82, 227-232 (2010).

8 Sikorski, P., Hori, R. & Wada, M. Revisit of alpha-Chitin Crystal Structure Using High Resolution X-ray Diffraction Data. *Biomacromolecules* 10, 1100-1105, doi:10.1021/bm801251e (2009).

9 Yui, T., Taki, N., Sugiyama, J. & Hayashi, S. Exhaustive crystal structure search and crystal modeling of beta-chitin. *Int. J. Biol. Macromol.* 40, 336-344, doi:10.1016/j.ijbiomac.2006.08.017 (2007).

10 Deringer, V. L., Englert, U. & Dronskowski, R. Nature, Strength, and Cooperativity of the Hydrogen-Bonding Network in α-Chitin. *Biomacromolecules* 17, 996-1003 (2016).

11 Kameda, T., Miyazawa, M., Ono, H. & Yoshida, M. Hydrogen bonding structure and stability of α-chitin studied by 13C solid-state NMR. . *Macromol. Biosci.* 5, 103-106 (2005).

12 Kameda, T., Miyazawa, M., Ono, H. & Yoshida, M. Hydrogen bonding structure and stability of alpha-chitin studied by C-13 solid-state NMR. *Macromol. Biosci.* 5, 103-106, doi:10.1002/mabi.200400142 (2004).

13 Sawada, D. *et al.* Direct determination of the hydrogen bonding arrangement in anhydrous β-chitin by neutron fiber diffraction. *Biomacromolecules* 13, 288-291 (2012).

14 Sawada, D. *et al.* Water in crystalline fibers of dihydrate β-chitin results in unexpected absence of intramolecular hydrogen bonding. *PLOS one* 7, e39376 (2012).

15 Ehrlich, H. *et al.* Isolation and identification of chitin from heavy mineralized skeleton of Suberea clavata (Verongida: Demospongiae: Porifera) marine demosponge. *Int. J. Biol. Macromol.* 104, 1706-1712, doi:10.1016/j.ijbiomac.2017.01.141 (2017).

16 Ehrlich, H. *et al.* First evidence of the presence of chitin in skeletons of marine sponges. Part II. Glass sponges (Hexactinellida: Porifera). *J. Exp. Zool. B* 308, 473-483, doi:10.1002/jez.b.21174 (2007).

17 Kaya, M. *et al.* On chemistry of gamma-chitin. *Carbohydr. Polym.* 176, 177-186, doi:10.1016/j.carbpol.2017.08.076 (2017).

18 Brunner, E. *et al.* Chitin-based scaffolds are an integral part of the skeleton of the marine demosponge Ianthella basta. *J. Struct. Biol.* 168, 539-547, doi:10.1016/j.jsb.2009.06.018 (2009).

19 Erwig, L. P. & Gow, N. A. R. Interactions of fungal pathogens with phagocytes. *Nat. Rev. Microbiol.* 14, 163-176 (2016).

20 Gow, N. A. R., Latge, J. P. & Munro, C. A. The Fungal Cell Wall: Structure, Biosynthesis, and Function. *Microbiol. Spectr.* 5 (2017).

21 Latge, J. P. The cell wall: a carbohydrate armour for the fungal cell. *Mol. Microbiol.* 66, 279-290, doi:10.1111/j.1365-2958.2007.05872.x (2007).

22 Latge, J. P. & Chamilos, G. Aspergillus fumigatus and Aspergillosis in 2019. *Clin. Microbiol. Rev.* 33, e00140-00118 (2020).

23 Latgé, J. P., Beauvais, A. & Chamilos, G. The Cell Wall of the Human Fungal Pathogen Aspergillus fumigatus: Biosynthesis, Organization, Immune Response, and Virulence. *Annu. Rev. Microbiol.* 71, 99-116 (2017).

24 Kang, X. *et al.* Molecular architecture of fungal cell walls revealed by solid-state NMR. *Nat. Commun.* 9, 2747, doi:Artn 274710.1038/S41467-018-05199-0 (2018).

25 Zhao, W., Fernando, L. D., Kirui, A., Deligey, F. & Wang, T. Solid-state NMR of plant and fungal cell walls: A critical review. *Solid State Nucl. Magn. Reson.* 107, 101660, doi:10.1016/j.ssnmr.2020.101660 (2020).

26 Brown, G. D. *et al.* Hidden Killers: Human Fungal Infections. *Sci. Transl. Med.* 4, doi:ARTN 165rv13 10.1126/scitranslmed.3004404 (2012).

27 Latge, J. P. & Calderone, R. A. in *Growth, Differentiation and Sexuality* Vol. 1 (eds Kües U. & Fischer R.) 73-104 (Springer,, 2006).

28 Kirui, A. *et al.* Preparation of Fungal and Plant Materials for Structural Elucidation Using Dynamic Nuclear Polarization Solid-State NMR. *J. Vis. Exp.* 144, e59152 (2019).

29 Perez-LIano, Y. *et al.* Stress Reshapes the Physiological Response ofHalophile Fungi to Salinity. *Cells* 9, 525 (2020).

30 Hou, G., Yan, S., Trebosc, J., Amoureux, J. P. & Polenova, T. Broadband homonuclear correlation spectroscopy driven by combined R2(n)(v) sequences under fast magic angle spinning for NMR structural analysis of organic and biological solids. *J. Magn. Reson.* 232, 18-30, doi:10.1016/j.jmr.2013.04.009 (2013).

31 Pauli, J., Baldus, M., van Rossum, B.-J., de Groot, H. & Oschkinat, H. Backbone and Side-Chain $^{13}C$ and $^{15}N$ Signal Assignments of the α-Spectrin SH3 Domain by Magic Angle Spinning Solid-State NMR at 17.6 Tesla *Chem. Biochem.* 2, 272-281 (2001).

32 Kang, X. *et al.* CCMRD: A Solid-State NMR Database for Complex Carbohydrates. *J. Biomol. NMR* 74, 239-250 (2020).

33 Tasic, L., Abraham, R. J. & Rittner, R. Substituent effects on 1H and 13C NMR chemical shifts in a-monosubstituted ethyl acetates: principal component analysis and 1H chemical shift calculations. *Magn. Reson. Chem.* 40, 449-454 (2002).

34 Sakurai, K., Maeno, A., Lee, Y. L. & Akasaka, K. Conformational Properties Relevant to the Amyloidogenicity of β2 Microglobulin Analyzed Using Pressure- and Salt-Dependent Chemical Shift Data. *J. Phys. Chem. B* 123, 836-844 (2019).

35 Kazumasa, S. & Goto, Y. Principal component analysis of the pH-dependent conformational transitions of bovine β-lactoglobulin monitored by heteronuclear NMR. *Proc. Natl. Acad. Sci. USA* 104, 15346-15351 (2007).

36 Kasaai, M. R. Determination of the degree of N-acetylation for chitin and chitosan by various NMR spectroscopy techniques: A review. *Carbohydr. Polym.* 79, 801-810, doi:10.1016/j.carbpol.2009.10.051 (2010).

37 King, C., Stein, R. S., Shamshina, J. L. & Rogers, R. D. Measuring the Purity of Chitin with a Clean, Quantitative Solid-State NMR Method. *ACS Sustain. Chem. Eng.* 5, 8011-8016, doi:10.1021/acssuschemeng.7b01589 (2017).

38 Kono, H. Two-dimensional magic angle spinning NMR investigation of naturally occurring chitins: Precise H-1 and C-13 resonance assignment of alpha- and beta-chitin. *Biopolymers* 75, 255-263, doi:10.1002/bip.20124 (2004).

39 Tanner, S. F., Chanzy, H., Vincendon, M., Roux, J. C. & Gaill, F. High-Resolution Solid-State C-13 Nuclear-Magnetic-Resonance Study of Chitin. *Macromolecules* 23, 3576-3583, doi:Doi 10.1021/Ma00217a008 (1990).

40 Reif, B., Ashbrook, S. E., Emsley, L. & Hong, M. Solid-state NMR spectroscopy. *Nat. Rev. Methods Primers* 1, 2 (2021).

41 Kelly, J. E., Chrissian, C. & Stark, R. E. Tailoring NMR experiments for structural characterization of amorphous biological solids: A practical guide. *Solid State Nucl. Magn. Reson.* 109, 101686 (2020).

42 Narasimhan, S. *et al.* DNP-Supported Solid-State NMR Spectroscopy of Proteins Inside Mammalian Cells. *Angew. Chem. Int. Edit.* 58, 12969-12973, doi:10.1002/anie.201903246 (2019).

43 Poulhazan, A., Arnold, A. A., Warschawski, D. E. & Marcotte, I. Unambiguous Ex Situ and in Cell 2D (13)C Solid-State NMR Characterization of Starch and Its Constituents. *Int. J. Mol. Sci.* 19, doi:10.3390/ijms19123817 (2018).

44 Ghormade, V., Pathan, E. K. & Deshpande, M. V. Can fungi compete with marine sources for chitosan production?. *Int. J. Biol. Macromol.* 104, 1415-1421 (2017).

45 Lecointe, K., Cornu, M., Leroy, J., Coulon, P. & Sendid, B. Polysaccharides Cell Wall Architecture of Mucorales. *Front. Microbiol.* 19 (2019).

46 Melida, H., Sain, D., Stajich, J. E. & Bulone, V. Deciphering the uniqueness of Mucoromycotina cell walls by combining biochemical and phylogenomic approaches *Environ. Microbiol.* 17, 1649-1662 (2015).

47 Loiko, V. & Wagener, J. The Paradoxical Effect of Echinocandins in Aspergillus fumigatus Relies on Recovery of the β-1,3-Glucan Synthase Fks1. *Antimicrob. Agents Chemother.* 61, e01690-01616 (2017).

48 Anderson, T. M. *et al.* Amphotericin forms an extramembranous and fungicidal sterol sponge. *Nat. Chem. Biol.* 10, 400-406 (2014).

49 Steinbach, W. J. & Stevens, D. A. Review of newer antifungal and immunomodulatory strategies for invasive aspergillosis. *Clin. Infect. Dis.* 37 Suppl 3, S157-187, doi:10.1086/376523 (2003).

50 Nix, D. E., Swezey, R. R., Hector, R. & Galgiani, J. N. Pharmacokinetics of nikkomycin Z after single rising oral doses. *Antimicrob. Agents Chemother.* 53, 2517-2521, doi:10.1128/AAC.01609-08 (2009).

51 Li, Y. *et al.* Identification of New Antifungal Agents Targeting Chitin Synthesis by a Chemical-Genetic Method. *Molecules* 24, doi:10.3390/molecules24173155 (2019).

52 Wang, T., Yang, H., Kubicki, J. D. & Hong, M. Cellulose Structural Polymorphism in Plant Primary Cell Walls Investigated by High-Field 2D Solid-State NMR Spectroscopy and Density Functional Theory Calculations. *Biomacromolecules* 17, 2210-2222, doi:10.1021/acs.biomac.6b00441 (2016).

53 Elkins, M. *et al.* Structural Polymorphism of Alzheimer's Beta-Amyloid Fibrils as Controlled by an E22 Switch: A Solid-State NMR Study. *J. Am. Chem. Soc.* 138, 9840-9852 (2016).

54 Qiang, W., Yau, W. M., Lu, J. X., Collinge, J. & Tycko, R. Structural variation in amyloid-β fibrils from Alzheimer's disease clinical subtypes. *Nature* 541, 217-221 (2017).

55 Ma, L. J. *et al.* Genomic analysis of the basal lineage fungus Rhizopus oryzae reveals a whole-genome duplication. *PLoS Genet.* 5, e1000549, doi:10.1371/journal.pgen.1000549 (2009).

56 Muszkieta, L. *et al.* Deciphering the role of the chitin synthase families 1 and 2 in the in vivo and in vitro growth of Aspergillus fumigatus by multiple gene targeting deletion. *Cell Microbiol.* 16, 1784-1805 (2014).

57 Lenardon, M. D., Whitton, R. K., Munro, C. A., Marshall, D. & Gow, N. A. Individual chitin synthase enzymes synthesize microfibrils of differing structure at specific locations in the Candida albicans cell wall. *Mol. Microbiol.* 66, 1164-1173 (2007).

58 Walker, L. A., Lenardon, M. D., Preechasuth, K., Munro, C. A. & Gow, N. A. Cell wall stress induces alternative fungal cytokinesis and septation strategies. *J Cell Sci.* 126, 2668-2677, doi:10.1242/jcs.118885 (2013).

59 Lenardon, M. D., Munro, C. A. & Gow, N. A. Chitin synthesis and fungal pathogenesis. *Curr. Opin. Microbiol.* 13, 416-423 (2010).

60 Chrissian, C. *et al.* Melanin deposition in two Cryptococcus species depends on cell-wall composition and flexibility. *J. Biol. Chem.* 295, 1815 (2020).

61 Chrissian, C. *et al.* Unconventional Constituents and Shared Molecular Architecture of the Melanized Cell Wall of C. neoformans and Spore Wall of S. cerevisiae. *J. Fungi* 6, 329 (2020).

62 Ogawa, K., Yui, T. & Okuyama, K. Three D structures of chitosan. *Int. J. Biol. Macromol.* 34, 1-8 (2004).

63 Franca, E. F., Lins, R. D., Freitas, L. C. & Straatsma, T. P. Characterization of chitin and chitosan molecular structure in aqueous solution. *J. Chem. Theory Comput.* 4, 2141-2149 (2008).

64 Mouyna, I. *et al.* What Are the Functions of Chitin Deacetylases in Aspergillus fumigatus? *Front. Cell. Infect. Microbiol.* 10, doi:ARTN 28 10.3389/fcimb.2020.00028 (2020).

65 Liu, W. *et al.* Enzymatic Degradation of Nanosized Chitin Whiskers with Different Degrees of Deacetylation. *ACS Biomater. Sci. Eng.* 5, 5316-5326, doi:10.1021/acsbiomaterials.9b00796 (2019).

66 Ehren, H. L. *et al.* Characterization of the cell wall of a mushroom forming fungus at atomic resolution using solid-state NMR spectroscopy. *Cell Surface* 6, 2020 (2020).

67 Arnold, A. A. *et al.* Whole cell solid-state NMR study of Chlamydomonas reinhardtii microalgae. *J. Biomol. NMR* 70, 123-131, doi:10.1007/s10858-018-0164-7 (2018).

68 Bougault, C., Ayala, I., Vollmer, W., Simorre, J. P. & Schanda, P. Studying intact bacterial peptidoglycan by proton-detected NMR spectroscopy at 100 kHz MAS frequency. *J. Struct. Biol.* 206, 66-72, doi:10.1016/j.jsb.2018.07.009 (2019).

69 Kang, X. *et al.* Lignin-polysaccharide interactions in plant secondary cell walls revealed by solid-state NMR. *Nat. Commun.* 10, 347, doi:10.1038/s41467-018-08252-0 (2019).

70 Rudall, K. M. in *Advances in Insect Physiology* Vol. 1 (eds J. W. L. Beament, J. E. Treherne, & V. B. Wigglesworth) 257-313 (Academic Press, 1963).

71 Jang, M. K., Kong, B. G., Jeong, Y. I., Lee, C. H. & Nah, J. W. Physicochemical characterization of α-chitin, β-chitin, and γ-chitin separated from natural resources. *Journal of Polymer Science Part A: Polymer Chemistry* 42, 3423-3432 (2004).

72 Kolbe, F. *et al.* Solid-state NMR spectroscopic studies of 13 C, 15 N, 29 Si-enriched biosilica from the marine diatom Cyclotella cryptica. *Discover Materials* 1, 1-12 (2021).

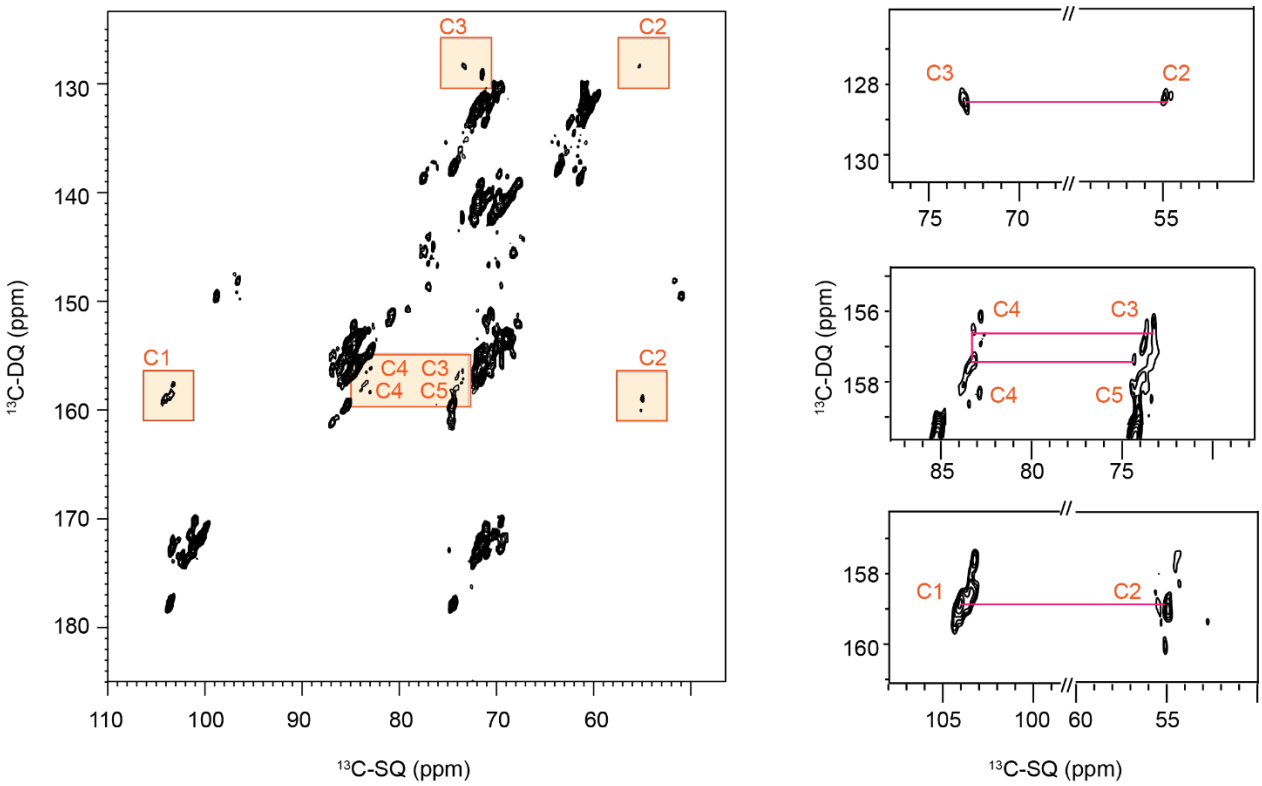


**Figure 4.7 2D $^{13}$C-$^{13}$C DQ-SQ spectra of *A. fumigatus*.** The full spectra (left) and selected regions of chitin signals (right) are shown. Chitin carbon peaks are labeled, and the carbon connectivity are shown in magenta lines.

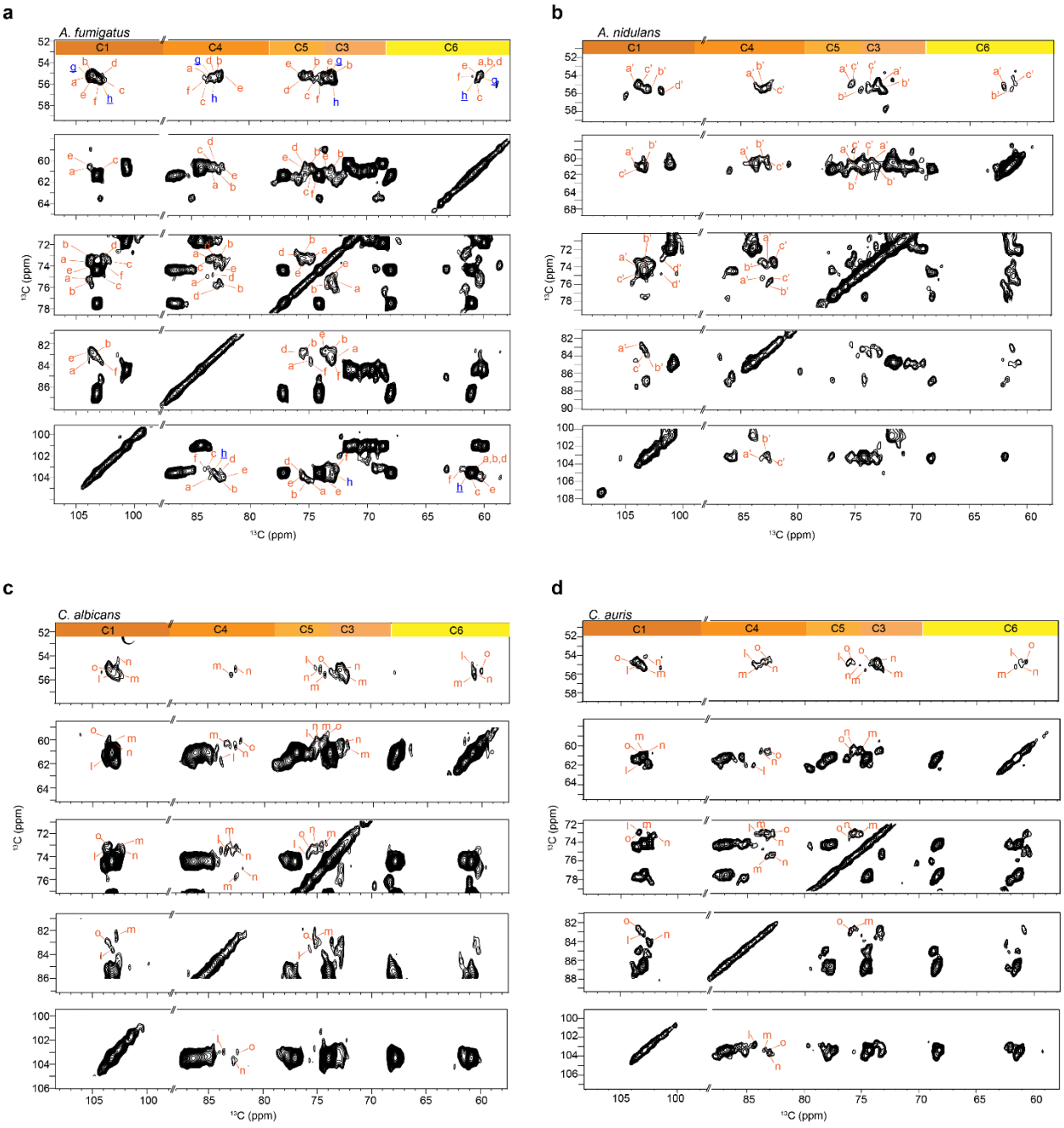


**Figure 4.8 2D $^{13}$C-$^{13}$C correlation spectra resolving chitin polymorphs in different fungi** including **a,** *A. fumigatus*, b, *A. nidulans*, **c,** *C. albicans*, and **d,** *C. auris*. $^{13}$C-$^{13}$C correlation spectra detect intramolecular interaction of chitin peaks. Different chitin forms are annotated using alphabetic letters and ambiguous chitin types are labeled in blue and ambiguous carbon sites are underlined.

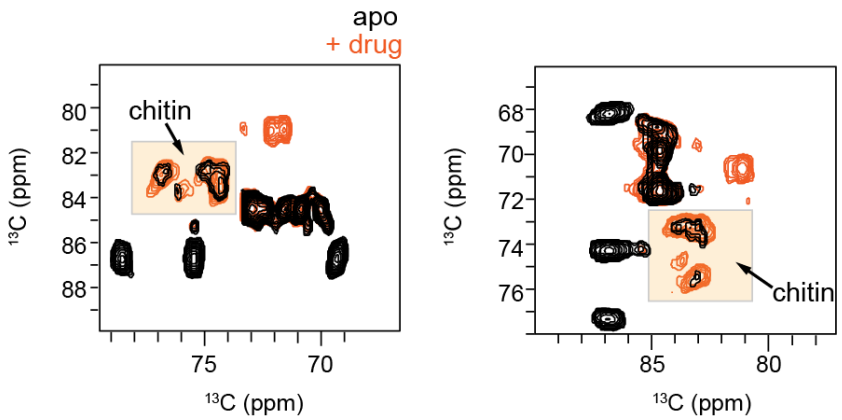


**Figure 4.9. 2D $^{13}$C-$^{13}$C correlation spectra of *A. fumigatus* showing the increased content of chitin after treatment by caspofungin.** The chitin signals are highlighted using boxes in light orange, which have higher intensity in the drug-treated sample.

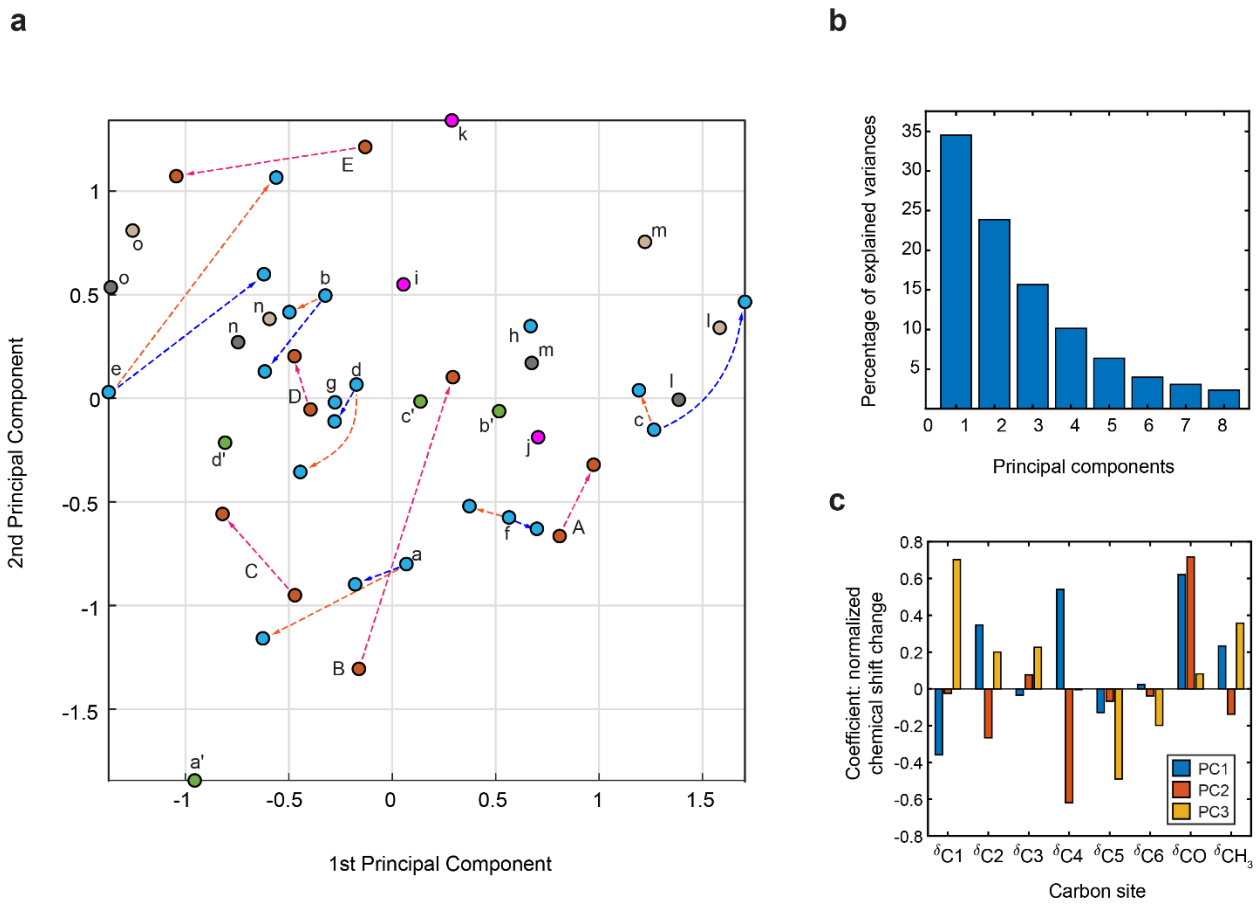


**Figure 4.10 PCA of different fungal chitin forms. a, PCA scores of fungal species and their respective allomorphs.** The color code is kept the same as Figure 4.4. *A. sydowii* allomorphs are shown at different salt concentrations, and *A. fumigatus* allomorphs are shown in the presence and absence of antifungal drugs. **b,** Variance explained by each principal component. **c,** Loadings for the PCA results. Both PC1 and PC2 are defined by a CO shift in the same direction, while the C4 shift contributes in the opposite direction. PC3 and PC1likewise share an inverse relationship to C1. The results delineated how the chemical shift difference in different chitin forms.

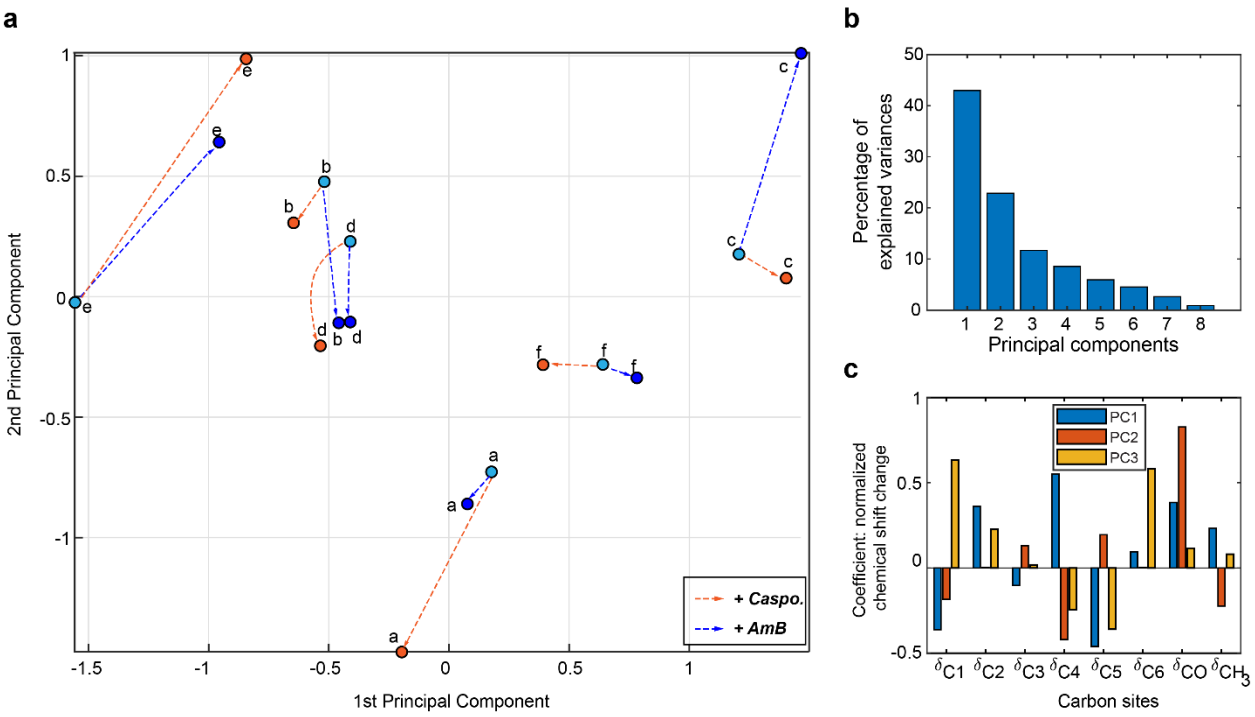


**Figure 4.11 PCA scores of *A. fumigatus* chitin with and without antifungal drugs. a,** PCA scores of the control sample (light blue), caspofungin-treated culture (orange), and amphotericin B-containing sample (dark blue) are shown. Arrows in orange and blue represent the changes induced by the caspofungin and AmB, respectively. The antifungal drug effect appears inconsistent and subtle from the perspective of the two dominant PC's. **b,** Variance explained by each principal component. PC1 and PC2 account for almost 66% of the variation. **c,** PCA loadings.

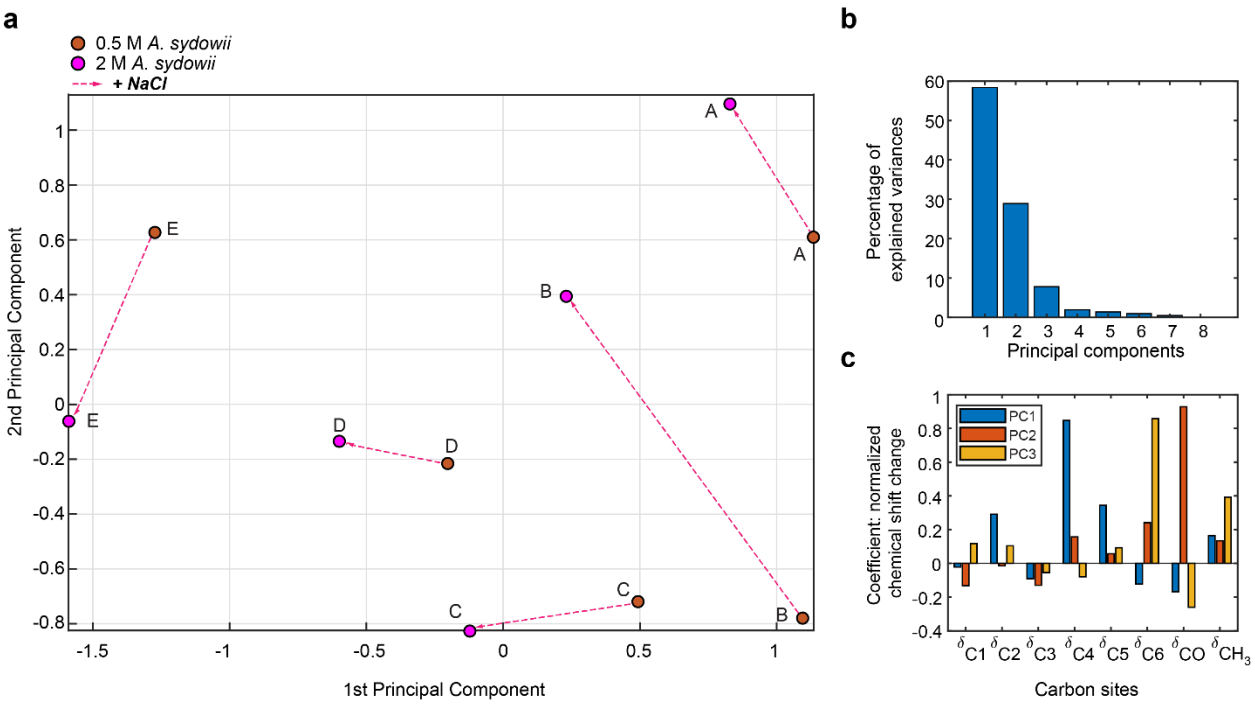


**Figure 4.12 Effects from hypersaline conditions. a,** PCA scores of *A. sydowii* chitin allomorphs at different salt concentrations. Each allomorph is coded labeled. Arrows in magenta represent the changes induced by a higher concentration of NaCl (from 0.5 M to 2.0 M). PC1 and PC2 scores are dominated by the differences between chitin allomorphs from E to D, to C, to B, then to A with PC1 increasing, rather than the salt concentration. Scores are distributed at the extreme ranges in both PC1 and PC2 for different allomorphs, while salt concentration caused only limited changes. **b,** Variance explained by each principal component. The SVD of the matrix produced 8 PCs with the first 2 PCs being able to describe 87% of the variance. **c,** PCA loadings. The effect of increasing salt concentration has a small but consistent effect on the chitin structure with respect to PC1: increasing the salt concentration decreases each chitin's PC1 score, which is mostly defined by the $\delta_{C4}$ chemical shift. Increasing the salt concentration has varied effects on the PC2 score, which is mostly defined by the carbonyl shift as indicated by PC2 loadings.

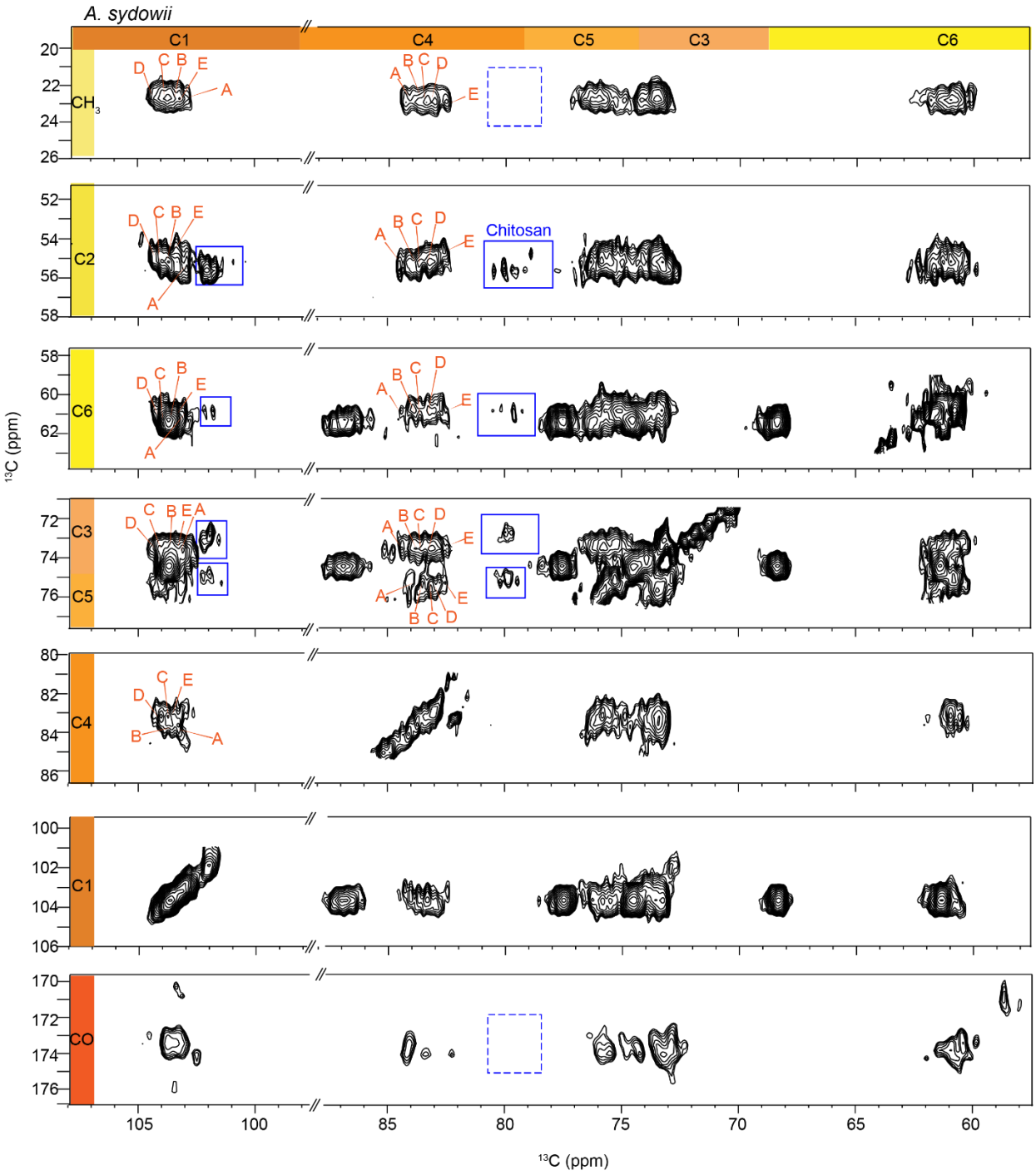


**Figure 4.13 2D $^{13}$C-$^{13}$C correlation spectra resolving chitosan signals in *A. sydowii*.** These $^{13}$C-$^{13}$C correlation spectra detect intramolecular cross-peaks. All chitin types are labeled with letters A-E. Blue boxes indicate the chitosan peaks, absence of $CH_3$ and CO peaks at 22 and 174 ppm (F1 dimension) confirms the chemical structure of these molecules.

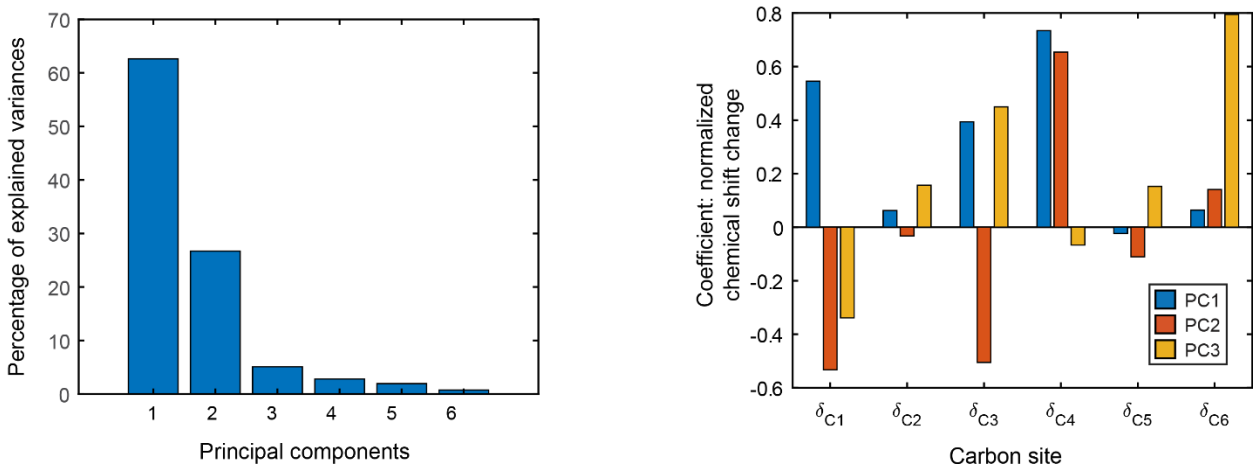


**Figure 4.14 Information related to the PCA scores of *A. sydowii* chitosan allomorphs.** Variance explained by each principal component (left), and the PCA loadings (right) are shown. The first 2 PCs describe 87% of the variance.

**Table 4.1 Experimental and processing parameters of 2D ssNMR.** 2D CP $^{13}C$-$^{13}C$ and $^{13}C$-$^{15}N$ correlation experiments allowed to resolve rigid chitin intramolecular peaks. The experimental parameters include the $^{1}H$ Larmor frequency, total experiment time (t), recycle delay (d1), number of scans (NS), The number of points for the direct (td2) and indirect (td1) dimensions, the acquisition time of the direct dimension (aq2) and the evolution time of indirect dimension (aq1), spectral width (sw1 and sw2), mixing time ($t_m$), increment delay (IN_F). The processing parameters include the window function and associated parameters.

| | | | Acquisition parameters | | | | | | | | | | | Processing parameters | |
|---|---|---|---|---|---|---|---|---|---|---|---|---|---|---|---|
| Sample | Experiment | $\omega_{0,1H}$ (MHz) | t (h) | d1 (s) | NS | td2 | td1 | aq2 (ms) | aq1 (ms) | sw2 | sw1 | $t_m$ (ms) | IN_F (μs) | Window function | Parameters |
| *A. fumagitus* | | | | | | | | | | | | | | | |
| *W/o drug* | CORD | 800 | 4.2 | 1.7 | 16 | 2400 | 560 | 17.9 | 7.2 | 332.8 | 191.1 | 53 | 26 | QSINE | SSB 6 |
| | N(CA)CX | 800 | 1.3 | 1.7 | 16 | 2400 | 180 | 17.9 | 9.0 | 332.8 | 123.3 | 30 | 100 | GM | LB -5.0, GB 0.1 |
| *+Caspo* | CORD | 800 | 4.2 | 1.7 | 16 | 2400 | 560 | 17.9 | 7.2 | 332.8 | 191.1 | 53 | 26 | QSINE | SSB 6 |
| | N(CA)CX | 800 | 1.3 | 1.7 | 16 | 2400 | 180 | 17.9 | 9.0 | 332.8 | 123.3 | 30 | 100 | GM | LB -5.0, GB 0.1 |
| +AmB | CORD | 850 | 9.1 | 2 | 32 | 2496 | 512 | 24.9 | 5.1 | 233.9 | 167.1 | 53 | 20 | QSINE | SSB 4, Tdeff 1400(F2) |
| *A. nidulans* | | | | | | | | | | | | | | | |
| | DARR | 850 | 9.1 | 2 | 32 | 2496 | 512 | 24.96 | 5.1 | 233.9 | 167.1 | 100 | 20 | QSINE | SSB 2.8, Tdeff 1400(F2) |
| *Candida* sp. | | | | | | | | | | | | | | | |
| *C.albicans* | CORD | 800 | 3.2 | 1.5 | 16 | 2400 | 490 | 17.9 | 7.1 | 332.8 | 171.3 | 53 | 29 | QSINE | SSB 2.6 |
| *C.auris* | CORD | 800 | 3.2 | 1.5 | 16 | 2400 | 490 | 17.9 | 7.1 | 332.8 | 171.3 | 53 | 29 | QSINE | SSB 4 |
| *A. sydowii* | | | | | | | | | | | | | | | |
| 0.5 M NaCl | DARR | 850 | 4.5 | 2 | 16 | 2496 | 512 | 24.96 | 5.1 | 233.9 | 167.1 | 100 | 20 | QSINE | SSB 3 |
| 2 M NaCl | DARR | 850 | 4.5 | 2 | 16 | 2496 | 512 | 24.96 | 5.1 | 233.9 | 167.1 | 100 | 20 | QSINE | SSB 3 |

**Table 4.2 $^{13}C$ chemical shifts of chitin microfibrils (α-chitin, β-chitin, γ-chitin) and chitosan molecules from literature.** Not applicable (/).

| Type | C1 | C2 | C3 | C4 | C5 | C6 | CO | CH3 | Sources | References |
|---|---|---|---|---|---|---|---|---|---|---|
| α-chitin | 103.9 | 54.6 | 72.9 | 82.8 | 75.4 | 60.5 | 172.6 | 22.5 | Crab shell | Jang, et al. 2004[71] |
| | 104.0 | 54.8 | 73.4 | 82.9 | 75.6 | 60.6 | 173.0 | 22.6 | Crab shell | Kono, et al. 2004[38] |
| | 104.1 | 55.1 | 73.2 | 83 | 75.7 | 60.9 | 173.7 | 22.7 | Crab shell | Kaya, et al. 2017[17] |
| | 104.5 | 55.4 | 73.6 | 83.2 | 76.0 | 61.0 | 173.7 | 23.1 | Crab shell | Tanner, et al. 1990[39] |
| | 104.4 | 55.3 | 73.6 | 83.3 | 76.0 | 61.3 | 174.2 | 23.1 | *I. basta* | Brunner, et al. 2009[18] |
| | 104.6 | 55.6 | 73.7 | 83.6 | 76.0 | 61.1 | 173.0 | 23.1 | Lobster tendon | Tanner, et al. 1990[39] |
| β-chitin | 104.8 | 56.0 | 74.5 | 83.7 | 75.4 | 59.9 | 174.8 | 23.3 | Wet squid pen | Tanner, et al. 1990[39] |
| | 104.2 | 55.2 | 74.8 | 84.1 | 74.8 | 60.9 | 173.1 | 22.5 | Squid | Jang, et al. 2004[71] |
| | 104.1 | 55.2 | 74.2 | 83.4 | 73.6 | 60.8 | 173.6 | 22.8 | Squid pen | Kono, et al. 2004[38] |
| | 105.4 | 55.3 | 73.1 | 84.5 | 75.5 | 59.9 | 175.6 | 22.8 | Diatoms spins | Tanner, et al. 1990[39] |
| | 105.3 | 55.2 | 73.1 | 84.4 | 75.4 | 59.8 | 175.5 | 22.7 | *Tevnia* tube dried | Tanner, et al. 1990[39] |
| | 105.2 | 55.2 | 74.5 | 83.1 | 75.4 | 59.2 | 175.0 | 24.1 | *Tevnia* tube hydrated | Tanner, et al. 1990[39] |
| | 105.3 | 55.8 | 73 | 84.4 | 75.4 | 59.8 | 175.0 | 23.4 | *C. cryptica* | Kolbe, et al. 2021[76] |
| | 105.3 | 55.6 | 73 | 84.4 | 75.4 | 59.8 | 175.8 | 22.7 | *T. rotula* | Brunner, et al. 2009[18] |
| | 104.3 | 55.6 | 75.2 | 84 | 75.2 | 61.7 | 174.4 | 22.9 | Cuttle fish | Kaya, et al. 2017[17] |
| γ-chitin | 103.7 | 54.8 | 73.1 | 82.7 | 75.4 | 61.1 | 173.4 | 22.6 | Lucainade | Jang, et al. 2004[71] |
| | 104.3 | 55.3 | 73.5 | 83 | 75.7 | 61.3 | 173.4 | 22.7 | Cocoon of *O. dubia* | Kaya, et al. 2017[17] |
| Chitosan | 104.7 | 56.8 | 74.1 | 85.7 | 74.1 | 60.7 | / | / | | Heux, et al, 2000[4] |
| | 104.1 | 56.6 | 74.4 | 84.3 | 74.6 | 59.8 | / | / | Crab tendon | Saito, et al, 1988[5] |
| | 105.0 | 56.4 | 75.5 | 85.6 | 75.0 | 60.3 | / | / | Crab shell | Saito, et al, 1987[5] |
| | 105.7 | 56.8 | 75 | 84.5 | 75.0 | 60.9 | / | / | Shrimp shell | |
| | 102.7 | 57.3 | 73.9 | 82.7 | 73.9 | 61.9 | / | / | annealed | |
| Type I | 101.0 | 56.0 | 70.8 | 85.1 | 74.8 | 61.7 | / | / | $HNO_3$ | Saito, et al, 1987[5] |

Table 4.2 (cont'd)

| | | | | | | | | | | |
|---|---|---|---|---|---|---|---|---|---|---|
| | 99.3 | 55.6 | 70.2 | 84.1 | 74.2 | 62.3 | / | / | $HClO_4$ | |
| Type II | 99.7 | 56.0 | 70.6 | 85.1 | 74.2 | 60.0 | / | / | HBr | Saito, et al, 1987[5] |
| | 98.7 | 55.6 | 70.0 | 84.7 | 73.8 | 61.3 | / | / | HI | |
| | 100.5 | 55.2 | 71.2 | 79.4 | 74.4 | 59.5 | / | / | HCl | |
| | 100.3 | 55.2 | 71.0 | 79.1 | 74.4 | 59.8 | / | / | $H_2SO_4$ | |
| | 100.9 | 55.8 | 70.8 | 79.5 | 74.4 | 59.2 | / | / | $H_3PO_4$ | |
| | 99.5 | 55.8 | 70.6 | 78.4 | 74.4 | 58.4 | / | / | $HIO_4$ | |

**Table 4.3 $^{13}$C chemical shifts of chitin and chitosan in different fungi observed from 2D $^{13}$C-$^{13}$C correlation spectra.** Alphabetical letters used to denote different allomorphs. The units are in ppm. Ambiguous chitin forms are in italics, ambiguous carbon sites are underlined. Not applicable (/). Unidentified (-).

| Chitin/ Chitosan | C1 | C2 | C3 | C4 | C5 | C6 | CO | $CH_3$ | Experiment methods |
|---|---|---|---|---|---|---|---|---|---|
| *Aspergillus fumigatus* | | | | | | | | | |
| a | 104.3 | 55.7 | 73.2 | 83.9 | 75.2 | 60.7 | 173.9 | 23.3 | $^{13}$C-$^{13}$C 53 ms CORD |
| b | 104.2 | 55.2 | 73.3 | 82.9 | 75.6 | 60.9 | 174.7 | 22.8 | |
| c | 103.0 | 55.7 | 73.4 | 84.1 | 74.9 | 60.4 | 174.9 | 23.4 | |
| d | 103.6 | 55.1 | 73.4 | 83.3 | 75.8 | 60.4 | 174.4 | 22.7 | |
| e | 104.0 | 54.9 | 73.9 | 82.7 | 76.1 | 60.5 | 173.6 | 22.4 | |
| f | 103.2 | 55.2 | 73.3 | 84.3 | 75.2 | 61.3 | 174.3 | 22.7 | |
| *g* | 104.5 | 55.1 | 74.1 | 83.7 | 75.0 | 60.4 | 174.4 | 22.4 | |
| *h* | 103.5 | 55.6 | 73.2 | 83.4 | 74.9 | 61.8 | 175.1 | 22.8 | |
| *Aspergillus nidulans* | | | | | | | | | |
| a′ | 104.2 | 55.4 | 73.6 | 84.1 | 75.6 | 60.2 | 1725 | 22.9 | $^{13}$C-$^{13}$C 53 ms CORD |
| b′ | 103.2 | 55.7 | 73.9 | 83.6 | 75.9 | 60.5 | 174.6 | 23.1 | |
| c′ | 104.0 | 55.6 | 72.9 | 83.4 | 75.6 | 60.0 | 174.6 | 23.1 | |
| d′ | 102.6 | 54.5 | 73.6 | 83.1 | 75.4 | 60.7 | 173.4 | 22.3 | |
| *Aspergillus sydowii* | | | | | | | | | |
| A | 103.3 | 55.5 | 72.9 | 84.5 | 76.2 | 60.7 | 174.6 | 22.7 | $^{13}$C-$^{13}$C 100 ms DARR |
| B | 103.5 | 55.2 | 73.4 | 84.4 | 75.9 | 60.0 | 173.4 | 22.7 | |
| C | 103.5 | 55.4 | 73.3 | 83.7 | 75.9 | 60.7 | 173.4 | 22.7 | |
| D | 103.6 | 55.0 | 73.2 | 83.4 | 75.5 | 60.5 | 174.1 | 22.4 | |
| E | 103.2 | 54.8 | 73.5 | 82.5 | 75.2 | 60.9 | 175.1 | 22.4 | |
| chitosan a′ | 102.2 | 55.6 | 74.5 | 80.4 | 74.9 | 60.7 | / | / | |
| chitosan b′ | 101.9 | 55.7 | 72.9 | 80.0 | 74.3 | 60.5 | / | / | |
| chitosan c′ | 102.9 | 55.7 | 72.5 | 79.7 | 75.3 | 60.9 | / | / | |
| chitosan d′ | 101.4 | 55.5 | 73.5 | 79.1 | 75.3 | 61.0 | / | / | |
| *Rhizopus delemar* | | | | | | | | | |
| i | 104.2 | 55.2 | 74.0 | 83.1 | 75.1 | 60.7 | 174.9 | 23.3 | $^{13}$C-$^{13}$C 53 ms CORD |
| j | 104.3 | 55.2 | 73.8 | 84.2 | 75.0 | 60.8 | 174.9 | 23.6 | |

Table 4.3 (cont'd)

| | | | | | | | | | |
|---|---|---|---|---|---|---|---|---|---|
| k | 104.2 | 54.9 | 74.0 | 83.1 | 75.1 | 58.9 | 175.7 | 22.8 | |
| chitosan a | 101.9 | 56.0 | 72.5 | 79.6 | 75.0 | 60.3 | / | / | |
| chitosan b | 98.0 | 56.4 | 72.5 | 79.8 | 75.1 | 60.4 | / | / | |
| chitosan c | 98.3 | 57.5 | 70 | 77.0 | 75.4 | 60.4 | / | / | |
| *Candida albicans* | | | | | | | | | |
| l | 102.5 | 55.5 | 73.2 | 84.2 | 75.9 | 60.4 | 175.2 | 22.9 | $^{13}C$-$^{13}C$ 53 ms CORD |
| m | 103.0 | 55.0 | 73.4 | 83.8 | 75.6 | 60.4 | 174.9 | 22.9 | |
| n | 103.9 | 54.6 | 73.1 | 83.0 | 75.7 | 60.3 | 174.2 | 22.5 | |
| o | 103.9 | 54.3 | 73.2 | 82.5 | 75.5 | 60.5 | 173.9 | 22.3 | |
| *Candida auris* | | | | | | | | | |
| l | 102.1 | 55.4 | 73.3 | 84.1 | 75.8 | 60.8 | 175.5 | 22.6 | $^{13}C$-$^{13}C$ 53 ms CORD |
| m | 103.0 | 55.0 | 73.2 | 83.7 | 75.0 | 60.6 | 175.7 | 23.2 | |
| n | 103.5 | 54.4 | 73.2 | 83.1 | 75.6 | 60.7 | 174.3 | 22.6 | |
| o | 103.9 | 54.2 | 73.3 | 82.4 | 75.5 | 60.8 | 174.2 | 22.3 | |

**Table 4.4 Drug Effect on Chitin types in *A. fumigatus.*** Chemical shift difference and RMSD of each type is calculated. The units are in ppm. Δ denotes the difference of with drug and without drug. w/o drug = without drug. Unidentified (-).

| | | | | | | | | | | |
|---|---|---|---|---|---|---|---|---|---|---|
| Caspofugin | | | | | | | | | | |
| | | C1 | C2 | C3 | C4 | C5 | C6 | CO | $CH_3$ | RMSD |
| With drug | a | 104.3 | 55.7 | 73.2 | 83.9 | 75.2 | 60.7 | 173.9 | 23.3 | |
| w/o drug | a | 104.2 | 55.2 | 73.2 | 83.7 | 74.8 | 60.6 | 173.1 | 23.5 | |
| | Δ | 0.1 | 0.5 | 0 | 0.2 | 0.4 | 0.1 | 0.9 | -0.2 | 0.4 |
| With drug | b | 104.2 | 55.2 | 73.3 | 82.9 | 75.6 | 60.9 | 174.7 | 22.8 | |
| w/o drug | b | 104.2 | 54.9 | 73.3 | 82.9 | 75.5 | 60.7 | 174.5 | 22.8 | |
| | Δ | 0 | 0.3 | 0 | 0 | 0.1 | 0.2 | 0.2 | 0 | 0.1 |
| With drug | c | 103 | 55.7 | 73.4 | 84.1 | 74.9 | 60.4 | 175.0 | 23.4 | |
| w/o drug | c | 103.1 | 55.4 | 73.1 | 84.1 | 74.1 | 60.3 | 175.0 | 23.1 | |
| | Δ | -0.1 | 0.3 | 0.3 | 0 | 0.8 | 0.1 | 0 | 0.3 | 0.3 |
| With drug | d | 103.6 | 55.1 | 73.4 | 83.3 | 75.8 | 60.4 | 174.4 | 22.7 | |
| w/o drug | d | 103.5 | 55.2 | 73.2 | 83.4 | 75.8 | 60.5 | 173.8 | 22.6 | |
| | Δ | 0.1 | -0.1 | 0.2 | -0.1 | 0 | -0.1 | 0.5 | 0.1 | 0.2 |
| With drug | e | 104.0 | 54.9 | 73.9 | 82.7 | 76.1 | 60.5 | 173.6 | 22.4 | |
| w/o drug | e | 104.0 | 54.9 | 73.7 | 82.6 | 75.5 | 60.6 | 174.9 | 22.3 | |
| | Δ | 0 | 0 | 0.2 | 0.1 | 0.6 | -0.1 | -1.3 | 0.1 | 0.5 |
| With drug | f | 103.2 | 55.2 | 73.3 | 84.3 | 75.2 | 61.3 | 174.3 | 22.7 | |
| w/o drug | f | 103.5 | 55.2 | 73.2 | 84.2 | 75.2 | 60.6 | 174.3 | 22.5 | |
| | Δ | -0.3 | 0 | 0.1 | 0.1 | 0 | 0.7 | 0 | 0.2 | 0.3 |
| Amphotericin B | | | | | | | | | | |
| With drug | a | 104.3 | 55.7 | 73.2 | 83.8 | 75.2 | 60.7 | 173.9 | 23.3 | |
| w/o drug* | a | 103.7 | 55.4 | 73.6 | 83.9 | 74.9 | 60.7 | 173.6 | 22.8 | |
| | Δ | 0.5 | 0.3 | -0.4 | -0.1 | 0.2 | 0 | 0.4 | 0.5 | 0.3 |
| With drug | b | 104.2 | 55.2 | 73.3 | 82.9 | 75.6 | 60.9 | 174.7 | 22.8 | |
| w/o drug | b | 104.0 | 55.2 | 73.4 | 82.9 | 74.9 | 60.6 | 174.1 | 22.7 | |
| | Δ | 0.2 | 0 | -0.1 | 0.0 | 0.7 | 0.3 | 0.6 | 0.1 | 0.3 |
| With drug | c | 103.0 | 55.7 | 73.4 | 84.1 | 74.9 | 60.4 | 174.9 | 23.4 | |
| w/o drug | c | 103.0 | 56.2 | 73.8 | 83.8 | 74.9 | 60.5 | 175.7 | 23.1 | |
| | Δ | 0 | -0.5 | 0.4 | 0.3 | 0 | -0.1 | -0.7 | 0.3 | 0.3 |

Table 4.4 (cont'd)

| | | | | | | | | | | |
|---|---|---|---|---|---|---|---|---|---|---|
| With drug | d | 103.6 | 55.1 | 73.4 | 83.3 | 75.8 | 60.4 | 174.4 | 22.7 | |
| w/o drug | d | 103.8 | 54.7 | 73.3 | 83.5 | 75.6 | 60 | 174.1 | 22.8 | |
| | Δ | 0.2 | 0.4 | 0.1 | -0.2 | 0.2 | 0.4 | 0.3 | -0.1 | 0.3 |
| With drug | e | 104 | 54.9 | 73.9 | 82.7 | 76.1 | 60.5 | 173.6 | 22.4 | |
| w/o drug | e | 103.4 | 54.7 | 73.6 | 82.8 | 75.9 | 60.3 | 174.4 | 22.5 | |
| | Δ | 0.6 | 0.2 | 0.3 | -0.1 | 0.2 | 0.2 | -0.8 | -0.1 | 0.3 |
| With drug | f | 103.2 | 55.2 | 73.3 | 84.3 | 75.2 | 61.3 | 174.3 | 22.7 | |
| w/o drug | f | 103.3 | 55.6 | 73.4 | 84.2 | 75 | 60.8 | 174.3 | 23.0 | |
| | Δ | -0.1 | -0.4 | -0.1 | 0.1 | 0.2 | 0.5 | 0 | -0.4 | 0.3 |

# CHAPTER 5: SOLID-STATE NMR ANALYSIS OF UNLABELED FUNGAL CELL WALLS FROM *ASPERGILLUS* AND *CANDIDA* SPECIES

Reprinted with permission from Liyanage D Fernando, Malitha C. Dickwella Widanage, S Chandra Shekar, Frederic Mentink-Vigier, Ping Wang, Sungsool Wi, and Tuo Wang *Journal of Structural Biology X* 6, 100070 (2022). 

## 5.1 Abstract

Fungal infections cause high mortality in immunocompromised individuals, which has emerged as a significant threat to human health. The efforts devoted to the development of antifungal agents targeting the cell wall polysaccharides have been hindered by our incomplete picture of the assembly and remodeling of fungal cell walls. High-resolution solid-state nuclear magnetic resonance (ssNMR) studies have substantially revised our understanding of the polymorphic structure of polysaccharides and the nanoscale organization of cell walls in *Aspergillus fumigatus* and multiple other fungi. However, this approach requires $^{13}C/^{15}N$-enrichment of the sample being studied, severely restricting its application. Here we employ the dynamic nuclear polarization (DNP) technique to compare the unlabeled cell wall materials of *A. fumigatus* and *C. albicans* prepared using both liquid and solid media. For each fungus, we have identified a highly conserved carbohydrate core for the cell walls of conidia and mycelia, and from liquid and solid cultures. Using samples prepared in different media, the recently identified function of α-glucan, which packs with chitin to form the mechanical centers, has been confirmed through conventional ssNMR measurements of polymer dynamics. These timely efforts not only validate the structural principles recently discovered for *A. fumigatus* cell walls in different morphological stages, but also open up the possibility of extending the current investigation to other fungal materials and cellular systems that are challenging to label.

## 5.2 Introduction

The carbohydrate components in the fungal cell walls are promising therapeutic targets of novel antifungal drugs for combating life-threatening infections by pathogenic fungi[1]. Two families of compounds (echinocandins and terpenoids) have been developed to disrupt the biosynthesis of β-glucans in the cell wall, and another antifungal named nikkomycin is a potent inhibitor of chitin synthesis[2-6]. Unfortunately, nikkomycin only has weak activity against most fungal species, and the β-glucan inhibitors often suffer from the compensatory paradoxical effect, through which the chitin level is massively elevated to compensate for the loss of β-glucans[7,8]. Hence, an in-depth understanding of the biosynthesis and structure of fungal polysaccharides, as well as the structural dynamics of the assembled cell walls, may facilitate the discovery of more effective antifungal compounds from the structural perspective.

Solid-state NMR (ssNMR) spectroscopy is a non-destructive and high-resolution method for elucidating the structure of fungal biopolymers[9]. This method has been extensively employed to track melanization in *Cryptococcus neoformans* and other fungi[10-12]. Studies have also been conducted on the analysis of *Aspergillus fumigatus* biofilm, with a focus on the quantification of carbon contributions in the extracellular matrix[13,14]. Additionally, multidimensional ssNMR methods have been employed to investigate the nanoscale organization of *A. fumigatus* cell walls as well as its responses to stresses[15,16]. The samples being used in these studies are intact cells without chemical treatment, which allowed the investigation of biomolecules in a fully native physical state. This method was also combined with chromatography and mass spectrometry to understand the cell wall structure of *Schizophyllum commune*[17].

Notably, in two recent ssNMR studies of *A. fumigatus*, a substantially revised structural scheme of the mycelial cell wall has been proposed[15,16]. The rigid and hydrophobic scaffold of the

*A. fumigatus* cell wall is formed by tightly associated chitin and α-1,3-glucan, which is dispersed in a mobile and hydrated matrix formed by branched β-1,3-glucans. Two other polysaccharides, including galactomannan and galactosaminogalactan, are found to mainly form the outermost dynamic layer, together with proteins on the cell surface. These structural aspects derived from ssNMR data provide a physical vision of polymer dynamics and packing, complementing the existing chemical analyses that reveals a chemical vision of the polymer cross-linking and extractability. Functional genomics approaches were also employed to generate mutant lines, each of which selectively remove an important carbohydrate component, to evaluate the functions of different polysaccharides and the remodeling of cell walls under internal stresses[16]. Statistical methods are also available for analyzing the polymorphic structure of polysaccharides in living fungal cells as demonstrated using chitin and chitosan[18].

These ssNMR studies often require isotopic enrichment of the sample, e.g., by $^{13}C$ and $^{15}N$, to allow 2D and 3D correlation experiments to be completed in a reasonable time frame, yet with adequate resolution. In fungal research, this has been achieved by germinating conidia into mycelia in minimal liquid media containing $^{13}C$-glucose and $^{15}N$ sources. But there is a dire need for a method to validate the recent structural findings by examining samples prepared in solid media, a condition more widely used in microbiology research, in order to better integrate the structural concepts derived from ssNMR and biochemical approaches to promotes sporulation[16,19]. Also, the previous studies of *A. fumigatus* were primarily focused on the mycelium. It is questionable if the structural concepts could be applied to cells at different developmental stages, for example, the conidium. The inhaled conidia *of A. fumigatus* germinate into vegetative hyphae, invading patient lungs during infection[20,21]. Even though it has been shown that the conidial and mycelial cell walls

of *A. fumigatus* differ in their composition and organization[22], at this moment, we still lack a detailed molecular-level understanding of the conidial cell walls[23].

Here we show that such challenges can be addressed by introducing natural-abundance (NA) magic-angle spinning dynamic nuclear polarization (MAS-DNP), which has been widely used in biopolymer and material research[24-28], to better characterize fungal cell walls. This sensitivity-enhancing technique has made it possible to collect 2D correlation spectra using unlabeled samples. The NMR linewidths of most fungal carbohydrates are found to be substantially broadened at the cryogenic temperature of MAS-DNP due to their highly dynamic nature. A reserved carbohydrate core has been identified in *A. fumigatus* mycelia and conidia using unlabeled samples prepared in solid and liquid media, which could not be possible without the atomic resolution provided by the DNP-enabled 2D $^{13}C$-$^{13}C$ correlation spectra of these unlabeled materials. Further examination of polymer dynamics using conventional ssNMR at ambient temperature confirmed the recently proposed structural function of α-1,3-glucan in forming the stiff core of *A. fumigatus* cell walls in both mycelia and conidia. Finally, we extend this study to another prevalent fungal pathogen *Candida albicans*, demonstrating the applicability of these approaches in fungal research.

## 5.3 Materials and Methods

### 5.3.1 Preparation of Fungal Materials

Four unlabeled samples from *A. fumigatus* (RL 578) and *C. albicans* (SC5314) were grown using both liquid and solid media for MAS-DNP investigations. Unlabeled *A. fumigatus* materials were prepared in two ways using either solid or liquid media. The solid culture was prepared in YPD (Yeast-Extract Peptone Dextrose) agar. The liquid cultures were prepared in 100 mL of modified minimal media containing 10.0 g/L of glucose and 6.0 g/L of sodium nitrate. The pH of

the media was adjusted to 6.5. Both liquid and solid cultures were incubated for 3 days at 30 °C (at 210 rpm). Similarly, both solid and liquid cultures were prepared for *C. albicans* without labeling. The solid culture was grown in YNB (Yeast Nitrogen Base) media with agar, 2% of glucose and 1 % of ammonium sulfate. The liquid culture was prepared using YNB, 2% of glucose and 1 % of ammonium sulfate with pH adjusted to 5.8-6. The fungal material was harvested by centrifugation at 7000 g for 20 minutes. The fungal material was washed using 10 mM phosphate buffer saline (pH 7.4) to remove excess ions. Only the greenish center region of the solid culture was collected.

To validate the results obtained on unlabeled materials described above, we also prepared $^{13}C$, $^{15}N$-labeled samples using liquid media. The uniformly $^{13}C$,$^{15}N$-labeled *A. fumigatus* sample was prepared by adding 10.0 g/L of $^{13}C$ glucose and 6.0 g/L of $^{15}N$-labeled sodium nitrate to the minimal liquid media[29]. The uniformly $^{13}C$,$^{15}N$-labeled *C. albicans* sample was prepared by adding 2% of $^{13}C$ glucose and 1% of $^{15}N$-labeled ammonium sulfate into the YNB liquid media. Both strains were grown for 3 days at 30 °C.

### 5.3.2 Transmission Electron Microscopy and Scanning Electron Microscopy

Transmission electron microscopy (TEM) was conducted using a JEOL JEM-1400 electron microscope. The sample was placed onto a glow discharged TEM grid for several minutes. It was stained using a mixture of 2% uranyl acetate and lead citrate solution. The cell wall thickness was measured using ImageJ software[30] after setting the scale in accordance with known bar scales on the cell images. Scanning electron microscopy (SEM) was conducted using an FEI Quanta 3D FEG field emission scanning electron microscope to examine the surface morphology of the cells. Briefly, cells were collected by filtration and fixed on 0.4 μm pore polycarbonate filter in 2% glutaraldehyde, 2% formaldehyde, and 1% OsO4. The sample was rinsed with distilled water,

dehydrated with graded ethanol series, and dried with HMDS reagent. The cells were mounted to aluminum specimen stubs and coated with platinum in an EMS550X sputter coater for imaging.

### 5.3.3 Sample preparation for MAS-DNP measurements

Unlabeled fungal materials were mixed with the stock solution containing the biradicals needed for MAS-DNP. The stock solution contains 30 mM of c-AsymPol-POK biradicals[31,32] in 40 µL of d6-DMSO-$D_2O$-$H_2O$ (1:8:1 vol%) that was used to avoid $^{13}C$ signal contribution from the solvents (e.g., from glycerol). The volume percentages of different solvents used here deviate from conventional recipes used for MAS-DNP of biomolecular samples. It is fully based on repeated optimizations of these fungal materials for the best sensitivity. To test the effect of the DNP juice, a different solvent of $^{13}C$-depleted, $d_8$-glycerol/$D_2O$/$H_2O$ (6:3:1 vol%), as well as the AMUPol biradicals[33], were used for the samples prepared in solid media. The fungal samples were mildly ground using a set of mortar and pestle when being wetted by the cryoprotectant solution. This allows the radicals to penetrate and distribute in the porous cell wall, without perturbing the appearance of the fungal pellet and the molecular-level structure of molecules. Around 30 mg of fungal material was packed into 3.2 mm sapphire rotors.

### 5.3.4 MAS-DNP experiments

The MAS-DNP experiments were conducted on a 600 MHz (14.1 T)/395 GHz instrument using a 3.2-mm HCN DNP probe. The power of microwave irradiation was around 12 W. The temperature was ~100 K with microwave irradiation and decreased to 94 K when the microwave was turned off. The DNP buildup time constants were 2.6-s and 3.1-s for *C. albicans* samples prepared in solid and liquid media, respectively. The number was shortened to 1.3-s for the *A. fumigatus* solid sample. The MAS rate was 10.5 kHz for all DNP experiments unless mentioned otherwise. 1D $^{1}H$-$^{13}C$ cross-polarization [34] experiments were measured using $^{1}H$ field of 50 kHz,

providing a sideband match to the $^{13}C$ field of 39.5 kHz, and 1-ms contact time. 2D refocused dipolar (SPC5)[35] INADEQUATE spectra[36] were collected under 10.5 kHz MAS. The field strength of $^{1}H$ decoupling during SPC5 blocks was 100 kHz. A Double-Quantum Filtered (DQF) 2D dipolar $^{13}C$-$^{13}C$ correlation NMR experiment[37] was carried out on *A. fumigatus* solid culture. The $^{1}H$ and $^{13}C$ 90-degree pulse lengths were 2.5-μs and 4-μs, respectively. In the indirect dimension, 200-300 increments were collected. In total, 64, 32, and 32 transients were added for signal-averaging purposes. The DARR mixing time was either 100-ms or 250-ms. The $^{1}H$-$^{13}C$ CP mixing was 0.5 ms. All the acquisition parameters are summarized in Table 5.1.

Spectral deconvolution was performed on 1D $^{13}C$ CP MAS-DNP spectra of unlabeled liquid culture and solid culture of *C. albicans* to obtain the chemical shift, linewidth, and intensity of carbohydrate peaks. Spectral deconvolution was performed from 120 to 40 ppm for all the carbohydrate regions, using DmFit[38]. The parameters are provided in Table 5.2

### 5.3.5 Conventional Solid-State NMR Experiments at Room Temperature

The experiments were conducted on 800 MHz (18.4 Tesla) and 400 MHz (9.4 Tesla) Brucker spectrometers equipped with 3.2 mm and 4 mm HCN probes, respectively. All experiments were conducted under 13 kHz or 13.5 kHz MAS at 298 K temperature. Approximately 30 mg of sample was packed to 3.2 mm MAS rotors and around 110 mg of sample was packed in a 4 mm $ZrO_2$ rotor. The $^{13}C$ chemical shifts were externally referenced to tetramethylsilane (TMS) scale by calibrating the Cδ peak of the Met residue in the model tri-peptide N-formyl-Met-Leu-Phe-OH (MLF) to 14.0 ppm. The radiofrequency field strength was 83 kHz for $^{1}H$ decoupling and 62.5 kHz for $^{13}C$ hard pulse and 50 kHz for $^{1}H$ and $^{13}C$ CP spin lock. The acquisition parameters are tabulated in Table 5.1.

To compare with the results of unlabeled samples, we measured 2D $^{13}$C CP refocused J-INADEQUATE spectra using a uniformly $^{13}$C-labeled *A. fumigatus* sample (liquid culture) on the 800 MHz spectrometer. We also measured a uniformly $^{13}$C-labeled *C. albicans* sample (liquid culture), resulting in a 2D $^{13}$C direct polarization (DP) refocused J-INADEQUATE spectrum measured on the 800 MHz spectrometer and a $^{13}$C CP refocused dipolar (SPC5) INADEQUATE spectrum collected on the 400 MHz NMR. To investigate the polymer dynamics in the unlabeled fungal cell wall, $^{13}$C-$T_1$ relaxation was measured. It was measured using CP-based $T_1$ pulse sequences[39] with a z-filter varied from 0 to 5 s. The relative intensity of each data point (relative to the first data point) was plotted as a function of time. The curve was fit using a bi-exponential equation. For $^{13}$C-$T_1$ relaxation measurements, the number of scans was between 1,024 and 4,096 for each data point of *A. fumigatus* samples prepared in solid and liquid media.

## 5.4 Results and Discussion

### 5.4.1 Morphological Difference of Fungal Cells Cultured in Solid and Liquid Media

*A.fumigatus* cells have different morphologies when prepared in solid and liquid media (Figure 5.1a)[40-44]. In a Petri dish containing YPD agar, *A. fumigatus* exhibited circular growth with greenish-blue conidia at the center and white mycelial threads at the edge (Figure 5.1a; top row). The surface morphology of the greenish-blue center region was examined using SEM images, which revealed a 2-3 μm diameter for the conidia of *A. fumigatus* (asexual spores) produced in conidiophores (fruiting body). Part of the outer cell wall of conidia should be covered with melanin, as indicated by the rough surface in the conidia observed in the zoomed-in regions of SEM images[45]. The conidia from fungal plates were taken and inoculated into liquid minimal media and cultured at 30 $^{o}$C for 3 days (Figure 5.1a; bottom row). The filamentous structures

observed by SEM have confirmed that *A. fumigatus* mainly grew into hyphal form under this culture condition.

Evidently, the use of solid media has promoted asexual sporulation in *A. fumigatus* samples (Figure 5.1a). *A. fumigatus* adapts to the stressful environments during host interactions and acquires different morphotypes in their life cycle[46,47]. The composition and organization of fungal cell walls are always changing in response to the morphotypes in the life cycle and growth conditions[48]. The mycelium is the vegetative morphotype and the conidium is typically considered the infective morphotype[43]. The conidia of *A. fumigatus* disperse and colonize different habitats, for instance, the lung alveoli, germinating into hyphae and causing invasive infections[40,49,50]. Therefore, it is of high significance to elucidating the cell wall structure in conidia.

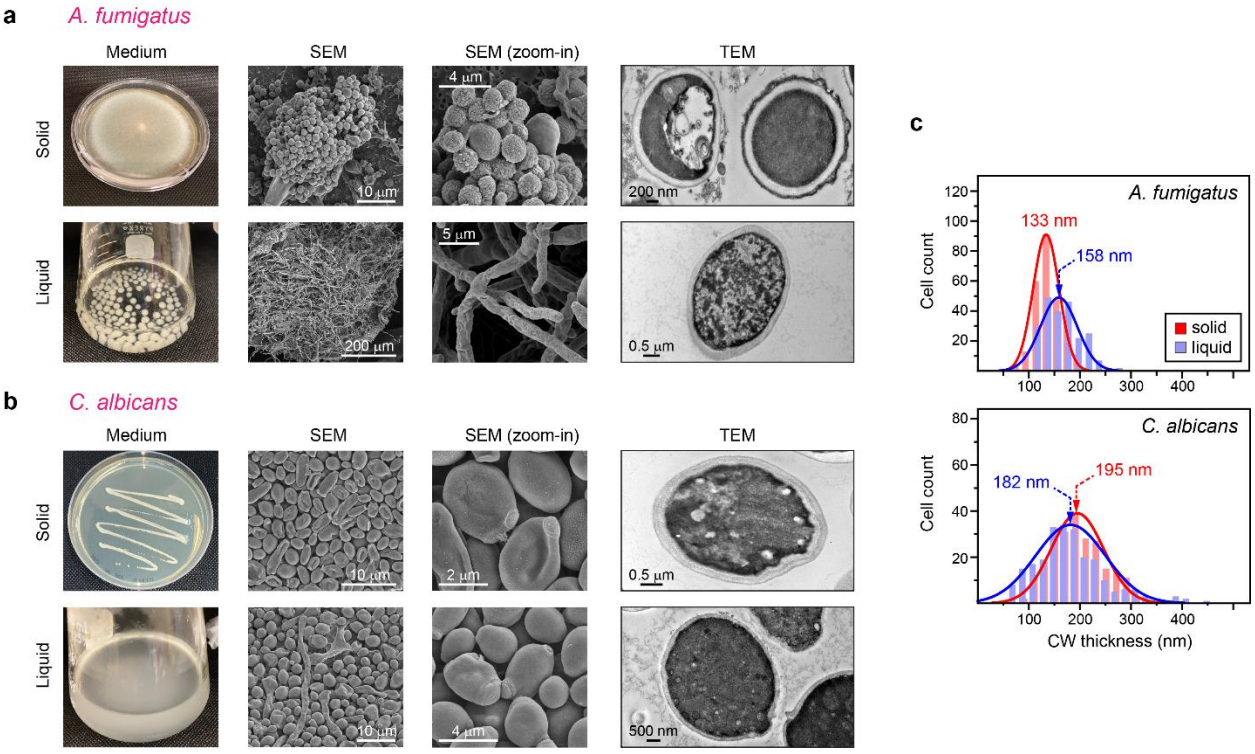


**Figure 5.1 Macro- and microscopic differences of cell morphology in 3-day-old solid and liquid cultures.** The ultrastructural features of cell walls are shown for **a,** *A. fumigatus* and **b,** *C. albicans*. From left to right, each row incorporates an image of culture, an SEM images, a zoomed-in region of the SEM images, and a TEM image. In both panels a, and b, the solid culture (top) and the liquid culture (bottom) are shown. **c,** The cell wall thickness of *A. fumigatus* (top) and *C.*

Figure 5.1 (cont'd)
*albicans* (bottom). Data are presented as a distribution, with means of 10 measurements from 15 biological replicates of each solid or liquid culture.

However, it is not trivial to convert the solid media (for example, yeast extracts) widely used in microbiology laboratories into uniformly $^{13}C$,$^{15}N$-labeled counterparts without worrying about the isotope-dilution from unlabeled components. This barrier has hindered the use of high-resolution solid-state NMR spectroscopy for characterizing fungal conidia. At the same time, fungal materials cultured in minimal liquid media could not fully represent those prepared using complex media. This situation can be improved through the development of MAS-DNP techniques, as detailed in later sections.

After 3 days of incubation in YNB solid media, *C. albicans* produced cream-colored, dull smooth yeast-like colonies (Figure 5.1b; top row). SEM images revealed the oval shape of yeast-like *C. albicans* cells with diameters of 2-4 μm. In the liquid culture (Figure 5.1b; bottom row), *C. albicans* cells exist as a mixture of hyphae, pseudo hypha, and yeast forms, with the yeast form being the most prominent. The hyphae and germ tubes were present as minor components and hence were excluded from further consideration. Interpretation and conclusion in later sections are drawn by treating the yeast form as the overwhelmingly dominant form in the liquid cultures.

TEM images were used to quantify the distribution of cell wall thickness (Figure 5.1c and Table 5.3) in *A. fumigatus* and *C. albicans* samples harvested from solid and liquid media. For *A. fumigatus*, the average thickness of the cell wall increased from 133 nm for the conidia (solid media) to 158 nm for the hypha (liquid culture). However, the change is much smaller between *C. albicans* materials prepared using solid and liquid conditions. Presently, it is not clear how the microscopic features of cellular morphology arise from the molecular-level organization of cell walls, warranting further investigations.

### 5.4.2 Sensitivity-Enhancement of Fungal Materials by MAS-DNP

The *A. fumigatus* and *C. albicans* samples harvested from solid media were impregnated in a matrix of DMSO/$D_2O$/$H_2O$ containing 20 mM AsympolPOK. This recently designed biradical promotes efficient polarization and provides fast DNP buildup through electron dipolar and exchange interactions[31]. AsympolPOK yielded a very short DNP buildup time of 1.3-3.1 s for these fungal samples (Table 5.4), making it possible to use short recycle delays, in turn resulting in the rapid acquisition of experiments. AsympolPOK biradicals were stable in fungal samples as confirmed by electron paramagnetic resonance (EPR) spectra (Figure 5.7). The sensitivity was enhanced by 26 to 30 times for both *A. fumigatus* and *C. albicans* under microwave irradiation (Figure 5.2a, b), reducing the experimental time by 676-900 fold. Though the 1D $^{13}C$ peaks were very broad, some fine features of the peaks could still be discerned. The major signals are from chitin (Ch), β-1,3-glucan (B), and α-1,3-glucan (A) in *A. fumigatus*. For *C. albicans*, the prominent peaks emanated from chitin, β-1,3-glucan, and β-1,6-glucan (H). Determination of the linewidth and analysis of the nature of these peaks were aided by 2D $^{13}C$ correlation spectra, as described in detail later.

Notably, a record high sensitivity enhancement factor of 90-fold was achieved using an *A. fumigatus* sample doped with AMUPol using $^{13}C$-depleted, $d_8$-glycerol/$D_2O$/$H_2O$ solvent (Figure 5.2c). The $^{13}C$-depleted solvent is chosen to avoid the detection of glycerol signals that overlay with carbohydrate peaks. To our best knowledge, the 90-fold enhancement is the highest value reported for any cell wall system on a 600 MHz/395 GHz DNP, but this sample was not used for measuring 2D experiments. The first reason is the prohibitively long DNP buildup time, 5.0 s for this sample instead of 1.3 s for the other A. fumigatus sample (Table 5.4). A longer buildup time requires proportionally longer recycle delays, hence negating any sensitivity gain per unit time.

Another consideration is the inhomogeneous hyperpolarization of this sample, with a preferentially higher enhancement for carbohydrate peaks relative to aromatic signals. It is a sign that the radicals were unevenly distributed across different polymer domains, and this spectrum may not accurately reflect the composition.

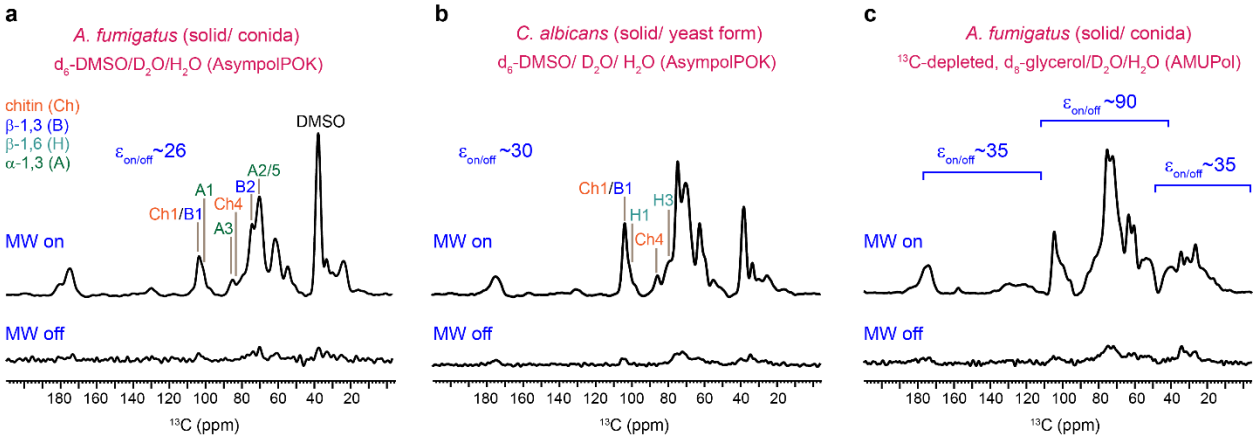


**Figure 5.2 Sensitivity enhancement by MAS-DNP on unlabeled fungal materials.** 1D $^{13}C$ spectra of unlabeled fungal samples were shown for **a,** *A. fumigatus* solid culture (mainly conidia) and **b,** *C. albicans* solid culture (mainly yeast form) prepared using $d_6$-DMSO/$D_2O$/$H_2O$ with 20 mM AsympolPOK. The spectra collected with and without microwave (MW) radiation were compared to give the enhancement factor ($\varepsilon_{on/off}$). **c,** 1D $^{13}C$ spectra of unlabeled cell walls of *A. fumigatus* solid culture (mainly conidia) in $^{13}C$-depleted, $d_8$-glycerol/$D_2O$/$H_2O$ matrix with 10 mM AMUPol radical. This sample has different enhancement factors for carbohydrate ($\varepsilon_{on/off}$ ~90) and protein and lipids ($\varepsilon_{on/off}$~35 for aliphatic, aromatic, and unsaturated carbons).

### 5.4.3 2D $^{13}C$ correlation spectra of unlabeled *A. fumigatus* in solid and liquid media

The enhancement of NMR sensitivity gained by MAS-DNP allowed us to collect 2D $^{13}C$-$^{13}C$ correlation spectra using unlabeled *A. fumigatus* materials harvested from the solid media, which is a mixture of conidia and mycelia. In this study, the greenish conidia region was used for NMR measurements. Chemical analysis has reported that the core polysaccharides are conserved (though with variable composition) in the cell walls of hypha and conidium, but the conidium has additional layers of rodlets and melanin on the cell surface while the hypha is covered by galactosaminogalactan[42]. The chemical similarity of carbohydrate structure is informed by the

similar spectral patterns of *A. fumigatus* materials cultured in liquid and solid media, providing an implication of the similarity in hyphae and conidia (Figure 5.3a, b). Most of the carbohydrate signals observed in the $^{13}$C-labeled samples of *A. fumigatus* liquid culture, which is hyphae-dominant, showed corresponding signals in the natural-abundance 2D $^{13}$C-$^{13}$C correlation MAS-DNP spectrum of the solid culture (Figure 5.3b).

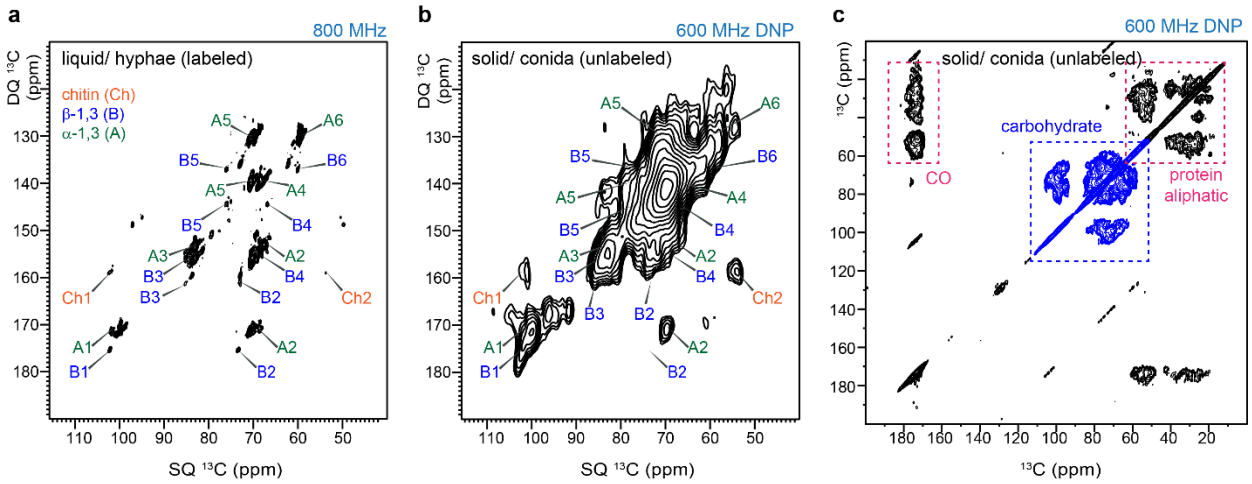


**Figure 5.3 2D $^{13}$C-$^{13}$C correlation spectra of unlabeled *A. fumigatus* samples. a,** CP refocused J-INADEQUATE spectrum measured on 800 MHz NMR at room temperature using $^{13}$C/$^{15}$N-labeled *A. fumigatus* sample prepared in liquid culture (hyphae). **b,** CP refocused dipolar-INADEQUATE spectrum of unlabeled *A. fumigatus* solid culture (mostly conidia) measured on 600 MHz/395 GHz DNP. **c,** DQF 2D dipolar $^{13}$C-$^{13}$C correlation spectra of unlabeled *A. fumigatus* solid culture sample measured on 600 MHz/395 GHz DNP.

The chitin signals became stronger in the solid culture, as exemplified by the well-resolved peaks of chitin carbons 1 and 2 (Ch1 and Ch2) that resonate at 103 ppm and 55 ppm on the single-quantum [51] chemical shift dimension. This is an indication of a larger amount of chitin in the samples prepared using solid media. Chitin is among the most rigid molecules of *A. fumigatus* cell walls and its signals be preferentially detected by CP-based experiments at room-temperature. However, chitin signals are very weak in the CP refocused INADEQUATE spectrum of liquid culture (Figure 5.3a), consistent with its low intensities observed in two recent studies of *A.*

*fumigatus*, which is likely due to the low content of this molecule in liquid cultures[15,16]. Signals were also observed for another two other major carbohydrates, α-1,3-glucans and β-1,3-glucans. The results suggest that at least the major constituents are shared between the hyphae and conidia. Many additional signals showed up in the DNP spectrum of the solid culture, likely from more mobile molecules, for example, galactomannan. Mobile carbohydrates are undetectable in the CP-based spectrum at room-temperature (Figure 5.3a) but will become visible at the cryogenic temperature of MAS-DNP (Figure 5.3b).

Unfortunately, the NMR linewidth, given by the full width at half maximum (FWHM), increased substantially at MAS-DNP conditions. The FWHM linewidths of resolved peaks in this 2D refocused INADEQUATE spectrum were 2-3 ppm. This is considerably broader than the 0.5-0.9 ppm reported for samples measured at ambient temperature at a higher magnetic field (800 MHz) and is worse than the expectation for a spectrum collected on a 600 MHz ssNMR at room temperature. The spectral quality presented in Figure 5.3b is much worse than that of unlabeled plant cell walls[52,53]. This is due to the more dynamic nature of fungal cell walls compared to their counterparts in plants[15,52]. Crystalline components efficiently retain their sharp linewidth at 100 K during MAS-DNP measurements, which has been shown using the cellulose microfibrils in plant biomass[52,53]. The major crystalline molecule in fungi is chitin, and it accounts for only 10-20% of the dry mass of *A. fumigatus* cell wall[47]. All other molecules, such as glucans, mannans, and exopolysaccharides, will suffer from the line-broadening effect due to their intrinsic disorder.

The most promising spectrum of unlabeled *A. fumigatus* was collected using a double-quantum filtered (DQF) 2D dipolar $^{13}C$-$^{13}C$ correlation scheme (Figure 5.3c)[37]. This experiment was finished in 30 hrs. The DQF-DARR spectrum of the solid *A. fumigatus* culture showed carbohydrate signals at 60-105 ppm, as well as unexpectedly strong signals of proteins, including

both aliphatic carbons (0-70 ppm) and carbonyl groups (165-180 ppm). The quality of the DQF-DARR spectrum is manifestly superior to that of the CP refocused dipolar-INADEQUATE spectrum, considering both resolution and sensitivity as well as simultaneous detection of proteins and carbohydrates. In addition, the dipolar-INADEQUATE spectra collected at natural abundance often exhibit unmatched intensities for two carbons in a spin pair, such as the B1-B2 pair in Figure 5.3b, which is not an issue in the DQF-DARR spectrum.

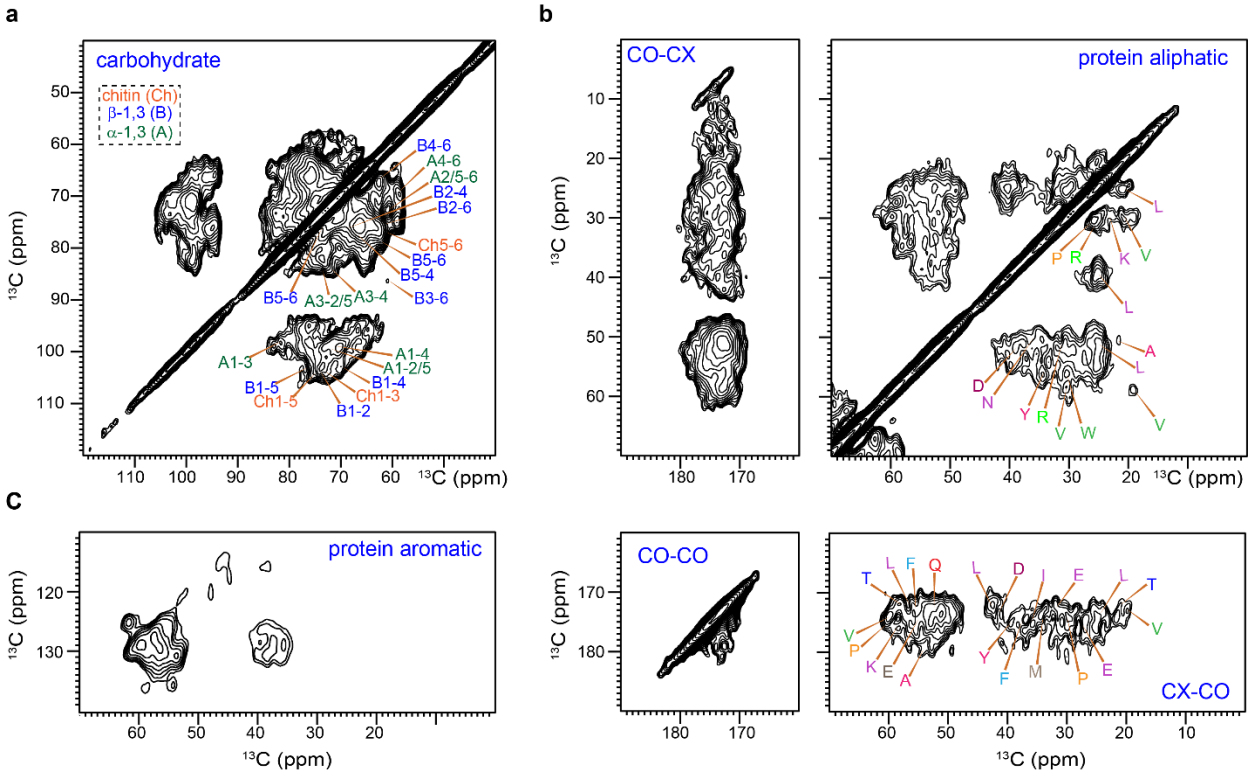


**Figure 5.4 DNP-enabled 2D correlation spectra of unlabeled *A. fumigatus* solid culture (mostly conidia).** Selected regions of DQF 2D dipolar $^{13}C$-$^{13}C$ correlation spectra are shown for **a,** carbohydrates, **b,** protein aliphatic and carbonyl signals, and **c,** aromatics. The CO presents the carbonyl group in proteins and the CX represents protein aliphatic carbons such as Cα and Cβ. CO-CX refers to the correlation between these carbon sites. The spectrum was acquired using the DQF-DARR sequence on a 600 MHz/395 GHz DNP.

The DQF-DARR spectrum also exhibited satisfactory resolution, allowing us to observe signals from chitin and glucans (Figure 5.4a). In addition to many one-bond correlations, the use

of 100-250 ms DARR mixing enabled the detection of many medium-range cross peaks. An example is the C1-C3 cross peak of α-1,3-glucan (denoted as A1-3), which showed up at a unique position of (101 ppm, 84 ppm). In addition, the adequate sensitivity allowed us to assign the protein signals to different amino acid types by tracking the correlations among the Cα, Cβ, and CO (Figure 5.4b). The chemical shifts are tabulated in Table 5.5. Notably, some cross peaks between the aromatic carbons and the Cα and Cβ were also identified for aromatic amino acids (Figure 5.4c). The performance of DQF-DARR is better than most other 2D $^{13}C$-$^{13}C$ correlation experiments, such as the refocused dipolar-INADEQUATE and CHHC that have been frequently employed to investigate unlabeled biomaterials[27,28,53,54]. This DQF-DARR experiment might be critical to elucidating unresolved structural aspects in fungal cell walls.

The DQF-DARR spectrum also exhibited satisfactory resolution, allowing us to observe signals from chitin and glucans (Figure 5.4a). In addition to many one-bond correlations, the use of 100-250 ms DARR mixing enabled the detection of many medium-range cross peaks. An example is the C1-C3 cross peak of α-1,3-glucan (denoted as A1-3), which showed up at a unique position of (101 ppm, 84 ppm). In addition, the adequate sensitivity allowed us to assign the protein signals to different amino acid types by tracking the correlations among the Cα, Cβ, and CO (Figure 5.4b). The chemical shifts are tabulated in Table 5.5. Notably, some cross peaks between the aromatic carbons and the Cα and Cβ were also identified for aromatic amino acids (Figure 5.4c). The performance of DQF-DARR is better than most other 2D $^{13}C$-$^{13}C$ correlation experiments, such as the refocused dipolar-INADEQUATE and CHHC that have been frequently employed to investigate unlabeled biomaterials[27,28,53,54]. This DQF-DARR experiment might be critical to elucidating unresolved structural aspects in fungal cell walls.

### 5.4.4 Examination of Biopolymer Dynamics at Room Temperature

The dynamics of biopolymers in unlabeled *A. fumigatus* materials were probed using $^{13}$C-$T_1$ relaxation, which was mapped using a series of 1D $^{13}$C spectra with a gradually increasing z-period. This ssNMR approach has been widely used in the field of polymer research, where the samples are typically difficult to label. The information on polysaccharide dynamics afforded by this method perfectly complements the insight about polysaccharide structure obtained using natural-abundance MAS-DNP, as recently demonstrated on rice stems[54].

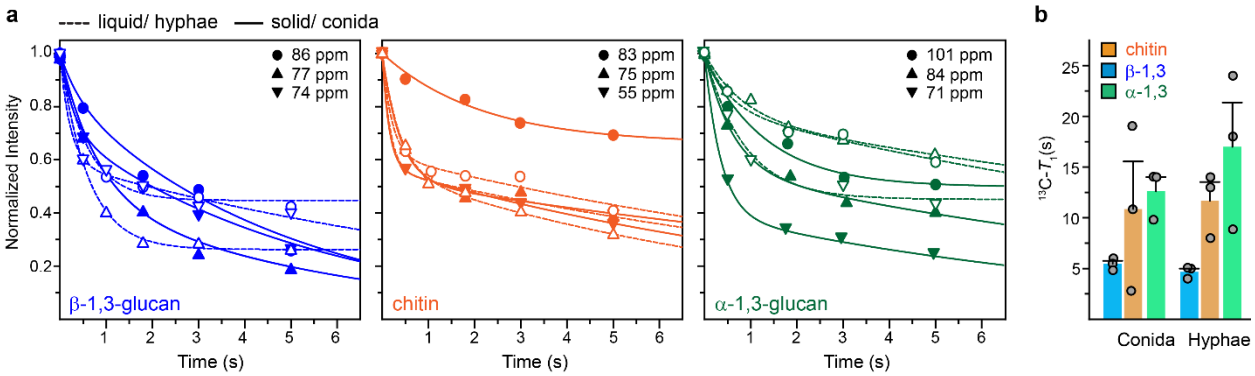


**Figure 5.5 Dynamics of biopolymers in unlabeled *A. fumigatus* cell walls measured at room temperature. a,** Representative $^{13}$C-$T_1$ relaxation curves of unlabeled *A. fumigatus* samples for β-1,3-glucans (left; blue), chitin (middle; orange), and α-1,3-glucans (right; green). The data of *A. fumigatus* grown in liquid cultures (hyphae) are plotted using open symbols and dash lines. The data of materials prepared in solid media (mainly conidia) are plotted using filled symbols and solid lines. The chemical shifts of key carbon peaks are labeled. **b,** $^{13}$C-$T_1$ time constants of different carbon sites in *A. fumigatus* samples prepared in solid and liquid media. The data are fit using bi-exponential equation, plotting only the long (or slow) component of $^{13}$C-$T_1$. Data are mean ± s.e.; data points are overlayed on the corresponding bar. The carbon sites and corresponding relaxation time constants are provided in Table 5.6.

Consistently observed in both the liquid and solid cultures, β-1,3-glucans have the fastest $^{13}$C-$T_1$ relaxation (Figure 5.5a), thus remaining the most mobile molecule in the cell walls, regardless of the fraction of hyphae and conidia. In contrast, α-1,3-glucans have the slowest relaxation, indicative of its immobility in *A. fumigatus* cell walls. The dynamics of chitin is between the α- and β-1,3-glucans, being intermediately rigid. It should be noted that one carbon

site of chitin, the C4 at 83 ppm, has exhibited very slow relaxation that is outside the range of the other carbons. This only happened to the sample prepared using solid media. We suspect that it is due to the insufficient resolution in 1D $^{13}C$ spectra, where the chitin C4 is influenced by the neighboring peak of α-1,3-glucan C3, which is just 1 ppm apart.

The bi-exponential feature became more pronounced in our unlabeled fungal materials (Figure 5.5a) compared to the data collected on uniformly $^{13}C$-labeled samples[15,16]. This is because the magnetization exchange between a pair of $^{13}C$ spins, mediated by $^{13}C$ -$^{13}C$ spin interactions, gives rise to additional relaxation pathways, thus speeding up the relaxation process, which is no longer efficient at natural $^{13}C$ abundance. The inefficient exchange with mobile motifs also accounts for the substantially longer $^{13}C$-$T_1$ time constants for the current unlabeled materials, than the uniformly $^{13}C$-labeled samples used in recent studies[15,16].

The dynamics can be better analyzed by comparing the $^{13}C$-$T_1$ derived from the slow-relaxing component, corresponding to the less mobile domain of the biopolymer (Figure 5.5b). The trends observed visually in Figure 5.5a still hold. In each sample, the $^{13}C$-$T_1$ time constants decreased successively for α-1,3-glucans, chitin, and then β-1,3-glucan. For example, the $^{13}C$-$T_1$ time constants of these three molecules in the solid media were 13 ± 1 s, 11 ± 5 s, and 5.5 ± 0.3 s, respectively (Figure 5.5b). On the other hand, $^{13}C$-$T_1$ was similar in both the solid (5.5 ± 0.3 s) and liquid (5.0 ± 0.3 s) samples for β-1,3-glucans. This recurred for chitin molecules in different sample: the $^{13}C$-$T_1$ remained similar in both solid and liquid cultures. In contrast, the $^{13}C$-$T_1$ time constant of α-1,3-glucan decreased slightly from 17 ± 4 s in the liquid culture (hyphae) to 13 ± 1 s in the solid culture (mainly conidia). Therefore, α-1,3-glucans are slightly more dynamic in the conidia, though remaining the most rigid molecule across the cell wall.

### 5.4.5 Insight into the molecular organization of *A. fumigatus* cell walls

It is generally accepted that the chitin molecule, due to its partial crystallinity, should be lending structural support to the fungal cell walls. This mechanical role is reminiscent of the function of cellulose in plant materials, consistent with its slow relaxation observed here. β-1,3-glucans are the major cross-linking polysaccharides in *A. fumigatus* cell walls and are the key components for forming the chitin-β-1,3-glucan-mannan core, a domain containing three covalently linked polysaccharides[55]. A branched analog, β-1,3/1,6-glucan, could also be introduced via the branching site of 3,6-linked glucose residue. With these considerations, it is not surprising that β-1,3-glucan stays as a relatively mobile polysaccharide to maintain its function of crosslinking and branching. The role and dynamics of β-1,3-glucan in the fungal cell wall are similar to those of hemicellulose and pectin (together, named matrix polysaccharides) in the primary plant cell walls[52].

For decades, α-1,3-glucan has remained a mysterious molecule in *A. fumigatus* cell walls. It is largely extractable by hot alkali, thus lacking covalent bonds to other components, which has led to the assumption that α-1,3-glucan is less important to the cell wall organization[40,55]. This chemical view has been revamped recently, where a large number of cross peaks (physical contact on the sub-nanometer scale) were identified between chitin and α-1,3-glucan. The ssNMR data support a model in which chitin and the majority of α-1,3-glucan are tightly associated to form rigid aggregates that exclude water molecules to a large extent[15,16]. Though this paradigm has come under scrutiny[15,16,19], the extremely slow $^{13}$C-$T_1$ relaxation of α-1,3-glucan observed in both liquid and solid cultures, with the latter being more relevant to the conditions used in most microbiology studies[44,56,57], confirms the stiffness of most α-1,3-glucans in *A. fumigatus* cell walls.

### 5.4.6 An Exploratory Investigation of Unlabeled *C. albicans* Samples

We further applied the natural-abundance MAS-DNP method to examine unlabeled *C. albicans* samples. Satisfactory enhancement factors of 26- and 30-fold were obtained from two samples harvested from liquid and solid media, respectively (spectra not shown). Based on the sensitivity, we managed to collect nearly noiseless 1D $^{13}C$ spectra (Figure 5.6a), which showed high similarity between the solid and liquid cultures as evidenced by their consistent spectral patterns. This leads to the inference that the growing conditions have relative minor effect on the composition of cell walls. Spectral deconvolution allowed us to disentangle the underlying carbohydrate resonances (Figure 5.6a), and this process is assisted by the resolvable carbon sites in the high-resolution 2D $^{13}C$-$^{13}C$ correlation spectra enabled by MAS-DNP (Figure 5.6b). To facilitate the assignment, the 2D $^{13}C$ correlation DNP spectrum of unlabeled *C. albicans* was overlaid with a high-resolution spectrum collected at ambient temperature on a $^{13}C$-labeled sample (Figure 5.6b). In the liquid culture, this comparison allowed us to resolve the signals from β-1,3-glucans, β-1,6-glucans, chitin, as well as some mannose units, which likely originate from peptidomannans in *C. albicans* cell walls[58]. Consistent with the 1D spectra, the 2D spectra also showed a high level of consistency between the cell walls from solid and liquid cultures. Though the spectral resolution is still limited, these observations constitute an early insight into the structural similarity of the core polysaccharides in the yeast form and hyphae of *C. albicans*, and demonstrate the feasibility of using MAS-DNP to investigate different fungal strains. Notably, the *C. albicans* cells mainly exist in the unicellular form (yeast form) observed here. The fungal cell walls, especially those of *C. albicans*, are substantially more mobile than the plant materials and are considered unfavorable for MAS-DNP. The success of natural-abundance DNP thus opens the

frontier to interrogate other cellular systems with similar dynamical characteristics, such as microalgae, bacteria, and human and animal cells[59-66], without isotopic enrichment.

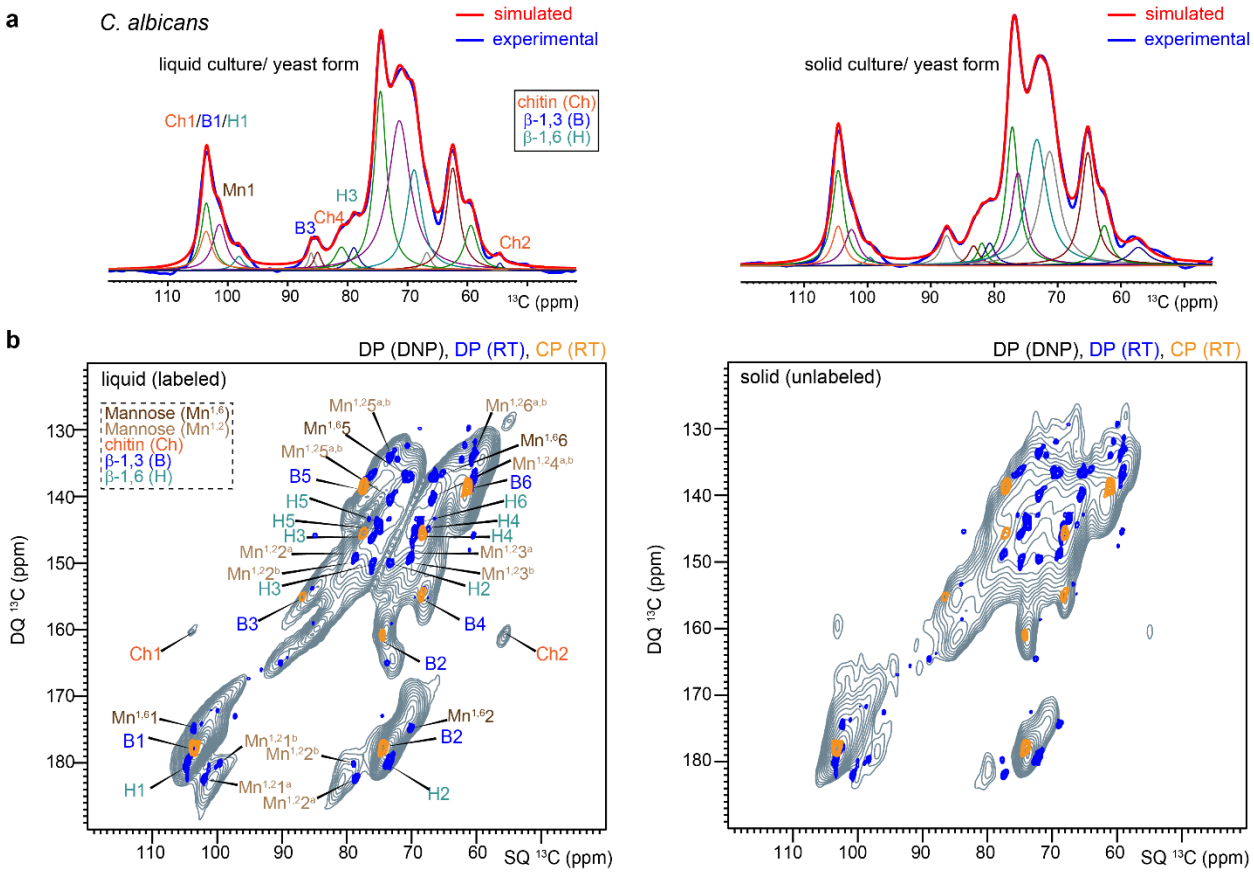


**Figure 5.6 DNP measurement of *C. albicans* samples. a,** Spectral deconvolution of 1D $^{13}$C CP spectra measured on *C. albicans* samples prepared in liquid cultures (left) and solid media (right). The spectra are measured on a 600 MHz/395GHz DNP system. The simulated spectra (red) match well with the experimentally measured spectra (blue). Underneath are many individual lines that add up to the simulated spectra. **b,** 2D $^{13}$C refocused INADEQUATE spectra of *C. albicans*. The left panel shows the CP refocused dipolar-INADEQUATE spectrum of unlabeled liquid culture measured using 600 MHz/395GHz DNP (black grey) and the right panel shows the same type of spectrum collected on unlabeled *C. albicans* materials grown in solid media. For each panel, the DNP spectrum is overlaid with two high-resolution 2D spectra measured on $^{13}$C-labeled liquid culture at room temperature (RT), including a DP refocused J-INADEQUATE spectrum measured on an 800 MHz NMR (blue) and a CP refocused dipolar-INADEQUATE spectrum measured on a 400 MHz ssNMR (yellow).

## 5.5 Conclusions

We have shown that the MAS-DNP enabled 2D $^{13}C$-$^{13}C$ correlation experiments of unlabeled fungal materials provides a way for addressing important structural questions that would remain unanswered otherwise. The fungal cell wall may however not be deemed to be the most ideal system for MAS-DNP due to the highly dynamic nature of most fungal carbohydrates (in contrast to plant cell walls) and the significant line-broadening at cryogenic temperature. Despite the difficulty, this strategy has led us to show the similarity of the major polysaccharides in unlabeled fungal materials prepared from solid and liquid media, which could not be possible without MAS-DNP. The carbohydrate fingerprints are also found to be consistent in the conidia and hyphae of *A. fumigatus*. Still, more experiments, especially those designed to measure intermolecular packing, are needed for further assessing the difference in the nanoscale organization. Such development could pave the way for investigating fungal materials that are difficult to label or replicate in the lab, such as disease-relevant fungal isolates and those requiring coculture with human and animal cells.

## 5.6 Acknowledgments

This work was supported by the National Science Foundation NSF MCB-1942665. A portion of this work was performed at the National High Magnetic Field Laboratory, which is supported by the National Science Foundation Cooperative Agreement No. DMR-1644779 and the State of Florida. The MAS-DNP system at NHMFL is funded in part by NIH S10 OD018519, NIH P41-GM122698 and NSF CHE-1229170. The authors thank Dr. Jean-Paul Latge for helpful discussions.

## REFERENCES


1 Brown, G.D. et al. Hidden Killers: Human Fungal Infections. *Sci. Transl. Med.* 4, 165rv13 (2012).

2 Perlin, D.S. Mechanisms of echinocandin antifungal drug resistance. *Ann. N. Y. Acad. Sci.* 1354, 1-11 (2015).

3 Denning, D.W. Echinocandin antifungal drugs. *Lancet* 362, 1142-1151 (2003).

4 Jallow, S. & Govender, N.P. Ibrexafungerp: A First-in-Class Oral Triterpenoid Glucan Synthase Inhibitor. *J. Fungi* 7, 163 (2021).

5 Li, Y. et al. Identification of New Antifungal Agents Targeting Chitin Synthesis by a Chemical-Genetic Method. *Molecules* 24, 3155 (2019).

6 Perlin, D.S. Cell Wall-Modifying Antifungal Drugs. *Curr. Top. Microbiol. Immunol.* 425, 255-275 (2020).

7 Aruanno, M., Glampedakis, E. & Lamoth, F. Echinocandins for the Treatment of Invasive Aspergillosis: from Laboratory to Bedside. *Antimicrob. Agents Chemother*. 63, e00399-19 (2019).

8 Loiko, V. & Wagener, J. The Paradoxical Effect of Echinocandins in Aspergillus fumigatus Relies on Recovery of the b-1,3-Glucan Synthase Fks1. *Antimicrob. Agents Chemother.* 61, e01690-16 (2017).

9 Ghassemi, N. et al. Solid-State NMR Investigations of Extracellular Matrices and Cell Walls of Algae, Bacteria, Fungi, and Plants. *Chem. Rev.* 122, 10036−10086 (2022).

10 Zhong, J.Y., Frases, S., Wang, H., Casadevall, A. & Stark, R.E. Following fungal melanin biosynthesis with solid-state NMR: Biopolyrner molecular structures and possible connections to cell-wall polysaccharides. *Biochemistry* 47, 4701-4710 (2008).

11 Chatterjee, S., Prados-Rosales, R., Itin, B., Casadevall, A. & Stark, R.E. Solid-state NMR Reveals the Carbon-based Molecular Architecture of *Cryptococcus neoformans* Fungal Eumelanins in the Cell Wall. *J. Biol. Chem.* 290, 13779-13790 (2015).

12 Chrissian, C. et al. Melanin deposition in two *Cryptococcus* species depends on cell-wall composition and flexibility. *J. Biol. Chem.* 295, 1815-1828 (2020).

13 Reichhardt, C. et al. Analysis of the *Aspergillus fumigatus* Biofilm Extracellular Matrix by Solid-State Nuclear Magnetic Resonance Spectroscopy. *Eukaryot. Cell* 14, 1064-1072 (2015).

14 Reichhardt, C., Joubert, L.M., Clemons, K.V., Stevens, D.A. & Cegelski, L. Integration of electron microscopy and solid-state NMR analysis for new views and compositional parameters of *Aspergillus fumigatus* biofilms. *Med. Mycol.* 57, S239-s244 (2019).

15 Kang, X. et al. Molecular architecture of fungal cell walls revealed by solid-state NMR. *Nat. Commun.* 9, 2747 (2018).

16 Chakraborty, A. et al. A molecular vision of fungal cell wall organization by functional genomics and solid-state NMR. *Nat. Commun.* 12, 6346 (2021).

17 Ehren, H.L. et al. Characterization of the cell wall of a mushroom forming fungus at atomic resolution using solid-state NMR spectroscopy. *Cell Surf.* 6, 100046 (2020).

18 Fernando, L.D. et al. Structural Polymorphism of Chitin and Chitosan in Fungal Cell Walls from Solid-State NMR and Principal Component Analysis. *Front. Mol. Biosci.* 8, 727053 (2021).

19 Latgé, J.P. & Wang, T. Modern Biophysics Redefines Our Understanding of Fungal Cell Wall Structure, Complexity, and Dynamics. *mBio* 13, e01145-22 (2022).

20 Dagenais, T.R.T. & Keller, N.P. Pathogenesis of Aspergillus fumigatus in Invasive Aspergillosis. *Clin. Microbiol. Rev.* 22, 447-465 (2009).

21 van de Veerdonk, F.L., Gresnigt, M.S., Romani, L., Netea, M.G. & Latge, J.P. Aspergillus fumigatus morphology and dynamic host interactions. *Nat. Rev. Microbiol.* 15, 661-674 (2017).

22 Latgé, J.-P., Beauvais, A. & Chamilos, G. The Cell Wall of the Human Fungal Pathogen Aspergillus fumigatus: Biosynthesis, Organization, Immune Response, and Virulence. *Annu. Rev. Microbiol.* 71, 99-116 (2017).

23 Ibrahim-Granet, O. et al. Phagocytosis and intracellular fate of Aspergillus fumigatus conidia in alveolar macrophages *Infect. Immun.* 75, 891-903 (2003).

24 Smith, A.N., Märker, K., Hediger, S. & De Paëpe, G. Natural Isotopic Abundance $^{13}$C and $^{15}$N Multidimensional Solid-State NMR Enabled by Dynamic Nuclear Polarization. *J. Phys. Chem. Lett.* 10, 4652-4662 (2019).

25 Märker, K. et al. Welcoming natural isotopic abundance in solid-state NMR: probing π-stacking and supramolecular structure of organic nanoassemblies using DNP. *Chem. Sci.* 8, 974-987 (2017).

26 Takahashi, H. et al. Rapid Natural-Abundance 2D $^{13}$C–$^{13}$C Correlation Spectroscopy Using Dynamic Nuclear Polarization Enhanced Solid-State NMR and Matrix-Free Sample Preparation. *Angew. Chem. Int. Ed.* 51, 11766-11769 (2012).

27 Viger-Gravel, J. et al. Topology of pretreated wood fibers using dynamic nuclear polarization. *J. Phys. Chem. C* 123, 30407-30415 (2019).

28 Perras, F.A. et al. Atomic-level structure characterization of biomass pre-and post-lignin treatment by dynamic nuclear polarization-enhanced solid-state NMR. *J. Phys. Chem. A* 121, 623-630 (2017).

29 Kirui, A. et al. Preparation of Fungal and Plant Materials for Structural Elucidation Using Dynamic Nuclear Polarization Solid-State NMR. *J. Vis. Exp.*, e59152 (2019).

30 Schneider, C.A., Rasband, W.S. & Eliceiri, K.W. NIH Image to ImageJ: 25 years of image analysis. *Nat. Methods* 9, 671-675 (2012).

31 Mentink-Vigier, F. et al. Computationally Assisted Design of Polarizing Agents for Dynamic Nuclear Polarization Enhanced NMR: The AsymPol Family. *J. Am. Chem. Soc.* 140, 11013-11019 (2018).

32 Harrabi, R. et al. Highly Efficient Polarizing Agents for MAS-DNP of Proton-Dense Molecular Solids. *Angew. Chem. Int. Ed.* 61, e202114103 (2022).

33 Sauvée, C. et al. Highly Efficient, Water-Soluble Polarizing Agents for Dynamic Nuclear Polarization at High Frequency. *Angew. Chem. Int. Ed.* 52, 10858-10861 (2013).

34 Hohwy, M., Rienstra, C.M., Jaroniec, C.P. & Griffin, R.G. Fivefold symmetric homonuclear dipolar recoupling in rotating solids: Application to double quantum spectroscopy. *J. Chem. Phys.* 110, 7983 (1999).

35 Lesage, A., Bardet, M. & Emsley, L. Through-bond carbon-carbon connectivities in disordered solids by NMR. *J. Am. Chem. Soc.* 188, 10987-10993 (1999).

36 Wi, S., Dwivedi, N., Dubey, R., Mentink-Vigier, F. & Sinha, N. Dynamic nuclear polarization-enhanced, double-quantum filtered $^{13}C$-$^{13}C$ dipolar correlation spectroscopy of natural $^{13}C$ abundant bone-tissue biomaterial. *J. Magn. Reson.* 335, 107144 (2022).

37 Massiot, D. et al. Modelling one and two-dimensional solid-state NMR spectra. *Magn. Reson. Chem.* 40, 70-76 (2002).

38 Torchia, D.A. Measurement of proton-enhanced $^{13}C$ $T_1$ values by a method which suppresses artifacts. *J. Magn. Reson.* 30, 613-616 (1978).

39 Bernard, M. & Latge, J.P. Aspergillus fumigatus cell wall: composition and biosynthesis. *Med. Mycol.* 39, 9-17 (2001).

40 Fontaine, T. et al. Cell wall α1-3glucans induce the aggregation of germinating conidia of Aspergillus fumigatus. *Fungal Genet. Biol.* 47, 707-712 (2010).

41 Latgé, J.-P. & Chamilos, G. Aspergillus fumigatus and Aspergillosis in 2019. *Clin. Microbiol. Rev.* 33, e00140-18 (2019).

42 Latgé, J.P. 30 years of battling the cell wall *Med. Mycol.* 55, 4-9 (2017).

43 Kang, S.E., Brandi, N.C., Bensasson, D. & Momany, M. Sporulation environment drives phenotypic variation in the pathogen Aspergillus fumigatus. *G3* 11, jkab208 (2021).

44 Walker, C.A. et al. Melanin Externalization in Candida albicans Depends on Cell Wall Chitin Structures. *Eukaryot. Cell* 9, 1329-1342 (2010).

45 Gow, N.A.R., Brown, A.J.P. & Odds, F.C. Fungal morphogenesis and host invasion. *Curr. Opin. Microbiol.* 5, 366-371 (2002).

46 Lee, M.J. & Sheppard, D.C. Recent advances in the understanding of the Aspergillus fumigatus cell wall. *J. Microbiol.* 54, 232-242 (2016).

47 Garcia-Rubio, R., de Oliveira, H., Rivera, J. & Trevijano-Contador, N. The fungal cell wall: Candida, Cryptococcus, and Aspergillus species. *Front. Microbiol.* 10, 2993 (2020).

48 Croft, C.A., Culibrk, L., Moore, M.M. & Tebbutt, S.J. Interactions of Aspergillus fumigatus Conidia with Airway Epithelial Cells: A Critical Review. *Front. Microbiol.* 7, 472 (2016).

49 Abad, A. et al. What makes Aspergillus fumigatus a successful pathogen? Genes and molecules involved in invasive aspergillosis. *Rev. Iberoam. Micol.* 27, 155-182 (2010).

50 Zhao, W., Fernando, L.D., Kirui, A., Deligey, F. & Wang, T. Solid-state NMR of plant and fungal cell walls: a critical review. *Solid State Nucl. Magn. Reson.* 107, 101660 (2020).

51 Kirui, A. et al. Atomic resolution of cotton cellulose structure enabled by dynamic nuclear polarization solid-state NMR. *Cellulose* 26, 329-339 (2019).

52 Zhao, W. et al. Solid-state NMR of unlabeled plant cell walls: high-resolution structural analysis without isotopic enrichment. *Biotechnol. Biofuels* 14, 14 (2021).

53 Latgé, J.-P. The cell wall: a carbohydrate armour for the fungal cell. *Mol. Microbiol.* 66, 279-290 (2007).

54 Gastebois, A., Clavaud, C., Aimanianda, V. & Latgé, J.-P. *Aspergillus fumigatus*: cell wall polysaccharides, their biosynthesis and organization. *Future Microbiol.* 4, 583-595 (2009).

55 Ashton, G.D. & Dyer, P.S. Culturing and mating of Aspergillus fumigatus. *Curr. Protoc. Microbiol.* 54, e87 (2019).

56 Hall, R.A. & Gow, N.A. Mannosylation in Candida albicans: role in cell wall function and immune recognition. *Mol. Microbiol.* 90, 1147-1161 (2013).

57 Takahashi, H. et al. Solid-state NMR on bacterial cells: selective cell wall signal enhancement and resolution improvement using dynamic nuclear polarization. *J. Am. Chem. Soc.* 135, 5105-10 (2013).

58 Overall, S.A. & Barnes, A.B. Biomolecular Perturbations in In-Cell Dynamic Nuclear Polarization Experiments. *Front. Mol. Biosci.* 8, 743829 (2021).

59 Albert, B.J. et al. Dynamic Nuclear Polarization Nuclear Magnetic Resonance in Human Cells Using Fluorescent Polarizing Agents. *Biochemistry* 57, 4741-4746 (2018).

60 Romaniuk, J.A.H. & Cegelski, L. Bacterial cell wall composition and the influence of antibiotics by cell-wall and whole-cell NMR. *Philos. Trans. R. Soc. B* 370, 20150024 (2015).

61 Poulhazan, A. et al. Identification and Quantification of Glycans in Whole Cells: Architecture of Microalgal Polysaccharides Described by Solid-State Nuclear Magnetic Resonance. *J. Am. Chem. Soc.* 46, 19374-19388 (2021).

62 Poulhazan, A., Arnold, A.A., Warschawski, D.E. & Marcotte, I. Unambiguous *Ex Situ* and in Cell 2D $^{13}$C Solid-State NMR Characterization of Starch and Its Constituents. *Int. J. Mol. Sci.* 19(2018).

63 Arnold, A.A. et al. Whole cell solid-state NMR study of *Chlamydomonas reinhardtii* microalgae. *J. Biomol. NMR* 70, 123-131 (2018).

64 Ghosh, R., Xiao, Y., Kragelj, J. & Frederick, K.K. In-Cell Sensitivity-Enhanced NMR of Intact Living Mammalian Cells. *J. Am. Chem. Soc.* 143, 18454-18466 (2021).

65 Lowman, D. W. *et al.* New insights into the structure of (1→ 3, 1→ 6)-β-D-glucan side chains in the Candida glabrata cell wall. *PloS one* **6**, e27614 (2011).

66 Fritzsching, K., Yang, Y., Schmidt-Rohr, K. & Hong, M. Practical use of chemical shift databases for protein solid-state NMR: 2D chemical shift maps and amino-acid assignment with secondary-structure information. *Journal of biomolecular NMR* **56**, 155-167 (2013).

# APPENDIX

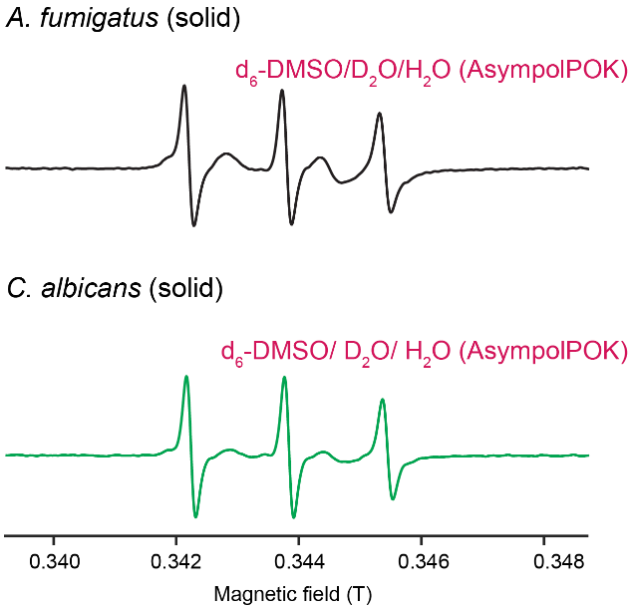


**Figure 5.7 Room-temperature EPR spectra of AsympolPok at 9.6 GHz.**

**Table 5.1 Experimental parameters used for MAS-DNP and ssNMR on intact fungal cells.** Abbreviations are used for $^{1}$H Lamour frequency ($\omega_{0,\,1H}$), total experimental time (t), recycle delay (d1), number of scans (NS), number of points in F2 (td2), number of increments in F1 (td1), acquisition time during t2 for F2 (aq2), and indirect acquisition time for F1 (aq1). Not appliable (-). Experiments were collected on either a 600 MHz/395 GHz MAS-DNP, an 800 MHz ssNMR, or a 400 MHz ssNMR.

| Sample | Experiment | $\omega_{0,\,1H}$ (MHz) | t (hr) | MAS (kHz) | NS | d1 (s) | td2 | td1 | aq2 (ms) | aq1 (ms) |
|---|---|---|---|---|---|---|---|---|---|---|
| *C. albicans* (solid) | 1D $^{1}$H (MW on/off) | 600 | 2.2 | 8 | 2 | 1.0 | - | 4096 | - | 5.7 |
| | 1D $^{13}$C (MW on/off) | | 63.7 | 10.5 | 64 | 3.5 | - | 1024 | - | 5.7 |
| | 1D CP | | 254 | | 256 | 3.5 | - | 1024 | - | 5.7 |
| | CP refocused dipolar (SPC5) INADEQUATE | | 20 | | 256 | 3.5 | 2048 | 80 | 17.2 | 1.2 |
| *C. albicans* (liquid) | 1D $^{1}$H (MW on/off) | 600 | 2.2 | 8 | 2 | 1.0 | - | 4096 | - | 5.7 |
| | 1D $^{13}$C (MW on/off) | | 72.8 | 10.5 | 64 | 4.0 | - | 1024 | - | 5.7 |
| | CP refocused dipolar (SPC5) INADEQUATE | | 5.6 | | 256 | 4.0 | 2048 | 80 | 17.2 | 1.2 |
| | DP refocused J-INADEUQATE | 800 | 0.4 | 13.5 | 8 | 1.5 | 2600 | 120 | 19.4 | 1.2 |
| | CP refocused dipolar (SPC5) INADEQAUTE | 400 | 5.2 | 7.5 | 112 | 1.7 | 1800 | 100 | 18.0 | 6.2 |
| *A. fumigatus* (solid) | 1D $^{1}$H (MW on/off) | 600 | 2.2 | 8 | 2 | 1.0 | - | 4096 | - | 5.7 |
| | 1D $^{13}$C (MW on/off) | | 27.3 | 10.5 | 64 | 1.5 | - | 1024 | - | 5.7 |
| | $^{13}$C-$T_1$ | 400 | 120 | 14 | 10-40k | 2.0 | - | 1800 | - | 18.0 |
| | CP refocused dipolar (SPC5) INADEQUATE | 600 | 18.4 | 10.5 | 1024 | 1.3 | 2048 | 50 | 17.2 | 0.8 |
| | DQF-DARR | 600 | 30 | 10.5 | 32/64 | 5.0 | 2048 | 200-300 | 17.2 | 0.3 |
| *A. fumigatus* (liquid) | CP J-INADEQUATE | 800 | 9 | 13.5 | 16 | 2.0 | 2400 | 1024 | 17.9 | 10.2 |
| | $^{13}$C-$T_1$ | 400 | 120 | 14 | 24-40k | 2.0 | - | 1800 | - | 18.0 |

**Table 5.2 Parameters used for the fit of $^{13}$C MultiCP spectra in Figure 5.6a.** unk: unknown or unresolved peaks. The error was estimated using the Monte Carlo error estimation of Dmfit.

| Δ | assignment | amplitude | width | integral (%) |
|---|---|---|---|---|
| *C. albicans* liquid culture | | | | |
| 103.1 | B1 | 7511 | 1.22±0.03 | 5.7±0.2 |
| 85.9 | B3 | 8000 | 1.05±0.03 | 2.26±0.07 |
| 78.1 | B5 | 8196 | 1.4±0.1 | 1.2±0.2 |
| 74.4 | B2 | 8305 | 0.83±0.01 | 20.1±0.3 |
| 68.6 | B4 | 8466 | 0.56±0.02 | 18±2 |
| 103.4 | Ch1 | 7482 | 1.43±0.03 | 3.9±0.2 |
| 82.9 | Ch3 | 8115 | 0.88±0.07 | 2.1±0.2 |
| 54.3 | Ch2 | 8861 | 1.54±0.07 | 0.54±0.06 |
| 101.8 | $Mn^{1,2}1^{a}$ | 7564 | 0.83±0.02 | 4.9±0.2 |
| 79.6 | $Mn^{1,2}2^{a}$ | 8161 | 1.11±0.09 | 1.5±0.2 |
| 70.5 | $Mn^{1,2}3^{a}$ | 84116 | 0.66±0.03 | 13±2 |
| 98.0 | $Mn^{1,2}1^{b}$ | 7651 | 1.05±0.07 | 1.33±0.09 |
| 72.1 | $Mn^{1,6}$ | 8365 | 0.73±0.03 | 9±2 |
| 62.3 | unk | 8642 | 0.82±0.02 | 10.9±0.2 |
| 59.26 | unk | 8725 | 0.80±0.02 | 5.0±0.2 |
| *C.albicans* solid culture | | | | |
| 103.1 | B1 | 7478 | 0.9±0.4 | 4.3±0.5 |
| 85.9 | B3 | 8002 | 0.63±0.03 | 2.3±0.1 |
| 78.1 | B5 | 8188 | 0.64±0.06 | 2.1±0.5 |
| 74.4 | B2 | 8305 | 0.53±0.01 | 21.1±0.5 |
| 68.6 | B4 | 8509 | 0.62±0.09 | 4±1 |
| 103.4 | Ch1 | 7514 | 0.95±0.03 | 4.3±0.4 |
| 82.9 | Ch3 | 8130 | 0.55±0.04 | 3.4±0.5 |
| 54.3 | Ch2 | 8775 | 0.11±0.01 | 2.5±0.1 |
| 101.8 | $Mn^{1,2}1^{a}$ | 7570 | 0.74±0.03 | 3.4±0.2 |
| 69 | $Mn^{1,2}2^{a}$ | 8453 | 0.51±0.03 | 12±1 |
| 70.5 | $Mn^{1,2}3^{a}$ | 8397 | 0.44±0.02 | 17±2 |
| 98.0 | $Mn^{1,2}1^{b}$ | 7646 | 0.89±0.08 | 1.1±0.2 |
| 62.3 | unk | 8641 | 0.56±0.08 | 11±4 |
| 59.26 | unk | 8715 | 0.8±0.1 | 1.8±0.5 |

**Table 5.3 The average cell wall thickness of *A. fumigatus* and *C. albicans*.** Results describe the average of 10 measurements from 15 biological replicates of each solid and liquid cultures.

| Sample | Cell wall thickness (nm) | |
|---|---|---|
| | *A. fumigatus* | *C albicans* |
| Solid culture | 134±21 | 195±50 |
| Liquid culture | 159±35 | 182±68 |

**Table 5.4 DNP buildup time and enhancement factor.** The enhancement factor ($\varepsilon_{on/off}$) is obtained by comparing the intensity of spectra measured with microwave on and off. The concentration of biradicals, the culture condition (solid or liquid media), and the composition of the DNP juice (matrix) are also listed.

| Sample | Radical | Matrix | DNP build-up time (s) | $\varepsilon_{on/off}$ |
|---|---|---|---|---|
| *A. fumigatus (solid)* | 20 mM c-AsymPol-POK | $d_6$-DMSO-$D_2O$-$H_2O$ (1:8:1) | 1.3 | 26 |
| *A. fumigatus (solid)* | 10 mM AMUPol, | $d_8$-glycerol/$D_2O$/$H_2O$ (6:3:1) | 5.0 | 90 |
| *C. albicans (solid)* | 20 mM c-AsymPol-POK | $d_6$-DMSO-$D_2O$-$H_2O$ (1:8:1) | 2.6 | 30 |
| *C. albicans (liquid)* | | | 3.1 | 26 |

**Table 5.5 $^{13}C$ chemical shifts of polysaccharides and proteins in fungal cell walls.** The units are in ppm. (/) unidentified. (-) not applicable.

| Carbohydrate | Chemical shifts | | | | | | | | References |
|---|---|---|---|---|---|---|---|---|---|
| | C1 | C2 | C3 | C4 | C5 | C6 | CO | $CH_3$ | |
| β-1,3-glucan | 103.6 | 74.2 | 87.5 | 68.3 | 77.2 | 61.5 | - | - | Chakraborty et al. 2021[16] |
| α-1,3-glucan | 101 | 71.9 | 84.5 | 69.5 | 71.7 | 60.5 | - | - | Chakraborty et al. 2021[16] |
| β-1,6-glucan | 103.9 | 74.6 | 76.6 | 70.6 | 75.7 | 69.6 | - | - | Lowman et al. 2011[65] |
| Chitin | 103.3 | 55.5 | 72.9 | 83.0 | 75.7 | 60.9 | 174.8 | 22.6 | Chakraborty et al. 2021[16] |
| α-1,2-Mannose[a] | 101.4 | 79.2 | 71.0 | 67.8 | 74.1 | 61.9 | - | - | |
| α-1,2-Mannose[b] | 99.1 | 79.5 | 71.4 | 67.8 | 74.1 | 61.9 | - | - | |
| α-1,6-Mannose | 102.9 | 71.1 | / | / | 72.0 | 66.6 | - | - | |
| Amino Acids | Cα | Cβ | Cγ | | | | CO | | |
| Alanine | 52.4 | 16.3 | | | | | 177.0 | | Fritzsching et al. 2013[66] |
| Aspartic acid | 54.8 | 38.3 | / | | | | 175.9 | | |
| Glutamic acid | 54.6 | 28.1 | 34.1 | | | | 174.0 | | |
| Phenyl alanine | 55.5 | 37.7 | / | | | | 172.8 | | |
| Iso leucine | 58.7 | 36.6 | 25.1 | / | / | | 173.5 | | |
| Lysine | 54.2 | 30.8 | 22.8 | | / | / | 175.0 | | |
| Leucine | 52.7 | 40.3 | 24.8 | | / | / | 174.4 | | |
| Methionine | 53.2 | 31.1 | 29.9 | | | / | 173.4 | | |
| Asparagine | 51.1 | 36.6 | / | | | | 172.6 | | |
| Proline | 61.1 | 30.0 | 25.2 | | | | 174.2 | | |
| Glutamine | 53.7 | 27.4 | 31.7 | | | | 173.4 | | |
| Arginine | 53.9 | 28.7 | 25.0 | | | | 173.7 | | |
| Threonine | 59.5 | 67.4 | / | | | | 172.4 | | |
| Valine | 59.7 | 30.7 | 19.2 | / | | | 173.4 | | |
| Tryptophan | 55.0 | 28.0 | / | / | / | / | 173.0 | | |
| Tyrosine | 58.6 | 36.0 | / | / | / | / | 173.0 | | |

**Table 5.6 $^{13}$C-$T_1$ relaxation times of polysaccharides.** The data are fit using bi-exponential equations: $I(t) = e^{\frac{-t}{T_{1b}}}$ and $I(t) = Ae^{\frac{-t}{T_{1a}}} + (1 - A)e^{\frac{-t}{T_{1b}}}$, where A is a perfector. Error bars are standard deviations of fit parameters.

| *A. fumigatus* (liquid culture) | | | | | |
|---|---|---|---|---|---|
| Assignment | $^{13}$C [4] | A | $T_{1a}$ (s) | B | $T_{1b}$ (s) |
| B3 | 86 | 70 % | 0.6 ± 0.1 | 30 % | 5 ± 3 |
| B5 | 77 | 40 % | 0.4 ± 0.1 | 60 % | 4 ± 2 |
| B2 | 74 | 20 % | 0.01 ± 0.01 | 80% | 5 ± 1 |
| Ch4 | 83 | 28 % | 0.20 ± 0.01 | 72% | 14 ± 4 |
| Ch5 | 75 | 50 % | 0.0045 ± 0.0001 | 50 % | 7 ± 2 |
| Ch2 | 55 | 43% | 0.17 ±0.06 | 57 % | 13 ± 2 |
| A1 | 101 | 20 % | 0.5 ± 0.2 | 80 % | 18 ± 6 |
| A3 | 84 | 23 % | 0.8 ± 0.2 | 77 % | 23 ± 10 |
| A2/5 | 71 | 23 % | 0.0010 ± 0.0005 | 77 % | 8 ± 2 |
| *A. fumigatus* (solid culture) | | | | | |
| B3 | 86 | 10 % | 0.20 ± 0.02 | 90 % | 5 ± 1 |
| B5 | 77 | 50 % | 0.8 ± 0.3 | 50% | 6 ± 3 |
| B2 | 72 | 20 % | 0.300 ± 0.001 | 80% | 5.420 ± 0.006 |
| B4 | 68 | 20 % | 0.0003 ± 0.0001 | 80% | 3.8 ± 0.4 |
| Ch4 | 83 | 11% | 0.5 ± 0.4 | 89% | 20 ± 6 |
| Ch5 | 75 | 11% | 0.11 ± 0.05 | 89% | 2.8 ± 0.3 |
| Ch2 | 55 | 14 % | 0.14 ± 0.01 | 86 % | 10.8 ± 0.3 |
| A1 | 101 | 30 % | 0.011 ± 0.002 | 60 % | 14 ± 5 |
| A3 | 84 | 44 % | 0.6 ± 0.1 | 56 % | 14 ± 4 |
| A2/5 | 71 | 60% | 0.348 ± 0.009 | 40 % | 9.7 ± 0.6 |

# CHAPTER 6: STRUCTURAL ADAPTATION OF FUNGAL CELL WALL IN HYPERSALINE ENVIROMENT

Preprint with permission from Liyanage D. Fernando, Yordanis Pérez-Llano, Malitha C. Dickwella Widanage, Liliana Martínez-Ávila, Andrew S. Lipton, Nina Gunde-Cimerman, Jean-Paul Latgé, Ramón Alberto Batista-García, and Tuo Wang, Submitted to *Nature Communication*

Preprint in BioRxiv DOI: 10.1101/2023.04.15.537024

## 6.1 Abstract

Halophilic fungi, which thrive in hypersaline habitats and face a range of extreme conditions, have gained considerable attention for their potential applications in harsh industrial processes. However, the role of the cell wall in surviving these environmental conditions remains unclear. Here we employ solid-state NMR spectroscopy to compare the cell wall architecture of *Aspergillus sydowii* and other halophilic and halotolerant fungi across salinity gradients. Analyses of intact cells reveal that *A. sydowii* cell walls contain a rigid core comprising chitin, β-glucan, and chitosan, shielded by a surface shell composed of galactomannan and galactosaminogalactan. When exposed to hypersaline conditions, *A. sydowii* enhances chitin biosynthesis and incorporates α-glucan to create thick, stiff, and hydrophobic cell walls. Such structural rearrangements enable the fungus to adapt to both hypersaline and salt-deprived conditions, providing a robust mechanism for withstanding external stress. These molecular principles can aid in the optimization of halophilic strains for biotechnology applications.

## 6.2 Introduction

Extremophiles are organisms that survive and thrive in harsh environments characterized by unfavorable temperature, pressure, acidity, and salinity[1,2]. Understanding their adaptation strategies can gain insights into the origin of life under extreme conditions and provide solutions to geo-ecological challenges[3-5]. Halophilic and halotolerant fungi inhabit hypersaline habitats and

have shown their potential in various industrial applications, such as contaminant treatment of saline wastewater, fermentation-based production of high-value molecules and pharmaceuticals, and biofuel production[6-8]. Halophilic fungi also hold promise as a source of transgenes encoding for salt-tolerant proteins to enhance the halotolerance of other organisms[7,9]. These applications have not reached their full potential due to our incomplete understanding of adaptation mechanisms.

When exposed to hypersaline environment, fungi need to maintain positive cell turgor pressure. This requires a multitude of cellular processes, including the accumulation of compatible organic solutes, modification of cell membrane composition and fluidity, pigment production, ion homeostasis, as well as cell wall remodeling[10,11]. These physiological responses involve changes in gene expression profiles to provide osmotic balance, oxidative stress management, and metabolic rewiring of the fungal cells[11,12]. Morphological changes have also been observed in the cell walls of the model basidiomycetous halophile *Wallemia ichthyophaga* and the extremely halotolerant black yeast *Hortaea werneckii*[10]. With high salinity, *W. ichthyophaga* produced three-fold thickened cell walls and bulky multicellular clumps while *H. werneckii* showed compromised cell wall integrity when melanin synthesis was inhibited[13-15]. Nevertheless, the ultrastructural change of the cell wall is yet to be explored.

Many *Aspergillus* species, such as *A. niger, A. flavus, A. tubingensis, A. atacamensis, A. destruens, A. versicolor,* and more recently *A. sydowii,* have been examined to understand their growth at high NaCl concentrations[16,17]. *A. sydowii* is an ascomycetous filamentous fungus found in various habitats, including salterns, dried food, decaying plant matter, and sea water, where it is a major contributor to coral disease aspergillosis[18]. Recent transcriptomic and imaging studies of *A. sydowii* revealed that under high salt concentration (2 M NaCl), there were significant

changes in gene expression related to cell wall biogenesis, which led to a significant thickening of the mycelial cell wall[16]. The upregulation of hydrophobin genes further supports the role of these proteins in cell wall haloadaptation. While these findings indicate that the thickness, composition, and architecture of the cell wall are crucial for fungal survival, characterizing such changes is challenging due to the heterogeneity and insolubility of this organelle.

Recently, the use of solid-state NMR (ssNMR) spectroscopy has led to a better understanding of the molecular architecture and dynamics of fungal cell walls[19-22]. Through integrated ssNMR and biochemical analyses of *Aspergillus fumigatus*, it has been discovered that a poorly hydrated, mechanically stiff core is formed by physically associated chitin and α-1,3-glucan[23-25], which is conserved in both mycelia and conidia[26], but with altered molecular composition during morphotype transition[27]. Highly branched β-1,3/1,6-glucans and linear terminal threads of β-1,3/1,4-glucans comprise the mobile and well-hydrated meshes. The inner domain is shielded by a dynamic outer layer that contains galactomannan (GM), galactosaminogalactan (GAG), α-1,3-glucan, and protein components[24]. By directly using intact fungal cells, the need for chemical extraction and solubilization procedures has been eliminated. The physical profiles of biopolymers observed through ssNMR, such as dynamics and hydrophobicity, naturally complement the chemical solubility, linkage pattern, and localization of carbohydrates investigated by chemical assays and imaging techniques[28-31], which allow for a complete portrait of the cell wall organization to be assembled[19].

In this study, we employ high-resolution ssNMR to examine uniformly $^{13}C$, $^{15}N$-labeled *A. sydowii* cells cultured at different salt concentrations. Under optimal salt concentration, the cell wall in *A. sydowii* exhibits an interlaced structure like that of *A. fumigatus* but with the addition of chitosan and the exclusion of α-1,3-glucan. These characteristics were repeatedly

observed in other halophilic *Aspergillus* species. The amount of chitin and the proportion of amino sugars in GAG progressively increases as the salt concentration rises, with a small amount of α-1,3-glucan reintroduced to the mobile phase at hypersaline conditions. Chitosan and β-glucans are tightly associated with chitin and each other, but a high concentration of salt weakens these packing interactions and promotes the self-aggregation of biomolecules. These structural adjustments allow *A. sydowii* to produce thick and rigid cell walls with limited water permeability. The dehydration and rigidification of protein and lipid components further contribute to this effect. These molecular-level modifications in the fungal cell walls and associated organelles help the microorganisms maintain the structural integrity of their carbohydrate frame and lower water potential than their surroundings.

## 6.3 Results

### 6.3.1 Structural Complexity of *A. sydowii* Carbohydrates

Variations in the structural organization of the fungal cell wall are often associated with the change in the environment[32]. We used *A. sydowii* as a halophile model and characterized its mycelia grown without and with NaCl at two different concentrations: optimal salinity (0.5 M) and hypersaline condition (2.0 M). The cell wall of *A. sydowii* grown at the optimal salt concentration of 0.5 M is a composite of biopolymers with distinct mobilities. We found that the rigid polysaccharides included chitin, β-1,3-glucan, and chitosan (Figure 6.1a), while the mobile fraction mainly contained β-1,3-glucans, GM, and GAG (Figure 6.1b). Rigid molecules were selectively detected using a two-dimensional (2D) $^{13}C$-$^{13}C$ correlation spectrum that relied on dipolar-based $^{1}H$-$^{13}C$ cross-polarization (CP) for creating the initial magnetization (Figure 6.1c). The spectrum was dominated by the signals of chitin and β-1,3-glucan, such as the characteristic C1-C2 cross peak of chitin at (103.6, 55.5 ppm) and the C1-C3 cross peak of β-1,3-glucan at

(103.6, 86.4 ppm). Chitosan, a deacetylated form of chitin, was also detectable, though relatively weak. These three types of polysaccharides form rigid scaffolds that share the mechanical load of the polymer network in the mycelial cell wall.

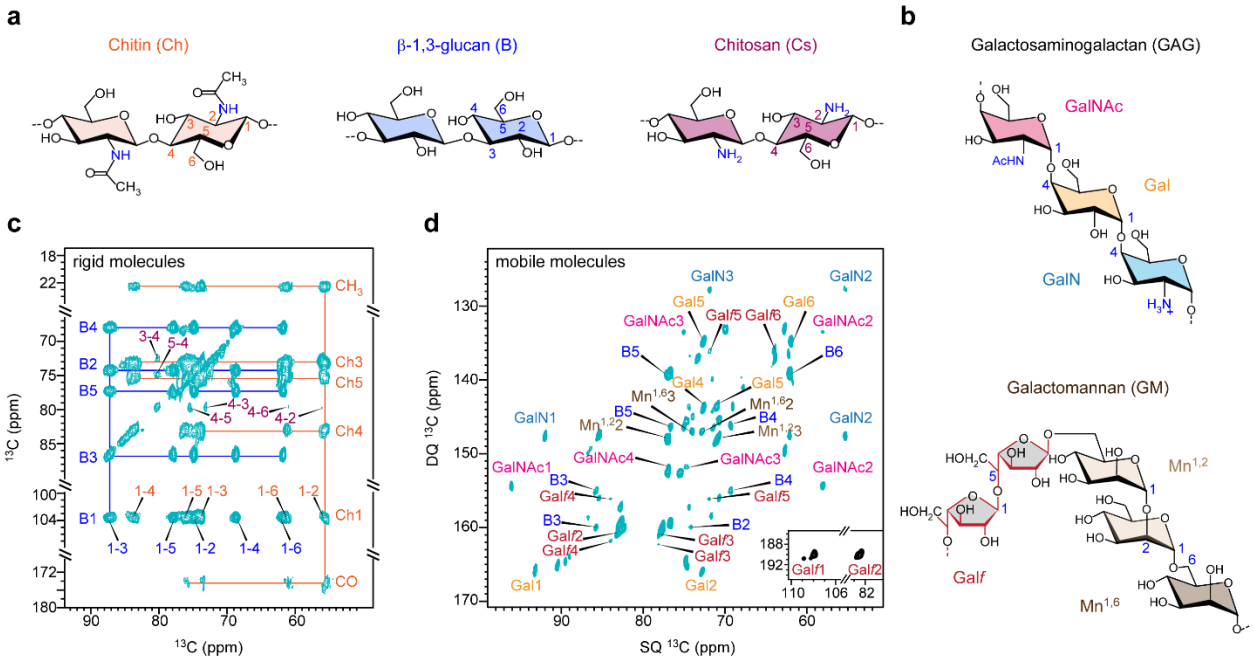


**Figure 6.1 Rigid and mobile polysaccharides of *A. sydowii*. a,** Simplified structural presentation of rigid polysaccharide in the cell wall. Carbon numbers and the NMR abbreviations are given for each polysaccharide. **b,** Representative structures of GAG and GM in the mobile domain, with key sugar units labeled. **c,** 2D $^{13}C$-$^{13}C$ correlation spectrum of *A. sydowii* measured with CP and 100 ms DARR detecting rigid molecules. Orange and blue solid lines trace the carbon linkages of chitin and β-1,3-glucan, respectively. Each cross peak is the correlation of two carbons, such as the 1-4 cross peak in orange, which represents the correlation between carbons 1 and 4 of chitin. **d,** $^{13}C$ DP refocused *J*-INADEQUATE spectrum detecting mobile polysaccharides. Assignments contain NMR abbreviation and carbon number, for example, B5 represents β-1,3-glucan carbon 5. All spectra were measured on an 850 MHz NMR spectrometer at 13 kHz MAS on intact *A. sydowii* cells grown with 0.5 M NaCl.

Mobile polysaccharides were detected by a combination of $^{13}C$ direct polarization (DP) and a short recycle delay of 2 s in the 2D refocused *J*-INADEQUATE[33] spectrum (Figure 6.1d). This technique filtered out rigid molecules with slow $^{13}C$-$T_1$ relaxation. The spectrum showed well-dispersed signals of galactose (Gal), galactosamine (GalN), and N-acetylgalactosamine

(GalNAc), which combine to form the heteroglycan GAG found on cell surfaces[34]. We also identified signals of 1,2- and 1,6-linked α-mannose ($Mn^{1,2}$ and $Mn^{1,6}$), which make up the backbone of GM, and the galactofuranose (Gal*f*) residues that form GM sidechains[35,36].

Although GM and chitin have been found to be covalently bridged through β-1,3-glucan as an integrated structural domain[28], our results identified these two molecules in two dynamically distinct fractions. This can result from the distribution of β-1,3-glucan in both rigid and mobile domains (Figure 6.1c, d), where it experiences a transition from the rigid side that is bridged to stiff chitin to a mobile end that is connected to dynamic GM. The GM-β-1,3-glucan-chitin complex accommodates a broad gradient of dynamics. It is also possible that this covalently linked complex may only have a low population, resulting in the observed dynamics being predominantly governed by the individual polysaccharides that exist separately in the bulk.

Polysaccharides are inherently polymeric when placed in the cellular environment. Five chitin forms and four chitosan forms were identified as clustered signals (Figure 6.1e), indicating a small range of structural variation within each molecule, probably by conformational distribution and H-bonding difference. The chemical shifts of these chitin molecules resembled those of the α-type model with antiparallel chain packing in the crystallite, while chitosan aligned with a non-flat, relaxed two-fold helix structure (called type-II chitosan) as recently reported[37]. These structural allomorphs, as well as the cell structural fingerprints, were fully retained across different halophilic *Aspergillus* species (Figure 6.6**)**.

### 6.3.2 Influence of NaCl Environment on *A. Sydowii* Carbohydrate Profile

The ultrastructure of the *A. sydowii* cell wall was examined using transmission electron microscopy (TEM) (Figure 6.7). The thickness of the cell wall was 140 nm ± 30 nm under the optimal culture condition of 0.5 M NaCl but increased to 200 ± 20 nm at hypersaline conditions,

respectively (Figure 6.2a). The ratio between the cell wall thickness and the total mycelial cell width was found to increase with the increasing concentration of salt in the medium. Under osmotic stress, the stiff carbohydrate core effectively retained its structural integrity. We observed generally consistent patterns in the polysaccharide region when comparing samples cultured at varying salt concentrations, while significant differences were exhibited by proteins and lipids (Figure 6.2b). Chitin signals were initially weak in the sample lacking NaCl but became stronger in the presence of NaCl (Figure 6.2c). Quantification of peak volumes revealed an upsurge in the chitin content with increasing salinity, while the amount of hydrophilic β-glucan decreased gradually (Figure 6.2d and Table 6.1). The introduction of more crystalline chitin to the cell wall inevitably strengthened this biomaterial.

As salt concentration increased, the amount of GM dropped substantially but the amount of GAG increased slightly (Figure 6.2d, e). Surprisingly, we also observed a low amount of mobile α-1,3-glucan in the hypersaline sample, but not in optimal or salt-free conditions (Figure 6.2f and Figure 6.8). Under the hypersaline condition, the contents of amino sugars, including GalNAc and GalN, were doubled compared to fungal cultures under normal and low salt conditions (Figure 6.2d). The slightly acidic pH of *A. sydowii* culture is well below the GalN pKa of ~11.8; therefore, GalN favorably occurs as $GalNH_3^+$ (Figure 6.1b) rather than as the conjugate base $GalNH_2$. The enrichment of GalN units should have modified the physicochemical properties of GAG and made it more cationic. This is crucial for facilitating its adherence to anionic surfaces, including human cells, and promoting the adhesion between mycelia, which helps the entire colony withstand unfavorable conditions[38,39].

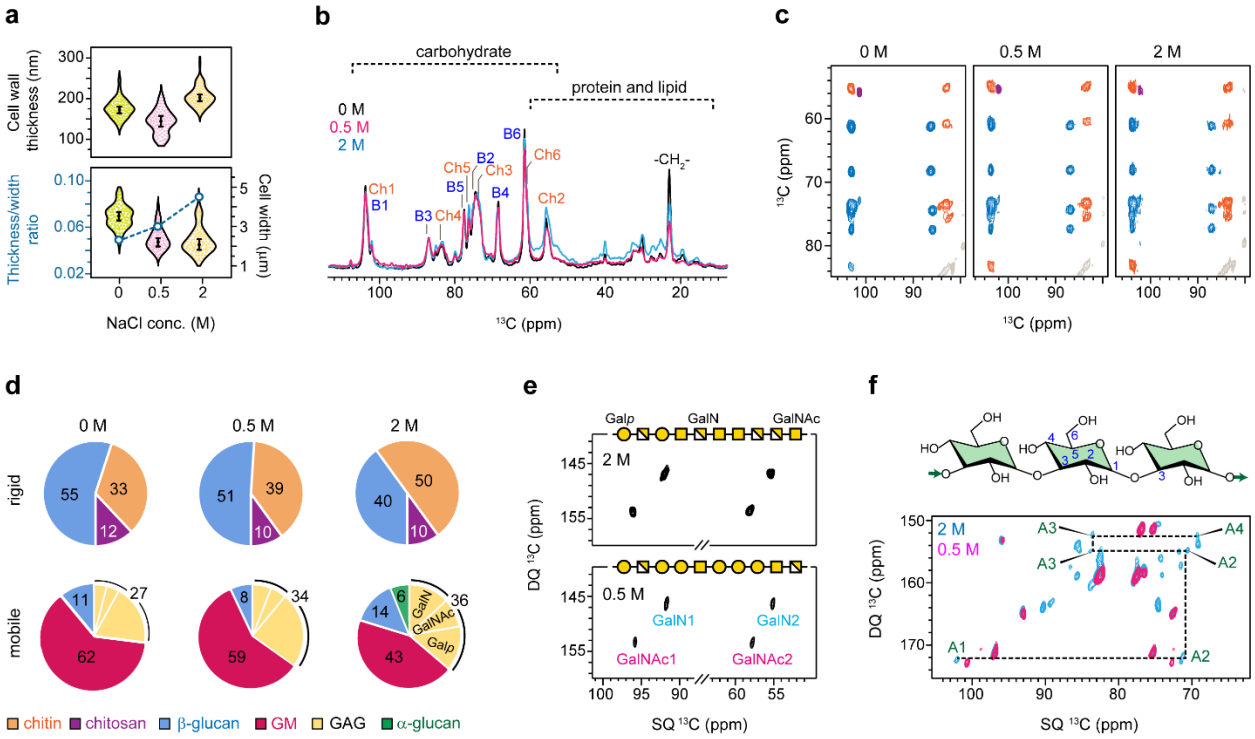


**Figure 6.2 Effect of salt concentration on *A. sydowii* polysaccharide composition. a,** Distribution of cell wall thickness (top panel) and its relative ratio to the cell thickness (bottom panel) in *A. sydowii* hyphae exposed to different NaCl concentrations. Each violin plot of cell wall thickness depicts 100 measurements from 10 cells (n=100), with the average value and standard deviation presented. The ratios of cell wall thickness to cell width were shown using blue open circles and connected by dashlines (left axis) while the violin plots of cell width values are projected to the right axis. n=100 (10 cells) for either the 0 M or 2 M sample and n=70 (7 cells) for the 0.5 M sample. **b,** Comparison of 1D $^{13}C$ CP spectra of *A. sydowii* cultures at 0 M, 0.5 M and 2.0 M NaCl. Key features of carbohydrate and protein/lipid signals are labeled for chitin (Ch), β-1,3-glucan (B) and the $CH_2$ of lipid acyl chain. **c,** 2D $^{13}C$-$^{13}C$ DARR correlation spectra of *A. sydowii* samples, with chitin signals (orange), β-1,3-glucan signals (blue), and chitosan (purple) signals marked. The relative abundance of chitin increases at high salt concentrations. **d,** Molar composition of the rigid (top row) and mobile (bottom row) polysaccharides in *A. sydowii* cell walls, determined by peak volumes of 2D $^{13}C$ CP DARR and $^{13}C$ DP *J*-INADEQUATE spectra, respectively. The fractions of Gal*p*, GalN, and GalNAc in GAG are also shown. **e,** Stronger signals of GalN and GalNAc units in GAG at the higher salt concentration in $^{13}C$ DP *J*-INADEQUATE spectra. GAG structures are constructed following the molar fraction using the Symbol Nomenclature for Glycans. **f,** Structure of α-1,3-glucan (A) and carbon connectivity tracked by $^{13}C$ DP *J*-INADEQUATE spectra. α-1,3-glucan is barely detectable in 0.5 M NaCl condition but becomes visible in 2.0 M NaCl condition. Source data of Figures 6.2a, d are provided as a Source Data file.

### 6.3.3 Remodeled Polymer Network of The Cell Wall

The mechanical properties and nanoscale assembly of cell walls are governed by the intermolecular interactions of biomolecules[40]. Sub-nanometer polymer contacts were identified through a 2D $^{13}C$-$^{13}C$ correlation measured with a 1.5 s proton-driven spin diffusion (PDSD) mixing period. For example, many cross-peaks were unambiguously identified between chitin methyl groups and chitosan carbons (Figure 6.3a). However, some cross-peaks observed at optimal conditions, such as the chitin carbon 4 and chitosan carbon 1 (Ch4-Cs1) and between β-1,3-glucan carbon 3 and chitosan carbon 4 (B3-Cs4) observed in Figure 6.3a, disappeared in the hypersaline sample (Figure 6.9), suggesting loosened packing interfaces between chitosan and chitin/glucan at hypersaline condition.

Analysis of 30 intermolecular cross peaks uncovered the organization pattern of the polysaccharide network (Table 6.2). The interactions between different carbon-4 sites of chitin units revealed the coexistence of these sub-forms in the same chitin crystallite (Figure 6.3b). This is a conserved feature found in both 0.5 M and 2.0 M *A. sydowii* samples. Crystalline chitin is physically supported by the β-glucan matrix and can also covalently link to β-glucan and then to GM, as reported by NMR and chemical assays of *A. fumigatus*[24,28]. Although the semi-dynamic β-glucan was disfavored in long-range correlation experiments, its carbon 3 and carbon 5 still showed strong cross peaks with the carbon 5 and methyl of chitin, regardless of the salt concentration. Under optimum salt concentration, chitosan was mixed with both chitin and β-glucan, but such contacts became limited in the hypersaline habitat. The hyperosmotic condition induced the restructuring of fungal cell walls.

### 6.3.4 Changes in Water Accessibility and Polymer Dynamics

The fungal cell wall has dramatically modified its water accessibility and polysaccharide dynamics in response to varying salt concentrations. Water accessibility refers to the number of immobilized water molecules present at each carbon site, while polysaccharide dynamics pertain to the movement of these molecules on the nanosecond and microsecond timescales. Polymer hydration was investigated in a site-specific manner using a 2D $^{13}C$-$^{13}C$ correlation water-edited experiment that only detects the signals of water-associated biomolecules (Figure 6.10)[41,42]. The intensity of the water-edited signals (S) was compared to the equilibrium condition ($S_0$) to determine the $S/S_0$ ratio for each carbon site, which is an indicator of water retention (Table 6.3). Such intensities were substantially higher for β-glucan than for chitin within each *A. sydowii* sample (Figure 6.3c), which confirmed the different structural roles of these polysaccharides as recently observed in other *Aspergillus* species: chitin constitutes the hydrophobic center, while β-glucans form the hydrated matrix[23].

*A. sydowii* cell walls were found to be best hydrated at the optimal concentration of 0.5 M NaCl (Figure 6.3c). Specifically, the average $S/S_0$ ratios for β-glucans and chitin are 0.51 for and 0.20. respectively. However, the extent of water association dropped substantially at 0 M and 2 M NaCl concentrations, both of which are considered stress conditions for *A. sydowii*. In the absence of NaCl, the hydration level of chitin remained unchanged but the $S/S_0$ ratio of β-glucan dropped by more than one-third. Under hypersaline conditions, both chitin and β-glucan were poorly hydrated, with $S/S_0$ ratios of 0.18 and 0.39, respectively.

The observed non-directional variations in polymer hydration cannot be easily correlated with the sequential changes in the polymer composition. The cell wall of *A. sydowii* grown in high salinity became more hydrophobic, which helps to prevent water loss from the cytoplasm. This is

likely due to a lower content of β-glucans, as shown in Figure 6.2d. However, the NaCl-free sample with a β-glucan-rich cell wall still exhibited limited exposure to water. This observation is intriguing and may be related to the increased thickness of the cell wall (Figure 6.2a), which suggests a change in the molecular assembly of the cell wall or other associated constituents. A potential explanation is the upregulation of hydrophobin genes in *A. sydowii* samples cultured in both 2 M and 0 M NaCl concentrations, which could lead to the formation of hydrophobic protein layers[13,16].

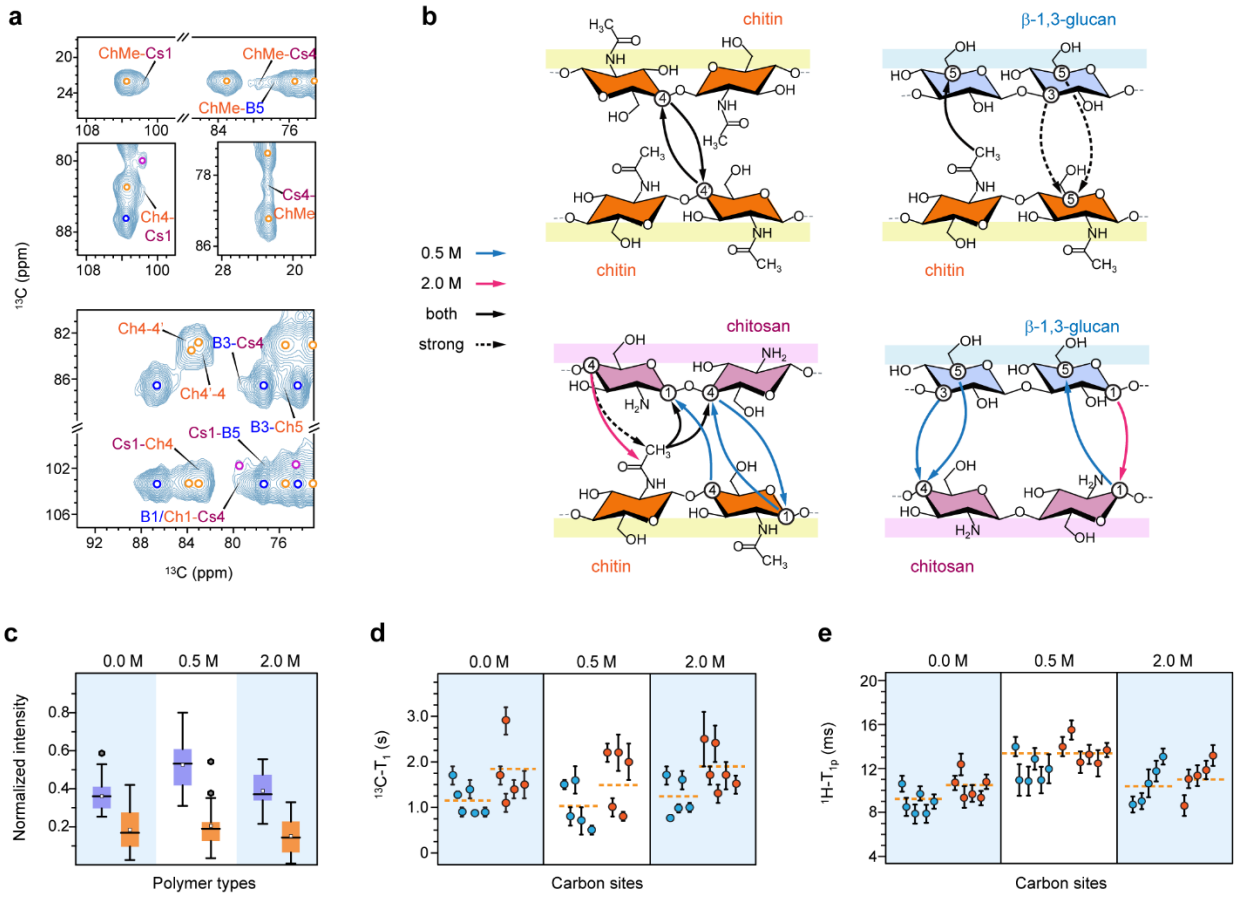


**Figure 6.3 Packing, hydration, and dynamics of *A. sydowii* polysaccharides. a,** Intermolecular cross peaks identified in 2D $^{13}C$ correlation spectra measured with long (1.5 s PDSD) mixing periods on 0.5 M sample. Signals of chitin (orange), β-glucan (blue) and chitosan (purple) are marked by open circles. Intermolecular peaks are labeled. **b,** Summary of intermolecular cross peaks observed in *A. sydowii*. Arrows show the direction of polarization transfer. Blue and magenta lines show the interactions observed only in 0.5 M and 2.0 M conditions, respectively. Black solid lines and dash lines represent interactions observed in both samples in both 1.5 s PDSD and 0.1 s

Figure 6.3 (cont'd)
PDSD spectra, respectively. **c,** Box-and-whisker diagram plotting the relative intensities ($S/S_0$) of β-1,3-glucan (blue; n=24, 25, 25) and chitin (orange; n=17, 15, 14) in three *A. sydowii* samples with varying salt concentrations. **d,** $^{13}C$-$T_1$ relaxation time constants of β-1,3-glucan (blue) and chitin (orange) in *A. sydowii*. The average $^{13}C$-$T_1$ are marked using yellow dash lines. **e,** $^{1}H$-$T_{1\rho}$ relaxation times of β-1,3-glucan (blue) and chitin (orange). The average values over all carbon sites within a polysaccharide are shown by dash lines. For both panels e and f, error bars indicate standard deviations of the fit parameters. Source data of Figures 3c-e are provided as a Source Data file.

The motional characteristics of cell wall polysaccharides were determined using NMR relaxation experiments (Figure 6.11 and Table 6.4). A molecule with fast $^{13}C$-$T_1$ relaxation is highly dynamic on the nanosecond (ns) timescale, likely due to rapid local reorientation motions (Figure 6.3d). Similarly, molecules exhibiting fast $^{1}H$-$T_{1\rho}$ relaxation are mobile on the microsecond (μs) time scale, typically attributed to slower collective movements and flipping (Figure 6.3e). Within each sample, β-glucan showed shorter $^{13}C$-$T_1$ and $^{1}H$-$T_{1\rho}$ time constants than chitin, demonstrating the dynamic nature of β-glucans.

When we deviated from the optimal condition of 0.5 M to either 0 M or 2.0 M, both chitin and β-glucans showed longer $^{13}C$-$T_1$ (Figure 6.3d) and shorter $^{1}H$-$T_{1\rho}$ (Figure 6.3e). The average $^{13}C$-$T_1$ increased from 1.6 s to 1.8-2.0 s for chitin and increased from 1.0 s to around 1.2 s for β-glucan. Meanwhile, the average $^{1}H$-$T_{1\rho}$ dropped from 14 ms to 10-12 ms for chitin and from 12 ms to 9-10 ms for β-glucan, likely caused by the loosened interface between different polymers. Therefore, in salt-free or hypersaline environments, biopolymers in the inner cell wall have restricted reorientation motions on the nanosecond timescale but accommodate slower and larger-scale movements on the microsecond timescale. Even though the centesimal composition of the cell wall polymers is different at 0 and 2M NaCl, the biophysical data showed that polymer dynamics and hydration, as well as cell wall thickness, lead to similar changes in the cell wall assembly when deviating away from the optimal concentration.

### 6.3.5 Protein and Lipid Components

We observed strong signals from proteins and lipids, which could have originated from various sources, including cell walls and plasma membrane components, as well as intracellular organelles. We found that the protein and lipid components mainly reside in the mobile phase (Figure 6.12). The signals of amino acids were distinguished using 2D refocused *J*-INADEQUATE spectra (Figure 6.4a). As protein backbone chemical shifts are sensitive to $\varphi$ and $\psi$ torsion angles[43], we determined the secondary structure by comparing the observed Cα chemical shifts to random-coil values. We found that mobile proteins were predominantly in α-helical conformation, which remained consistent across the salt gradient (Figure 6.4b).

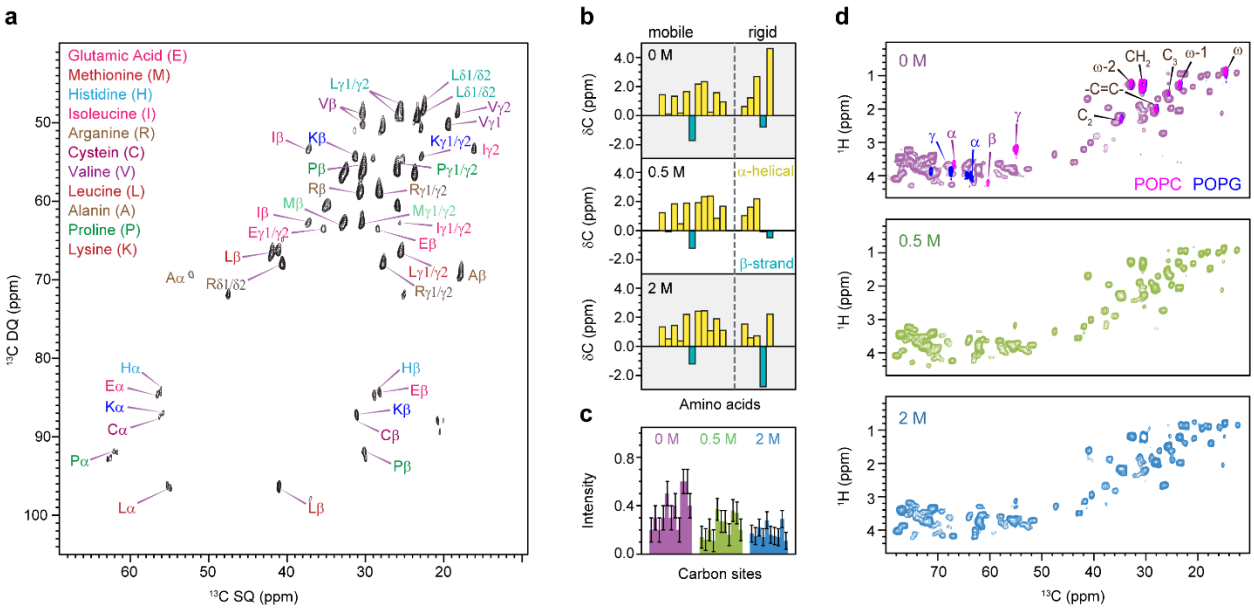


**Figure 6.4 Fingerprints of *A. sydowii* proteins and lipids. a,** Protein region of DP refocused J-INADEQUATE spectra collected using *A. sydowii* (0.5 M NaCl). **b,** Secondary structure of proteins denotated by $^{13}$C chemical shifts of Cα. α-helical and β-strand conformations are in yellow and blue, respectively. The amino acid residues in mobile fraction (left) and rigid fraction (right) are separated by dash lines. **c,** Water-edited intensities of protein carbon sites in *A. sydowii* samples cultured with different salt concentrations. **d,** 2D refocused INEPT $^{1}$H-$^{13}$C correlation spectra of *A. sydowii* samples cultured with 0 M, 0.5 M and 2 M NaCl. The spectra are compared with the

Figure 6.4 (cont'd)
control spectra of model lipids POPC (magenta) and POPG (blue), showing the α, β, and γ carbons in phospholipid headgroups and the carbons in lipid tails.

By exclusively selecting rigid molecules in structurally robust components, we noticed a distinctive and plentiful presence of proteins and lipids at 2M NaCl condition (Figure 6.2b and Figure 6.13). The amino acid residues identified in this inflexible portion had a noticeable contribution to the β-strand conformation and experienced substantial dehydration in hypersaline condition (Figure 6.4c and Table 6.5). The rigidification and dehydration of both protein and lipid components have suggested a global change to the cell wall and its adjacent layers, including the underlying membranes and the surface hydrophobins. These spectroscopic results also support the biochemical concept that halophilic fungi increase the expression of hydrophobins to moderate surface tension and water penetration[16,44,45].

The lipid components were also examined using the 2D $^{1}H$-$^{13}C$ refocused Insensitive Nuclei Enhanced by Polarization Transfer (INEPT) experiment (Figure 6.4d)[46]. Spectral superposition of *A. sydowii* lipids and model compounds in the glycerol/headgroup region confirmed the presence of phosphatidylcholines (PC) and phosphatidylglycerols (PG) (Figure 6.14). Sterols and polyisoprenoids were not detectable in either mobile or rigid portion, likely due to their relatively low abundance in a cellular sample. We spotted the putative signals of triglyceride (TG), which became pronounced in 0 M and 2.0 M NaCl conditions (Figure 6.15 and Table 6.6). This molecule has been identified in multiple *Aspergillus* and *Cryptococcus* species and was reported to modulate membrane fluidity[27,47]. However, due to the severe overlap of its putative signals with those from other lipids and proteins, and due to the broad distribution of lipid polymers in the cell, more biochemical studies should be undertaken here to explain these changes.

## 6.4 Discussion

High-resolution solid-state NMR analysis has unveiled the molecular-level organization of *A. sydowii* cell walls. At optimum salt concentration, the inner cell wall of *A. sydowii* was found to contain rigid chitin and chitosan in partially crystalline and highly polymorphic structures[37], surrounded by a matrix mainly consisting of β-glucans that regulate the water accessibility of the cell wall mesh in the absence of α-1,3-glucan (Figure 6.5a). Chitin and β-glucan, along with chitosan, are well mixed on the nanoscale, with extensive intermolecular interactions. This inner domain is covered by an outer shell rich in highly dynamic molecules, mainly containing GM and GAG. *Aspergillus* cell walls are characterized by covalently linked chitin-β-glucan-GM complex[28,30], which could explain the observed bimodal distribution of β-1,3-glucan in both rigid and mobile domains. The rigid segment is in contact with chitin or chitosan, while the mobile part forms the soft matrix and bridges to even more dynamic GM in the outer shell. GM and GAG should covalently connect to structural proteins through linkers formed by hydrophobic amino acid residues, as suggested by recent analyses of *A. fumigatus* cell walls[24].

To survive in hypersaline habitats with restricted water activity[17,18], halophilic fungi have to accommodate structural modifications at macroscopic and molecular levels (Figure 6.5b). The inner domain of the cell wall contains more chitin molecules, which provide high rigidity, and less β-1,3-glucans, which abolish water permeability. The packing interactions between chitin-chitin and chitin-glucan remain unchanged. However, chitosan becomes better isolated from other molecules, possibly due to self-aggregation. The surface layer has a reduced amount of GM but an increased content of α-1,3-glucan and GAG with an enriched fraction of deacetylated GalNAc, which supports fungal adherence and virulence[34,39,48]. The fungus develops a thickened, stiff, waterproof, and adhesive cell wall for better survival in salty conditions.

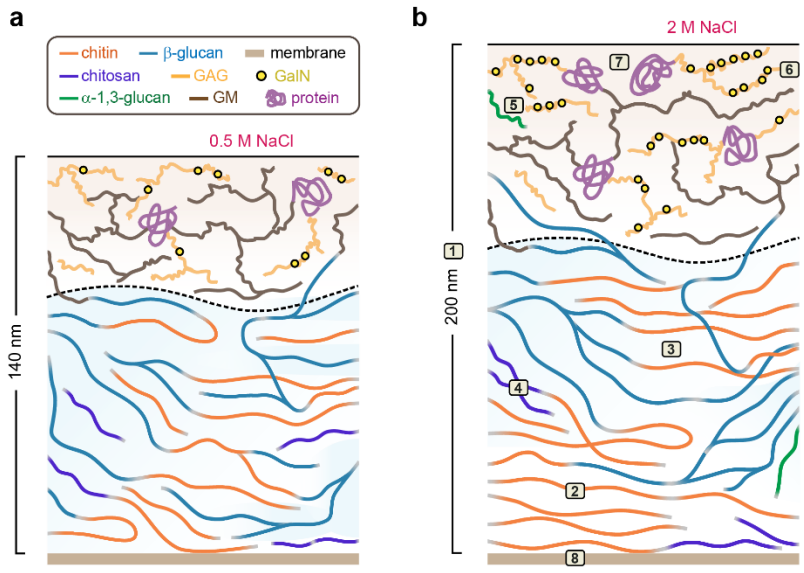


**Figure 6.5 Schematic representation of fungal cell wall adaptation to salinity.** The diagram illustrates key components of the *A. sydowii* cell walls and their distributions in the surface and inner domains separated by the dash line. The blue color gradient of the inner domain represents the extent of water retention. The cell wall thickness and the molecular composition are shown, but not strictly to scale. Compared to 0.5 M condition, the cell wall in 2.0 M NaCl exhibits 1, increased thickness, 2, enhanced biosynthesis of crystalline chitin resulting in higher cell wall rigidity and restricted local motions in the inner domain, 3, reduced water retention due to lower β-glucan content, 4) chitosan aggregation and reduced interactions with other components, 5) inclusion of α-glucan in the mobile phase, 6) enriched content of cationic GalN units in GAG on the surface, 7) increased protein content and rigidity, dehydration of protein, and reshuffled secondary structure, and 8) elevated content of rigid lipids.

In mycelia obtained under hypersaline conditions, proteins and lipids undergo a similar trend of rigidification and dehydration as observed in the cell wall polysaccharides. These effects may occur to the two layers of hydrophobins and cell membrane that sandwich the cell wall, as well as the protein and lipid components included in the macromolecular assembly of the cell wall itself. These structural changes help to constrain the cell wall permeability and better protect the organism from the stressful environment, contributing to the adaptation of *A. sydowii* as a successful halophile.

The halophilic fungal species investigated in this study do not contain a significant amount of α-1,3-glucan (Figure 6.2c). This finding contradicts previous observations in *A. fumigatus*, where α-1,3-glucan was found to be present in the rigid and mobile phases of the alkaline soluble and insoluble fractions[24]. This versatile molecule supports mechanical properties by interacting with chitin and enhances fungal virulence by shielding the surface[19,31,49]. The lack of α-1,3-glucan in halophilic species inevitably necessitates other molecules, such as β-glucans, to play a more prominent role in stabilizing cell wall assembly. This observation could also explain the moderate virulence of these fungal strains in pathogenicity.

It is notable that the thickened cell wall, limited water permeability, and altered motional characteristics were consistently observed in both 0 M and 2 M NaCl conditions, revealing a general mechanism of cell wall restructuring to resist external stress. This is a new paradigm in cell wall biology where similar cell wall modifications only indicate the presence of stress regardless of the nature of the stress encountered by the fungus. These molecular-level insights provide a structural vision of the osmoprotective strategies adopted by halophiles, which could inform the use of these microbes in agricultural applications and biotechnology in extreme environments[8,9].

## 6.5 Methods

### 6.5.1 Microorganism and Culture Conditions.

*A. sydowii* strain EXF-12860 was used as the primary model fungus in this study. The mycelium was routinely propagated and preserved in Potato Dextrose Agar (PDA) in the presence of 0.5 M NaCl (optimum concentration) for seven days at 28℃. For isotopic labeling, *A. sydowii* was grown in 100 mL of liquid media containing 20 g/L $^{13}$C-glucose and 2 g/L $^{15}$N-labeled $NH_4NO_3$ as labeled materials together with other salt and trace elements as detailed in Table 6.7.

The culture was grown at 28℃ with 150 rpm shaking for seven days. The fungus was grown in parallel without NaCl and with NaCl but under two different concentrations of 0.5 M (optimal) and 2.0 M (hypersalinity). The mycelium was collected and washed twice with deionized water, and later washed with PBS to remove the excess isotope-labeled molecules and NaCl. The harvested fungal mycelia were used for both solid-state NMR and TEM experiments.

To compare with the *A. sydowii* strain EXF-12860, uniformly $^{13}C$,$^{15}N$-labeled mycelia were also obtained for other fungal species including *A. atacamensis* (EXF-6660) and *A. destruens* (EXF-10411). 20 g/L of glucose and 2 g/L of $NH_4NO_3$ were added to 100 mL mineral base media (Table 6.7), which were then incubated for seven days at 28°C and 200 rpm. Each strain was exposed to two different NaCl concentrations for comparison. The optimal salt concentration was 1.0 M for *A. atacamensis* and 1.9 M (optimal) for *A. destruens*.

### 6.5.2 TEM Imaging of Cell Wall Thickness and Morphology

The *A. sydowii* mycelia obtained from the three culture conditions used in this study (0 M, 0.5 M, and 2.0 M NaCl) were fixed overnight at 4 °C using 2.5% glutaraldehyde and 2 % paraformaldehyde in 0.1 M phosphate buffer (pH 7.4) to halt metabolic processes and preserve the cells. The mycelia were then embedded in 3% agarose gel and rinsed four times with 0.1 M phosphate buffer pH 7.4 and 0.05 M glycine. After washing, the samples were fixed with 2% $OsO_4$ in the dark for 1 h and rinsed three times using deionized water. En Bloc staining in 1% uranyl acetate was used to increase the contrast. Dehydration was achieved using 70% ethanol series and propylene oxide for two times followed by infiltration in propylene oxide:Epon resin series. Ultra-thin sections for TEM were cut on a Dupont Sorvall MT-2 microtome. TEM sections were mounted on carbon-coated copper grids (EMS FCF-150-CU) and stained with 2% uranyl acetate

and Reynolds lead citrate. Measurements were performed on the perpendicular cross-sections of 100 hyphae per culture condition using a JEOL JEM-1400 (120 kV) electron microscope.

### 6.5.3 Solid-State NMR Analysis of Carbohydrates and Proteins

For solid-state NMR analysis, 30 and 100 mg of mycelia were packed into 3.2 mm and 4 mm MAS rotors, respectively. High-resolution 1D and 2D solid-state NMR experiments were performed on a Varian VNMRS 850 MHz (19.9 Tesla) spectrometer using a 3.2 mm MAS triple-resonance HCN probe under 13 kHz MAS at 290 K. Water-editing, relaxation, and $^{1}H$-$^{13}C$ refocused INEPT experiments were conducted on a Bruker Avance 400 MHz (9.4 Tesla) spectrometer under 10 kHz MAS at 293 K. The $^{13}C$ chemical shifts were externally referenced to the adamantane $CH_2$ signal at 38.48 ppm on the tetramethylsilane (TMS) scale. The typical radiofrequency field strengths were 83 kHz for $^{1}H$ hard pulses and decoupling, and 50-62.5 kHz for $^{13}C$ pulses, unless otherwise specified. The key experimental parameters are listed in Table 6.8.

The initial magnetization for the experiments was created in three ways: 1) using $^{1}H$-$^{13}C$ cross-polarization to preferentially detect rigid molecules, 2) using $^{1}H$-$^{13}C$ refocused INEPT to select the most mobile molecules[46], and 3) using $^{13}C$ direct polarization to selectively detect mobile molecules with a short recycle delay of 2 s, or to quantitatively probe all carbons and molecules with a long recycle delay of 35 s. The CP typically uses a 1 ms Hartmann-Hahn contact, with a centerband match of 50 kHz for $^{1}H$ and $^{13}C$ channels. The stepwise spectral filtration of biomolecules using the dynamical gradient was shown in Figure 6.12.

The narrow $^{13}C$ peak linewidths of 0.4-1.0 ppm allowed us to unambiguously identify the signals of major polysaccharides. To resolve and assign the $^{13}C$ signals of polysaccharides and proteins, 2D $^{13}C$-$^{13}C$ correlation experiments were conducted. The 2D DP refocused *J*-INADEQUATE experiment[33] correlates the double-quantum (DQ) chemical shift, the sum of the

two directly bonded $^{13}C$ spins, with single quantum (SQ) chemical shifts. The experiment using DP, $^{13}C$-$^{13}C$ J coupling, and 1.7 s recycle delays preferentially detects mobile molecules, while the CP-based analog detects rigid molecules. The $^{13}C$-$^{13}C$ intramolecular interactions were probed using a 100 ms dipolar-assisted rotational resonance (DARR) scheme. Long-range intermolecular cross-peaks were detected using a 1.5 s proton-driven spin diffusion (PDSD) experiment. The resolved chemical shifts were compared with the values indexed in the Complex Carbohydrate Magnetic Resonance Database (CCMRD)[50], and the confirmed resonance assignments are listed in Table 6.9**.**

Protein secondary structure was determined by the chemical shift differences between the observed $^{13}C$ chemical shifts of Cα and the standard values of random coil conformation[43]. The chemical shifts were obtained using 2D DP refocused *J*-INADEQUATE spectra for mobile amino acid residues and using 2D $^{13}C$-$^{13}C$ DARR spectra for rigid proteins.

### 6.5.4 Estimation of Carbohydrate Composition

The peak volumes in 2D $^{13}C$-$^{13}C$ spectra measured using 100 ms DARR and DP refocused *J*-INADEUQTAE schemes were analyzed to estimate the composition of the rigid and mobile polysaccharides, respectively (Table 6.1). The integration function of the Bruker Topspin software was used to get the peak volumes in 2D spectra. To minimize uncertainty caused by spectral crowding, only well-resolved signals were used for compositional analysis. The NMR peaks used for quantification, their resonance assignments, and the corresponding peak volumes, were provided in Source Data file.

### 6.5.5 Solid-State NMR Analysis of Lipids

To probe phospholipid signals in membranes, 2D $^{1}H$-$^{13}C$ refocused INEPT spectra were collected. This experiment is based on through-bond $^{1}H$-$^{13}C$ magnetization transfer[46]. The two spin

echoes contain two delays set to $1/4J_{CH}$ followed by another two delays set to $1/6J_{CH}$, which were calculated using a CH J-coupling of 140 Hz for carbohydrates. In solid samples, only the most mobile molecules with long transverse relaxation times could be observed using this experimental scheme. Therefore, the intrinsically dynamic lipids were efficiently detected. In addition, model phospholipids (POPC and POPG) were measured for comparison. Around 50 mg of samples were packed into a 4 mm rotor. 1D $^{13}C$ DP experiments (with a recycle delay of 3 s) and 2D $^{1}H$-$^{13}C$ refocused INEPT experiments were conducted on both model lipid samples on a 400 MHz NMR spectrometer.

### 6.5.6 Measurements of Water Contact and Polymer Dynamics

To examine the site-specific water contacts of polysaccharides and proteins, 1D and 2D water-edited $^{13}C$ experiments were conducted[41,42,51]. Briefly, a $^{1}H$-$T_2$ relaxation filter (1.2 ms × 2) was used to suppress the polysaccharide signals to less than 5%, while retaining 80% of water magnetization as shown in Figure 6.10. The water $^{1}H$ polarization was then transferred to spatially proximal biomolecules through a $^{1}H$-$^{1}H$ mixing period before transferring it to carbon via a 1-ms CP for high-resolution $^{13}C$ detection. The $^{1}H$ mixing time was ranged from 0 ms to 100 ms for measuring 1D spectra and was fixed to 4 ms when the 2D spectrum was measured. Data obtained from the 1D spectra were analyzed by plotting the relative intensities as a function of the square root of the $^{1}H$ mixing time, which gave a buildup curve of peak intensity. The data obtained from the 2D scheme were analyzed by comparing the intensities between the water-edited spectrum (S) and the non-edited control spectrum ($S_0$), for each resolved carbon site. These $S/S_0$ intensity ratios reflect the extent of water retention around different carbon sites, which were documented in Tables 6.3 and 6.5 for polysaccharides and proteins.

$^{13}$C-$T_1$ relaxation was measured using CP-based Torchia $T_1$ scheme[52], with the z-filter duration varying from 0.1 μs to 8 s to provide complete relaxation curves as shown in Figure 6.11. $^{13}$C-detected $^{1}$H-$T_{1\rho}$ relaxation were measured using the Lee-Goldburg spin-lock sequence in which $^{1}$H spin diffusion was suppressed during both the spin-lock period and the CP period to obtain site-specific $^{1}$H relaxation information for protons that are directly bonded to a carbon site. A single exponential function was used to fit the data of both $^{13}$C-$T_1$ and $^{1}$H-$T_{1\rho}$ to obtain relaxation time constants, which are documented in Table 6.4.

## 6.6 Acknowledgments

This work was supported by the National Institutes of Health grant AI173270 to T.W. and Project-Conacyt-CB-285816 to R.A.B-G. N. G-C. acknowledge the support by the Slovenian Research Agency to Infrastructural Centre Mycosmo (MRIC UL, I0-0022) and program P4-0432. The high-field NMR spectra were collected at the Environmental Molecular Sciences Laboratory (grid.436923.9), a DOE Office of Science scientific user facility sponsored by the Department of Energy's Office of Biological and Environmental Research and located at PNNL under contract DE-AC05-76RL01830.

## REFERENCES


1. Rothschild, L.J. & Mancinelli, R.L. Life in extreme environments. *Nature* 409, 1092-1101 (2001).

2. Merino, N. et al. Living at the Extremes: Extremophiles and the Limits of Life in a Planetary Context. *Front. Microbiol.* 10, 780 (2019).

3. Albers, S.V. Extremophiles: Life at the deep end. *Nature* 538, 457 (2016).

4. Spang, A. et al. Complex archaea that bridge the gap between prokaryotes and eukaryotes. *Nature* 521, 173-179 (2015).

5. van den Burg, B. Extremophiles as a source for novel enzymes. *Curr. Opin. Microbiol.* 6, 213-218 (2003).

6. Batista-García, R.A. et al. Characterization of lignocellulolytic activities from a moderate halophile strain of Aspergillus caesiellus isolated from a sugarcane bagasse fermentation. *PLoS One* 9, e105893 (2014).

7. Gunde-Cimerman, N., Ramos, J. & Plemenitaš, A. Halotolerant and halophilic fungi. *Mycol. Res.* 113, 1231-1241 (2009).

8. DasSarma, S. & DasSarma, P. Halophiles and Their Enzymes: Negativity Put to Good Use. *Curr. Opin. Microbiol.* 25, 120-126 (2015).

9. Ali, I., Khaliq, S., Sajid, S. & Akbar, A. Biotechnological applications of halophilic fungi: Past, present, and future. in *Fungi in Extreme Environments: Ecological Role and Biotechnological Significance* 291-306 (Springer, 2019).

10. Gunde-Cimerman, N., Plemenitas, A. & Oren, A. Strategies of adaptation of microorganisms of the three domains of life to high salt concentrations *FEMS Microbiol. Rev.* 42, 353-375 (2018).

11. Kis-Papo, T. et al. Genomic adaptations of the halophilic Dead Sea filamentous fungus Eurotium rubrum. *Nat. Commun.* 5, 3745 (2014).

12. Tafer, H., Poyntner, C., Lopandic, K., Sterflinger, K. & Pinar, G. Back to the Salt Mines: Genome and Transcriptome Comparisons of the Halophilic Fungus Aspergillus salisburgensis and Its Halotolerant Relative Aspergillus sclerotialis. *Genes* 10, 381 (2019).

13. Zajc, J. et al. Genome and transcriptome sequencing of the halophilic fungus Wallemia ichthyophaga: haloadaptations present and absent. *BMC Genom.* 14, 617 (2013).

14. Kogej, T. et al. Osmotic adaptation of the halophilic fungus Hortaea werneckii: role of osmolytes and melanization. *Microbiology* 153, 4261-4273 (2007).

15. Kuncici, M.K., Kogej, T., Drobne, D. & Gunde-Cimerman, N. Morphological Response of the Halophilic Fungal Genus Wallemia to High Salinity. *App. Environ. Microbiol.* 76, 329 - 337 (2010).

16. Pérez-Llano, Y. et al. Stress reshapes the physiological response of halophile fungi to salinity. *Cells* 9, 525 (2020).

17. Jimenez-Gomez, I. et al. Haloadaptative Responses of Aspergillus sydowii to Extreme Water Deprivation: Morphology, Compatible Solutes, and Oxidative Stress at NaCl Saturation *J. Fungi* 6, 316 (2020).

18. Alker, A.P., Smith, G.W. & Kim, K. Characterization of Aspergillus sydowii (Thom et Church), a fungal pathogen of Caribbean sea fan corals. *Hydrobiologia* 460, 105-111 (2001).

19. Latgé, J.P. & Wang, T. Modern Biophysics Redefines Our Understanding of Fungal Cell Wall Structure, Complexity, and Dynamics. *mBio* 13, Modern Biophysics Redefines Our Understanding of Fungal Cell Wall Structure, Complexity, and Dynamics (2022).

20. Ehren, H.L. et al. Characterization of the cell wall of a mushroom forming fungus at atomic resolution using solid-state NMR spectroscopy. *Cell Surf.* 6, 100046 (2020).

21. Safeer, A. et al. Probing Cell-Surface Interactions in Fungal Cell Walls by High-Resolution 1H-Detected Solid-State NMR Spectroscopy. *Chem. Euro. J.* 29, e202202616 (2022).

22. Kelly, J.E., Chrissian, C. & Stark, R.E. Tailoring NMR experiments for structural characterization of amorphous biological solids: A practical guide. *Solid State Nucl. Magn. Reson.* 109, 101686 (2020).

23. Kang, X. et al. Molecular architecture of fungal cell walls revealed by solid-state NMR. *Nat. Commun.* 9, 2747 (2018).

24. Chakraborty, A. et al. A molecular vision of fungal cell wall organization by functional genomics and solid-state NMR. *Nat. Commun.* 12, 6346 (2021).

25. Ghassemi, N. et al. Solid-State NMR Investigations of Extracellular Matrices and Cell Walls of Algae, Bacteria, Fungi, and Plants. *Chem. Rev.* 122, 10036–10086 (2022).

26. Fernando, L.D. et al. Solid-state NMR analysis of unlabeled fungal cell walls from Aspergillus and Candida species. *J. Struct. Biol. X* 6, 100070 (2022).

27. Lamon, G. et al. Solid-state NMR molecular snapshots of Aspergillus fumigatus cell wall architecture during a conidial morphotype transition. *Proc. Natl. Acad. Sci. USA* 120, e2212003120 (2022).

28. Latgé, J.-P. The cell wall: a carbohydrate armour for the fungal cell. *Mol. Microbiol.* 66, 279-290 (2007).

29. Gow, N.A.R. & Lenardon, M.D. Architecture of the dynamic fungal cell wall. *Nat. Rev. Microbiol.* 21, 248-259 (2022).

30. Latgé, J.P. & Chamilos, G. Aspergillus fumigatus and Aspergillosis in 2019. *Clin. Microbiol. Rev.* 33, e00140-18 (2019).

31. Wagener, J., Striegler, K. & Wagener, N. α- and β-1,3-Glucan Synthesis and Remodeling. in *The Fungal Cell Wall: An Armour and a Weapon for Human Fungal Pathogens*, Vol. 425 (ed. Latgé, J.P.) 53-82 (Springer, Cham., 2020).

32. Gow, N.A.R., Latge, J.P. & Munro, C.A. The Fungal Cell Wall: Structure, Biosynthesis, and Function. *Microbiol. Spectr.* 5, 1-25 (2017).

33. Lesage, A., Bardet, M. & Emsley, L. Through-bond carbon-carbon connectivities in disordered solids by NMR. *J. Am. Chem. Soc.* 188, 10987-10993 (1999).

34. Speth, C., Rambach, G., Lass-Florl, C., Howell, P.L. & Sheppard, D.C. Galactosaminogalactan (GAG) and its multiple roles in Aspergillus pathogenesis. *Virulence* 10, 976-983 (2019).

35. Latge, J.P. Galactofuranose containing molecules in Aspergillus fumigatus. *Med. Mycol.* 47, S104-S109 (2009).

36. Lee, M.J. & Sheppard, D.C. Recent advances in the understanding of the Aspergillus fumigatus cell wall. *J. Microbiol.* 54, 232-242 (2016).

37. Fernando, L.D. et al. Structural Polymorphism of Chitin and Chitosan in Fungal Cell Walls from Solid-State NMR and Principal Component Analysis. *Front. Mol. Biosci.* 8, 727053 (2021).

38. Mauff, F.L. & Sheppard, D.C. Understanding Aspergillus fumigatus galactosaminogalactan biosynthesis: A few questions remain. *Cell Surf.* 9, 100095 (2023).

39. Gravelat, F.N. et al. Aspergillus galactosaminogalactan mediates adherence to host constituents and conceals hyphal beta-glucan from the immune system. *PLOS Pathog.* 9, e1003575 (2013).

40. Zhang, Y. et al. Molecular insights into the complex mechanics of plant epidermal cell walls. *Science* 372, 706-711 (2021).

41. Ader, C. et al. Structural Rearrangements of Membrane Proteins Probed by Water-Edited Solid-State NMR Spectroscopy. *J. Am. Chem. Soc.* 131, 170-176 (2009).

42. White, P.B., Wang, T., Park, Y.B., Cosgrove, D.J. & Hong, M. Water–Polysaccharide Interactions in the Primary Cell Wall of Arabidopsis thaliana from Polarization Transfer Solid-State NMR. *J. Am. Chem. Soc.* 136, 10399-10409 (2014).

43. de Dios, A.C., Pearson, J.G. & Oldfield, E. Secondary and Tertiary Structural Effects on Protein NMR Chemical Shifts: an ab Initio Approach. *Science* 260, 1491-1496 (1993).

44. Bayry, J., Aimanianda, V., Guijarro, J.I., Sunde, M. & Latgé, J.-P. Hydrophobins—Unique Fungal Proteins. *PLOS Pathog.* 8, e1002700 (2012).

45. Plemenitaš, A. et al. Adaptation to high salt concentrations in halotolerant/halophilic fungi: a molecular perspective. *Front. Microbiol.* 5, 199 (2014).

46. Elena, B., Lesage, A., Steuernagel, S., Böckmann, A. & Emsley, L. Proton to Carbon-13 INEPT in Solid-State NMR Spectroscopy. *J. Am. Chem. Soc.* 127, 17296-17302 (2005).

47. Chrissian, C. et al. Solid-state NMR spectroscopy identifies three classes of lipids in Cryptococcus neoformans melanized cell walls and whole fungal cells. *J. Biol. Chem.* 295, 15083-15096 (2020).

48. Briard, B. et al. Galactosaminogalactan activates the inflammasome to provide host protection. *Nature* 588, 688-692 (2020).

49. Rappleye, C.A., Eissenberg, L.G. & Goldman, W.E. Histoplasma capsulatum α-(1, 3)-glucan blocks innate immune recognition by the β-glucan receptor. *Proc. Natl. Acad. Sci. USA* 104, 1366-1370 (2007).

50. Kang, X. et al. CCMRD: a solid-state NMR database for complex carbohydrates. *J. Biomol. NMR* 74, 239-245 (2020).

51. Lesage, A., Emsley, L., Penin, F. & Bockmann, A. Investigation of dipolar-mediated water-protein interactions in microcrystalline Crh by solid-state NMR spectroscopy. *J. Am. Chem. Soc.* 128, 8246-8255 (2006).

52. Torchia, D.A. Measurement of proton-enhanced $^{13}C$ $T_1$ values by a method which suppresses artifacts. *J. Magn. Reson.* 30, 613-616 (1978).

53. Consolacion, Y. *et al.* Chemical constituents of Aglaia loheri. *Pharmacognosy Journal* 4 (2012).

54. Suttiarporn, P. *et al.* Structures of phytosterols and triterpenoids with potential anti-cancer activity in bran of black non-glutinous rice. *Nutrients* 7, 1672-1687 (2015).

55. Tuckey, R. C. *et al.* Human cytochrome P450scc (CYP11A1) catalyzes epoxide formation with ergosterol. *Drug Metabolism and Disposition* 40, 436-444 (2012).

56. Shim, J. H. *et al.* Antitumor effect of soluble beta-1,3-glucan from Agrobacterium sp. R259 KCTC 1019. *J. Microbiol. Biotechnol.* 17, 1513-1520 (2007).

57. Bhanja, S. K. *et al.* Water-insoluble glucans from the edible fungus Ramaria botrytis. *Bioactive Carbohydrates and Dietary Fibre* 3, 52-58 (2014).

58. Fritzsching, K., Yang, Y., Schmidt-Rohr, K. & Hong, M. Practical use of chemical shift databases for protein solid-state NMR: 2D chemical shift maps and amino-acid assignment with secondary-structure information. *Journal of biomolecular NMR* 56, 155-167 (2013).

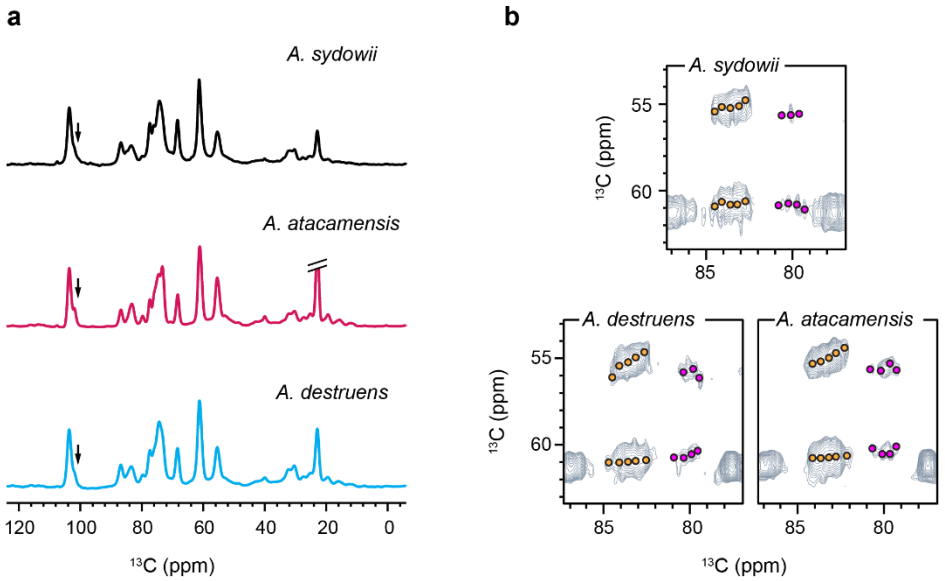


**Figure 6.6 Structural similarity of different halophilic *Aspergillus* species. a,** 1D $^{13}C$ CP spectra collected on three halophilic fungi cultured in optimum salt concentrations. The expected position for α-1,3-glucan carbon 1 is marked by arrows. **b,** Structural polymorphism of chitin and chitosan. Ch2-4 and Ch6-4 cross peaks indicate five forms of chitin (orange circles) while Cs2-4 and Cs6-4 cross peaks show three to four types of chitosan (magenta circles) consistently identified in halophilic *Aspergillus* species with minor changes.

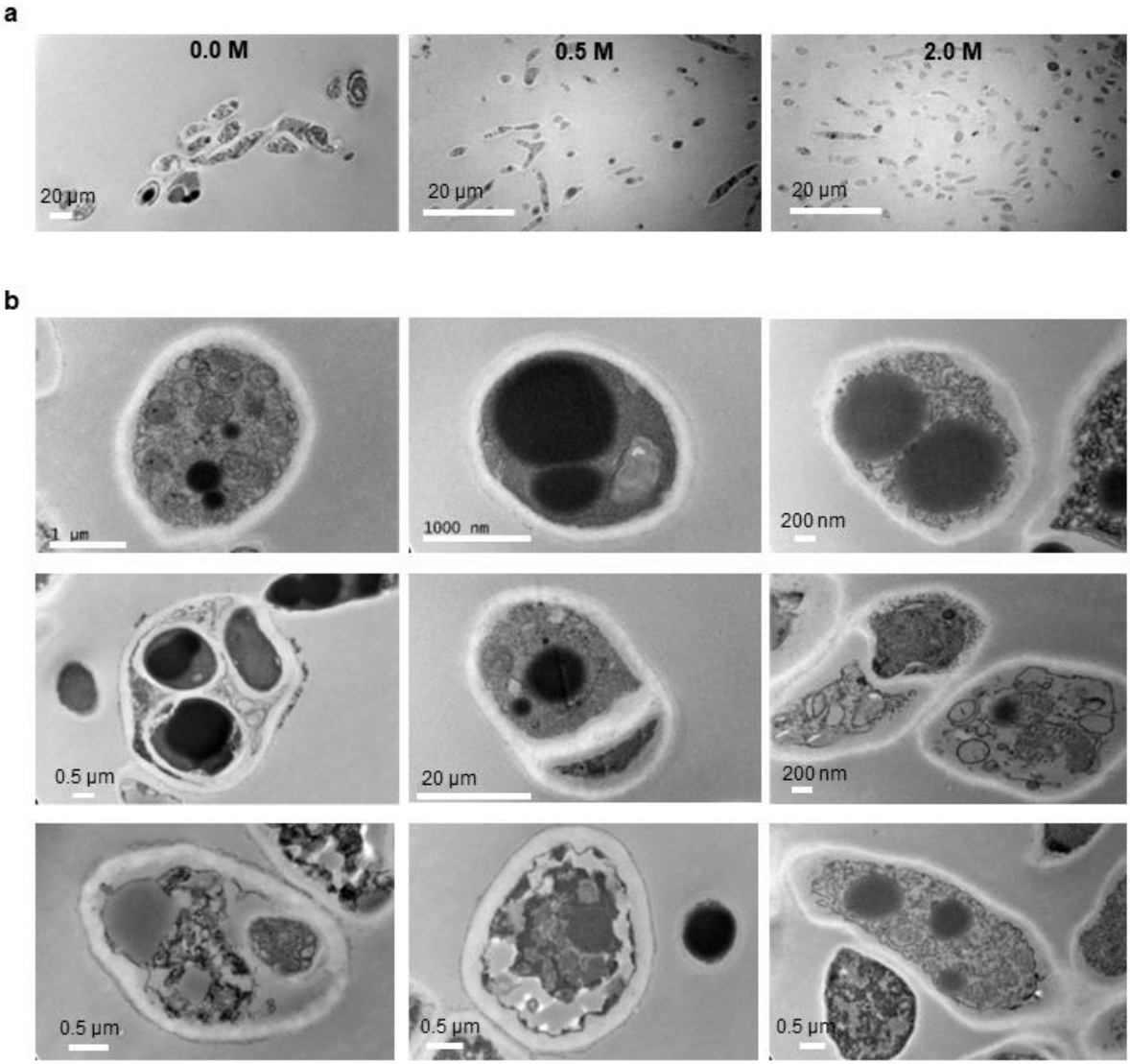


**Figure 6.7 Representative TEM images of *Aspergillus sydowii.*** The images were taken from the perpendicular cross-sections of *A. sydowii* hyphae under **a,** low-magnification and **b,** high-magnification. White bars indicate the scale.

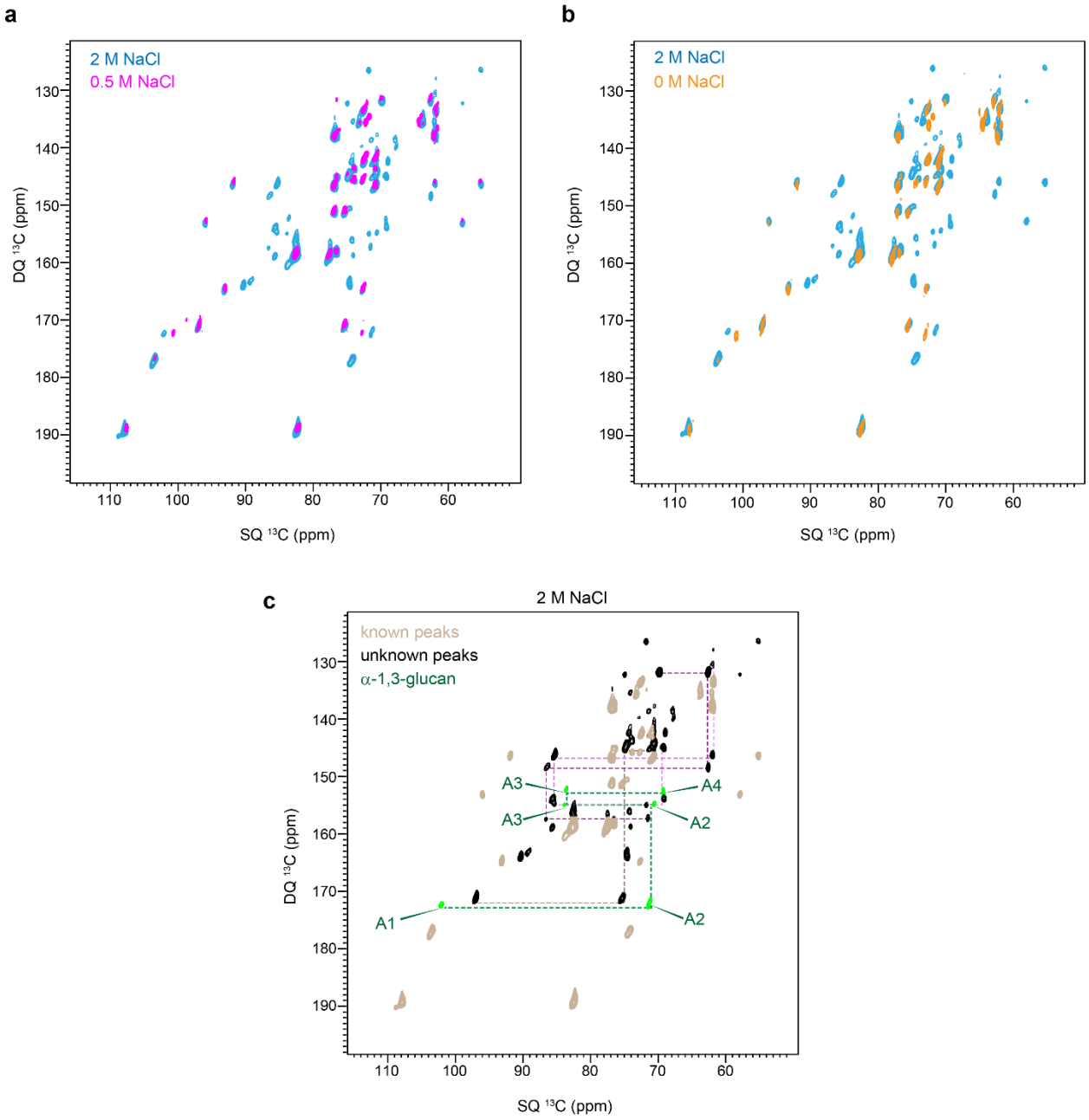


**Figure 6.8 Changes in mobile carbohydrate in response to high salinity. a,** Overlay of 2D $^{13}$C DP J-INADEQUATE spectra of *A. sydowii* samples cultured in 0.5 M (magenta) and 2 M (cyan) NaCl. **b,** Overlay of 2D $^{13}$C DP J-INADEQUATE spectra of *A. sydowii* samples cultured in 0 M (orange) and 2 M (cyan) NaCl. **c,** 2D $^{13}$C DP J-INADEQUATE spectra of 2 M NaCl showing the new peaks and α-1,3-glucan peaks. All spectra were measured in 850 MHz at 13 kHz MAS.

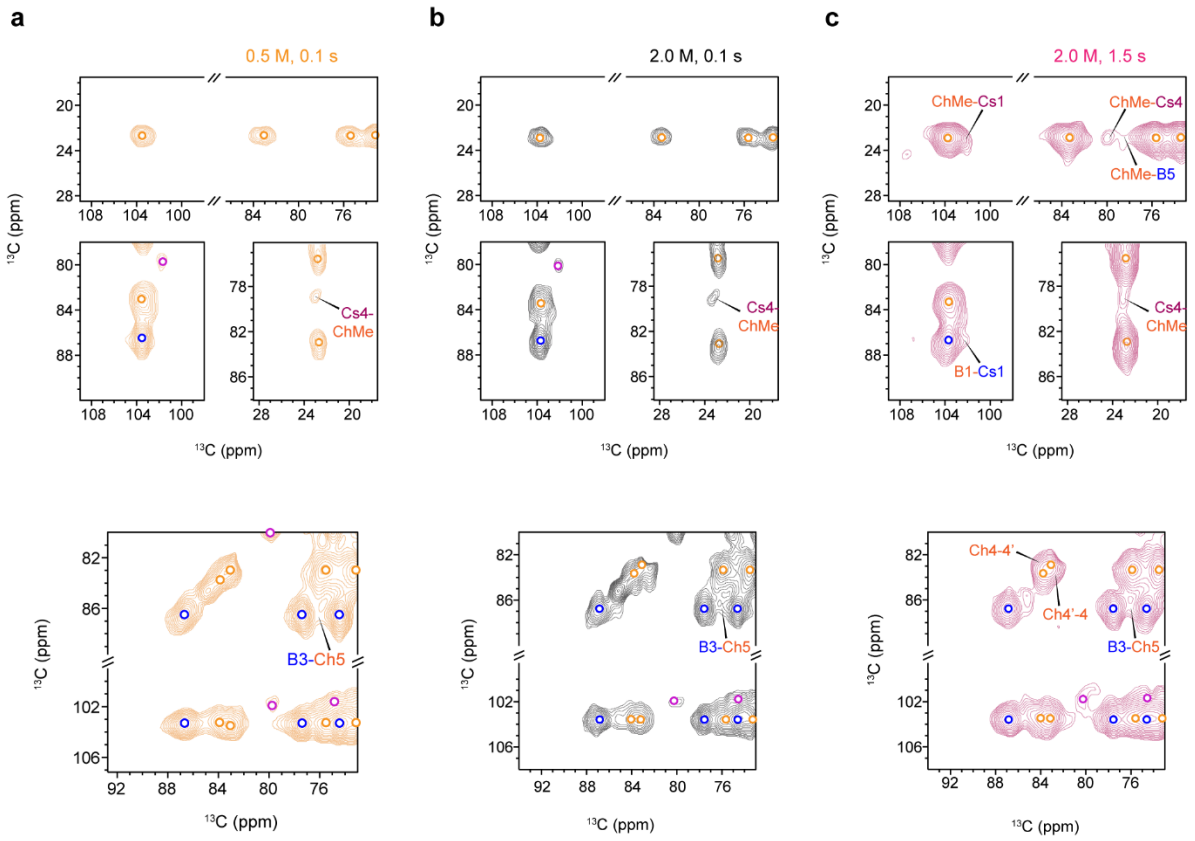


**Figure 6.9 Intermolecular contacts between *A. sydowii* polysaccharides.** Comparison of selected regions were presented for **a,** 0.1 s DARR spectrum of sample cultured at 0.5 M NaCl, **b,** 0.1 s DARR spectrum of sample cultured at 2.0 M NaCl. and **c,** 1.5 s PDSD spectrum of *A. sydowii* sample cultured at 2.0 M NaCl. Open circles indicate the positions of intramolecular signals. Intermolecular interactions are labeled. For example, ChMe-Cs1 represents the cross peak between chitin methyl and chitosan carbon 1. All spectra were measured on an 850 MHz NMR.

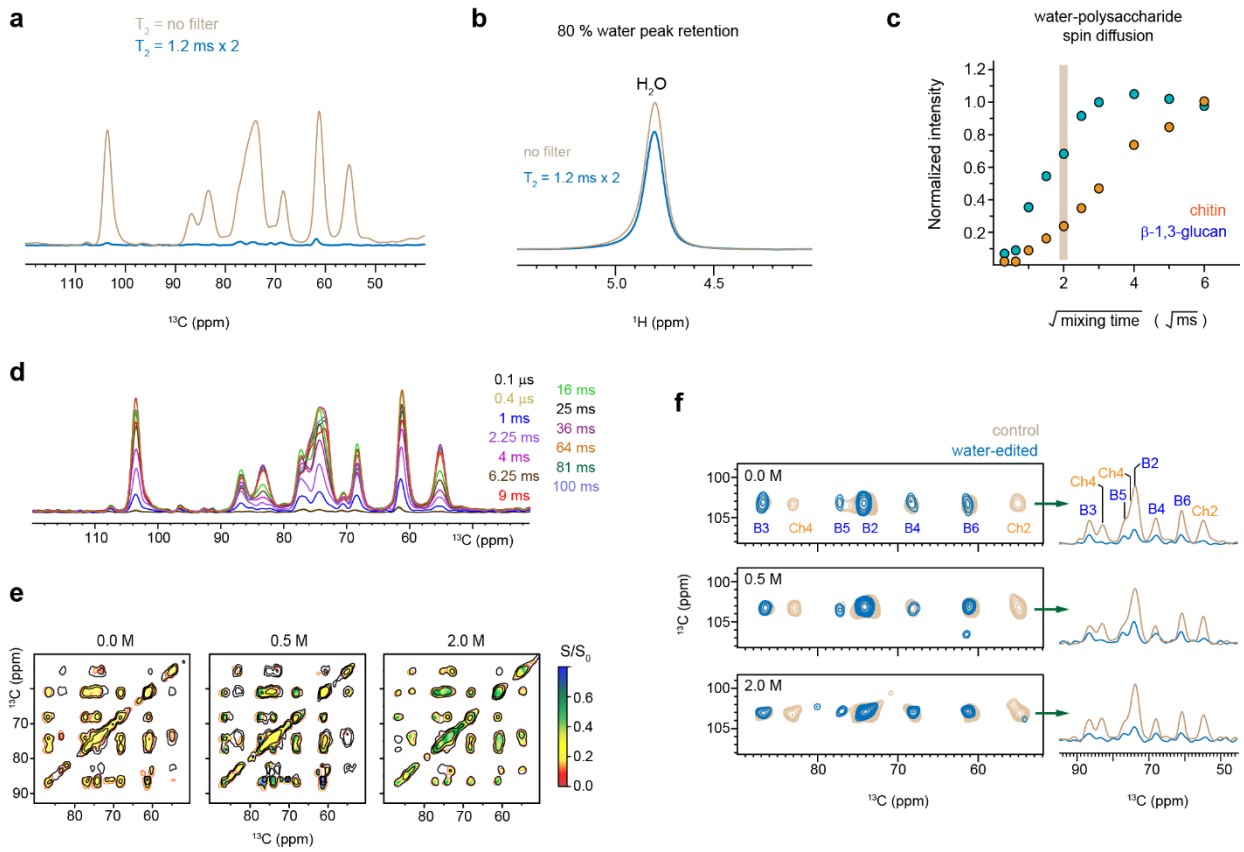


**Figure 6.10 Water-edited experiments for examining polymer hydration. a**, Overlay of $^{13}C$ CP spectra of *A. sydowii* 0.5 M sample (in almond) with a $^{1}H$ $T_2$ filtered spectrum ($T_2$ = 1.2 ms x 2, blue). No spin diffusion was applied. 96% of carbohydrate signals was removed by the filter. **b**, 80% of water magnetization was retained after the $^{1}H$-$T_2$ filter. **c**, Representative water-to-polysaccharide $^{1}H$ spin diffusion build-up curves. The β-1,3-glucan has faster buildup curve than chitin, revealing the hydrophilic nature of β-1,3 glucan. The curves are obtained from peak intensities of water-edited $^{13}C$ spectra. **d**, 1D water-edited $^{13}C$ spectra with different $^{1}H$ mixing times. **e**, Heatmap of relative water-edited intensity ratios ($S/S_0$) of *A. sydowii* cell wall polysaccharides presented as a 2D $^{13}C$-$^{13}C$ correlation spectra. **f**, Overlay of 2D water-edited spectra (blue) and control spectra (almond). The β-1,3-glucan peaks were selectively retained due to the water-association of this polysaccharide. 1D $^{13}C$ cross sections were extracted for comparison. All the spectra were measures on a 400 MHz spectrometer at 10 kHz MAS.

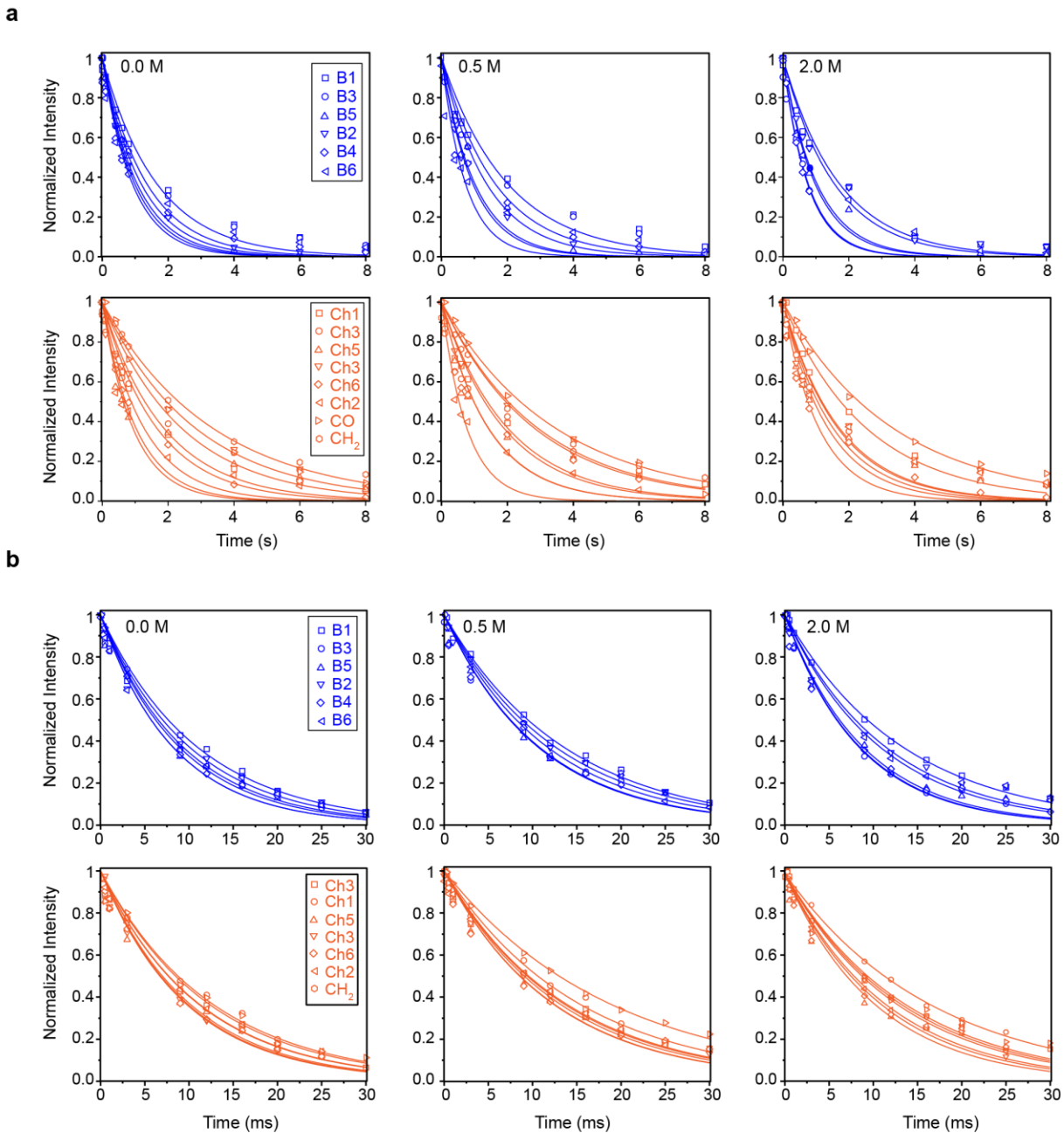


**Figure 6.11 NMR relaxation curves of polysaccharides. a,** $^{13}C$-$T_1$ and **b,** $^{1}H$-$T_{1\rho}$ relaxation curves of polysaccharides in intact *A. sydowii* cell wall across 0 M, 0.5 M and 2 M NaCl. The data are collected on 400 MHz (9.4 Tesla) spectrometer at 10 kHz MAS and best fit is achieved using single exponential equation. Blue curves are β-1,3-glucan and orange curves are chitin. Symbols are used for assigning different carbons in the polysaccharides.

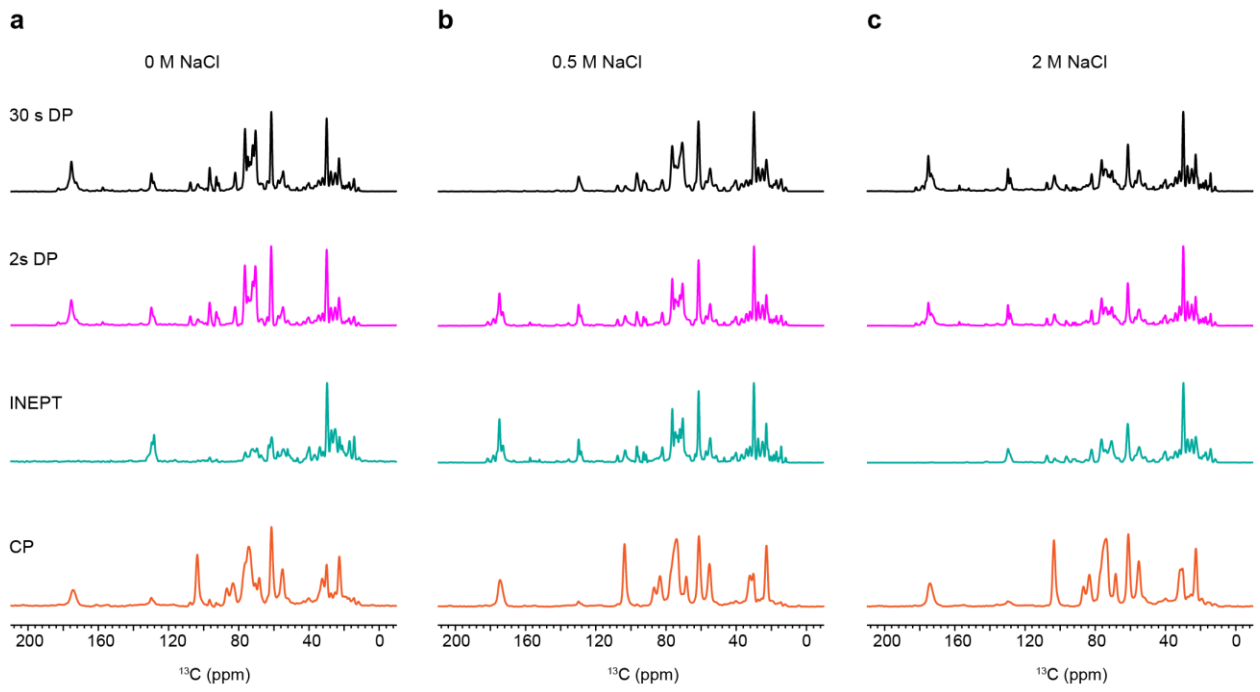


**Figure 6.12 *A. sydowii* proteins and lipids mainly reside in the mobile phase.** An array of 1D $^{13}C$ spectra that detect different components with distinct dynamics are compared for *A. sydowii* samples cultured with **a,** 0 M, **b,** 0.5 M, and **c,** 2 M NaCl. These spectra include the 1D $^{13}C$ DP spectra measured with long recycle delays of 30 s (quantitative detection) and short recycle delays of 2 s (preferential detection of mobile molecules), 1D INEPT spectra (very mobile components) and 1D CP spectra (rigid molecules). All the spectra were measured on 400 MHz NMR under 10 kHz MAS.

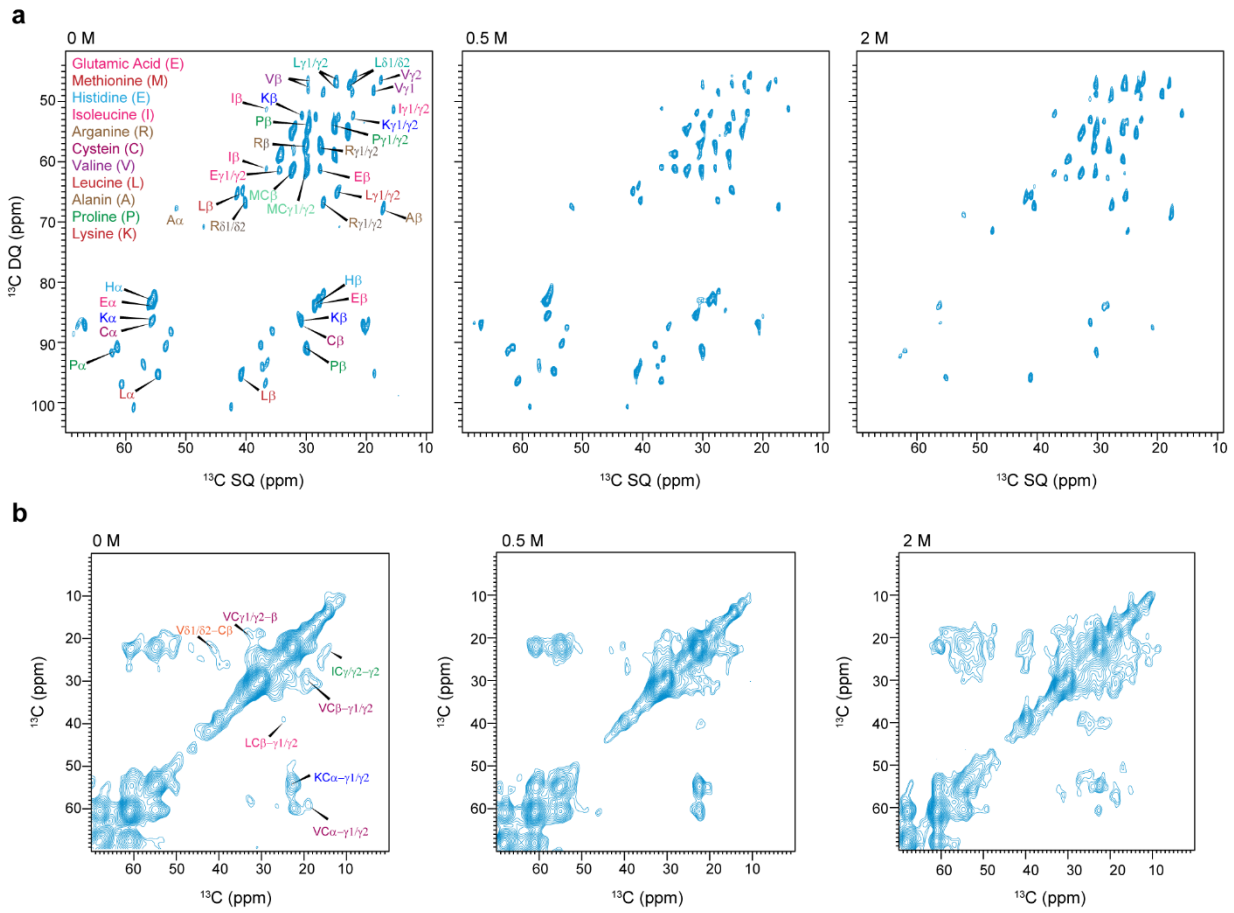


**Figure 6.13 Protein signals of mobile and rigid phases.** **a,** 2D $^{13}$C DP refocused J-INADEQUATE spectra showing signals of mobile proteins. **b,** 2D $^{13}$C-$^{13}$C CP-based 100 ms DARR spectra showing the rigid proteins of 0 M, 0.5 M, and 2 M samples. All the refocused INADEQUATE spectra were measured on a 850 MHz spectrometer at 13 kHz MAS and all the DARR spectra were measured on a 400 MHz spectrometer at 10 kHz MAS.

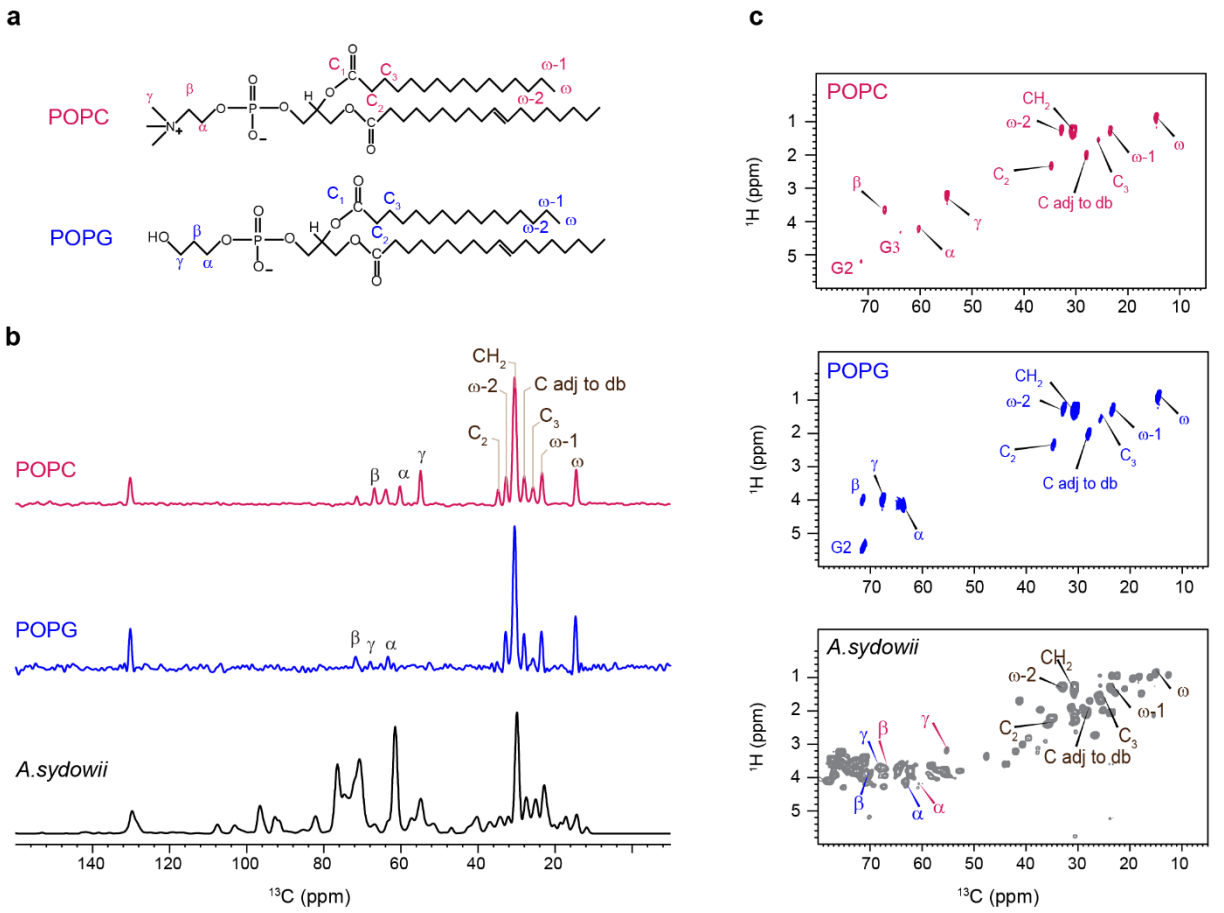


**Figure 6.14 2D $^{1}$H-$^{13}$C refocused INEPT spectra of phospholipids. a,** Chemical structure of model phospholipids POPC and POPG with carbons labeled. **b,** 1D $^{13}$C INEPT spectra and **c,** 2D $^{1}$H-$^{13}$C spectra of POPC, POPG and *A. sydowii*. The spectra were measured in 400 MHz spectrometer at 10 kHz MAS.

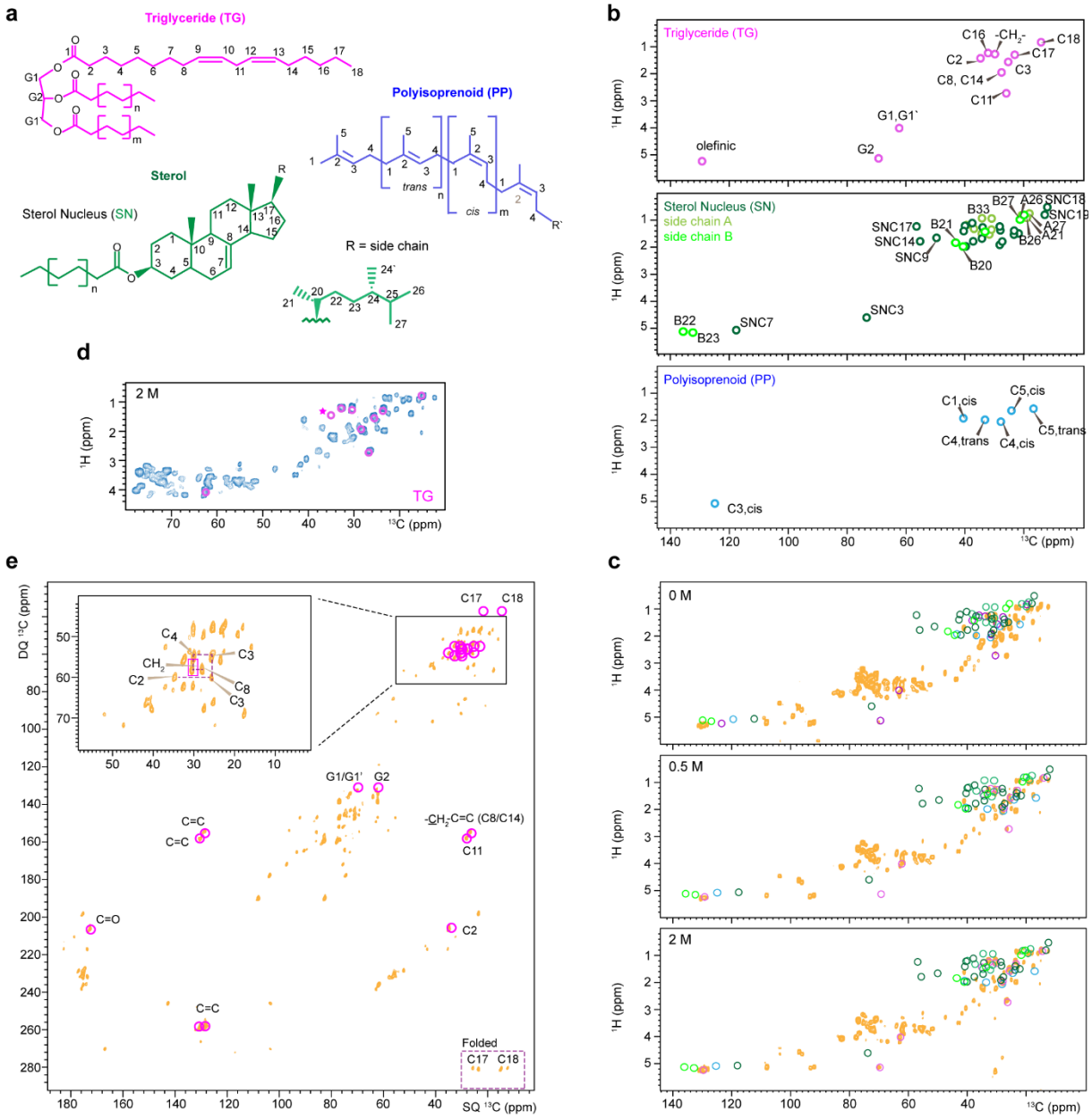


**Figure 6.15 Membrane and lipid components in *A. sydowii*. a,** Representative structures of three lipid components: triglycerides (TG), Sterol (S), and polyisoprenoid (PP). **b,** Simulated 2D $^{1}$H-$^{13}$C spectra using literature reported chemical shifts of TG, and S, and PP documented in **Table 6.6**. **c,** Overlay of 2D $^{1}$H-$^{13}$C refocused INEPT spectra of 0 M, 0.5 M and 2 M samples with stimulated spectra. The spectra do not contain signals from triglycerides and sterols. **d,** Most TG signals are present in 2D $^{1}$H-$^{13}$C refocused INETP spectrum except for the signals of C2 (highlighted by asterisk). **e,** Overlay of simulated TG signals and experimentally measured DP refocused *J*-INADEQUATE spectrum of 2 M *A. sydowii*. All expected signals are present, though the signals are heavily overlapped with other lipids, amino acids, as well as the C5-C6 of some carbohydrates. Note that the signals of the C17-C18 spin pair is folded to the bottom right corner of the spectrum due to limited window width of the spectrum.

**Table 6.1 Molar composition of rigid polysaccharides in *A. sydowii* cell wall.** The numbers were calculated using the integrals of well-resolved cross peaks of β-1,3 glucan and chitin in 2D $^{13}C$-$^{13}C$ CORD spectra. The results were already normalized by the number of scans. Not detected (-).

| Rigid molecules | | | | |
|---|---|---|---|---|
| Polysaccharide | | 0.5 M NaCl | 0 M NaCl | 2 M NaCl |
| β-1,3-glucan | | 55 ± 8%[a] | 51 ± 9%[b] | 40 ± 7%[c] |
| Chitin | | 33 ± 7 %[d] | 39 ± 8%[e] | 50 ± 13%[f] |
| Chitosan | | 12 ± 3% | 10 ± 2% | 10 ± 3% |
| Mobile molecules | | | | |
| GAG | GalN | 6 ± 2% | 4 ± 1% | 13 ± 3% |
| | GalNAc | 5 ± 1% | 4 ± 1% | 9 ± 2% |
| | Gal*p* | 24 ± 3 | 20 ± 6% | 14 ± 7% |
| GM | | 58 ± 15% | 62 ± 13% | 43 ± 17% |
| β-1,3-glucan | | 7 ± 2% | 11 ± 3% | 14 ± 5% |
| α-1,3-glucan | | - | - | 6 ± 1% |

[a] Percentage taken from the average of $B^a$1-3, $B^a$1-5, $B^a$1-2, $B^a$1-4, $B^a$3-5, $B^a$3-4 cross peak integrations.
[b] The average of $B^a$1-3, $B^a$1-5, $B^a$1-2, $B^a$1-4, $B^a$5-6, $B^a$3-4 cross peak integrations.
[c] The average of $B^a$1-3, $B^a$1-5, $B^a$1-4, $B^a$3-2, $B^a$3-5, $B^a$3-4, $B^a$3-6, $B^a$5-4, $B^a$5-2 cross peak integrations.
[d] The average of $Ch^a$1-4, $Ch^a$1-6, $Ch^a$1-2, $Ch^a$4-2, $Ch^a$5-2, cross peak integrations.
[e] The average of $Ch^a$1-2, $Ch^a$1-6, $Ch^a$4-2, $Ch^a$5-2, $Ch^a$3-2, $Ch^a$3-6 cross peak integrations.
[f] The average of $Ch^a$1-4, $Ch^a$1-6, $Ch^a$1-3, $Ch^a$1-2, $Ch^a$4-2, $Ch^a$5-4, $Ch^a$5-2 cross peak integrations.

**Table 6.2 Intermolecular interactions identified by ssNMR.** The table documented the cross peaks between different polysaccharides in *A. sydowii* samples cultured at 0.5 M and 2 M salinity condition. The chemical shifts for the two dimensions of the spectra ($\omega_2$ and $\omega_2$), the assignment of the cross peak, and the type of spectra, and the sample condition are summarized.

| Cross peak | $\omega_1$, $\omega_2$ (ppm, ppm) | 0.5 M 0.1 s PDSD | 0.5M 1.5 s PDSD | $\omega_1$, $\omega_2$ (ppm, ppm) | 2M 0.1 s PDSD | 2M 1.5 s PDSD |
|---|---|---|---|---|---|---|
| Ch4-Ch4’ | 82.3, 84.1 | | x | 82.3, 84.1 | | x |
| Ch4’-Ch4 | 84.1, 82.3 | | x | 84.1, 82.3 | | x |
| ChMe-B5 | 23.1, 77.1 | | x | 23.1, 77.1 | | x |
| B3-Ch5 | 86.1, 76.1 | x | x | 86.1, 76.1 | x | x |
| B5-Ch5 | 68.2, 75.5 | x | x | 68.5, 75.8 | x | x |
| ChMe-Cs4 | 22.9, 79.4 | | x | 22.7, 79.9 | | x |
| ChMe-Cs1 | 22.9, 101.5 | | x | 22.7, 102.0 | | x |
| Ch4-Cs1 | 83.5, 101.5 | | x | | | |
| Ch1/B1-Cs4 | 103.2, 79.5 | | x | | | |
| Cs4-ChMe | 79.2, 22.9 | x | x | 79.2, 22.8 | x | x |
| Cs4-ChCO | 79.7, 173.6 | | | 79.7, 173.8 | | x |
| Cs1-Ch4 | 102.1, 83.1 | | x | | | |
| B1-Cs1 | | | | 86.8, 102.1 | | x |
| B3-Cs4 | 86.5, 79.2 | | x | | | |
| B5-Cs4 | 68.2, 79.2 | | x | | | |
| Cs1-B5 | 101.5, 77.2 | | x | | | |

**Table 6.3 Water-edited intensities of polysaccharides cross peaks.** The intensity ratios were obtained by comparing the peak intensity in water-edited and control spectra, with normalization by the number of scans. Error bars are standard deviations propagated from NMR signal-to-noise ratios.

| | 0.5 M NaCl | | 0 M NaCl | | 2 M NaCl | |
|---|---|---|---|---|---|---|
| | Cross peak | Intensity | Cross peak | Intensity | Cross peak | Intensity |
| β-1,3-glucan | B1-3 | 0.5±0.1 | B1-3 | 0.42±0.09 | B1-3 | 0.4±0.1 |
| | B1-5 | 0.5±0.1 | B1-5 | 0.37±0.09 | B1-5 | 0.5±0.1 |
| | B1-2 | 0.41±0.04 | B1-2 | 0.26±0.03 | B1-2 | 0.31±0.04 |
| | B1-4 | 0.5±0.1 | B1-4 | 0.29±0.07 | B1-4 | 0.5±0.1 |
| | B1-6 | 0.39±0.07 | B1-6 | 0.28±0.06 | B1-6 | 0.34±0.09 |
| | B3-1 | 0.7±0.1 | B3-1 | 0.43±0.06 | B3-1 | 0.5±0.1 |
| | B3-2 | 0.61±0.09 | B3-5 | 0.34±0.06 | B3-5 | 0.4±0.1 |
| | B3-4 | 0.5±0.1 | B3-2 | 0.44±0.06 | B3-2 | 0.3±0.1 |
| | B3-6 | 0.80±0.07 | B3-4 | 0.38±0.07 | B3-4 | 0.4±0.1 |
| | B5-1 | 0.45±0.08 | B3-6 | 0.59±0.06 | B3-6 | 0.5±0.1 |
| | B5-3 | 0.7±0.2 | B5-1 | 0.35±0.07 | B5-1 | 0.36±0.09 |
| | B5-2 | 0.40±0.07 | B5-3 | 0.4±0.1 | B5-3 | 0.5±0.2 |
| | B5-4 | 0.44±0.08 | B5-2 | 0.25±0.07 | B5-2 | 0.21±0.07 |
| | B5-6 | 0.39±0.05 | B5-4 | 0.28±0.06 | B5-4 | 0.36±0.07 |
| | B2-1 | 0.39±0.04 | B5-6 | 0.30±0.05 | B5-6 | 0.37±0.06 |
| | B2-3 | 0.6±0.1 | B2-1 | 0.29±0.03 | B2-1 | 0.25±0.04 |
| | B2-5 | 0.66±0.09 | B2-3 | 0.39±0.09 | B2-3 | 0.6±0.2 |
| | B2-4 | 0.6±0.1 | B2-5 | 0.53±0.09 | B2-5 | 0.5±0.1 |
| | B2-6 | 0.31±0.04 | B2-4 | 0.36±0.07 | B2-4 | 0.38±0.07 |
| | B4-1 | 0.6±0.1 | B2-6 | 0.25±0.04 | B2-6 | 0.26±0.05 |
| | B4-3 | 0.6±0.1 | B4-1 | 0.36±0.07 | B4-1 | 0.5±0.1 |
| | B4-5 | 0.6±0.1 | B4-3 | 0.37±0.09 | B4-3 | 0.3±0.1 |
| | B4-2 | 0.43±0.09 | B4-5 | 0.38±0.07 | B4-5 | 0.4±0.1 |
| | B4-6 | 0.45±0.09 | B4-2 | 0.42±0.08 | B4-2 | 0.28±0.08 |
| | | | B4-6 | 0.26±0.07 | B4-6 | 0.33±0.09 |
| Chitin | Ch1-3 | 0.13±0.02 | Ch1-3 | 0.21±0.02 | Ch1-3 | 0.14±0.09 |
| | Ch1-6 | 0.38±0.07 | Ch1-5 | 0.38±0.07 | Ch1-3 | 0.23±0.04 |
| | Ch4-1 | 0.12±0.09 | Ch1-2 | 0.12±0.05 | Ch4-1 | 0.2±0.1 |
| | Ch4-4 | 0.23±0.08 | Ch4-4 | 0.22±0.08 | Ch5-1 | 0.27±0.08 |
| | Ch5-1 | 0.35±0.06 | Ch5-1 | 0.42±0.06 | Ch5-3 | 0.06±0.04 |
| | Ch5-4 | 0.15±0.09 | Ch5-4 | 0.17±0.09 | Ch5-6 | 0.19±0.5 |
| | Ch5-3 | 0.21±0.03 | Ch5-3 | 0.21±0.05 | Ch5-2 | 0.2±0.1 |
| | Ch5-6 | 0.27±0.05 | Ch5-6 | 0.31±0.04 | Ch3-1 | 0.26±0.07 |
| | Ch3-1 | 0.22±0.05 | Ch5-2 | 0.09±0.06 | Ch3-5 | 0.1±0.1 |
| | Ch3-5 | 0.12±0.01 | Ch3-1 | 0.31±0.05 | Ch3-6 | 0.29±0.09 |
| | Ch3-6 | 0.21±0.07 | Ch3-5 | 0.29±0.02 | Ch3-2 | 0.14±0.08 |
| | Ch3-2 | 0.13±0.07 | Ch3-6 | 0.23±0.06 | Ch2-1 | 0.2±0.1 |
| | Ch2-1 | 0.22±0.07 | Ch3-2 | 0.15±0.05 | Ch2-6 | 0.2±0.1 |

Table 6.3 (cont'd)

| | | | | | | |
|---|---|---|---|---|---|---|
| | Ch2-4 | 0.2±0.1 | Ch2-1 | 0.17±0.09 | Ch2-2 | 0.1±0.04 |
| | Ch2-5 | 0.12±0.07 | Ch2-3 | 0.08±0.07 | | |
| | Ch2-3 | 0.13±0.06 | | | | |
| | Ch2-6 | 0.2±0.1 | | | | |

**Table 6.4 $^{13}$C-$T_1$ and $^{1}$H-$T_{1\rho}$ relaxation time constants of polysaccharides in *A. sydowii*.** A single exponential equation was used to fit the $T_1$ data $I(t) = e^{-t/T_1}$. A single exponential equation was used to fit the $T_{1\rho}$ data: $I(t) = e^{-t/T_{1\rho}}$. Error bars are standard deviations of the fit parameters.

| Sample Type | Cross peaks | $T_1$ (s) | Cross peaks | $T_{1\rho}$ (ms) |
|---|---|---|---|---|
| 0.5 M NaCl | B3 | 1.5±0.1 | B1 | 13.8±0.8 |
| | B5 | 0.8±0.2 | B3 | 11±1 |
| | B2 | 1.6±0.3 | B5 | 11±1 |
| | B4 | 0.7±0.3 | B2 | 12.7±0.9 |
| | B6 | 0.5±0.1 | B4 | 11±1 |
| | Ch1 | 2.2±0.2 | B6 | 12±1 |
| | Ch5 | 1.0±0.2 | Ch1 | 13.8±0.8 |
| | Ch3 | 2.2±0.4 | Ch4 | 15.3±0.8 |
| | Ch6 | 0.8±0.1 | Ch5 | 12.4±0.9 |
| | Ch2 | 2.0±0.4 | Ch3 | 13.1±0.8 |
| | | | Ch6 | 12±1 |
| | | | Ch2 | 13.5±0.8 |
| 0 M NaCl | B1 | 1.7 ±0.2 | B1 | 11±0.6 |
| | B3 | 1.28±0.07 | B3 | 8.9±0.9 |
| | B5 | 0.9±0.1 | B5 | 8.3±0.8 |
| | B2 | 1.4±0.2 | B2 | 10.1±0.6 |
| | B4 | 0.88±0.05 | B4 | 8.3±0.8 |
| | B6 | 0.9±0.1 | B6 | 9.4±0.6 |
| | Ch1 | 1.7±0.2 | Ch1 | 11.0±0.6 |
| | Ch4 | 2.9±0.3 | Ch4 | 12.6±0.9 |
| | Ch5 | 1.1±0.2 | Ch5 | 9.8±0.9 |
| | Ch3 | 1.4±0.2 | Ch3 | 10.1±0.7 |
| | Ch2 | 1.5±0.3 | Ch6 | 9.7±0.6 |
| | | | Ch2 | 11.1±0.6 |
| 2.0 M NaCl | B1 | 1.7±0.2 | B1 | 13.5±0.6 |
| | B3 | 0.77±0.07 | B3 | 8.6±0.7 |
| | B5 | 0.98±0.09 | B2 | 8.9±0.7 |
| | B2 | 1.6±0.2 | B4 | 11±1 |
| | B6 | 1.0±0.1 | B6 | 11.6±0.9 |
| | Ch1 | 1.7±0.2 | Ch4 | 8.5±0.9 |
| | Ch4 | 2.4±0.4 | Ch5 | 10.9±0.8 |
| | Ch5 | 1.3±0.2 | Ch3 | 11.2±0.9 |
| | Ch3 | 1.7±0.3 | Ch6 | 11.7±0.8 |
| | Ch2 | 1.5±0.2 | Ch2 | 13.0±0.9 |

**Table 6.5 Water-edited intensities of amino acid residues.** The intensity ratios are obtained by comparing the peak intensity in 1D $^{13}C$ water-edited and control spectra, with normalization by the number of scans. Error bars are standard deviations propagated from NMR signal-to-noise ratio.

| 0.5 M NaCl | | 0 M NaCl | | 2 M NaCl | |
|---|---|---|---|---|---|
| $^{13}C$ | Intensity | $^{13}C$ | Intensity | $^{13}C$ | Intensity |
| 52.0 | 0.14± 0.09 | 52.0 | 0.2 ± 0.1 | 52.0 | 0.17 ± 0.07 |
| 43.2 | 0.12 ± 0.09 | 46.9 | 0.3 ± 0.1 | 43.2 | 0.15 ± 0.07 |
| 40.3 | 0.20 ± 0.09 | 43.2 | 0.20 ± 0.09 | 40.3 | 0.22 ± 0.07 |
| 32.6 | 0.11 ± 0.08 | 40.3 | 0.3 ± 0.1 | 32.6 | 0.14 ± 0.07 |
| 30.1 | 0.37 ± 0.09 | 30.1 | 0.5 ± 0.1 | 30.1 | 0.28 ± 0.07 |
| 27.6 | 0.27 ± 0.09 | 27.6 | 0.30 ± 0.09 | 27.6 | 0.16 ± 0.07 |
| 25.2 | 0.27 ± 0.09 | 25.2 | 0.4 ± 0.1 | 25.2 | 0.15 ± 0.07 |
| 19.2 | 0.16 ± 0.09 | 19.2 | 0.2 ± 0.1 | 19.2 | 0.14 ± 0.07 |
| 17.3 | 0.36± 0.09 | 17.3 | 0.6 ± 0.1 | 14.6 | 0.29 ± 0.07 |
| 14.6 | 0.34 ± 0.09 | 14.6 | 0.6 ± 0.1 | 12.0 | 0.11 ± 0.07 |
| 12.0 | 0.20± 0.09 | 12.0 | 0.4 ± 0.1 | | |

**Table 6.6 Chemical shifts of lipids. Chemical shifts of PC and PG lipids are from measurements.** The other components were from literature. Not applicable (/). Unidentified (-).

| Lipid | Carbon | $^{13}C$ (ppm) | $^{1}H$ (ppm) | Reference | Lipid | Carbon | $^{13}C$ (ppm) | $^{1}H$ (ppm) | Reference |
|---|---|---|---|---|---|---|---|---|---|
| PC | C2 | 34.8 | 2.3 | | PG | C2 | 34.8 | 2.3 | |
| | C3 | 25.7 | 1.6 | | | C3 | 25.7 | 1.6 | |
| | -CH2 | 30.5 | 1.31 | | | -CH2 | 30.5 | 1.31 | |
| | $\omega - 2$ | 32.7 | 1.3 | | | $\omega - 2$ | 32.7 | 1.3 | |
| | $\omega - 1$ | 23.4 | 1.3 | | | $\omega - 1$ | 23.4 | 1.3 | |
| | $\omega$ | 14.02 | 0.9 | | | $\omega$ | 14.02 | 0.9 | |
| | α | 60.3 | 4.3 | | | α | 63.4 | 4.1 | |
| | β | 66.8 | 3.6 | | | β | 71.1 | 4.0 | |
| | γ | 54.7 | 3.2 | | | γ | 68.1 | 3.9 | |
| | G1 | 63.5 | - | | | G1 | - | - | |
| | G2 | 71.4 | 4.4 | | | G2 | 71.4 | 5.3 | |
| | G3 | 63.8 | 4.0 | | | G3 | - | - | |
| Triglycerides | C1 | 172.4 | / | Chrissian et al. 2020[47] Lamon et al. 2023[27] | Polyisoprenoids | C1 trans | 39.9 | 1.94 | Chrissian et al 2020[47] |
| | C2 | 34.3 | 1.44 | | | C1, trans | 134.4 | / | |
| | C3 | 25.0 | 1.57 | | | C3 trans | 124.4 | 5.07 | |
| | $-(CH2)_n-$ | 29.3-29.9 | 1.26-1.29 | | | C4, trans | 27.1 | 2.06 | |
| | C8,C14 | 27.3 | 1.96 | | | C5, trans | 16.0 | 1.56 | |
| | C9-C10,C12,13 | 128.1-130.0 | 5.26-5.29 | | | C1, cis | 32.4 | 1.99 | |
| | C11 | 25.6 | 2.74 | | | C2, cis | 135.0 | / | |
| | C16 | 32.0 | 1.25 | | | C3, cis | 124.8 | 5.07 | |
| | C17 | 22.8 | 1.29 | | | C4, cis | 26.7 | 1.99 | |
| | C18 | 14.1 | 0.86 | | | C5, cis | 23.5 | 1.63 | |
| | G1,G’ | 62.2 | 4.04(α), 4.25 (β) | | | C1 | 37.1 | 1.13 (α), 1.79 (β) | |

Table 6.6 (cont'd)

| | | | | | | | | | |
|---|---|---|---|---|---|---|---|---|---|
| Triglycerides | G2 | 69.1 | 5.18 | | $\Delta^7$- sterol nucleus | C2 | 27.7 | 1.79 (α), 1.39 (β) | |
| Sterol side chain A | C20 | 36.9 | 1.33 | Suttiarporn et al. 2015[54] Chrissian et al 2020[47] | | C3 | 73.1 | 4.62 | |
| | C21 | 19.1 | 0.93 | | | C4 | 34.1 | 1.69 (α), 1.28 (β) | Consolacion et al. 2012[53] Chrissian et al. 2020[47] |
| | C22 | 34.2 | 0.93 (α), 1.49 (β) | | | C5 | 40.2 | 1.42 | |
| | C23 | 30.9 | 0.93 (α), 1.37 (β) | | | C6 | 29.7 | - | |
| | C24 | 39.2 | 1.2 | | | C7 | 117.6 | 5.12 | |
| | C25 | 31.7 | 1.55 | | | C8 | 139.7 | / | |
| | C26 | 20.7 | 0.81 | | | C9 | 49.5 | 1.66 | |
| | C27 | 18.1 | 0.77 | | | C10 | 34.2 | / | |
| Sterol side chain B | C20 | 40.6 | 1.98 | Tuckey et al. 2012[55] | | C11 | 21.7 | 1.54 (α), 1.48(β) | |
| | C21 | 21.3 | 1.00 | | | C12 | 39.8 | 1.21 (α), 1.97 (β) | |
| | C22 | 135.6 | 5.15 | | | C13 | 43.3 | / | |
| | C23 | 132.0 | 5.20 | | | C14 | 55.1 | 1.80 | |
| | C24 | 43.1 | 1.83 | | | C15 | 23.2 | 1.55 (α), 1.97 (β) | |
| | C25 | 33.3 | 1.44 | | | C16 | 28.1 | 1.89 (α), 1.26 (β) | |
| | C26 | 19.9 | 0.81 | | | C17 | 56.3 | 1.23 | |
| | C27 | 19.9 | 0.81 | | | C18 | 11.9 | 0.53 | |
| | | | | | | C19 | 12.9 | 0.79 | |

**Table 6.7 Recipe of mineral-base liquid medium.** The pH is adjusted to 6.0 with $H_3PO_4$ or 0.25 M KOH. Each sample uses 100 mL of medium that contains 2 g of $^{13}C$- glucose and 0.2 g $^{15}NH_4NO_3$.

| Reagent | For 1 liter |
|---|---|
| $CuSO_4 \cdot 5H_2O$ | 7.8 mg |
| $FeSO_4 \cdot 7H_2O$ | 18 mg |
| $MgSO_4 \cdot 7H_2O$ | 500 mg |
| $ZnSO_4$ | 10 mg |
| KCl | 50 mg |
| $K_2HPO_4$ | 1 g |
| $^{15}NH_4NO_3$ | 2 g |
| $CuSO_4 \cdot 5H_2O$ | 7.8 mg |

**Table 6.8 Solid-state NMR experiments and parameters for each of the three *A. Sydowii* samples.** To be quantitative, direct pulse (DP) experiments with 30 s long recycling delay were used. cross-polarization, most rigid molecules. With DP and a shorter recycling delay of 2 seconds, suppress the rigid molecules from the spectra, and with Insensitive Nuclei Enhanced by Polarization Transfer (INEPT) the most mobile molecules were selected. For 2D $^{13}C$-$^{13}C$ correlation experiments, DARR (Dipolar Assisted Rotational Resonance) allowed to resolve rigid intramolecular peaks. While 1.5 s PDSD (Proton Driven Spin Diffusion) detects intra- and inter-molecular peaks. 2D DQ-SQ, DP J-INADEQAUTE and CP INADEQUATE spectra were used to detect through-bond correlations. The experimental parameters include the $^{1}H$ Larmor frequency, total experiment time (t), recycle delay (d1), number of scans (NS), The number of points for the direct (td2) and indirect (td1) dimensions, the acquisition time of the direct dimension (aq2) and the evolution time of indirect dimension (aq1), spectral width (sw1 and sw2), mixing time ($t_m$), increment delay (IN_F) and T filter times. * Indicates the water-polysaccharide spin diffusion and the DARR mixing time. The processing parameters include the window function and associated parameters.

| | Acquisition parameters | | | | | | | | | | | | | Processing parameters | |
|---|---|---|---|---|---|---|---|---|---|---|---|---|---|---|---|
| Experiment | $\omega_{0,\,1H}$ (MHz) | t (h) | d1 (s) | NS | td2 | td1 | aq2 (ms) | aq1 (ms) | sw2 [1] | sw1 [1] | $t_m$ (ms) | IN_F (μs) | T filters | Window function | Parameter |
| 1D CP | 850 | 0.1 | 2 | 256 | 7360 | | 14.7 | | 1169 | | | | | QSINE | SSB 3 |
| 1D DP | 850 | 0.1 | 2 | 256 | 7360 | | 14.7 | | 1169 | | | | | QSINE | SSB 3 |
| 1D DP | 850 | 2.1 | 30 | 256 | 7360 | | 14.7 | | 1169 | | | | | QSINE | SSB 3 |
| 1D INEPT | 400 | 0.1 | 3 | 64 | 3600 | | 36.0 | | 496.6 | | | | | GM | LB-5, GB0.01 |
| 1D $^{13}C$ T1 | 400 | 3.5 | 2 | 256 | 1600 | | 16.0 | | 496.6 | | | | $T_1(10^{-3}$-8 s) | | |
| 1D $^{1}H$ T1ρ | 400 | | 2 | 256 | 1400 | | 14.0 | | 496.6 | | | | SL ($10^{-3}$-30 ms) | | |
| 2D DARR | 850 | 4.2 | 2 | 48 | 1472 | 512 | 14.7 | 5.1 | 233.9 | 233.9 | 100 | 20 | | QSINE | SSB 3 |
| 2D CORD | 800 | 4.2 | 1.7 | 16 | 2400 | 560 | 17.9 | 7.2 | 332.8 | 191.2 | 53 | 26 | | QSINE | SSB 4 |
| 2D PDSD | 850 | 13.6 | 2 | 32 | 2496 | 512 | 24.9 | 5.1 | 233.9 | 233.9 | 1500 | 20 | | QSINE | SSB 2.8 |

Table 6.8 (cont'd)

| | | | | | | | | | | | | | | | |
|---|---|---|---|---|---|---|---|---|---|---|---|---|---|---|---|
| 2D DP INADE` | 850 | 4.5 | 2 | 32 | 7360 | 256 | 14.7 | 2.5 | 1169 | 243.4 | | 19.2 | | QSINE | SSB 3 |
| Water edited - control | 400 | 17 | 1.6 | 256 | 1400 | 152 | 14.0 | 4.9 | 496.6 | 152.8 | $10^{-4}$ /50* | 65 | $T_2$ $10^{-4}$ ms | QSINE | SSB 4.5 |
| Water edited | 400 | 17 | 1.6 | 256 | 1400 | 152 | 14.0 | 4.9 | 496.6 | 152.8 | 4/50 * | 65 | $T_2$ 1.2 ms | QSINE | SSB 4.5 |
| C-H INEPT | 400 | | 3.0 | 8 | 2048 | 160 | 20.0 | 11.0 | 496.6 | 18.1 | | 137 | | QSINE | SSB 3 |

**Table 6.9 $^{13}C$ and $^{15}N$ chemical shifts of *A. sydowii* polysaccharides and proteins.** Superscripts are used to denote different allomorphs. Underline denotes the $^{13}C$ connectivity with ambiguity. Not applicable (/). Unidentified (-). Unknown: (Unk).

| Polysaccharides | NMR abbreviation | C1 (ppm) | C2 (ppm) | C3 (ppm) | C4 (ppm) | C5 (ppm) | C6 (ppm) | CO (ppm) | $CH_3$ (ppm) | References |
|---|---|---|---|---|---|---|---|---|---|---|
| β-1,3-glucan | B | 103.6 | 74.4 | 86.4 | 68.7 | 77.1 | 61.3 | / | / | Shim et al. 2007[58] |
| Chitin | $Ch^a$ | 103.3 | 55.5 | 72.9 | 84.5 | 76.2 | 60.7 | 174.6 | 22.7 | Fernando et al. 2021[37] |
| | $Ch^b$ | 103.5 | 55.2 | 73.4 | 84.4 | 75.9 | 60.0 | 173.4 | 22.7 | |
| | $Ch^c$ | 103.5 | 55.4 | 73.3 | 83.7 | 75.9 | 60.7 | 173.4 | 22.7 | |
| | $Ch^d$ | 103.6 | 55.0 | 73.2 | 83.4 | 75.5 | 60.5 | 174.1 | 22.4 | |
| | $Ch^e$ | 103.2 | 54,8 | 73.5 | 82.5 | 75.2 | 60.9 | 175.1 | 22.4 | |
| Chitosan | $Cs^a$ | 102.2 | 55.6 | 74.5 | 80.4 | 74.9 | 60.7 | / | / | |
| | $Cs^b$ | 101.9 | 55.7 | 72.9 | 80.0 | 74.3 | 60.5 | / | / | |
| | $Cs^c$ | 101.4 | 55.5 | 73.5 | 79.1 | 75.3 | 61.0 | / | / | |
| | $Cs^d$ | 101.4 | 55.5 | 73.5 | 79.1 | 75.3 | 61.0 | / | / | |
| α-1,3-glucan | A | 101.0 | 71.9 | 84.6 | 69.5 | 71.7 | 60.5 | / | / | Bhanja et al.2014[57] |
| α-1,4-galactan | Gal | 93.2 | 72.2 | 70.7 | 73.5 | 72.5 | 60.9 | / | / | Chakraborty et al. 2021[24] |
| α-1,4-galactosamine | GalN | 91.7 | 54.8 | 71.1 | 81.1 | - | - | / | / | |
| α-1,4-N-acetylgalactosamine | GalNAc | 95.7 | 57.5 | 75.2 | 76.9 | - | - | - | - | |
| α-1,6-manose | $Mn^{1,6}$ | 102.7 | 70.6 | 73.2 | 72.5 | 73.7 | 66.1 | / | / | |
| α-1,2-manose | $Mn^{1,2}$ | 101.3 | 78.7 | 71.2 | 67.7 | 73.9 | 61.7 | / | / | |
| β-1,5 galactofuranose | Galf | 107.5 | 81.5 | 77.7 | 83.5 | 71.5 | 63.4 | / | / | |
| Unknown | Unk | 102.6 | 84.9 | 73.5 | 68.5 | - | - | | | |
| Amino Acid | Abbreviation | Cα | Cβ | Cγ/γ1 | Cγ2 | Cδ/δ1 | | | | |
| Glutamic Acid | E | 55.8 | 27.8 | 34.4 | | | | | | Fritzsching. et al 2013[58] |
| Methionine | M | | 32.8 | 30.1 | | | | | | |
| Histidine | H | 55.8 | 28.2 | | | | | | | |

Table 6.9 (cont'd)

| | | | | | | | | | | |
|---|---|---|---|---|---|---|---|---|---|---|
| Isoleucine | I | | 37.3 | 25.3 | 15.6 | | | | | |
| Arginine | R | | | 27.7 | | 40.4 | | | | |
| Cysteine | C | 55.8 | 31.0 | | | | | | | |
| Valine | V | | 30.0 | 19.2 | | | | | | |
| Leucine | L | | | 25.3 | | 22.4 | | | | |
| Alanine | A | 52.1 | 17.6 | | | | | | | |
| Proline | P | 61.7 | 30.1 | 25.8 | | | | | | |
| Lysine | K | 55.2 | 41.3 | 40.8 | 25.0 | | | | | |